Jordan Journal of Mechanical and Industrial Engineering (JJMIE)

JJMIE is a high-quality scientific journal devoted to fields of Mechanical and Industrial Engineering. It is published by the Hashemite University in corporation with the Jordanian Scientific Research Support Fund.

SUBMISSION ADDRESS:

Prof. **Mousa S. Mohsen**, Editor-in-Chief
Jordan Journal of Mechanical & Industrial Engineering,
Hashemite University, PO Box 330127, Zarqa, 13133 , Jordan
E-mail: jjmie@hu.edu.jo

Hashemite Kingdom of Jordan

Hashemite University

Jordan Journal of Mechanical and Industrial Engineering

JJMIE

An International Peer-Reviewed Scientific Journal

http://jjmie.hu.edu.jo/

ISSN 1995-6665

Jordan Journal of Mechanical and Industrial Engineering (JJMIE)

JJMIE is a high-quality scientific journal devoted to fields of Mechanical and Industrial Engineering. It is published by the Hashemite University in corporation with the Jordanian Scientific Research Support Fund.

Introduction: The Editorial Board is very committed to build the Journal as one of the leading international journals in mechanical and industrial engineering sciences in the next few years. With the support of the Ministry of Higher Education and Scientific Research and Jordanian Universities, it is expected that a heavy resource to be channeled into the Journal to establish its international reputation. The Journal's reputation will be enhanced from arrangements with several organizers of international conferences in publishing selected best papers of the conference proceedings.

Aims and Scope: Jordan Journal of Mechanical and Industrial Engineering (JJMIE) is a refereed international journal to be of interest and use to all those concerned with research in various fields of, or closely related to, mechanical and industrial engineering disciplines. Jordan Journal of Mechanical and Industrial Engineering aims to provide a highly readable and valuable addition to the literature which will serve as an indispensable reference tool for years to come. The coverage of the journal includes all new theoretical and experimental findings in the fields of mechanical and industrial engineering or any closely related fields. The journal also encourages the submission of critical review articles covering advances in recent research of such fields as well as technical notes.

Guide for Authors

Manuscript Submission

High-quality submissions to this new journal are welcome now and manuscripts may be either submitted online or mail.

Online: For online submission upload one copy of the full paper including graphics and all figures at the online submission site, accessed via E-mail: jjmie@hu.edu.jo. The manuscript must be written in MS Word Format. All correspondence, including notification of the Editor's decision and requests for revision, takes place by e-mail and via the Author's homepage, removing the need for a hard-copy paper trail.

By Mail: Manuscripts (1 original and 3 copies) accompanied by a covering letter may be sent to the Editor-in-Chief. However, a copy of the original manuscript, including original figures, and the electronic files should be sent to the Editor-in-Chief. Authors should also submit electronic files on disk (one disk for text material and a separate disk for graphics), retaining a backup copy for reference and safety.

Note that contributions may be either submitted online or sent by mail. Please do NOT submit via both routes. This will cause confusion and may lead to delay in article publication. Online submission is preferred.

Submission address and contact:

Prof. **Mousa S. Mohsen**, Editor-in-Chief
Jordan Journal of Mechanical & Industrial Engineering,
Hashemite University,
PO Box 330127, Zarqa, 13133 , Jordan
E-mail: jjmie@hu.edu.jo

Types of contributions: Original research papers

Corresponding author: Clearly indicate who is responsible for correspondence at all stages of refereeing and publication, including post-publication. Ensure that telephone and fax numbers (with country and area code) are provided in addition to the e-mail address and the complete postal address. Full postal addresses must be given for all co-authors.

Original material: Submission of an article implies that the work described has not been published previously (except in the form of an abstract or as part of a published lecture or academic thesis), that it is not under consideration for publication elsewhere, that its publication is approved by all authors and that, if accepted, it will not be published elsewhere in the same form, in English or in any other language, without the written consent of the Publisher. Authors found to be deliberately contravening the submission guidelines on originality and exclusivity shall not be considered for future publication in this journal.

Supplying Final Accepted Text on Disk: If online submission is not possible: Once the paper has been accepted by the editor, an electronic version of the text should be submitted together with the final hardcopy of the manuscript. The electronic version must match the hardcopy exactly. We accept MS Word format only. Always keep a backup copy of the electronic file for reference and safety. Label the disk with your name. Electronic files can be stored on CD.

Notification: Authors will be notified of the acceptance of their paper by the editor. The Publisher will also send a notification of receipt of the paper in production.

Copyright: All authors must sign the Transfer of Copyright agreement before the article can be published. This transfer agreement enables Jordan Journal of Mechanical and Industrial Engineering to protect the copyrighted material for the authors, but does not relinquish the authors' proprietary rights. The copyright transfer covers the exclusive rights to reproduce and distribute the article, including reprints, photographic reproductions, microfilm or any other reproductions of similar nature and translations.

PDF Proofs: One set of page proofs in PDF format will be sent by e-mail to the corresponding author, to be checked for typesetting/editing. The corrections should be returned within 48 hours. No changes in, or additions to, the accepted (and subsequently edited) manuscript will be allowed at this stage. Proofreading is solely the author's responsibility. Any queries should be answered in full. Please correct factual errors only, or errors introduced by typesetting. Please note that once your paper has been proofed we publish the identical paper online as in print.

Author Benefits

Page charge: Publication in this journal is free of charge.

Free off-prints: Three journal issues of which the article appears in along with twenty-five off-prints will be supplied free of charge to the corresponding author. Corresponding authors will be given the choice to buy extra off-prints before printing of the article.

Manuscript Preparation:

General: Editors reserve the right to adjust style to certain standards of uniformity. Original manuscripts are discarded after publication unless the Publisher is asked to return original material after use. If online submission is not possible, an electronic copy of the manuscript on disk should accompany the final accepted hardcopy version. Please use MS Word for the text of your manuscript.

Structure: Follow this order when typing manuscripts: Title, Authors, Affiliations, Abstract, Keywords, Introduction, Main text, Conclusions, Acknowledgements, Appendix, References, Figure Captions, Figures and then Tables. For submission in hardcopy, do not import figures into the text - see Illustrations. For online submission, please supply figures imported into the text AND also separately as original graphics files. Collate acknowledgements in a separate section at the end of the article and do not include them on the title page, as a footnote to the title or otherwise.

Text Layout: Use double spacing and wide (3 cm) margins. Ensure that each new paragraph is clearly indicated. Present tables and figure legends on separate pages at the end of the manuscript. If possible, consult a recent issue of the journal to become familiar with layout and conventions. All footnotes (except for table and corresponding author footnotes) should be identified with superscript Arabic numbers. To conserve space, authors are requested to mark the less important parts of the paper (such as records of experimental results) for printing in smaller type. For long papers (more that 4000 words) sections which could be deleted without destroying either the sense or the continuity of the paper should be indicated as a guide for the editor. Nomenclature should conform to that most frequently used in the scientific field concerned. Number all pages consecutively; use 12 or 10 pt font size and standard fonts. If submitting in hardcopy, print the entire manuscript on one side of the paper only.

Corresponding author: Clearly indicate who is responsible for correspondence at all stages of refereeing and publication, including post-publication. The corresponding author should be identified with an asterisk and footnote. Ensure that telephone and fax numbers (with country and area code) are provided in addition to the e-mail address and the complete postal address. Full postal addresses must be given for all co-authors. Please consult a recent journal paper for style if possible.

Abstract: A self-contained abstract outlining in a single paragraph the aims, scope and conclusions of the paper must be supplied.

Keywords: Immediately after the abstract, provide a maximum of six keywords (avoid, for example, 'and', 'of'). Be sparing with abbreviations: only abbreviations firmly established in the field may be eligible.

Symbols: All Greek letters and unusual symbols should be identified by name in the margin, the first time they are used.

Units: Follow internationally accepted rules and conventions: use the international system of units (SI). If other quantities are mentioned, give their equivalent in SI.

Maths: Number consecutively any equations that have to be displayed separately from the text (if referred to explicitly in the text).

References: All publications cited in the text should be presented in a list of references following the text of the manuscript.

Text: Indicate references by number(s) in square brackets in line with the text. The actual authors can be referred to, but the reference number(s) must always be given.

List: Number the references (numbers in square brackets) in the list in the order in which they appear in the text.

Examples:

Reference to a journal publication:

[1] M.S. Mohsen, B.A. Akash, "Evaluation of domestic solar water heating system in Jordan using analytic hierarchy process". Energy Conversion & Management, Vol. 38, No. 9, 1997, 1815-1822.

Reference to a book:

[2] Strunk Jr W, White EB. The elements of style. 3rd ed. New York: Macmillan; 1979.

Reference to a conference proceeding:

[3] B. Akash, S. Odeh, S. Nijmeh, "Modeling of solar-assisted double-tube evaporator heat pump system under local climate conditions". 5th Jordanian International Mechanical Engineering Conference, Amman, Jordan, 2004.

Reference to a chapter in an edited book:

[4] Mettam GR, Adams LB. How to prepare an electronic version of your article. In: Jones BS, Smith RZ, editors. Introduction to the electronic age, New York: E-Publishing Inc; 1999, p. 281-304

Free Online Color: If, together with your accepted article, you submit usable color and black/white figures then the journal will ensure that these figures will appear in color on the journal website electronic version.

Tables: Tables should be numbered consecutively and given suitable captions and each table should begin on a new page. No vertical rules should be used. Tables should not unnecessarily duplicate results presented elsewhere in the manuscript (for example, in graphs). Footnotes to tables should be typed below the table and should be referred to by superscript lowercase letters.

PAGES	**PAPERS**

JJMIE

Volume 4, Number 5, November 2010
ISSN 1995-6665
Pages 531- 542

Jordan Journal of Mechanical and Industrial Engineering

Design, Fabrication and Experimental Study of Heat Transfer Characteristics of a Micro Heat Pipe

R.A. Hossain [a,*], M.A.K Chowdhuri [b], C. M. Feroz [c]

[a] Department of Mechanical Engineering,University of Alberta,Edmonton, AB, Canada, T6G 2G8.

[b,c] Department of Mechanical Engineering,Bangladesh University and Technology University, Dhaka 1000, Bangladesh.

Abstract

In order to study the heat transfer characteristics, a micro heat pipe (MHP) of circular geometry having inner diameter 1.8 mm and length 150 mm is designed and fabricated. An experimental investigation is carried out also to investigate the performance of the MHP with different experimental parameters. These experimental parameters include inclination angle, coolant flow rate, working fluid and heat input. Inclination angle are varied from 30^0 to 90^0, where as coolant flow rate and heat input are varied from 0.3 lit/min to 1.0 lit/min and 0.612 W to 8.71W respectively. Three different types of working fluids are used; acetone, ethanol and methanol. For each working fluid, heat transfer characteristics are determined experimentally for different inclination angle and different coolant flow rate at different heat input. Acetone is proved to be better as working fluid. A correlation is also made for acetone to relate other experimental parameters for determination of heat transfer coefficient.

Keywords: Micro Heat Pipe, Heat transfer characteristics, Inclination angle.

Nomenclature

Ae:	Surface area of evaporator	mm^2
m_c:	Coolant flow rate	lit/min
Q:	Heat Input	W
R:	Thermal Resistance	$^0C/W$
Tc:	Average condenser temp	^0C
Te:	Average evaporator temp	^0C
T_w:	Wall temperature	^0C
U:	Overall heat transfer coefficient	$W/m^2\,^0C$
X:	Axial distance	mm
θ:	Inclination angle	^0C

* Corresponding author. rhossain@ualberta.ca

1. **Introduction**

Overheating of integrated circuit (IC), microchip etc. is a potential threat to these electronic components. It is very important to facilitate optimum cooling of electronic components in a smaller electronic device because integrated circuit lifetime depends on it. An increasing market demand on powerful gadgets in smaller and smaller cabinets creates a trade off situation: either to enlarge the package to accept additional cooling or to sacrifice IC lifetime. This is a great challenge in thermal design management. Among other cooling techniques heat pipes emerge as the most appropriate technology and cost effective thermal design solution due to its excellent heat transfer capability, high efficiency and its structural simplicity. Due to the space constraint in most of personal computers and telecommunication devices, the size of heat pipes has to be carefully decided. Thus application of micro heat pipe (MHP) has been extended gradually. So investigation on MHP is indispensable for further development and improvement of its performance.

Besides electronic cooling, there are many other applications, where MHPs may be useful. For example, MHPs are interesting to be used in implanted neural stimulators, sensors and pumps, electronic wrist watches, active transponders transponders, self-powered temperature displays, temperature warning systems. MHPs are promising to cool and heat some biological micro-objects [1].

A heat pipe is a heat transfer mechanism that can transport large quantities of heat with a very small difference in temperature between the hot and cold interfaces. Heat pipes are pencil-sized metal tubes that move heat from one end of the tube to the other without the aid of a pump. Within the heat pipe, heat vaporizes a small amount of fluid at the pipe's hot end; the fluid travels to the other, slightly cooler end and condenses before returning to the hot end through a capillary wick, where it repeats the process. The device efficiently transfers large quantities of heat. The heat pipe can, even in its simplest form, provide a unique medium for the study of several aspects of fluid dynamics and heat transfer, and it is growing in significance as a tool for use by the practicing engineer or physicist in applications ranging from heat recovery to precise control of laboratory experiments. Today heat pipes are widely used in computer, telecommunication, and other various electronics equipment. It is a light weight device with no moving parts, silent in operation and having several hundred times the heat transport capacity as compared to the best metallic heat conductor like silver and copper. They are often called the "superconductors" of heat, as they possess an extra ordinary heat transfer capacity with almost no heat loss. Moreover, the thermal management problems of microelectronic components will worsen with further miniaturization. The size of microprocessors has been reducing day by day with the development of electronics. Consequently, the number of active semi-conductor devices per unit chip area has been increasing. In the last decade, the number of active semi-conductor devices per unit chip area has almost quadrupled [2]. The minimum feature size in microprocessors has reduced from 0.35 μm in 1990 to 0.25 μm in 1997 and which will go down further to 0.05 μm by the year 2012 [3]. This has increased the heat dissipation density for desktop microprocessors. As an example, heat flux has increased from 2W/cm2 for an Intel 486 microprocessor to almost 21 W/cm2 for the Intel P II 300-400 MHz microprocessors [4]. The current heat dissipation rates for some of desktop computers are approximately 25 W/cm2. It is expected that microprocessor chips for some of the next generation work stations will dissipate 50-100 W/cm2. Thus reduction in size also brings severe limitations to the conventional cooling techniques [5].

Development of efficient thermal management scheme is essential to dissipate these high heat fluxes and maintain suitable operating temperature of the device. Micro heat pipes are increasingly filling this role. To keep up with today's thermal solution challenges, micro heat pipes must improve efficiency and integrate remote heat transfer into thermal management solutions. Thus application of MHP has been extended gradually. Jin Zhang [6] studied the heat transfer and fluid flow in an idealized micro heat pipe. Yuichi et al. [7] experimentally confirmed steady-state heat transfer characteristics of flat MHP in detail and proposed a method for determining its maximum heat transfer rate. Moon et al. [8] studied performance of a triangular micro heat pipe mounted horizontally and found that its heat transport limit 6-15 W/cm2 for the operating temperature ranging from 45-80 oC. Zhuang et al. [9] compared the performance of heat pipes placed at different inclination angles in terms of maximum heat transfer capacity using three different structural wicks. It is found that all structures of wicks have little influence on the heat transfer capacity of heat pipes working with the aid of gravity. Under the condition of anti gravity, the structure of wicks has obvious influence on the heat transfer capacity of miniature heat pipes.

Moon et al. [10] experimentally investigated the thermal performance of micro heat pipe with polygon cross-sections. They showed that in the case of the MHP with a small sized equivalent diameter smaller than 2 mm, the effect of the pipe length on the thermal performance of the MHP could be large because of the pressure losses by friction at the vapor–liquid interface and the capillary limitation for returning of condensed liquid are significantly dominant as an increase of the pipe length. They also showed, the thermal performance of the triangular MHP tends to be increased according to the decrease of the pipe length. For this study the length of the pipe is chosen as close to specified by Moon et al. [10].

From the above discussion it may be noted that a number of research works on micro heat pipes have been carried out but very limited research work has done so far to completely determine the performance of MHP. Again researches that include effects of different experimental parameters such as inclination angle, coolant flow rates, heat input and working fluid on the performance of MHP has not studied yet to the best of our knowledge. This study completely investigates the effect of all the above experimental parameters on the performance of MHP.

2. Design of Micro Heat Pipe

Since a micro heat pipe (MHP) generally refers to small heat pipe with a diameter of less than 3 mm, selection of diameter is an important design consideration for fabrication of MHP. Heat pipe of circular geometry is used in this experiment. In this study for MHP a copper tube of 2 mm outer diameter and 1.8 mm inner diameter is selected. This dimension is chosen because it fulfils the required range for MHP and its availability in local market as well. The reasons behind selecting copper tube are: The compatibility of copper with both the working fluid and the external environment is very high., Thermal conductivity of copper is also a higher than the other container materials such as stainless steel, mild steel etc, Copper facilitates the ease of fabrication, including weld ability, machine ability and ductility and also there are some other important properties required for heat pipe container like porosity, wet ability, strength to weight ratio - which is more important in spacecraft applications etc.

The heat pipe consists of three sections; evaporator section, adiabatic section and condenser section (Fig. 1). The total length of MHP is arbitrarily selected as 150 mm. This dimension is convenient to handle and can easily be used in practical applications. The detail dimension of

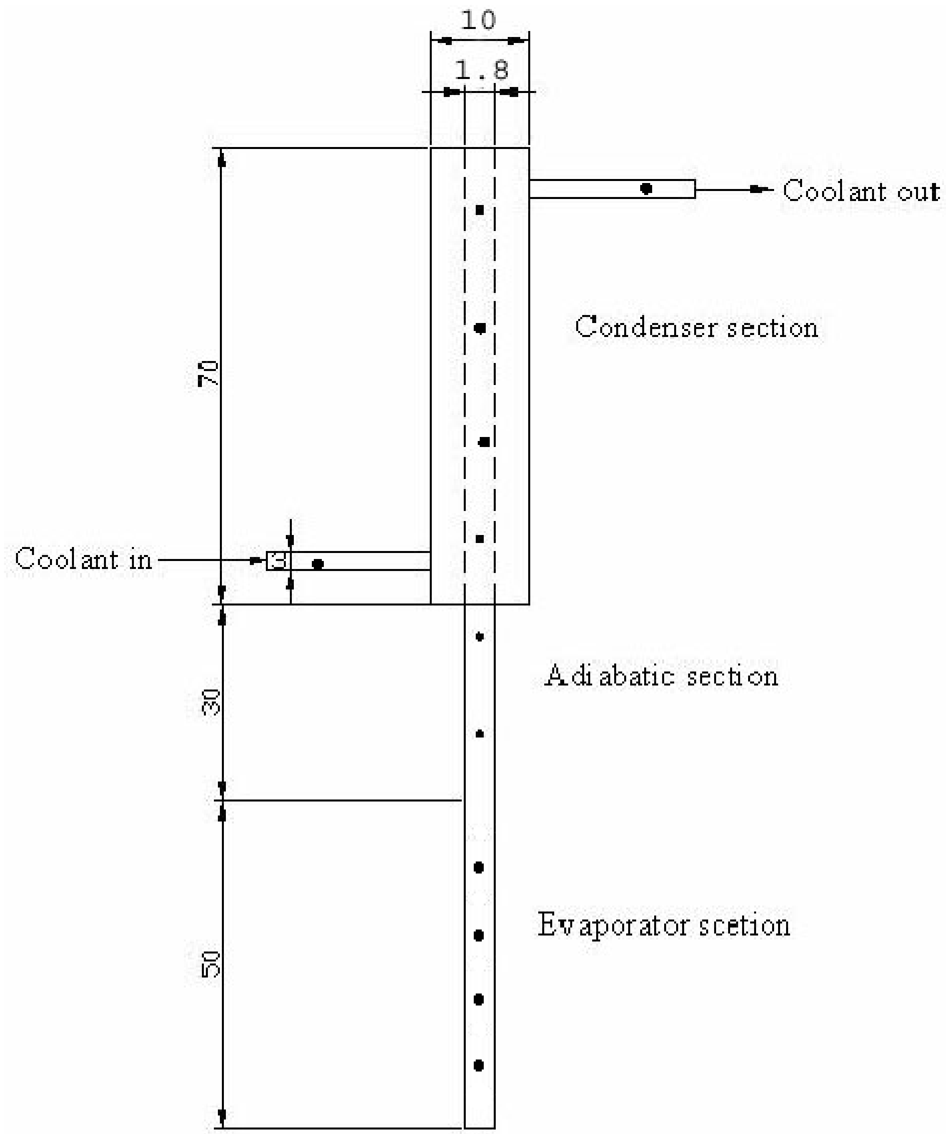

Figure 1: Schematic view of circular MHP.

MHP used in the experiment is summarized in Table 1.

Table 1: The detail dimension of MHP

Parameter	Dimension (mm)
Hydraulic diameter of pipe, d_h	1.8
Length of Heat Pipe, L	150
Length of evaporator section, L_e	50
Length of adiabatic section, L_a	30
Length of condenser section, L_c	70

Evaporator section is located at the bottom of the heat pipe. Heat is added to the heat pipe through evaporator section. Adiabatic section is located in between the evaporator and condenser section. This section is actually kept with heat pipe to distinguish evaporator section and condenser section. Condenser section is the uppermost part of the heat pipe. There is a water jacket around this section which is concentric with the container section. Water flowing through the jacket cools the condenser section of the pipe and thus takes away the latent heat of condenser of vapor.

3. Experimental Procedure

The schematic diagram of the experimental setup is shown in Fig. 2. At first working fluid is poured to the evaporator section of MHP. The amount of working fluid is selected to maintain a charge ratio, which is the volume of the evaporator filled by the working fluid to the total volume of the evaporator to 0.9 because previous studies on MHP show that, this value of charge ratio is convenient. In other words the evaporator is 90 percent filled by the working fluid. Since no vacuum pump is used, the remaining portion of MHP may contain air. Ni-Cr thermic wires having width of 1.5 mm, thickness of 0.1 mm and total resistance of 16 Ω are wound around the

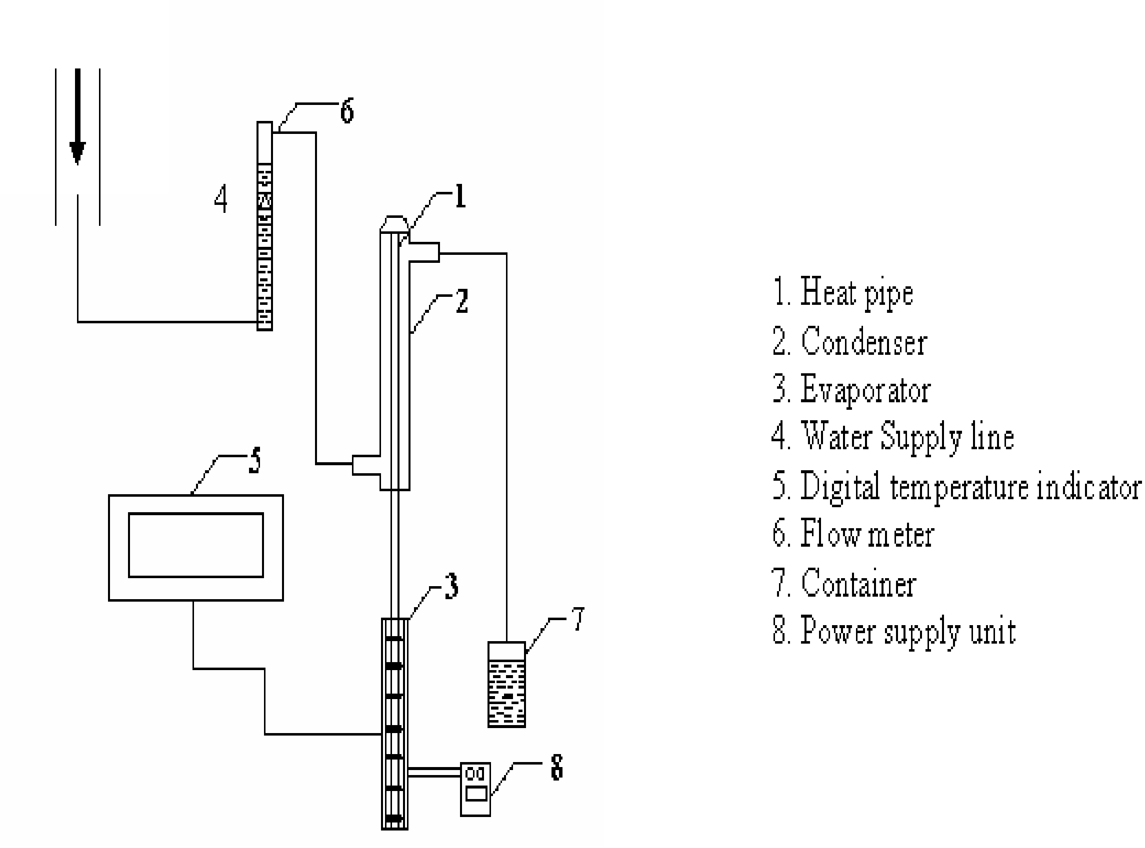

Figure 2: Schematic diagram of the experimental setup.

evaporator wall maintaining equal spacing of 1.5 mm. For electrical insulation in the evaporator section, insulation tape is used. The heat added to the evaporator section of MHP is processed in the electric method by using the AC power supply (variac). To minimize heat losses, evaporator section is covered with glass wool.

The condenser section is cooled by a constant temperature water coolant, circulating in an annular space between the copper tube and the jacket. The water coolant is taken from supply line trough pipe and the flow is controlled by the flow meter. The inlet and outlet coolant temperatures are measured. Twelve calibrated *K* type (Cooper-Constantan, Φ 0.18 mm) thermocouples are used. Ten are attached at the wall of each MHP to measure the wall temperature; four units at the evaporator section, two units at the adiabatic section and four units are at the condenser section. Remaining two are used to measure the inlet and outlet temperature of the condenser water. The thermocouples are attached at the wall surface-using adhesive. Temperatures are measured by a digital thermometer.

An input power to the heater in the evaporator section is increased by using a variac from 0.612 W to 8.71 W. Ammeter and voltmeter were used to measure the voltage and current in the heater circuit so that a relation can be made between the variac reading and actual heat transfer from the heater to the heat pipe. The measurements are made under a steady state condition at each input power. To understand the effects of inclination as well as the change of coolant flow rate in the condenser, the same procedure is followed at each fixed inclination angle and coolant flow rate.

4. Math Model

This paper is focused on the experimental works only. The performance and other mathematical analysis are not presented here. However, interested reader may referred to Reay et al.[11] and Valeri and Roger [12].

The thermal resistance, *R* (^{0}C/W) is defined as

$$R = \frac{T_e - T_c}{Q} \tag{1}$$

and the overall heat transfer coefficient, U (W/m^2 ^{0}C) is by

$$U = \frac{Q}{A_e(T_e - T_c)} \tag{2}$$

5. Results and Discussion

Experiment is carried out with MHP for different working fluids; methanol, ethanol and acetone at different inclination angles, $30^0 \le \theta \le 90^0$ for various heat input, $0.612\text{W} \le Q \le 8.71\text{W}$ and coolant flow rates, 0.3 lit/min ≤

$m_c \leq$ to 1.0 lit/min. To keep the volume of the paper minimum only representative curves (similar nature curves are not shown) are given. Fig. 3 shows the distribution of wall temperature along the length of MHP for different coolant flow rate where as Fig. 4 is drawn wall temperature profile for different heat input.. From this figure it is seen that in evaporator section temperature remains same, which indicates uniform heating. After that temperature drops in adiabatic section and in condenser section. Again it indicates coolant flow rate has a little effect on wall temperatures. From Fig. 4, it is seen that the nature of the curve in different section of MHP is similar as Fig. 3. Wall temperature is higher for higher heat input in each section of MHP. From Fig. 5, it is seen that effect of coolant flow rates is insignificant on thermal resistance. From Fig. 5 it is clear that thermal resistance exhibited a decreasing trend as the heat input is increased. It could be mentioned here, as the heat input is raised, heat transfer rate is increased due to the increase of vapor density; this is consistent with the result found by Jon H. B. [13] and Kim, K. S. [14]. Thermal resistance decreases slightly with inclination angle up to 50^0 at constant heat input. After that sharp decrease is visible up to 70^0 and then increases (Fig. 6). For this working fluid and heating condition MHP will work better at inclination angle 70^0. Again, coolant flow rate has a little effect on thermal resistance. Overall heat transfer coefficient is higher for high heat input (Fig. 7). Fig. 8 shows the effect of inclination angle on overall heat transfer coefficient. It is evident that overall heat transfer coefficient is maximum at $\theta = 70^0$ for MHP with ethanol as working fluid when Q = 3.67 W. Fig. 9 depicts the variation of overall heat transfer coefficient with heat input for MHP with ethanol as working fluid. The overall heat transfer coefficient is increased with the increase of heat input. Again this figure also shows overall heat transfer coefficient is better for inclination angle 70^0. To find the effect of working fluid, Fig.10 is plotted. This figure is plotted for inclination angle 70^0 and heat input is 3.67 W. From the figure it is quite clear that performance of MHP with acetone is better than MHP with methanol or ethanol.

An empirical equation is developed as described in Appendix-A for MHP with acetone as working fluid. The same relation can be developed for MHP with other two working fluids. The developed equation is

$$U/U_{\max} = 0.695\,(Q/Q_{\max})^{0.785}\,(m_c/m_{c\,\max})^{-0.114}\,(1+\sin\theta)^{.0634} \quad (3)$$

The relation is valid for

Q = 0.612 W to 8.71 W, m_c = 0.3 lit/ min to 1.0 lit/min and $\theta = 30^0$ to 90^0

The relation is developed for the specified range of different parameters used in this experiment. For this reason U_{max}, Q_{max} and m_{cmax} terms are used; which could be defined as the maximum values of the range of corresponding parameters. Further studies can be carried on to generalize this relation.

Then some of the experimental data are correlated with the developed equation and presented in Fig. 11. From this figure it is clear that the developed equation can correlate the experimental data within ± 7% error only.

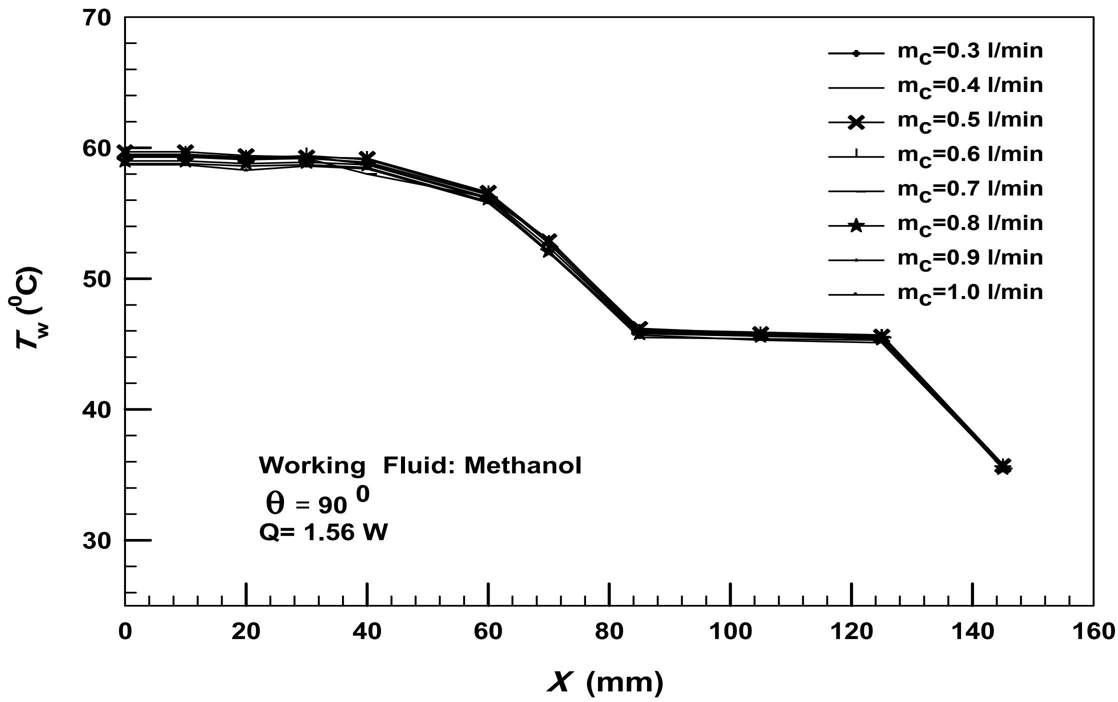

Figure 3: Wall temperature distribution along the length of MHP with methanol for various coolant flow rates when $\theta = 90^0$ and Q= 1.56 W.

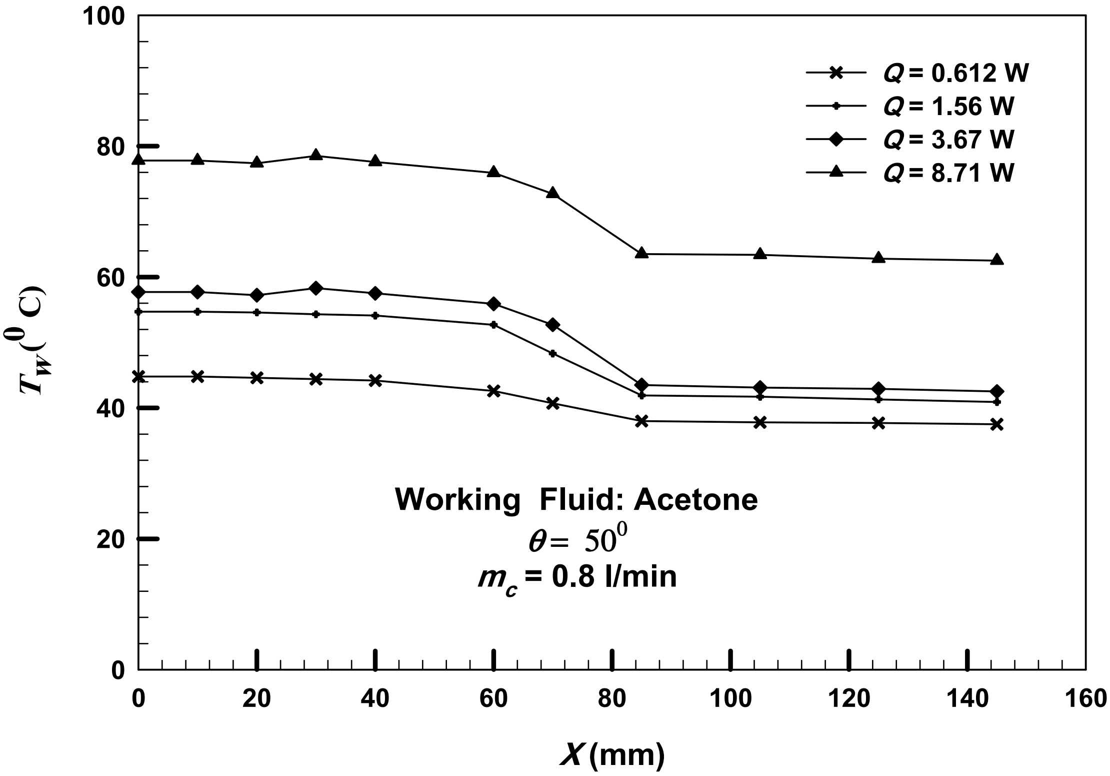

Figure 4: Wall temperature distribution along the length of MHP with acetone for various heat inputs when $\theta = 50^0$ and $m_c = 0.8$ lit/min.

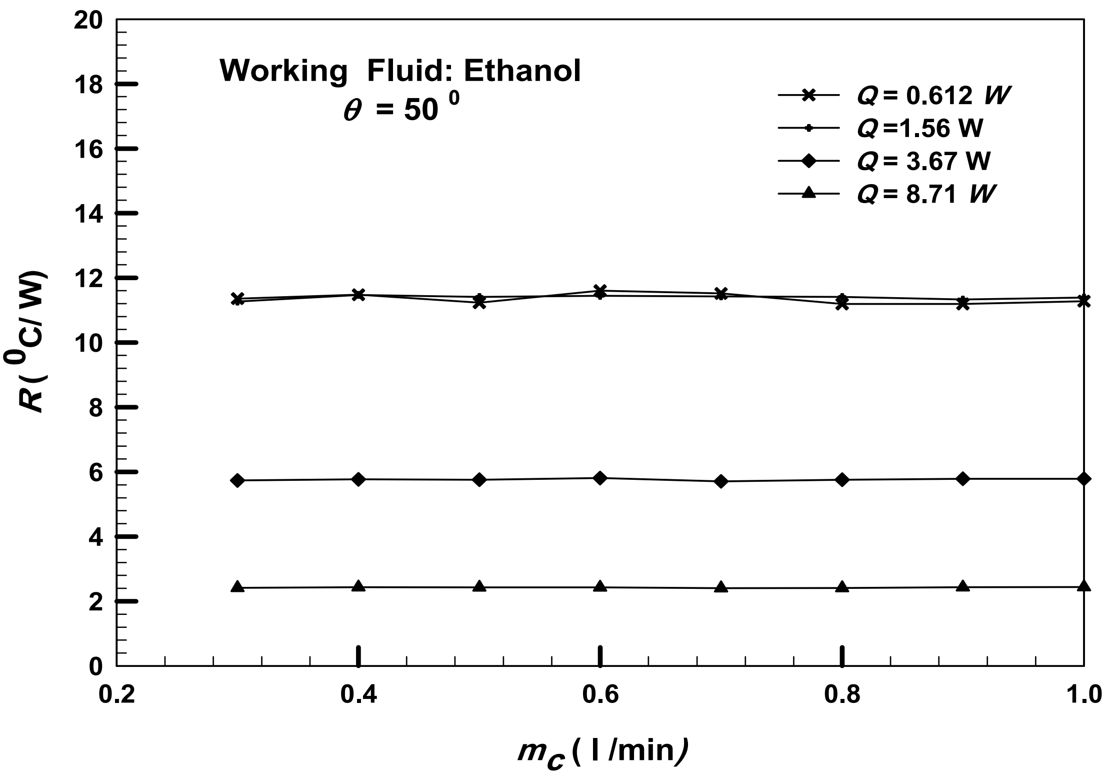

Figure 5: Effect of coolant flow rate on thermal resistance of MHP with ethanol for various heat inputs when $\theta = 50^0$.

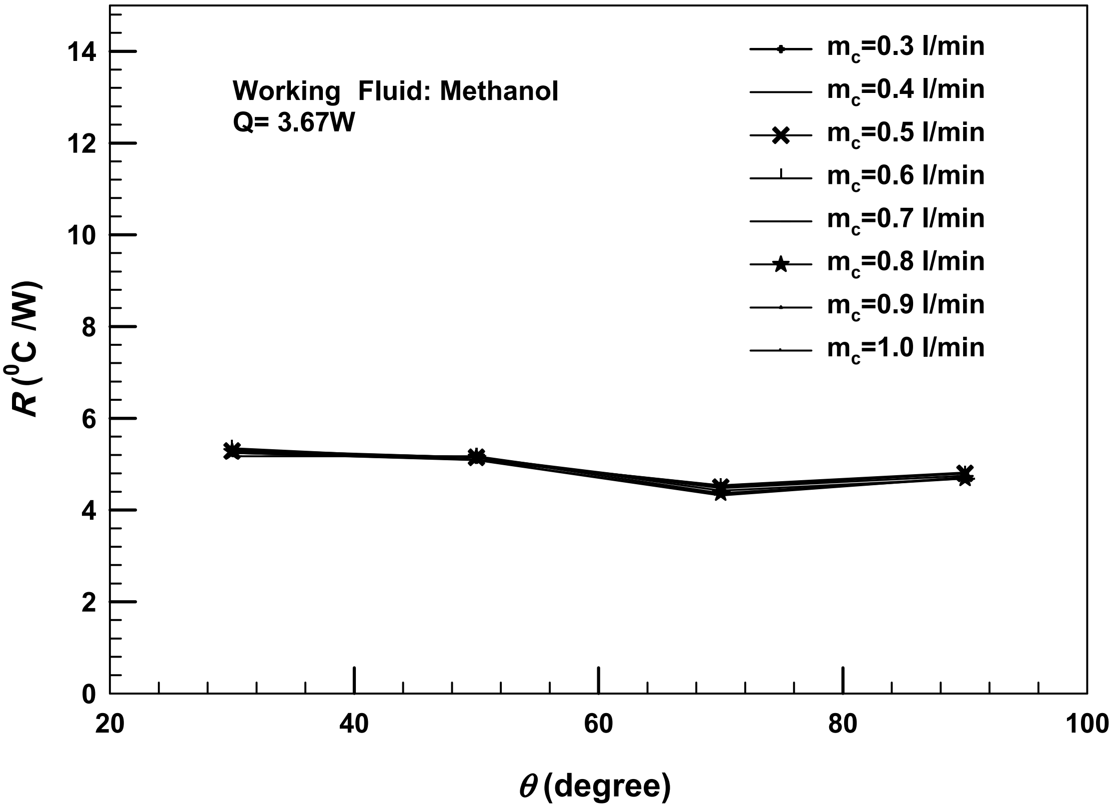

Figure 6: Effect of inclination angle on thermal resistance of MHP with methanol for various coolant flow rate when Q =3.67 W.

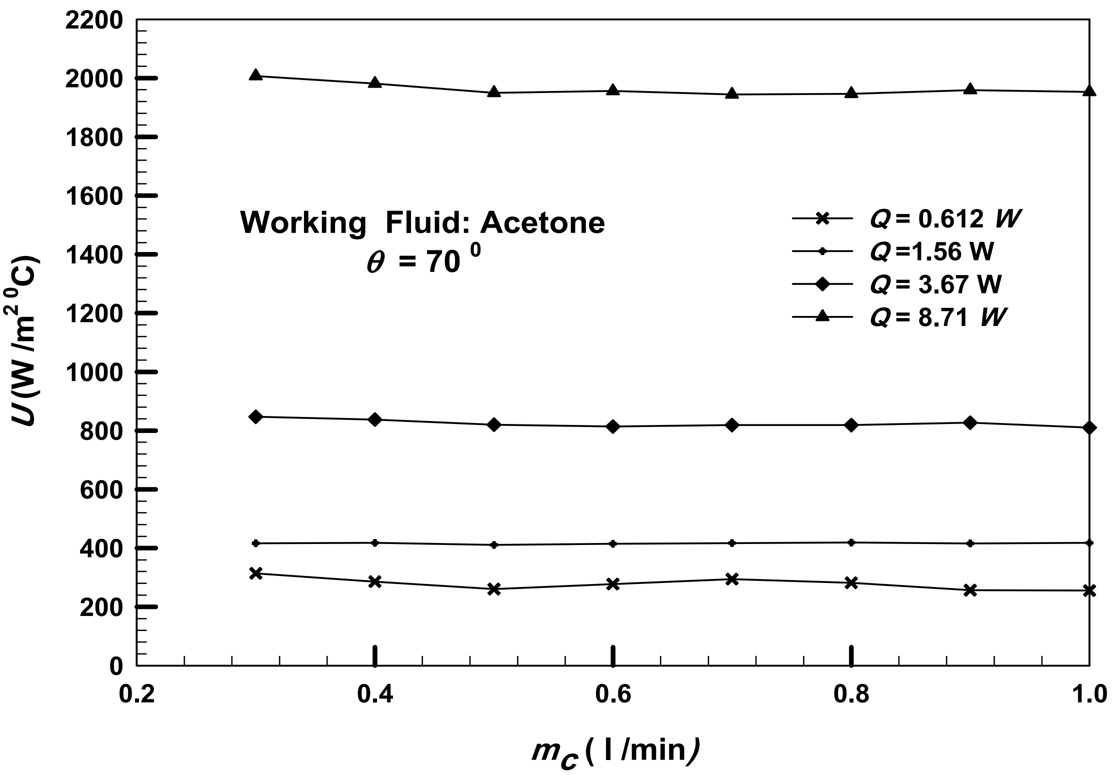

Figure 7: Effect of coolant flow rate on overall heat transfer coefficient of MHP with acetone for various heat inputs when θ =70^0.

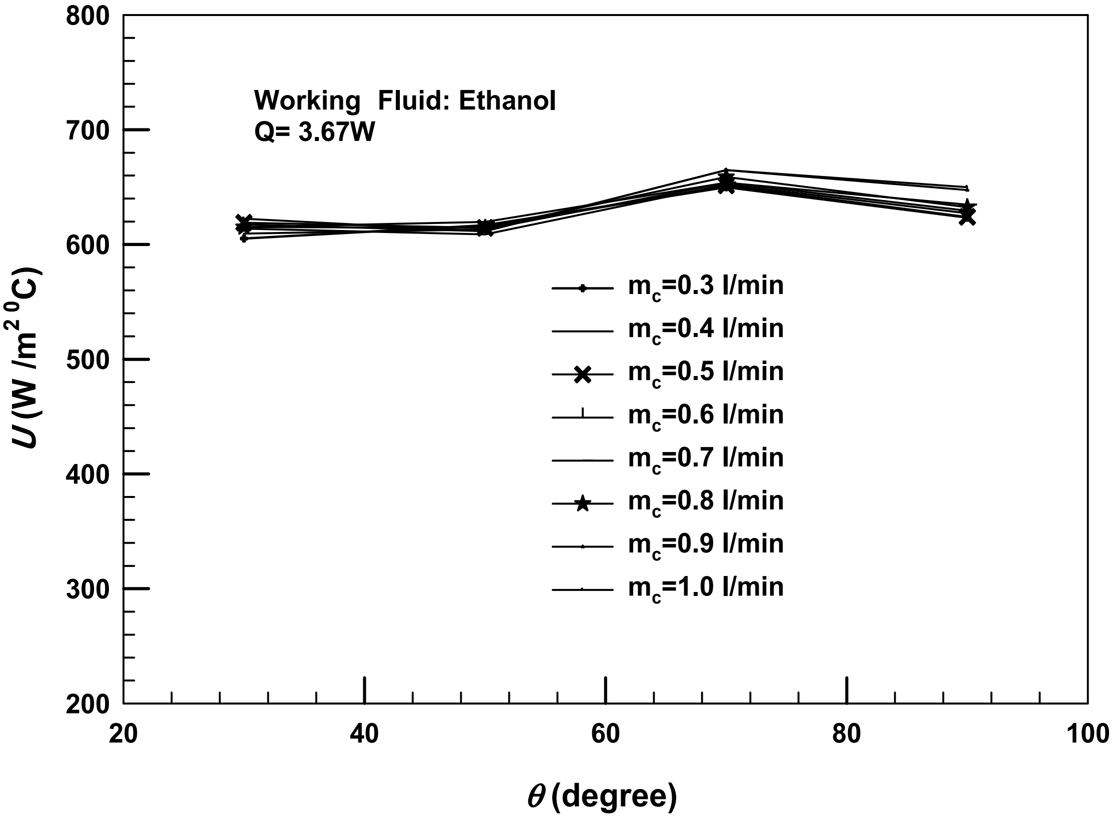

Figure 8: Effect of inclination angle on overall heat transfer coefficient of MHP with ethanol for various coolant flow rate when Q =3.67W.

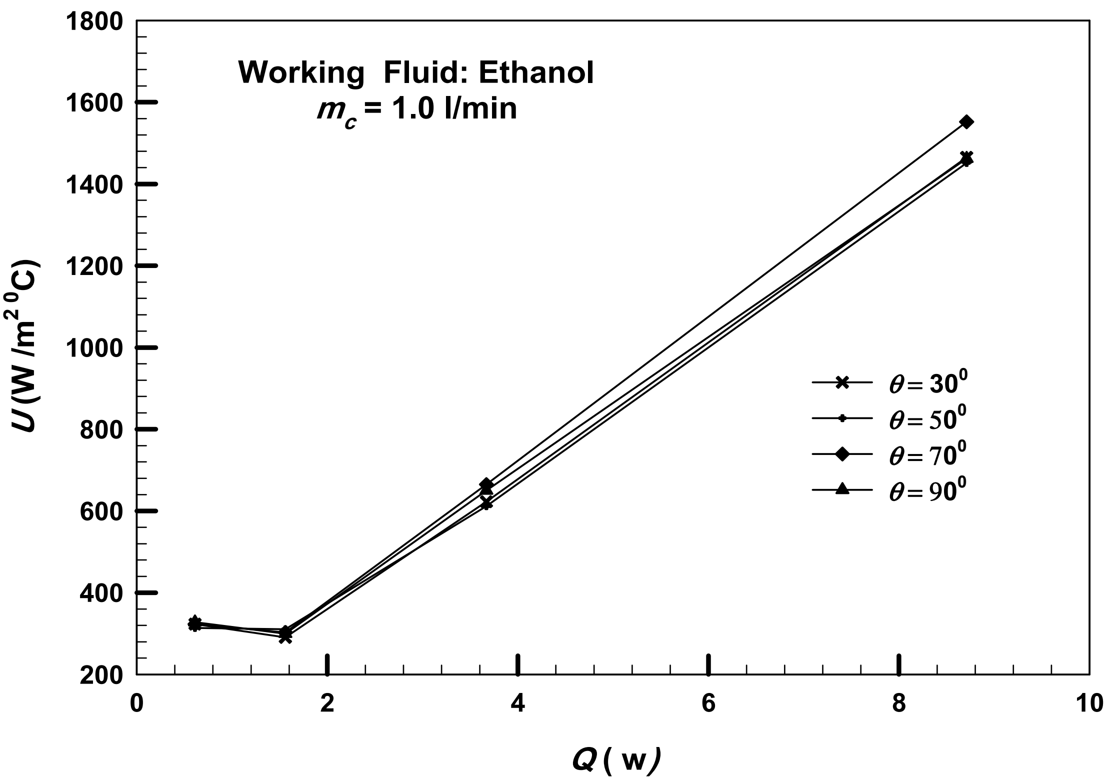

Figure 9: Effect of heat input on overall heat transfer coefficient of MHP with ethanol for various inclination angles when m_c = 1.0 lit/min.

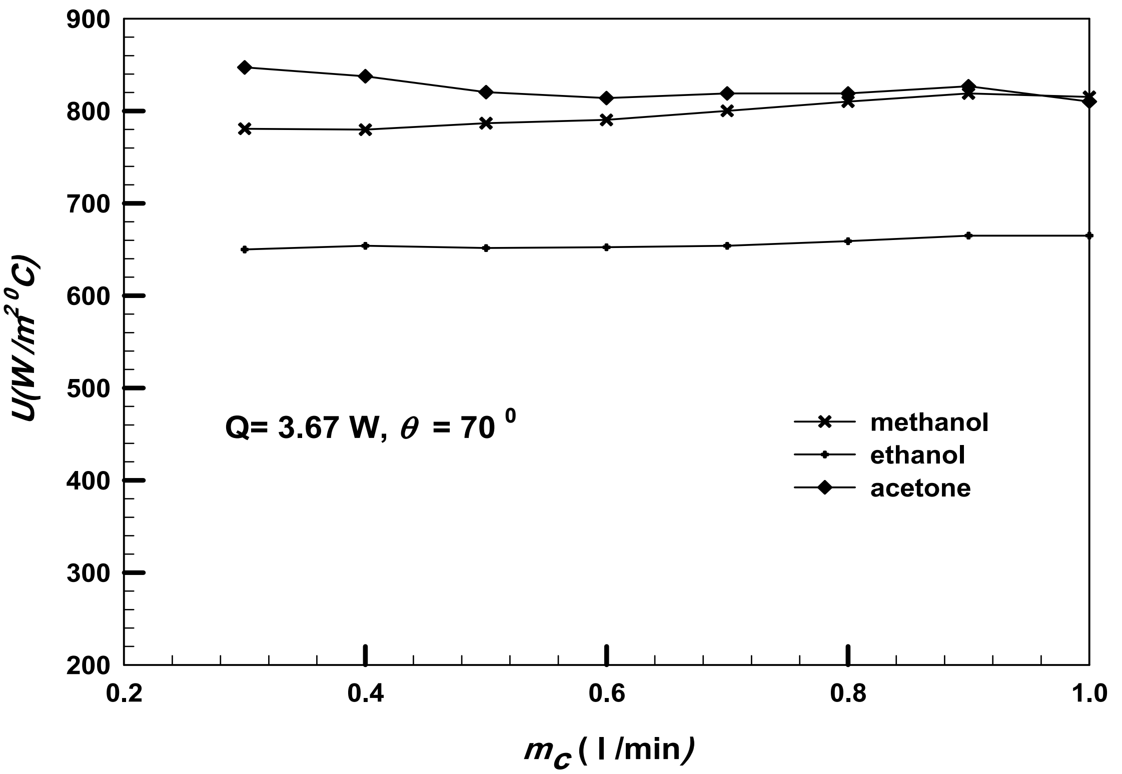

Figure 10: Variation of overall heat transfer coefficient of MHP with m_c for different working fluid when Q=3.67W and $\theta = 70^0$.

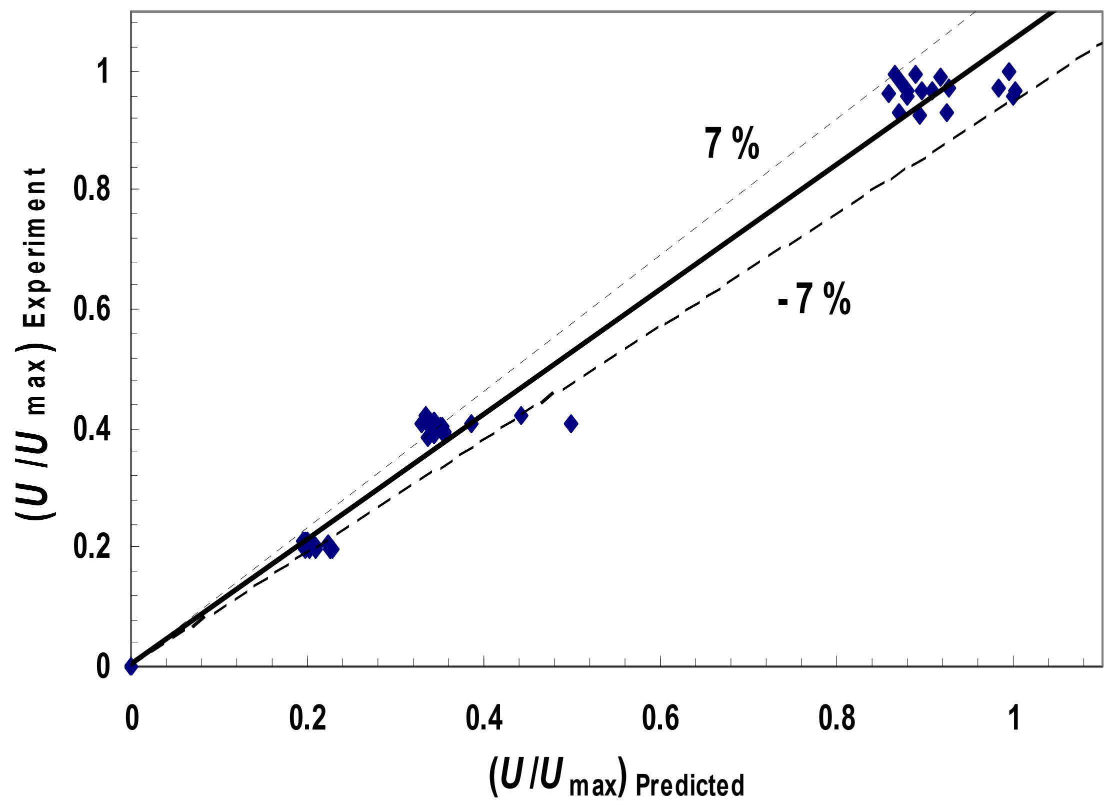

Figure 11: Variation of results obtained from empirical formula and those of from experiment.

6. Uncertainty Analysis

A precise method of estimating uncertainty in experimental results has been described by Kline and McClintock [15]. If the result R is a given function of the independent variables $X_1, X_2, X_3,\ldots\ldots\ldots\ldots X_n$ andt $G_1,G_2,G_3,\ldots\ldots\ldots\ldots G_n$ be the uncertainty in the independent variables given with the same odds.

Then the uncertainty in the result having this same odd is given in Eq. (4)

$$G_R = \left[\sum_{i=1}^{n} \left(\frac{\partial R}{\partial X_i} \times G_i \right)^2 \right] \tag{4}$$

Using Eq. (4) and the uncertainty of primary measurands, the uncertainty of R and overall heat transfer coefficient, U are calculated as 9.11 % and 0.2 % respectively.

7. Conclusions

The experiment of investigating thermal performance of MHP is done by varying the angle of inclination, coolant flow rates, working fluids and heat inputs. From the results the following conclusion can be made.

- Coolant flow rate has an insignificant effect on the performance of MHP.
- Performance of MHP depends upon angle of inclination. Better performance is found for an inclination angle of 70^0.
- Heat input has significant effect on the performance of MHP. It is found that overall heat transfer coefficient is higher for higher heat input.
- It is observed that for the same heat input and inclination angle MHP with acetone as working fluid performs better.

References

[1] Vasiliev, L.L., “Micro and miniature heat pipes – Electronic component coolers”, Applied Thermal Engineering, Vol. 28, 2008, 266–273.

[2] Babin, B.R. Peterson, G. P., Wu, D., “Steady State Modeling and Testing of a Micro Heat Pipe.” ASME J. of Heat Transfer, Vol. 112, No. 3, 1990, 595-601.

[3] Zhou. J., Yao, Z., Zhu, J., “Experimental Investigation of the Application Characters of Micro Heat Pipe”. 8th Int. Heat Pipe Conf., Beijing, China, 1992.

[4] Kim, C. J., Moon, S. H., Kim, J. O., “Fundamental Study on Performance Characteristics of a Micro Heat Pipe with Triangular Cross Section ,” Korean J. of Air-Conditioning and Refrigeration Engineering , Vol. 11, No. 2, 1999, 176-184.

[5] Rossi, L., ‘Thermal Control of Electronic equipment by Heat Pipes and Two-Phase Thermosyphons’ELBOMEC thermalloy , Via del Tipografo, 440138 Bologna, Italy.

[6] Zhang. J. “Heat transfer and fluid flow in idealized Micro heat pipe”. Proceedings of the ME Graduate Student Conference, USA, 2002.

[7] Kimura, Y., Nakamura, Y., Sotani, J., Katsuta, M., “Steady and Transient Heat TransferCharacteristics of Flat Micro heat pipe”. Japan, Furukawa Review No. 27, 2005, 3-8.

[8] Moon, S. H., Kim, C.J., Kim, B.H., Lee, S. “An experimental study on the performance limitation of a micro heat pipe with triangular cross-section”. 11th International Heat Pipe Conference-Tokyo, Japan, 1999, 234-238.

[9] Zhuang, J., Zhang, H., Jining LU., “Comparison of Heat transfer Performance of Miniature heat pipes”, 11th International Heat Pipe Conference-Tokyo, Japan, 1999, 226-229.

[10] Moon, S.H., Hwang, G., Ko, S.C., Kim., Y.T., “Experimental study on the thermal performance of micro-heat pipe with cross-section of polygon”, Microelectronics Reliability, Vol. 44, 2004, 315–321.

[11] Reay, D.A., Kew, Peter A., Kew. P.A., “Heat Pipes, Theory design and applications”, 5th edition, 2006, Butterworth-Heinemann, Burlington, M.A, U.S.A

[12] Valeri, V., Roger, R. R., “Mathematical model of a loop heat pipe with cylindrical evaporator”, Applied Thermal Engineering, Vol. 28, 2008, 942–954.

[13] Jon H. B., “An Experimental Study of a Slab-wick Heat Pipe for Medium-high Condenser Temperatures,” 11th International Heat Pipe Conference –Tokyo 1999, 143-148.

[14] Kim, K. S. “Cooling Characteristics of Micro Heat Pipes with Woven Wired Wick”. 11th international Heat Pipe Conference – Tokyo, 1999, 239 -244.

[15] Kline, S. J., McClintock, F. A., "Describing Uncertainties in Single-Sample Experiments", Mech. Eng., 1953, 3.

Appendix- A

Correlation Procedure

In order to develop an empirical formula, selection of experimental parameters is extremely important. In this study experimental parameters are heat input, angle of inclination, coolant flow rate and working fluid. Because Acetone shows better performance as a working fluid over methanol and ethanol and to avoid futher difficulties, only MHP with acetone as working fluid is considered for correlation purpose. So no term for working fluid is considered in the equation. Eq. (A.1) is assumed considering the above experimental parameters with some unknown co-efficient C, a, b and c:

$$\frac{U}{U_{\max}} = C\left(\frac{Q}{Q_{\max}}\right)^{a}\left(\frac{m_c}{m_{c\max}}\right)^{b}(1+\sin\theta)^{c} \tag{A.1}$$

This equation can be written as

$$\ln\frac{U}{U_{\max}} = \ln C + a\ln\left(\frac{Q}{Q_{\max}}\right) + b\ln\left(\frac{m_c}{m_{c\max}}\right) + c\ln(1+\sin\theta) \tag{A.2}$$

Eq. (A.2) is subjected to experimental data and has obtained many equations. Those equations are needed to solve simultaneously. They may be arranged in matrix form as given below:

$$\begin{bmatrix} A_i \\ A_{i+1} \\ A_{i+2} \\ A_{i+3} \end{bmatrix} = \begin{bmatrix} 1 & M_i & N_i & S_i \\ 1 & M_{i+1} & N_{i+1} & S_{i+1} \\ 1 & M_{i+2} & N_{i+2} & S_{i+2} \\ 1 & M_{i+3} & N_{i+3} & S_{i+3} \end{bmatrix} \begin{bmatrix} x \\ a \\ b \\ c \end{bmatrix} \tag{A.3}$$

where, $A = \ln\left(\frac{U}{U_{\max}}\right)$, $M = \ln\left(\frac{Q}{Q_{\max}}\right)$, $N = \ln\left(\frac{m_c}{m_{c\max}}\right)$,

$S = \ln(1+\sin\theta)$ and $x = \ln C$

Equation (A.3) is solved by Reduced Gaussian Elimination Method with the help of computer programming and coefficient ‘C’, ‘a’, ‘b’ and ‘c’ are determined. Computer programming language ‘C’ is used in this case.

JJMIE

Volume 4, Number 5, November 2010
ISSN 1995-6665
Pages 543- 552

Jordan Journal of Mechanical and Industrial Engineering

A comparative Analysis of the Performance of Monocrystalline and Multiycrystalline PV Cells in Semi Arid Climate Conditions: the Case of Jordan

M. R. Abdelkader [a,*], A. Al-Salaymeh [a], Z. Al-Hamamre [b], Firas Sharaf [c]

[a] Department of Mechanical Engineering, Faculty of Engineering and Technology, University of Jordan, Amman 11942 Jordan

[b] Department of Chemical Engineering, Faculty of Engineering and Technology, University of Jordan, Amman 11942 Jordan

[c] Department of Architecture, Faculty of Engineering and Technology, University of Jordan, Amman 11942 Jordan

Abstract

The energy consumption in the world is increasing greatly owing to the growing population, and to increasing energy consumption per capita. This high energy consumption is associated with a high life quality. Due to this fact, and to the energy price and availability and to the potential threat of global climate changes, there is a great motivation to use energy from renewable sources such as solar energy. Jordan is a developing non-oil production country and its energy needs are imported from abroad as oil and petroleum products. On the other hand, Jordan has an abundance amount of solar radiation 300 days a year. Photovoltaic modules provides safe, reliable, maintenance-free, without noise, and environmentally friendly source of power. This paper evaluates the performance of different solar modules in semi arid climate as in Jordanian. An experiment to investigate the performance of two photovoltaic modules is conducted at different times of the year. The measured parameters in this paper are: output open circuit voltage and short circuit current from the PV modules, ambient temperature and solar intensity. The relationship between the performance and the efficiency of monos crystalline PV and multi crystalline PV is measured in this experiment. The performance value of the PV solar module is identified and compared with the output values supplied by the producer of the PV modules and with other PV models.

Keywords: Renewable Energy, PV cells, PV Performance; PV Modules; PV in Jordan.

1. Introduction

There are several factors that form present interest in utilizing solar energy in the production of electricity. An earlier cause of this interest was the need to reduce dependency on imported oil of countries such as Jordan and to secure long term requirement of energy needs. Interest in renewable energy sources has been increasing rapidly as energy prices increased particularly after the Gulf wars in the 1990s.

Additionally, industrial practices and consumption patterns of the developed world seriously damage the environment and stimulated a search for clean and renewable energy sources.

As many countries concerned with increased levels of air pollution and climate change, Jordan is concerned with the reduction of CO_2 emissions to atmosphere. Data indicates that CO_2 emission in Jordan is below the world average value of 3.1 tons/capita/year [1].

In addition to other renewable energy sources, photovoltaic cells (PV) present a prime source of clean energy that utilizes energy from sunlight. Solar energy is converted directly to power without intermediate production of heat. Solar cells are used to heat water and PV cells to produce electricity. Photovoltaic cells are manufactured from fine films or wafers made from silicon [2,3]. They are semiconductor devices capable of converting incident solar light to DC current. Efficiency of produced power vary from 3% to 17%, depending on different causes such as the kind of technology used, the light spectrum, ambient temperature, system design, semiconductor characteristics and material of solar cell [4, 5]. The series or parallel connection of cells allows the design of solar panels with high currents and voltages (reaching up to 1 kilovolt). Solar panels are slow in degradation if they are sealed properly, which make them durable particularly as they have no movable parts and requires little maintenance. Different modules produce

* Corresponding author. abdlkadr@ju.edu.jo

different amount of electricity according to required amount ranging from few watts to megawatts [3].

Photovoltaic energy conversion in solar cells consists of two essential steps. First, absorption of light generates an electron-hole pair. The electron and hole are then separated by the structure of the device; electrons go to the negative terminal and holes to the positive terminal, in effect generating electrical power.

At present, almost 95% of available solar cells are made of silicon. The advantage of using silicon is its mature processing technology, the large abundance in the crust of the earth, and non-toxicity that is imperative for the environmental. The silicon is used in PV cells for monocrystalline (single crystalline) and multiycrystalline wafer production and the production of thin film silicon modules. More than 90% of produced solar cell every year is based on crystalline silicon wafers. Thus, silicon-wafer based technology is important for the production of PV cells at present time [6].

The development of Si-PV technology materials is driven by cost reduction. The large growth in the PV market and need for lower cost material than monocrystalline make multicrystalline silicon a favorable alternative [7].

In general, performance of monocrystalline- silicon wafer is more expensive but better in performance than the multiycrystalline-silicon wafers. In single crystal silicon, the crystal lattice of the entire sample is continuous and unbroken with no grain boundaries. Multiycrystalline are composed of a number of smaller crystals or multiple small silicon crystals. Polycrystalline cells can be recognized by a visible grain (metal flake effect) and are more sensitive to thermal processing. Multicrystalline silicon wafers are usually characterized by their different grain sizes, orientations and higher content of defects and impurities [7].

Conversion efficiencies of commercial types of multiycrystalline –silicon cells are in range of 12–15% and could reach 17% using more sophisticated solar cell designs [8, 9]. In fact, the performance and the efficiency of multicrystalline solar cells is mainly limited by minority carrier recombination. Depending on the crystallization process, materials develop different defect structure, which determine and limit their efficiency. In general dislocations and **intragrain** defects such as certain impurities, small clusters of atoms or precipitates are mainly responsible for the recombination processes. Particularly localized regions of high dislocation densities are known to be rather detrimental [10]. Grain boundaries are less important because of the relatively large grains in the centimeter range. In order to improve multicrystalline cell efficiency, reduction of thermal load is required and implementation of guttering steps [11].

Multicrystalline silicon is either grown by an ingot or ribbon technique. The microstructures of multicrystalline silicon materials differ considerably depending on whether the material is grown by an ingot or a sheet growth technique [2,3]. Dislocations in ingot silicon are formed during crystal growth by plastic deformation to reduce the thermal stresses. Some of these dislocation networks show high recombination rates and are thus very detrimental to the lifetime of minority charge carriers. Therefore, improvement of multicrystalline silicon can be achieved both by the reduction of the dislocation density and the elimination of the bad regions where dislocations cannot be made passive [11].

Moreover, to modify the performance of multicrystalline silicon wafers, it is necessary to minimize the level of transition metals in the raw silicon material. To achieve low enough impurity levels, it is important to use the route via an easily cleanable silicon compound such as trichlorosilane (TCS) or monosilane.

2. Jordan Strategy for Solar Energy

During the last two decades, the increasing energy cost has posed difficult challenges for Jordan due to country's limited economic resources. To address these challenges Jordan has established a strategic transformation and restructuring of its national economy and energy strategy. The energy strategy aims to increase private sector participation in generation and distribution of electricity, promote competition and to establish an independent regulatory body for the power sector [14]. In accordance to this strategy, Jordan has assisted programs promoting solar energy. Assessment involved systematic monitoring of implementation of appropriate technologies, demonstrations and pilot projects [15–21].

A rural PV electrification program initiated by Quality-of-life improvement for the users—was launched in Jordan in 2002. An important element of this program is access to essential electricity of low-income and rural users [22]. Yet, the percentage of solar energy to total energy consumption in Jordan in 2002 - 2007 was estimated to be as low as 1.7–2.1% [23].

The potential of utilizing photovoltaic (PV) technology in Jordan is substantial as many remote and isolated locations are far from the national electrical grid and are not expected to be connected in near future. In 2002, the Jordanian Government launched a project aimed at utilization of PV generators in rural sites. A solar hybrid power facility to produce 100-150MW was constructed in Quwairah, south of the country. Jordan is aiming to add 300MW of Concentrating Solar Power (CSP) by the year 2020 [14].

Decreasing cost of PV cells and market trends raise motivation towards developing PV systems. For example, between 1976 and 2008, the capital cost of PV modules per watt of power capacity in Jordan has declined from about $58 per watt to less than $4 per watts [24].

This paper evaluates the performance of two solar modules. Experimental data was collected in three locations in Amman city in Jordan. The performance was investigated at different times in the day and different months. Ambient temperature and solar radiation was registered.

3. Existing Knowledge

3.1. PV Modules

Solar cells are assembled into modules or module connected to charged battery, available modules are designed to deliver direct current (DC) at slightly over 12 Volts (V). A typical crystalline silicon module consists of a series circuit of 36 cells, encapsulated in a glass and plastic package for protection from the environment. This package is framed and provided with an electrical connection enclosure, or junction box. Typical conversion efficiencies (solar energy to electrical energy) for common crystal line silicon modules are in the range 11 to 15% [3].

There are four advanced thin film technologies, their names are derived from the active cell materials: cadmium telluride (CdTe), copper indium diselenide (CIS), amorphous silicon (a-Si) and thin film silicon (thin film-Si). Amorphous silicon is in commercial production while the other three technologies are slowly reaching the market. Thin film modules are made directly on the substrate, without the need for the intermediate solar cell fabrication step. Some manufacturers are developing PV modules that concentrate sunlight onto small area high efficiency PV cells using lenses. The concept here is that the lens material will be less expensive per unit area than conventional silicon modules thus resulting in a $/Wp advantage. To ensure that the concentrating lenses are always focused on the PV cells, these modules must always be directed at the sun and therefore must be used in conjunction with sun trackers. These modules are limited to areas which has a considerable amount of direct beam sunlight, as in desert regions [5].

3.2. PV Applications

Photovoltaic can be classified based on the end-use application of the technology. The most common PV projects are off-grid applications. Water pumping also represents an important application of PV, particularly in developing countries. The largest long term market potential for PV, in volume of sales, is with on-grid applications.

On-grid applications

In grid connected applications, also called “On-grid” applications, the PV system feeds electrical energy directly into the electric utility grid (this includes central grids and isolated grids). Two application types can be distinguished, distributed and central power plant generation . An example of a distributed grid-connected application is building integrated PV for individual residences or commercial buildings. The system size for residences is typically in the 2 to 4 kWp range. For commercial buildings, the system size can range up to 100 kWp or more. Batteries are not necessary when the system is grid-connected. Another application is the installation of “PV generators” by utilities at power substations and “end-of-line” sites. These applications can be on the threshold of cost competitiveness for PV, depending on location. For example, the Sacramento Municipal Utility District (SMUD) in California has been implementing a plan to install more than 1 MWp per year of distributed PV in its service area [4].

Benefits of grid-connected PV power generation are generally evaluated based on its potential to reduce costs for energy production and generator capacity, as well as its environmental benefits. For distributed generation, the electric generators (PV or other) are located at or near the site of electrical consumption. This helps reduce both energy (kWh) and capacity (kW) losses in the utility distribution network. In addition, the utility can avoid or delay upgrades to the transmission and distribution network where the average daily output of the PV system corresponds with the utility’s peak demand period (e.g afternoon peak demand during summer months due to air conditioning loads), as described in Leng and Martin (1994) . PV manufacturers are also developing PV modules which can be incorporated into buildings as standard building components such as roofing tiles and curtain walls. This helps reduce the relative cost of the PV power system in buildings.

Off-grid applications

Using PV is most competitive in distant sites from electric grid and relatively requiring small amounts of power, less than 10kWp. In off-grid applications, PV panels are used to charge batteries, storing the produced electricity the modules and providing users with electrical energy as demand.

Competition in the use of PV in remote off-grid power applications is with grid extension; disposable batteries; fossil fuel and thermoelectric generators. The cost of grid extension in the US, estimated by the Utility Photovoltaic Group (UPVG) ranges from $20,000 to $80,000 per mile. Thus, PV competes well against grid extension for small loads, far from the utility grid. Compared to fossil fuel generators and primary batteries, key advantage of PV is reduction in operation, maintenance and replacement costs; these often result in lower lifecycle costs for PV system. Off-grid application includes both stand-alone and hybrid systems, which are similar to stand-alone systems but also include a fossil fuel generator to meet some of the load requirements and provide higher reliability [4,5].

4. Experimental Setup and Devices

In order to carry out the performance test for different PV modules, the following experimental setup has been conducted in the experiment.

4.1. The photovoltaic System

Two different modules of PV panels arranged in a series–parallel connection are tested:

- a PV module has solar cells made of mono-crystalline silicon (Fig. 1, a).
- a PV module has solar cells made of multi-crystalline silicon (mc-silicon) (Fig. 1, b).

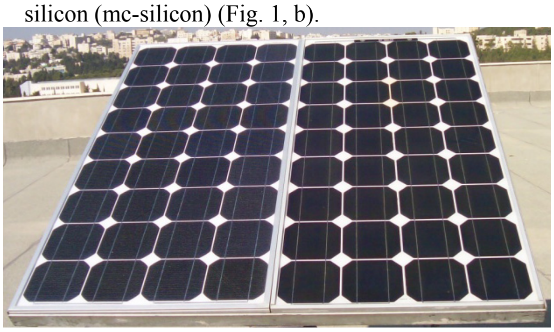

Figure 1 (a): Monocrystalline PV Cells

Figure 1 (b): Multiycrystalline PV Cells

Orientation and inclination angle of the solar panel significantly affect efficiency and output power. The two tested panels were installed on the same frame to inshore a similar inclination angle for both PV models. Best orientation for PV panels is to the south in Jordan to increase total energy incident on the collector surface during day light. The PV panels were placed to face south at 32º angle as Amman has a latitude of 31º57' north [25]. This angle can be reduced to less than altitude to maximize power in summer and to be larger than latitude in winter to maximize collected energy.

4.2. Battery Storage

PV systems require energy storage to store the generated electricity during day light to use when needed. Most used battery types are lead-calcium and lead-antimony. Nickel- cadmium batteries are also used particularly if battery is subjected to a range of temperatures. The changing nature of solar radiation requires batteries that can undergo charge and discharge cycles without damaging. The amount of battery capacity that can be discharged without damaging the battery depends on battery type. Lead calcium batteries are most suitable in "shallow cycle" applications where less than 20% discharge occurs in each cycle. Nickel-cadmium batteries and some lead-antimony batteries can be used in "deep cycle" applications where the depth of discharge may exceed 80%. Depending on site conditions and presence of a backup generator, battery banks are sized to provide a period of system autonomy ranging from a few days to a couple of weeks [e.g. 25].

Batteries are distinguished by their voltage, which for most applications is a recurrent of 12V. Battery capacity is expressed in Ampere-hours (Ah). For example, a 50 Ah, 48 V battery stores 50 × 48 = 2,400 Wh of electricity under nominal conditions. Optimization of battery size is important to extend battery life and optimal system performance and life-cycle costs. Unnecessary battery replacement is costly, particularly for remote applications.

4.3. Inverter

Inverters are power electronic devices used in various photovoltaic systems to convert direct current to a 50-Hz alternating current conforming to the grid.

The output power of tested photovoltaic panels in the present investigation was measured by calculating output current and voltage using an ohmmeter.

4.4. *Pyranometer*

A pyranometer is used to measure broadband solar irradiance on a plan surface and solar radiation flux density (W/m^2) of an angle view of 180º.

4.5. *Speedometer*

A speedometer is used to collect and record air velocity, temperature, humidity and wet bulb.

5. Experimental Approach

The experimental investigation has been carried out at the venue of the University of Jordan in Amman, Jordan. Experiment measurements started from January to the end of May. Measurements were taken from the two PV modules in three days of each month. Taken readings included the following:

- Open circuit voltage and short circuit current readings produced at the output of the PV cell. Solar radiation, ambient temperature, humidity and wetness, wind speed. Keeping similar conditions for the two tested PV panels.
- Efficiency of each panel under the recorded conditions was calculated. Input power has been calculated by multiplying the incident solar radiation with the PV area. Output power has been calculated using measured values of the generated voltage and current. Efficiency variation accordance to solar radiation and output conditions has been calculated and presented in the next section.
- Computer software has been used to specify cash flow diagram and to calculate payback period of the PV system.

Figure 2 shows the schematic diagram of PV panel system with all components such as charge controller, inverter, batteries and DC and AC load. The devices that have been used in the experimental work and their specifications are presented in Table 1.

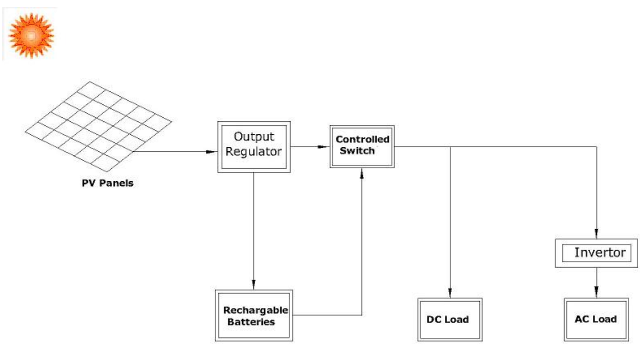

Figure 2: Schematic diagram for the PV system

Table 1: Specifications of devices used in this experiment

Devices	Manufacturer	Model	Specifications
PV Solar Panels Type 1	KYO CERA Corporation	KC 70	Max. power 75w outputs power 70v circuit volt 2105v output volt 16.9v Current 4.14 A
PV Solar Type 2 multi	TUV Rheinland	BP 585F	Nominal peak power Pm = 85. w Peak power voltage 18.v Power peak current 4.72 Short e.c I_{sc}=5A opent c. Volt V oc= 22.03v
Pyranometer +	Solar light co. inc. +	PMA 2144	Min. power Pmin=80w
Integrator	KIP and Zonen B.V	01127	Sensitivity = 15.42± 0.24 µV/W/m^2.
Voltmeter	UNI -T	DT 830	

6. Experimental Results

Solar radiation on a horizontal surface in Amman city varies from one month to another. There's also a wide variation in total daily radiation on horizontal surface in a same month, caused by the inclination angle of solar radiation and weather conditions.

Radiation intensity has high level in sunny days, and decreases to an insufficient level in cloudy weather. Variation in solar radiation is also caused by earth's rotation around its axis. At early morning solar radiation has a low angle and solar rays penetrate a thick atmospheric layer. Abundance in radiation occurs at noon, when sun is at the highest angle above the horizon and radiation encounters minimum thickness of the atmosphere. Solar radiation also differs according to seasons, in winter the sun becomes lower in the sky and higher in summer because sun ray's angle changes due to the earths tilt angle [25].

Figure 3(a-e) shows the measured ambient temperature as a function of time for several days in each month from January to May. Ambient temperature was measured at different times during test days starting 8:00am to 4pm. Fig. 3 indicates that temperature varies significantly during the day and in most cases from one day to another of the same month. For example, Fig. 3(a) shows that in January at 8am, measured temperature was 9^{o}C and rises to about 17^{o}C at midday and decrease to 14^{o}C at 4pm. Yet, the measured temperature is higher than the measured temperature in the morning. This temperature behavior is noted in the months January to May. Such rapid climate change in the same season produces a noted gap in temperature readings which affects the efficiency performance, as shown in the efficiency curve below Figure 3.

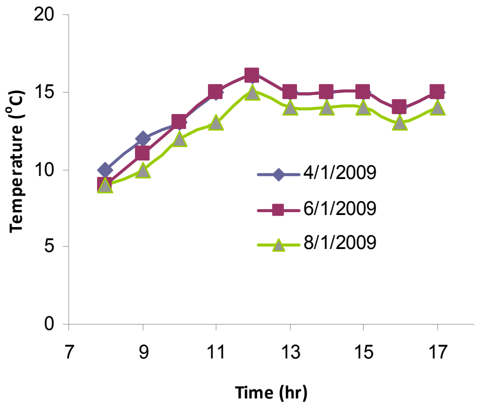

Figure 3 (a) January 2009

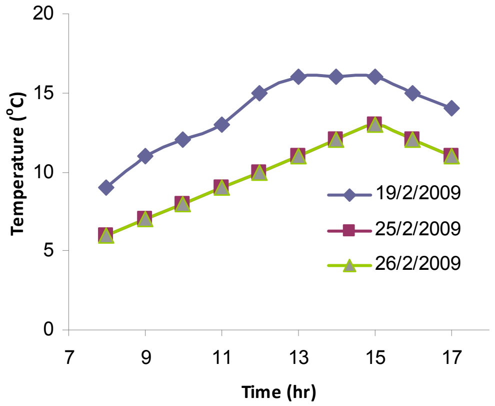

Figure 3 (b) February 2009

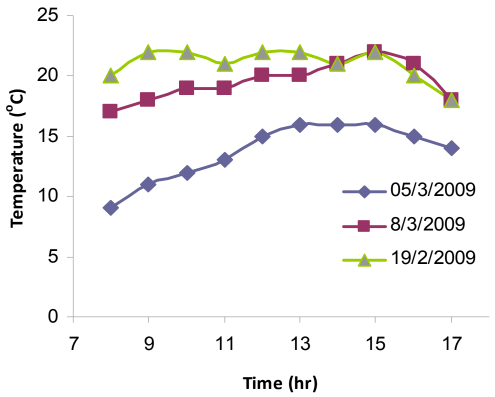

Figure 3 (c) March 2009

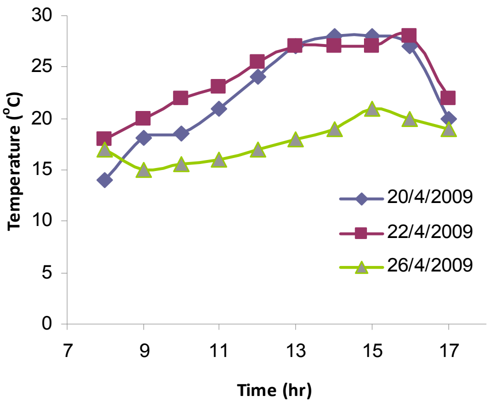

Figure 3 (d) April 2009

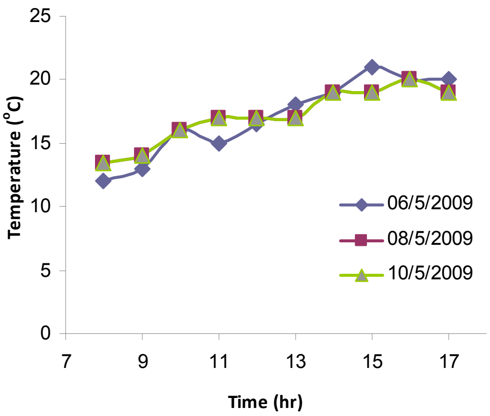

Figure 3 (e) May 2009

Figure 3 (a-e): Ambient temperature measurement as a function of time for different days in the months January to May

Variation in ambient temperature during the day affects received radiation intensity accordingly. The highest radiation intensity was obtained at mid day when sun ray is perpendicular on the surface. The recorded values are in the range 600 W/m^2 in the morning and afternoon and 1100W/m^2 at midday. The variation in radiation intensity caused variation in the measured output current which affects efficiency in the same manner. Fig. 4 shows solar radiation measurement per hour in randomly selected three days in the months January to May. January to March represent winter season in Jordan, April and May spring. Figure 4 shows radiation intensity is a little lower during the days in winter than those in spring particularly in the morning. However, it can be concluded from Figure 4 below that solar radiation in winter is enough to utilize PV system in Jordan.

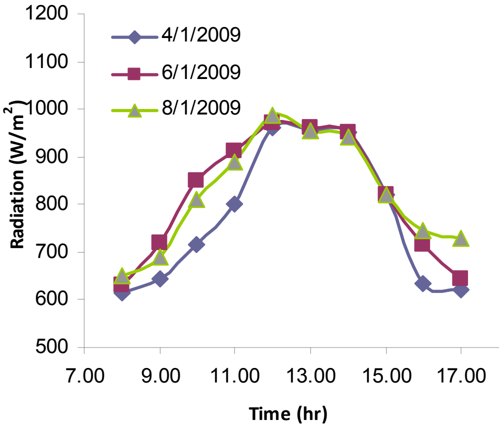

Figure 4 (a) January 2009

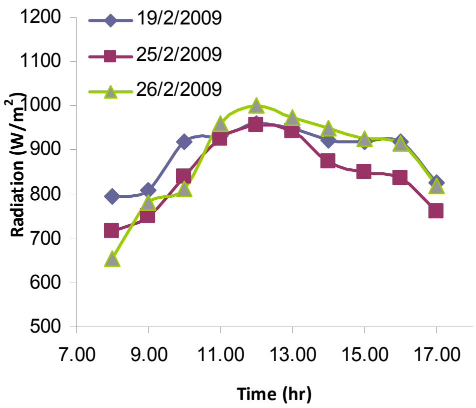

Figure 4 (b) February 2009

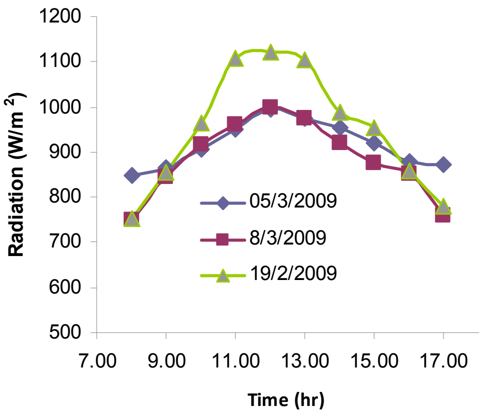

Figure 4 (c) March 2009

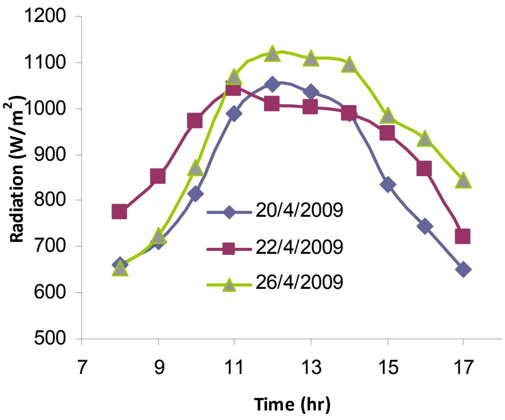

Figure 4 (d) April 2009

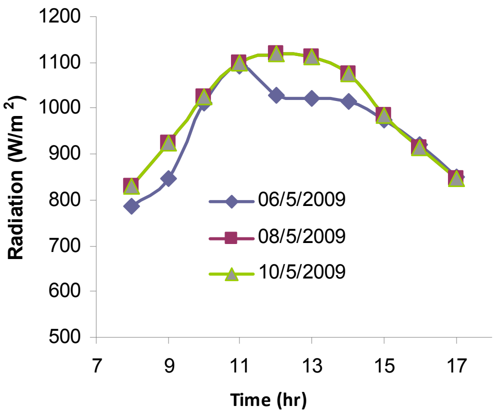

Figure 4 (e) May 2009

Figure 4 (a-e): Measured solar radiation as a function of time for different days each month

Output current and voltage of each panel was measured every hour in a randomly selected day each month under similar conditions. The open circuit voltage and short circuit current has been measured directly from the PV panels output without battery connection or electrical load. The efficiency curve of mono crystalline and multi crystalline PV panels is plotted.

Figure 5(a-e) shows the comparison of the produced current of mono crystalline and multi crystalline PV panels of each month. The output current of mono crystalline is higher than that of the multi crystalline PV panel at all times in days and months.

Finally, factors that affect the electrical characteristics of the PV solar panels are summarized as:

- The amount of sun rays reaching the cells
- number of cells in the panel
- types of silicon PV solar cells
- temperature of the PV solar panels
- area of each PV panel
- system losses effect such as losses due to cables and blocking diodes
- charge status of battery.

In the present experimental investigations, the batteries did not used in the measurements. Also, the inverter which changes the DC output battery to AC voltage of the load was not used in this experiment. Therefore, the effect of the inverter and batteries on the system efficiency has been not discussed in this work.

However, the ambient temperature has a considerable effect on the efficiency of PV system. As the ambient temperature increases cell temperature increases, the open circuit voltage decreases and the short circuit current become slightly higher to reach the maximum output current. In the present investigations, the measurements for both types of PV panels have been carried out at the same time which means that the ambient temperature and temperature of the PV panels were identical. Therefore, the influence of ambient temperature on the efficiency of PV panels is abandon.

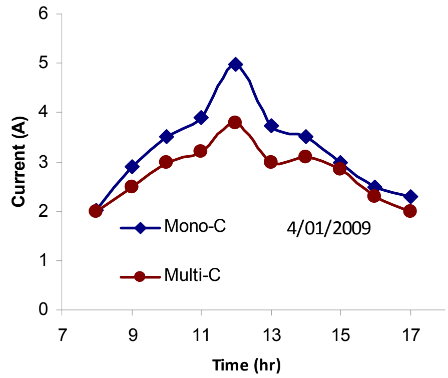

Figure 5 (a) January 2009

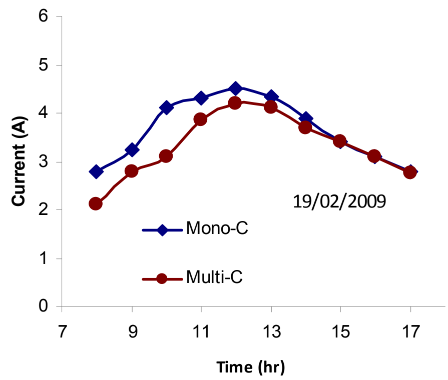

Figure 5 (b) February 2009

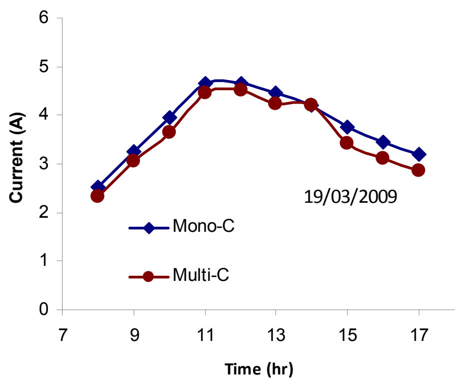

Figure 5 (c) March 2009

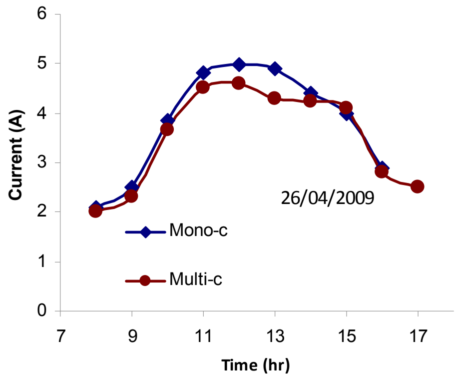

Figure 5 (d) April 2009

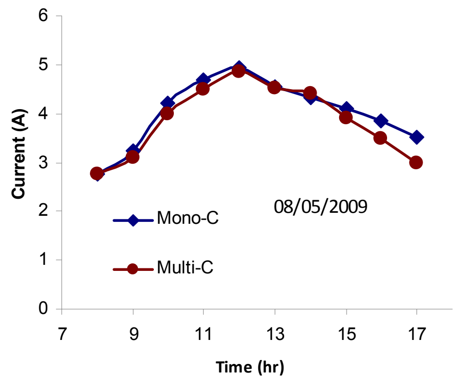

Figure 5 (e) May 2009

Figure 5 (a-e): Output current measurement of mono-crystalline & and multi crystalline PV panels as a function of time of one day in each month

Figure 6 (a-e) illustrates the efficiency curves for both mono crystalline and multi crystalline PV cells. Figure 6 indicates that mono crystalline PV cells have higher efficiency value than multi crystalline PV cells. The efficiency of mono crystalline PV cells can reach 18% while efficiency of multi -crystalline PV cells reaches 16%. Thus, output power of mono crystalline is higher than that of multi crystalline PV cells. Efficiency curves display constant values owing to weather change during the day. Efficiency increases rapidly with solar irradiance. A maximum peak occurs at midday when radiation intensity reaches maximum.

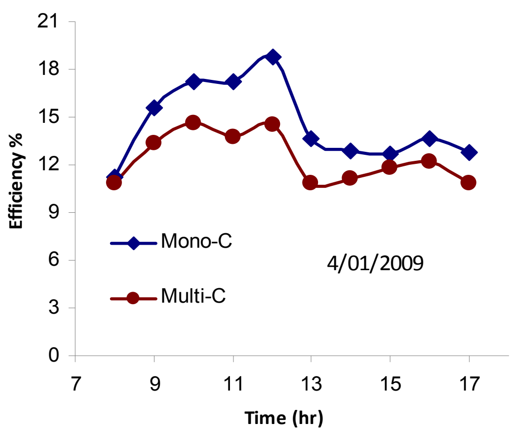

Figure 6 (a) January 2009

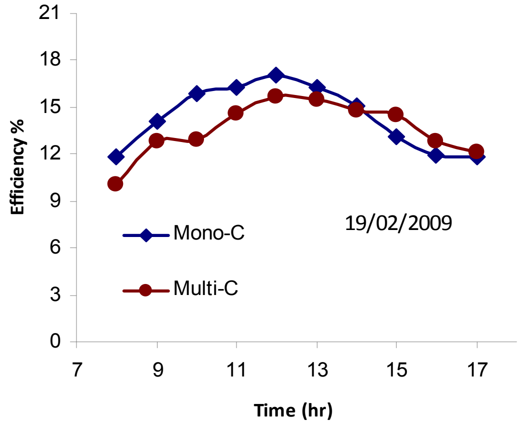

Figure 6 (b) February 2009

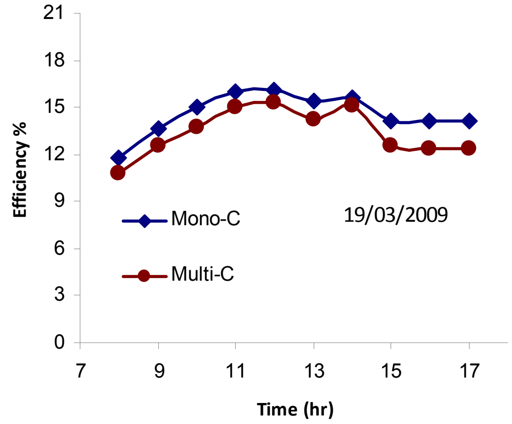

Figure 6 (c) March 2009

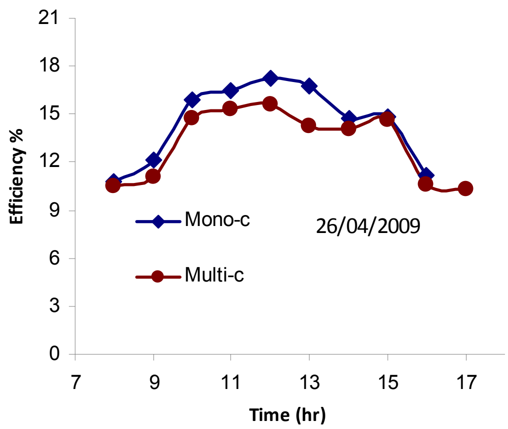

Figure 6 (d) April 2009

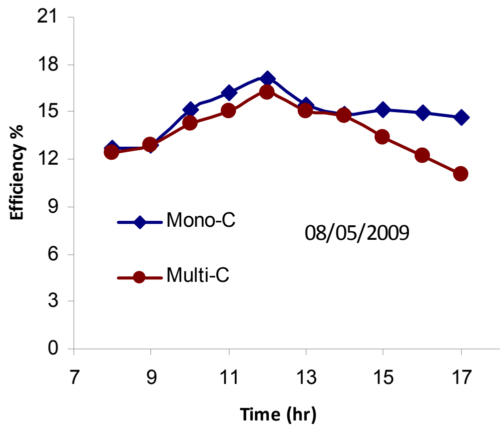

Figure 6 (e) May 2009

Figure 6 (a-e): efficiency behaviors of mono-crystalline &-multi crystalline PV panels as a function of time of the selected days in each month

Figures 5a and 6a show output current and efficiency of the two PV modules in January, both indicate graduate increase in irradiance. The PV solar modules show the peak values for the output current and efficiency at noon time. Cloudy sky on the 4th of January caused efficiency reduction and the generated power from 2:00pm onward. Figure 5b and 6b shows similar results for February. It is found that maximum values of output current and efficiency occur at noon time. The same trend is noted in March, April and May.

7. Conclusion and Recommendations

A performance test of mono-crystalline and multi-crystalline PV panels has been carried out in this paper. This test was conducted in **semi arid climate conditions** in Jordan. Short circuit current and open circuit voltage data were recorded of the tested PV panels. Input power has been calculated based on measured solar radiation. Output power of the panels is calculated from the measured values of generated current and voltage. Efficiency of mono-crystalline and-multi crystalline PV panels was measured in different days of each month. Findings indicate that efficiency of mono-crystalline is higher than that of the multi-crystalline PV panels.

Factors found to be taken into consideration while comparing the two PV types include:

1. Wear of utilized cells as the efficiency is reduced with a longer life-time period.
2. Cell type affects its performance in which the semi-silicon is classified as the best.
3. weather conditions, readings in rainy days are excluded because of absence of adequate radiation.

The comparison of the efficiency of the multi-crystalline and mono-crystalline PV panels indicates that despite similar behavior of both PV modules in the selected days and months, mono-crystalline panel efficiency was higher than that of the multi-crystalline panel. However, the difference between the efficiency of both models was relatively small.

References

[1] G. I. Abdel, "Framework conditions for solar thermal energy use in the southern Mediterranean countries, Solaterm project report, Center for the Environment and Development for the Arab Region and Europe (CEDARE), Egypt; December 2007.

[2] H. J. Moller, C. Funke, M. Rinio, S. Scholz, "Multicrystalline silicon for solar cells", Thin Solid Films, Vol. 487, 2005, 179– 187.

[3] A. Luque, S. Hegedus, "Handbook of Photovoltaic Science and Engineering", John Wiley & Sons Ltd, West Sussex, England, 2003.

[4] F. A. Farret & G. M. Simoes, "Integration of alternative Energy sources, John Wiley & Sons, Inc., Hoboken, New Jersey, 2006.

[5] R. A. Messenger, J. Ventre, "Photovoltaic Systems Engineering, 2nd edition, CRC Press LLC, 2004.

[6] F. Ferrazza, C. Silicon, "Manufacture and properties Solar Cells", 2005, 71-88.

[7] S. Ponce Alcantara, C. Del Canizo, A. Luque, "Adaptation of monocrystalline solar cell process to multicrystalline materials", Solar Energy Materials & Solar Cells, Vol. 87, 2005, 411–421.

[8] H. Lautenschlager, F. Lutz, C. Schetter, U. Schubert, R. Schindler, in: H.A. Ossenbrink, P. Helm, H. Ehmann (Eds.), "Photovoltaic Energy Conversion", Proceedings 14th Europ. Photovoltic Solar Energy Conference, Stephens and Associates, Bedford, UK, 1997, pp. 1358.

[9] H.J. Möller, C. Funke, M. Rinio and S. Scholz, "Multicrystalline silicon for solar cells", Volume 487, Issues 1-2, 2005, 179-187.

[10] M. Rinio, S. Peters, M. Werner, A. Lawerenz, H.J. Mo¨ller, " Measurement of the Normalized Recombination Strength of Dislocations in Multicrystalline Silicon Solar Cells", Solid State Phenom, Vol. 701, 2002, 82–87.

[11] H.J. Moller, in: K.A. Jackson, W. Schro¨ter (Eds.), "Electronic Structure and Properties of Semiconductors", Handbook of Semiconductor Technology, vol. 1, Wiley-VCH, Weinheim, Germany, 2000, 715.

[12] D. Helmreich, Symposium on Electronic and Optical Properties of Polycrystrystalline or Impure Semiconductors and Novel Silicon Growth Methods, Electrochemical Society, Princeton, 1977, p. 184.

[13] R. Kawamura, K. Sasatani, T. Onizuka, "Solid Energy Mater", Solid Cells 49, 1997, 307.

[14] International Executive Conference on Concentrating Solar Power (CSP) IPP Solar Power Project in Jordan, The Ministry of Energy and Mineral Resources of Jordan, Berlin, 19-20 June, 2002.

[15] B. I, Bentenrieder M, K. H, AlTaher A., "Introducing advanced testing methods for domestic hot water storage tanks in Jordan". Renewable Energy, Vol. 10, No. 2–3, 1997, 207–11.

[16] M. M, A. B. "Evaluation of domestic solar water heating system in Jordan using analytic hierarchy process". Energy Conversion and Management, Vol. 38, No. 18, 1997, 1815–22.

[17] H. M. "Characteristics of solar water pumping in Jordan", Energy, Vol.24 , No. 2, 1999, 85–92.

[18] H. M. Photovoltaic, "Wind and Diesel, A cost comparative study of Water Pumping Options in Jordan". Fuel & Energy Abstracts 1996, Vol. 37, No. 1, 39–44.

[19] R. Mamlook, B. Akash, S. Nijmeh, "Fuzzy Sets Programming to Perform Evaluation of Solar Systems in Jordan", Energy Conversion and Management, Vol. 42 , No. 14, 2001, 1717–26.

[20] The Royal Scientific Society (RSS), A Guide for Renewable Energy Installations, Test facilities, and Laboratories, Amman, RSS press, 1994.

[21] A. Badran, "A Study in industrial applications of solar energy and the range of its utilization in Jordan, Renewable Energy, Vol. 24, No. 3–4, 2001, 485–90.

[22] M. S. Al-Soud, E. S. Hrayshat, "Rural photovoltaic electrification program in Jordan", Renewable and Sustainable Energy Reviews Vol. 8, 2004, 593–598.

[23] E. S. Hrayshat, M. S. Al-Soud, "Solar energy in Jordan: current state and prospects", Renewable and Sustainable Energy Reviews, Vol. 8, 2004, 193–200.

[24] A. Al-Salaymeh, Z. Al-Hamamre, F. Sharaf, M.R. Abdelkader, "Technical and economical assessment of the utilization of photovoltaic systems in residential buildings:the case of Jordan, "Energy Conversion and Management, 2009, doi:10.1016/j.enconman.2009.11.026.

[25] Z. Jibril, "Estimation of solar radiation over Jordan—predicted tables", Renewable Energy, Vol. 1, No. 2, 1991, 277–91.

[26] M. Alsaad, "The applicability of hourly radiation models to Jordan. Solar and Wind Technology, Vol. 7, No. 3, 1990, 473–7.

JJMIE

Volume 4, Number 5, November 2010
ISSN 1995-6665
Pages 553 - 566

Jordan Journal of Mechanical and Industrial Engineering

Numerical Modelling of a Turbocharger Splitter-Vaned Centrifugal Impeller at off-Design Conditions, Part I: Impeller Flow Field

A. Fatsis [a,*], A. Panoutsopoulou[b], N. Vlachakis [b]

[a] *Technological University of Chalkis, Department of Mechanical Engineering, 34400 Psachna Evoias, Greece.*

[b]*Hellenic National Defence Systems S.A., 1, Ilioupoleos Avenue, 17236, Greece*

Abstract

The 3D unsteady flow field in a centrifugal impeller with splitter vanes, due to a downstream static pressure distortion imposed by the volute collector at off-design operations, is analysed by means of numerical modelling. Two cases are examined: one analysing the impeller flow field at higher than nominal mass flows and one at lower than nominal mass flows. The hub streamsurface, where the channel length is longer reacts with smoother changes with respect to the shroud. For both cases, it is demonstrated that the exit static pressure non-uniformity propagates upstream and creates unsteady flow in the channels between the impeller full blades and splitter vanes resulting in changes in incidence, velocity components and relative flow angles. In the higher mass flow case the unsteady phenomena are more pronounced.

Keywords: Unsteady Flow, Centrifugal Impeller, Splitter Blades, Static Pressure Distortion.

Nomenclature

c	Speed of sound
f	Frequency
t	Time
L	Length of blade channel
M	Mach number
N_{bl}	Number of blades
P	Static pressure
S_r	Strouhal number
V	Absolute velocity
Δt	Time step
Ω	Reduced frequency
α	Absolute flow angle
β	Relative flow angle
ρ	Density
ω	Non-dimensional rotational impeller speed

Superscripts

bl	Blade
spl	Splitter

Subscripts

ps	Blade or splitter pressure side
r	Radial
rel	Relative
ss	Blade or splitter suction side
z	Axial
θ	Circumferential
0	Total conditions
1	Impeller inlet
2	Impeller trailing edge

* Corresponding author. afatsis@tee.gr.

1. Introduction

Centrifugal compressor impellers often employ the use of splitter vanes in order to achieve the high pressure ratio for which they are designed, avoiding thus the chocking of the flow in the vicinity of the leading edge of the blades where the free surface for the flow between two consecutive blades is minimum, [1]. It is proven experimentally that when a centrifugal compressor impeller is followed by a non-axisymmetric volute operating at off-design conditions, the circumferential distribution at the diffuser outlet and at the diffuser inlet is not uniform, [2]. It was also found that the circumferentially non-uniform profile of the static pressure follows a rather saw-tooth distribution, with its peak value (in the case of higher mass flows) or its lowest value (in the case of lower mass flows) corresponding to the volute tongue position, [2].

The propagation of the outlet static pressure distortion towards the impeller inlet was confirmed in [3]. Sudden changes in the flow field observed at the volute tongue, result from two counter-rotating vortices (because the total vorticity has not yet changed) at the impeller inlet. At mass flows lower than the optimum one, one of the vortices creates counter-rotating flow resulting in an increased incidence. The other vortex causes a decrease in incidence. A similar phenomenon occurs at higher than the optimum mass flows.

A simple 1D model was presented to predict the impeller response due to the circumferential static pressure variation caused by the volute, [4]. The model is applicable only for incompressible flows and assumes a circumferentially constant relative outlet flow angle. This is in contrast to experimental observations in which circumferential variations in the relative outlet flow angle were reported [5].

Better predictions were obtained by 2*D* unsteady models, solving the 2*D* unsteady potential flow equations by means of singularity or finite element method, [6]. Incompressible flow calculations solving the 2*D* Navier-Stokes flow using the k-ε model for turbulence were also done, [7]. Quasi-3*D* unsteady models predict the unsteady flow variations in the blade to blade surface at the shroud [2]. All these models, however, fail to provide information about the 3 *D* effects in the impeller.

A 3D numerical model based on the Euler equations was developed in order to study the unsteady flow field inside the impeller due to a circumferential variation of the static pressure at the impeller outlet, for the case of full-bladed impellers, [8]. The modelling of unsteady flows using the Euler equations assumes that the main unsteady flow characteristics are dominated by the propagation of pressure waves across the flow field.

In the present study, the extension of the method is presented for the case of 3D centrifugal impellers with splitter vanes operating at circumferentially non-uniform static pressure. Computations are performed for centrifugal impeller with backward leaned blades for lower and higher mass flows. Results obtained show that the present model is able to handle the unsteady flow field inside the impeller full and splitter blades. The outlet static pressure non-uniformity propagates upstream and causes unsteady flow in the impeller and creates incidences variations upstream the impeller blades.

1.1. Numerical Method

The numerical model used to analyse the unsteady impeller flow field consists of the 3D Euler equations. These equations can accurately capture flows where viscous phenomena are limited in certain regions of the flow, and this makes them an attractive tool for the computation of the dynamic behaviour of the unsteady flow inside the impeller. Adopting the Euler equations means that the viscous terms from the full Navier-Stokes equations are neglected, and the transport of momentum and energy in the fluid is done only by means of convective fluxes. Since viscous forces are neglected, this implies that the considered model is not valid at relatively low rotational speed. Using the Euler equations compressible rotational flow, steady or unsteady flow fields can be calculated. Flow unsteadiness due to circumferential inlet and outlet pressure distortions is governed mainly by wave propagation and to a lesser extent by viscous phenomena. This justifies the use of an unsteady 3 *D* Euler solver instead of a full 3 *D* Navier-Stokes solver. This simplification results in an affordable computer time and gives useful information on the dynamics of the flow in the case where the impeller is not heavily loaded and flow separation is limited. The model was validated for the case of full-bladed centrifugal impeller, showing fairly good agreement against available experimental results in the literature and predicting the unsteady flow features that are in agreement with experimental investigations, [8].

The 3D Euler equations in non-dimensional form are written in conservative form in cylindrical coordinates, *(r,θ,z)* as follows:

$$\frac{\partial \vec{u}}{\partial t}+\frac{1}{r}\cdot\frac{\partial\left(r\, f(\vec{u})\right)}{\partial r}+\frac{1}{r}\cdot\frac{\partial g(\vec{u})}{\partial \theta}+\frac{\partial h(\vec{u})}{\partial z}+\vec{b}(u)=0 \qquad (1)$$

where $\vec{u}$ is the vector of conservative variables, $f(\vec{u}), g(\vec{u}), h(\vec{u})$ are the vectors of convective fluxes and $b(\vec{u})$ is the source term, defined in detail in [8].

The space discretization of the equations is done by means of the finite volume technique. More specifically the bitrapezoidal cell, Figure 1, was used, offering second order spatial accuracy in smooth grids, [9].

The partial differential equations are written in a semi-discrete form as follows:

$$\frac{d}{dt}\left(\vec{u}\right)+\vec{R}=0 \qquad (2)$$

where $\vec{R}$ are the residuals of the equations. Since the purpose of this study is the calculation of unsteady flows, the choice of the time integration scheme has a significant role on the accuracy of the results.The Runge-Kutta four steps scheme, providing second order accuracy for non-linear partial differential equations and extensive stability limits up to a CFL number of $2\cdot\sqrt{2}$, was used for this purpose.

$$\begin{aligned}
&\vec{u}^{(0)}=\vec{u}^{n}\\
&\vec{u}^{(1)}=\vec{u}^{(0)}-\frac{\Delta t}{2}\cdot\vec{R}^{(0)}\\
&\vec{u}^{(2)}=\vec{u}^{(0)}-\frac{\Delta t}{2}\cdot\vec{R}^{(1)}\\
&\vec{u}^{(3)}=\vec{u}^{(0)}-\Delta t\cdot\vec{R}^{(2)}\\
&\vec{u}^{(4)}=\vec{u}^{(0)}-\frac{\Delta t}{6}\cdot(\vec{R}^{(0)}+2\cdot\vec{R}^{(1)}+2\cdot\vec{R}^{(2)}+\vec{R}^{(3)})\\
&\vec{u}^{n+1}=\vec{u}^{(4)}
\end{aligned} \qquad (3)$$

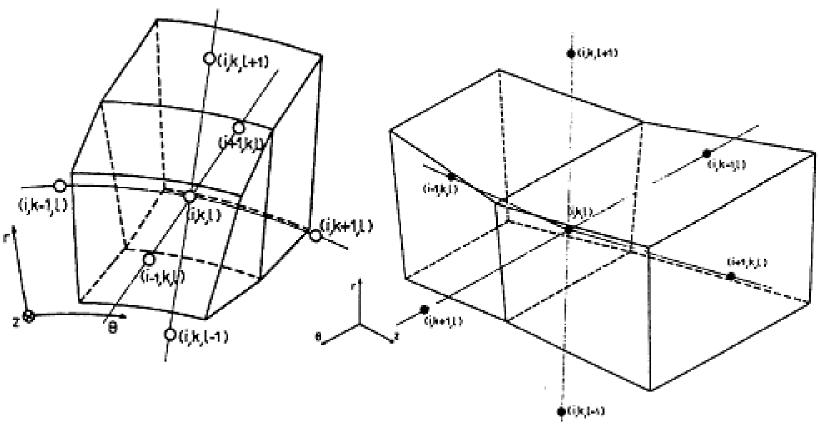

Figure 1: The bitrapezoidal volume used for the space discretisation

Extensive testing of the method in special test cases for which analytical solutions exist, has demonstrated the accuracy of this scheme for unsteady flow predictions, [2].

Impermeable wall boundary conditions are imposed on the solid walls (i.e. on the blade and splitter suction and pressure side and on the hub and shroud walls) by considering only the static pressure when computing the convective fluxes. The evaluation of the artificial dissipation on the solid walls is done by means of higher order extrapolation polynomials in order to minimize the dissipative fluxes, [8]. At the inflow and outflow boundaries, non-reflecting boundary conditions based on the Fourier decomposition, were used, [8]. Non-reflecting boundary conditions suggest infinitely long pipes upstream and downstream of the impeller and it is shown in [8] that the solution is not affected by the upstream location of the inflow boundary.

The physical boundary conditions specified upstream assuming subsonic inflow, are: Total pressure, total temperature and two flow angles (4 physical boundary conditions). The fifth boundary condition is a numerical one coming from the interior point of the computational domain.

The physical boundary condition specified downstream assuming subsonic outflow, is taken to be the static pressure (1 physical boundary condition required). The rest four boundary conditions are numerical ones coming from the interior point of the computational domain.

Since the outflow static pressure is not uniform along the circumference, this means that as the impeller rotates, a virtual point attached at the trailing edge experiences different values of the static pressure through out a full rotation, which consists the period of the phenomenon. Phase-lagged periodicity conditions were used to simulate this non-uniformity and to compute the fluxes through the upstream and downstream streamlines.

An H-grid was used for the calculations. A projection of this grid in the meridional plane (r-z) and in the blade-to-blade plane (θ-z), as well as a three-dimensional view of some of the impeller blades is given in Figure 2.

The unsteadiness of the incompressible flow in a channel of length L is normally characterized by the reduced frequency,

$$\Omega = \frac{f \cdot L}{V} \tag{4}$$

where V is the speed by which a particle is transported through the channel. In Turbo-

machinery applications, L is normally defined as the length of a blade passage, whereas f is the number of rotations per second times the number of perturbation waves around the circumference.

The acoustic Strouhal number is more appropriate to characterize compressible flows. It is defined as the product of the reduced frequency and the Mach number:

$$S_r = \Omega \cdot M = \frac{f \cdot L}{c} \tag{5}$$

It relates the time needed by a pressure wave to travel a distance L, at the speed of sound c to the period of the pressure perturbation 1/f. Unsteady effects are small for Sr < 0.1 and the flow can be evaluated by means of steady calculations. For Sr > 0.1 accurate results can be obtained only by means of unsteady flow calculations.

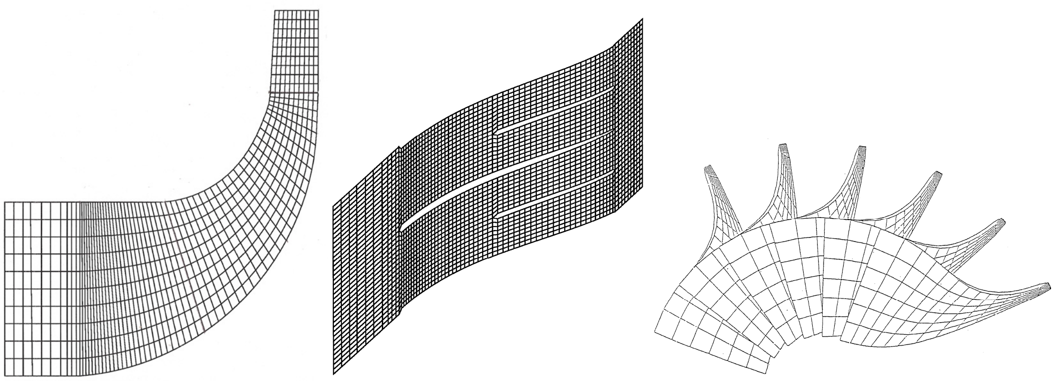

(a) (b) (c)

Figure 2: (a)Meridional *(r-z), (b)*Blade-to-blade *(θ-z)* view of the H-grid used for the calculations, (c)Three-dimensional view of some of the impeller blades

2. Impeller flow analysis

2.1. Mach number distributions at lower than optimum mass flows

The centrifugal impeller analysed has 10 full backward leaned blades and 10 splitter vanes. The circumferential static pressure distribution specified at the downstream boundary, shown in Figure 3, is typical for lower (Figure 3a) and higher (Figure 3b) than nominal flow rates.

A blade-to-blade projection of the numerical domain used at shroud streamsurface, is shown in Figure 4. Dashed lines define the lower channel between the blade suction side and the splitter vane pressure side. Continuous lines define the upper channel between the splitter vane suction side and the full blade pressure side.

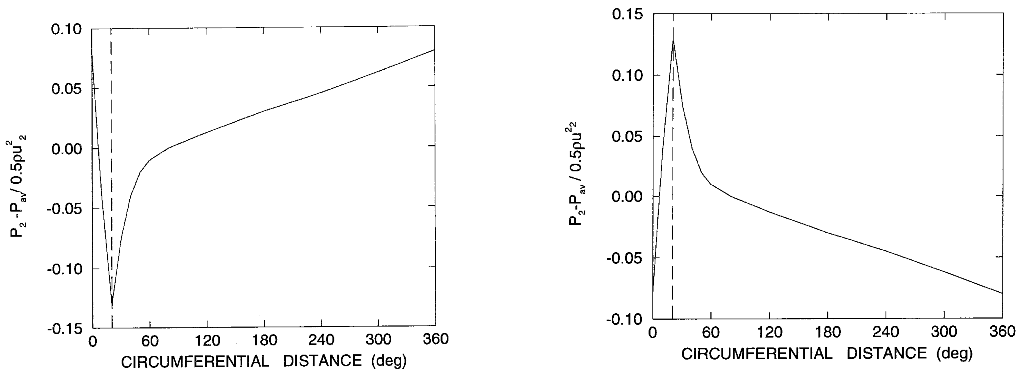

(a) (b)

Figure 3: Circumferential outlet static pressure distribution at (a) lower than optimum mass flows and (b) at higher mass flows (- - - tongue position)

Phase-lagged periodicity conditions are used to update the upstream and downstream stagnation pseudo-streamlines AB, CD and EF, GH, respectively. The points along the pseudo-streamlines upstream and downstream of the splitter vanes (namely KL, MN in Figure 4) are treated as interior points of the numerical domain and simple continuity of the fluxes is imposed.

The acoustic Strouhal number based on the length of the full blade, as defined by equation (5), is $S_r^{bl} = 0.22$, while the acoustic Strouhal number based on the length of the splitter vane is $S_r^{spl} = 0.146$.

Unsteady flow calculations begin having as initial guess the steady state converged solution at $t = t_0$. Convergence to a periodic state is reached when the calculated flow field repeats itself after every rotation of the impeller (which corresponds to several hundred computations). The distribution of the relative blade Mach number at shroud, mean and hub for the full blades and the splitter vanes is plotted on Figures 5–7 for different angular positions, θ, around the circumference. The dashed lines indicate the Mach number on the surfaces indicated with dashed lines on Figure 4 (lower channel). The continuous lines show the Mach numbers in what is called the upper channel.

The low back pressure at $\theta = 45^{o}$ results in a local increase of mass flow, propagating upstream as an expansion wave. At $\theta = 90^{o}$ it has reached the leading edge of the splitter where it results in a small incidence, shown by the small differences between the suction and pressure side Mach number at leading edge. It reaches the full blade leading edge at $\theta = 135^{o}$, where the smallest difference between the suction and pressure side Mach number is observed.

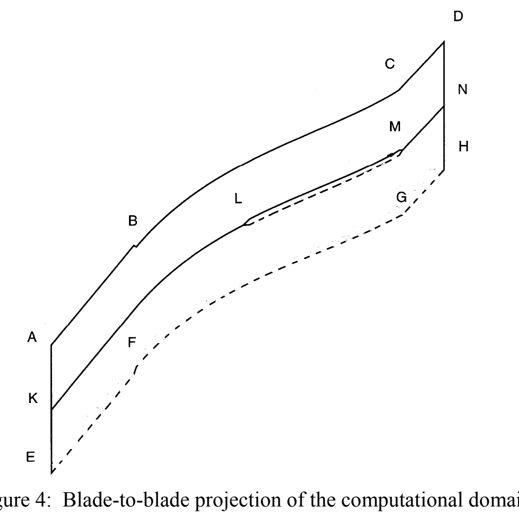

Figure 4: Blade-to-blade projection of the computational domain used for the splitter-vaned impeller computations

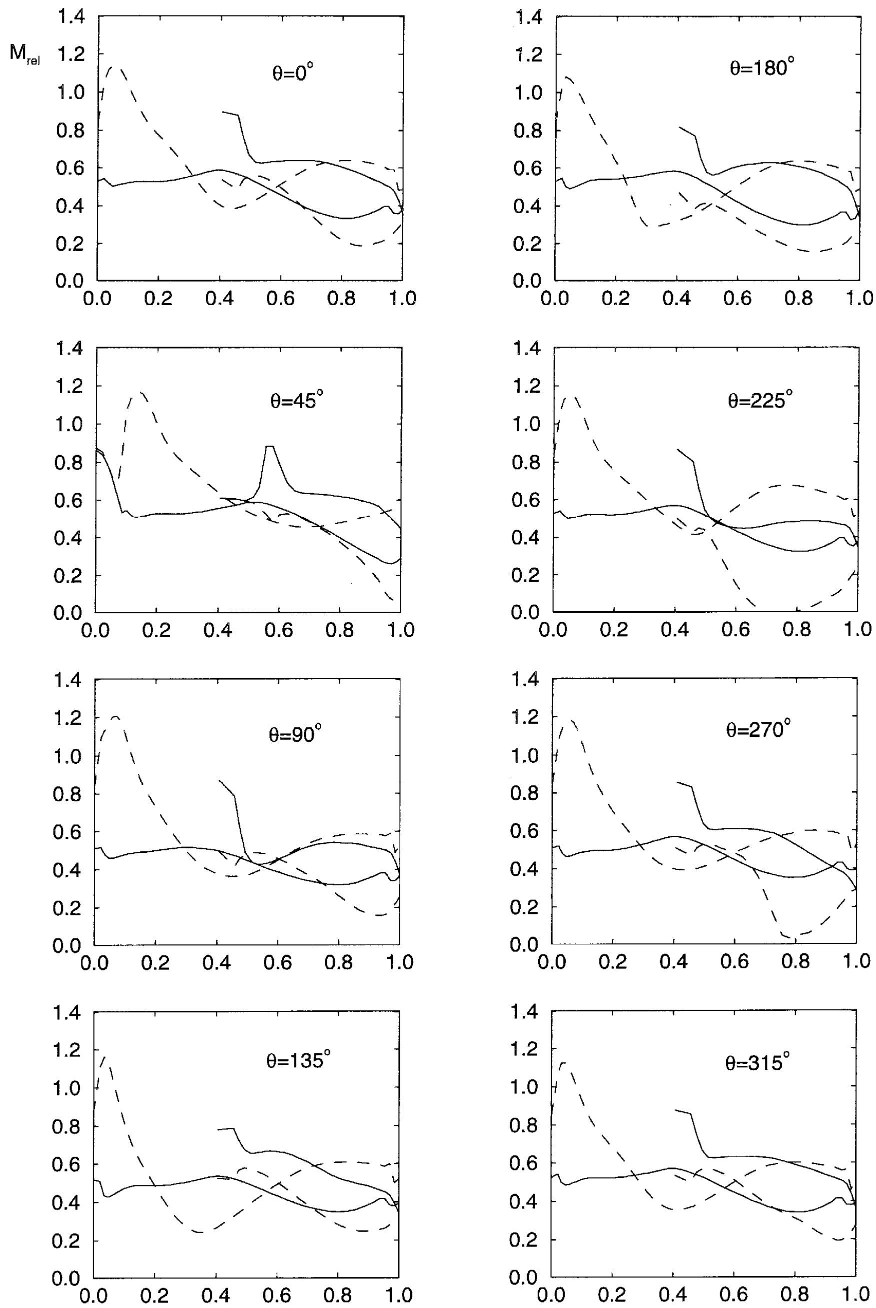

Figure 5: Blade relative Mach number versus the blade length at shroud streamsurface for the lower mass flow case during one rotation. Dashed lines illustrate the distribution in the lower channel of figure 4 and continuous lines the distribution in the upper channel of figure 4.

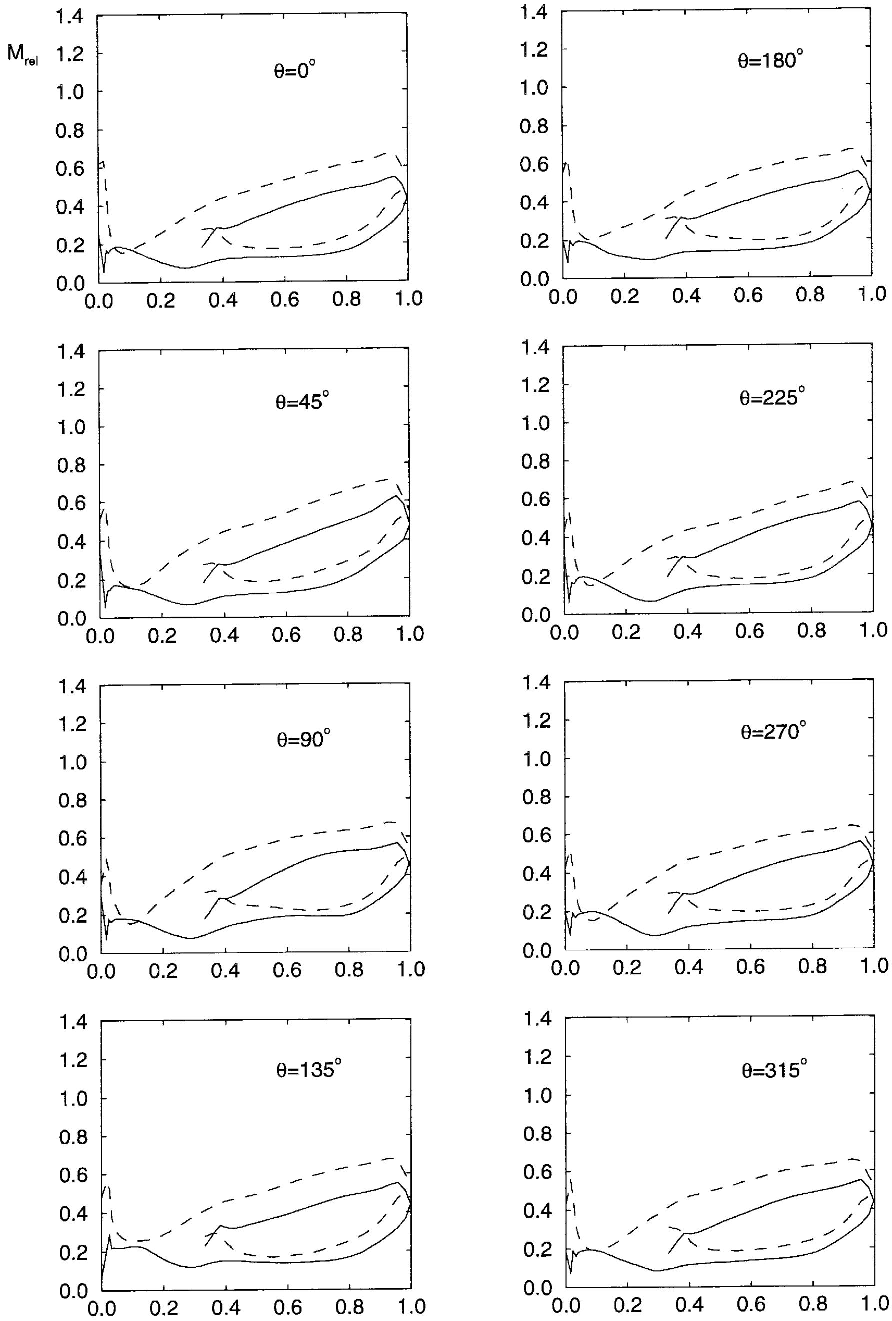

Figure 6: Blade relative Mach number versus the blade length at mean streamsurface for the lower mass flow case during one rotation. Dashed lines illustrate the distribution in the lower channel of figure 4, and continuous lines the distribution in the upper channel of figure 4.

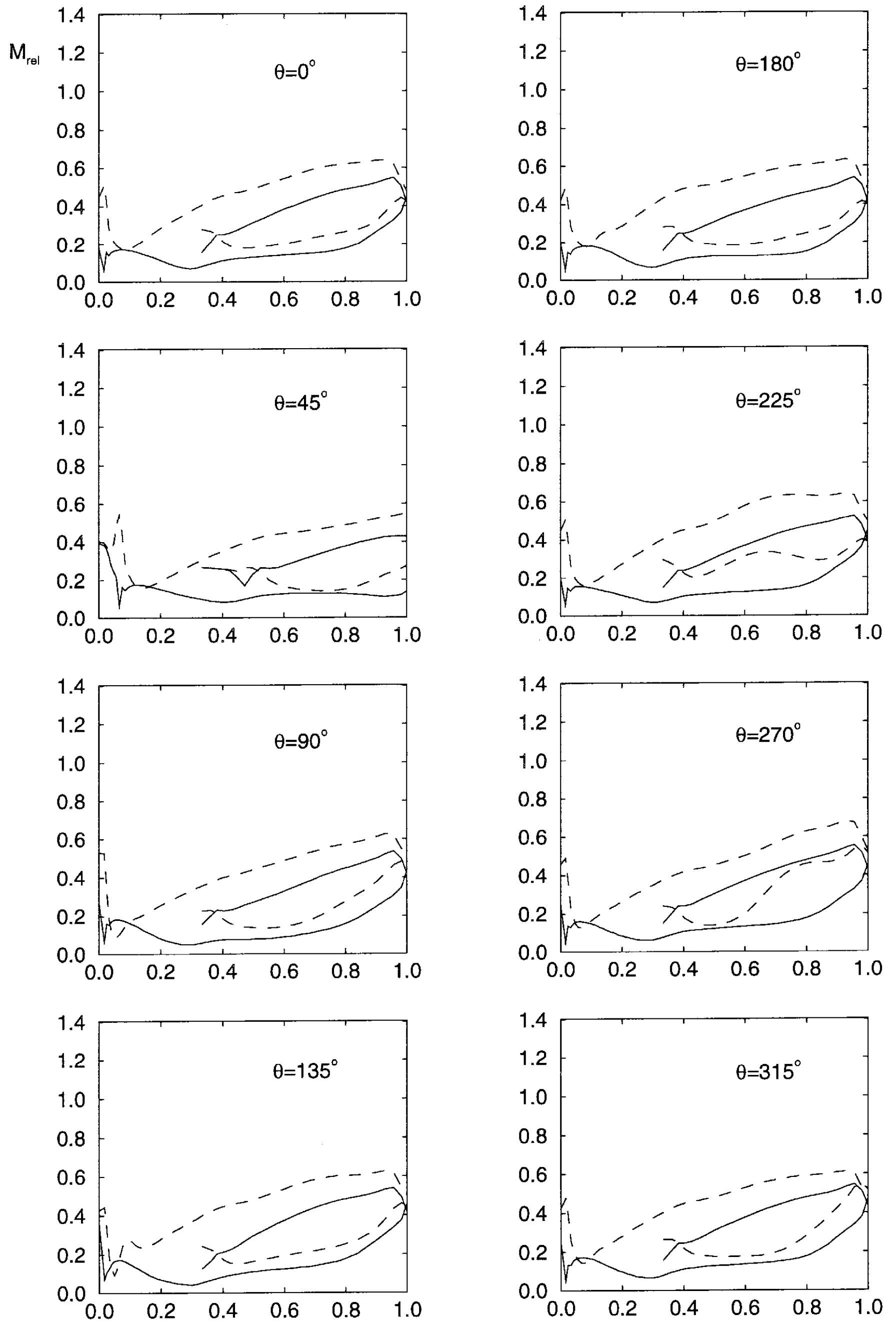

Figure 7: Blade relative Mach number versus the blade length at hub streamsurface for the lower mass flow case during one rotation. Dashed lines illustrate the distribution in the lower channel of figure 4, and continuous lines the distribution in the upper channel of figure 4.

In the mean time a pressure wave resulting from the sudden pressure increase between $\theta = 30^o$ and $\theta = 90^o$ has started to move upstream. It reaches the leading edge of the splitter at $\theta = 135^o$, where it creates a high splitter vane suction side Mach number because of the high incidence. The same pressure wave reaches the full blade leading edge at $\theta = 180^o$ and 225^o where the suction side Mach number has its maximum.

From the value of the acoustic Strouhal number, one can conclude that it takes half a rotation for a wave to move from trailing edge to leading edge and back, so that a pressure wave travels twice forth and back during one rotation (the second time at lower amplitude because of damping). This is confirmed by the similarity between the

left and the right column of Figure 5 indicating that the relative Mach number distribution is almost repeating itself every 180^o. Variations in blade loading in transonic regime due to static pressure distortion were also calculated in [12]. In that article it was also concluded that the unsteadiness influences the impeller flow field and creates acoustic wave structures inside the impeller.

The variations of Mach number are much smaller on the mean streamsurface (Figure 6). The changes in blade loading are mainly due to variations of the suction side Mach number distribution. The pressure side distribution shows almost no variations. A twice per rotation variation of the incidence can be concluded from the variation of the full blade suction side Mach number near to leading edge. Observations from the results of [12] confirm that the mean streamsurface reacts less that the shroud streamsurface.

The relative Mach number distribution at hub is shown in Figure 7. In this figure a given blade passage between two consecutive full blades is captured as it rotates around the circumference. The circumferential angle, θ, of the passage varies from 0 to 360 degrees. Eight different circumferential positions were selected, having a peripheral increment of 45 degrees each. From that figure one can see that the Mach number at blade suction side at shroud is slightly higher than one, indicating a transonic area standing at the suction side area. After a peak in the suction side Mach number due to incidence, a nearly constant loading of the full and splitter vanes is observed. Since the suction side Mach number remains supersonic for all values of the circumferential angle, θ, the downstream static pressure distortion cannot propagate upstream at the shroud radius. This means that the upstream-propagating pressure waves are reflected at the transonic area and they return downstream affecting the loading of the splitter vanes. One observes a periodic variation of the Mach number at the suction side leading edge and at 30% of the blade length. The lower blade channel has a higher Mach number.

2.2. Inlet and outlet flow distortion at lower than optimum mass flow

In Figure 8 one can see the mass averaged variation of the relative flow angle, β_2, the absolute flow angle α_2, and the non-dimensional radial and absolute tangential flow velocity components, V_{R2} and $V_{\theta 2}$ downstream the trailing edge, at R/R2 = 1.10. The circumferential distance of 20o corresponds to the volute tongue position where the static pressure reaches a minimum value on the outlet boundary (Figure 3a). The minimum value of $\beta_2, \alpha_2, V_{R2}$ and $V_{\theta 2}$ is not at 20o, but approximately at 40o because some time is needed by the pressure waves to travel from the outlet of the computational domain to the trailing edge position. For circumferential distances larger than 100o where the rate of increase of static pressure is small, no significant variations in β_2 are observed, except a second small minimum at 230o. This minimum can be seen well on the α_2 distribution (Figure 8b). The distributions of V_{R2} and $V_{\theta 2}$ follow the trend of the previous two distributions. However $V_{\theta 2}$ shows a sharp increase and decrease whereas V_{R2} shows only a sudden decrease.

Superposed on the variation with length Δθ = 180o, one also observes a small variation with a length Δθ = 90o, resulting from the reflection of the waves at the splitter vane leading edge.

Stars indicate the outlet flow conditions obtained from steady flow calculations, in which the local static pressure is imposed at the outlet. They show a monotonic increase or decrease with the outlet static pressure, but completely fail to capture the large local variations of the flow parameters.

The circumferential variation of the flow variables at the leading edge (Figure 9) also shows a 180o period. As it was observed in experiments [13], the static pressure variation propagates upstream and influences the whole impeller flow. Variations of the absolute flow angle α_1 and the absolute tangential and radial velocity components $V_{\theta 1}$ and V_{Z1} show variations, which can be related to each other. The β_1 variation is completely different. Changes in the sign of α_1 and $V_{\theta 1}$, indicate the presence of two counter rotating vortices upstream of the leading edge, as was observed in [3]. The β_1 variation is a result of it. The upstream vortices have to be counter rotating because no net vorticity has been created yet, upstream of the leading edge. Numerical simulations using a Navier-Stokes commercial code for the case of impeller-volute interaction [14] reported discrepancies between experimental and numerical data due to the jet and wake structure between the impeller blades and due to the difficulty to have a turbulence model to treat the flow separation at the blade suction side.

2.3. Inlet and outlet flow distortion at higher than optimum mass flow

The circumferential outlet static pressure distortion for higher than nominal mass flow is shown in Figure 10. It was concluded in [15] that both in case of lower and of higher mass flows, the circumferential static pressure distortion causes unsteady impeller flow field. The relative blade Mach number distribution at hub, mean and shroud

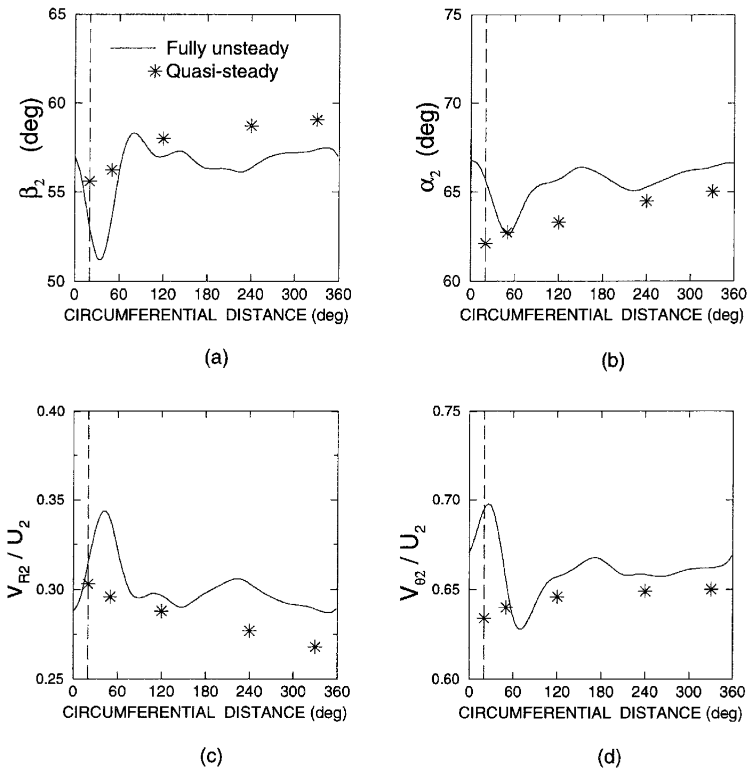

Figure 8: Circumferential variation of mass averaged β_2, α_2, V_{R2}, $V_{\theta 2}$ at R/R_2=1.10, S_r=0.22, for the lower mass flow case (- - - tongue position)

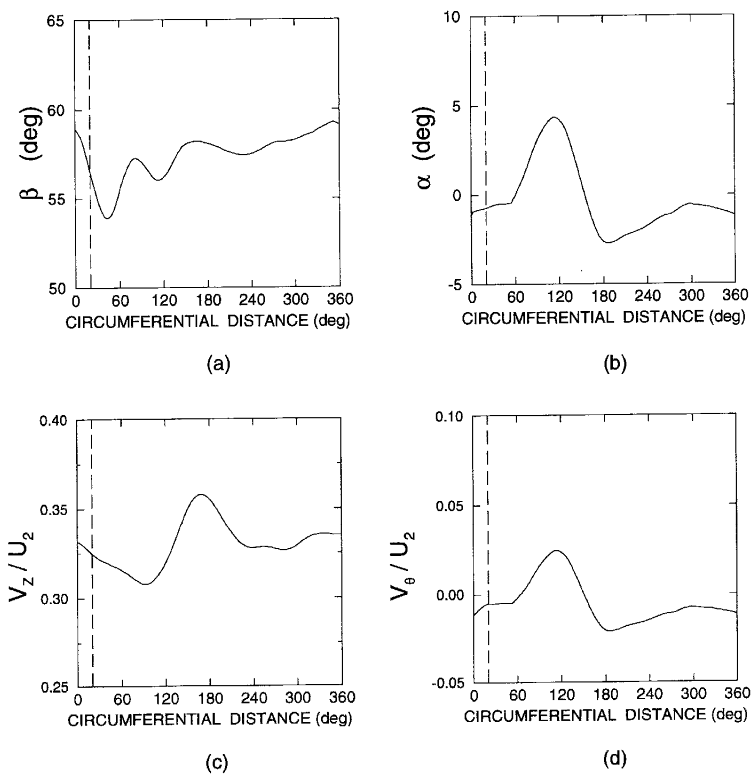

Figure 9: Circumferential variation of mass averaged β_1, α_1, V_{Z1}, $V_{\theta 1}$, at leading edge, S_r = 0.22 for the lower mass flow case (- - - tongue position).

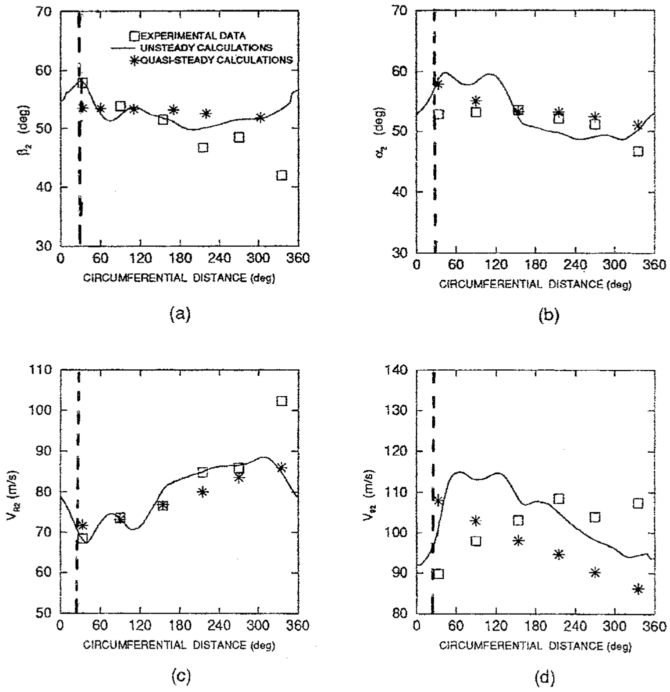

Figure 10: Circumferential variation of mass averaged $\beta_2, \alpha_2, V_{R2}, V_{\theta 2}$ at R/R_2=1.10, Sr=0.22, for the higher mass flow case (- - - tongue position).

streamsurfaces is not shown here but it has also a wavy variation with periodicity of one impeller rotation, similar to the one observed at lower than optimum mass flow. The flow unsteadiness inside the impeller repeats itself after a period of the phenomenon, as it was also concluded in [16]

The circumferential variation of the mass averaged relative flow angle β_2, absolute flow angle α_2, radial velocity V_{R2} and absolute tangential velocity $V_{\theta 2}$ at *R/R2* = 1.10 are compared to the steady flow solution in Figure 10. In this figure stars show results obtained from steady flow calculations, in which the local static pressure is imposed at the outlet. They show a monotonic increase or decrease with the outlet static pressure, but completely fail to capture the large local variations of the flow parameters. Squares show experimental results available in the literature [2]. The numerical predictions of the unsteady flow model show a fair agreement with the measurements, taking into account the complexity of the phenomenon. Possible explanation of the discrepancies can be attributed to the fact that downstream the trailing edge of the blades, at *R/R2* = 1.10, there is the formation of the jet and wake structure [1] affecting the slip factor of the blades and all the flow variables. The numerical model used in the present study cannot take into account this effect.

One observes again a 2 wave per rotation variation. The first peak in β_2 occurs at 35^{o} (Figure 10a). It is due to the peak in exit static pressure shown in Figure 3. This variation shows a small phase shift when compared to the variation of V_{R2} and α_2, whose variations are closely related to each other.

All variations show again a 2-period per rotation behaviour as a result of the pressure waves reflected at the leading edge, travelling twice upstream and downstream the impeller during one rotation. This was also observed for the case of full-bladed centrifugal impeller operating at higher than optimum mass flows and a similar value of the acoustic Strouhal number, in [8]. The two waves per rotation were even more clearly visible because the waves were not perturbed by reflections at the leading edge of the splitter vanes.

The circumferential variation of the mass averaged $\beta_1, \alpha_1, V_{Z1}, V_{\theta 1}$ at leading edge position is shown in Figure 11. A minimum in the axial flow velocity V_{Z1} is observed at 120^{o}. This occurs at a $\Delta\theta$ = 90^{o} later than the minimum value of V_{R2}. This shift corresponds to the time needed by a perturbation to travel upstream over a length L. One can conclude from this that there is no direct interaction between the high downstream static pressure and the high relative flow angle at θ = 50^{o}.

Observing the β_2 distributions for the case of lower mass flows (in Figure 8a), as well as for the case of higher mass flows (in Figure 10a), one can conclude that the assumption of circumferentially constant *β2*, made in many *1D* models (such as [4]), is not in agreement with reality. This is, in the authors' opinion, the main source of errors in *1D* models at higher reduced frequency or acoustic Strouhal number.

The importance of the pressure waves, travelling upstream and downstream, applies only to compressible flows. The use of the rigid column theory remains a good approximation for incompressible flows.

3. Conclusions

The present model solving the *3D* unsteady Euler equations can give valuable information about unsteady flows in impellers at an affordable computer time and cost.

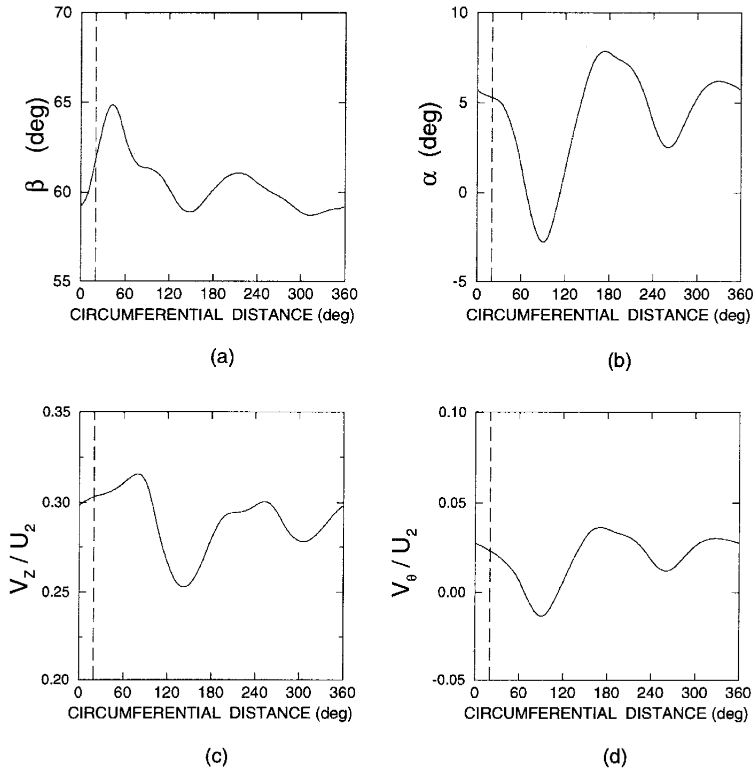

Figure 11: Circumferential variation of mass averaged β_1, α_1, V_{Z1}, $V_{\theta 1}$ at leading edge, S_r=0.22, for the higher mass flow case (- - - tongue position).

Calculations of the relative blade Mach number distribution in the splitter-vaned impeller show that the flow unsteadiness is governed by pressure waves propagating in the blade to blade channels.

Different response to the outlet static pressure distortion by the upper and lower channels between two main blades is observed. More specifically, the channel between the main blade suction side and the splitter vane pressure side is more loaded than the channel between the splitter suction side and the main blade pressure side. Such a conclusion was never reported in the past.

The variation of the impeller outlet flow is much larger than the one obtained from quasisteady calculations although the acoustic Strouhal number is only 0.22. The latter are applicable only in cases of very low Strouhal numbers, $Sr < 0.1$.

Strong circumferential variations of the outlet relative flow angle β_2 show that the assumption of constant outlet relative flow angle, used in many existed 1*D* models, is incorrect. Circumferential variations in β_2 at higher and lower mass flows were experimentally observed [14, 15]. Circumferential variations in the absolute tangential velocity at the impeller exit indicate slip factor variations during one rotation. Variations in the radial velocity show local mass flow variations.

The flow perturbation extends upstream of the impeller and creates significant variations of the flow at the leading edge region for both higher and lower than optimum mass flows.

When comparing the variations in flow quantities at leading edge, at R/R_2=1.10, as well as the blade relative Mach number distributions at lower and higher mass flows, one can see that the variations in the latter case are larger than in the former one, although the imposed static pressure distribution has the same amplitude for both cases. This means that static pressure distortions at higher mass flows have a larger effect on the impeller flow, than distortions at lower mass flows. Navier-Stokes computations reported in the literature [17] are time consuming and require large computational effort. They can provide valuable information if they are coupled with experimental data, fact that allows the correct tuning of the empirical coefficients included in the turbulence models.

References

[1] A. Whitfield, N.C. Baines. Design of Radial Turbomachines. Longman Group UK Limited; 1990.

[2] M. Sideris. Circumferential distortion of the flow in Centrifugal Compressors due to Outlet Volutes. PhD.Thesis, RUG-Von Karman Institute, 1988.

[3] H. Pfau, ‘‘Temperaturmessungen zur Stromungsuntersuchung, insbesondere an Radialverdichtern’’. Konstruktion, Heft 12, 1967, 478-484.

[4] J.A. Lorett, S. Gopalakrishnan, ‘‘Interaction in between Impeller and Volute of Pumps at off-design conditions’’. ASME Journal Fluids Engineering. Vol. 108, 1986.

[5] H. Uchida, M. Inayoshi, K. Sugiyama, ‘‘Effect of a Circumferential Static Pressure Distortion on Small-Sized Centrifugal Compressor Performance.’’ International Gas Turbine Congress held in Tokyo, Japan, 1987.

[6] R. Badie, J.B. Jonker, T.G. van Essen, ‘‘Calculations on the Time-Dependent Potential Flow in a Centrifugal Pump’’ ASME Paper 92-GT-151.International Gas Turbine and Aeroengine Congress and Exposition in Cologne, Germany, 1992.

[7] D. Croba. Modélisation de l’écoulement instationnaire dans les pompes centrifuges. Interaction roue-volute. PhD.Thesis, Institut National Polytechnique de Grenoble, 1992.

[8] A. Fatsis. Computation of the 3-Dimensional Unsteady Flow in a Centrifugal Impeller due to a downstream Static Pressure Circumferential Distortion. PhD.Thesis, RUG-Von Karman Institute, 1995

[9] A. Fatsis, ‘‘Three dimensional unsteady flow calculations in radial components”. von Karman Institute Lecture Series 1993-01 ‘Spacecraft Propulsion’, 1993

[10] M. Murakami, K. Kikuyama, E. Asakura, ‘‘Velocity and Pressure distributions in the impeller passages of Centrifugal Pumps’’, Journal of Fluids Engineering, Vol. 102, 1980, 420-426.

[11] K. Kikuyama, K. Minemura, Y. Hasegawa, E. Asakura, M. Murakami, ‘‘Unsteady pressure distributions on the impeller blades of a centrifugal pump-impeller operating off-design’’. ASME Paper No. 87-GT-144, 1987.

[12] N. Bulot and I. Tribinjac,“Impeller-diffuser interaction: analysis of the unsteady flow structures based on their direction of propagation”. Proceedings of the 8th International Symposium on Experimental and Computational Aerothermodynamics of Internal Flows Lyon, July 2007.

[13] K.U.Ziegler, H.E.Gallus, and R.Niehuis, “A Study on Impeller-Diffuser Interaction—Part I: Influence on the Performance”, ASME Journal of Turbomachinery Vol. 125, No. 1, 2003, 173-183.

[14] T. Meakhail and S. O. Park, “A Study of Impeller-Diffuser-Volute Interaction in a Centrifugal Fan“. ASME Journal of Turbomachinery, Vol.127, No. 1, 2005, 84-91.

[15] H.-P.Dickmann, T.S.Wimmel, J.Szwedowicz, D.Filsinger, and C.H.Roduner, “Unsteady Flow in a Turbocharger Centrifugal Compressor: Three-Dimensional Computational Fluid Dynamics Simulation and Numerical and Experimental Analysis of Impeller Blade Vibration”. J. Turbomachinery, Vol. 128, No. 3, 455-466.

[16] K. Majidi, “Numerical Study of Unsteady Flow in a Centrifugal Pump”. ASME Journal of Turbomachinery, Volume 127, No. 2, 2005, 363-372

[17] M Younsi, F Bakir, S Kouidri, R Rey, ‘‘Numerical and experimental study of unsteady flow in a centrifugal fan”. Proceedings of the Institution of Mechanical Engineers, Part A: Journal of Power and Energy, Vol. 221, No. 7, 2007, 1025-1036.

JJMIE

Volume 4, Number 5, November 2010
ISSN 1995-6665
Pages 567 - 578

Jordan Journal of Mechanical and Industrial Engineering

Application of the Analytic Hierarchy Process (AHP) in Multi-Criteria Analysis of the Selection of Cranes

Doraid Dalalah *, Faris AL-Oqla, Mohammed Hayajneh

Industrial Engineering Department, Faculty of Engineering, Jordan University of Science and Technology, P.O. Box 3030, Irbid, 22110, Jordan

Abstract

Due to the central role of cranes in construction operations, specialists in the construction industries have cooperated in the development of structured methods and software to help select the best crane type in construction sites. Crane selection is a time consuming process which needs extensive data exploitation. Moderately few systems have been developed to aid in selecting cranes and in setting their lifts. These systems although may have rich databases, they lack the support of knowledge based decision making. The process of crane selection is a multi-criteria decision-making problem with conflicting and diverse objectives. In this work, a systematic methodology is presented under the consideration of multiple factors and objectives that are witnessed to be crucial to the construction process. The model includes building an analytic hierarchy structure with a tree of hierarchical criteria and alternatives to ease the decision-making. Three alternative crane types were considered, namely, Tower, Derrick and Mobile cranes. An Analytical Hierarchy Process (AHP) was used to assist in building the model and help draw decisions. While deploying the crane selection objectives into layered sub-goals, conclusions could be drawn on the type to be used in construction according to knowledge based evaluation and assessment. Expert Choice™ software is used to conduct the experimental assessments. The judgments were found to be consistent, precise and justifiable with narrow marginal inconsistency values. The paper also presents a thorough sensitivity analysis to demonstrate the confidence in the drawn conclusions.

Keywords: Analytical Hierarchy Process, Multi-Criteria Decision-Making, Expert Choice, Cranes, Construction.

1. Introduction

Cranes are considered to be one of the most important equipment used in construction due to their key role in performing lifting tasks all over the construction site. The scale of investment in choosing a crane emphasizes the importance of the crane selection process. Thus, careful attention to such selection should be considered owing to the huge price that may be paid in case of mistakes, [1, 2, 19].

Numerous factors may be considered when thinking about the best crane to use in a construction site such as the factors that affect stability, capacity and the proper setup. Besides, the weights, the dimensions, the lift radii, the type of lifting to be done, serviceability of the equipment as well as the site conditions are considered to be crucial in the crane operation which may affect and complicate the judgment, [3, 18]. Practitioners recommend to have the capability of making all the crane lifts in their standard configuration. Customized configurations are not preferred due to the time required in the installation and narrowing the lifting margins.

Close attention should also be paid to the site review and the crane setup such as the job site conditions including the supporting surfaces, soil condition, access and stability (when transporting a crane), the working area as well as the assembly hazards that may entail lattice boom assembly, disassembly and leveling the crane.

Plenty of crane models are available in different shapes and sizes, though, they usually fall into three categories, [4]:

1. Derrick Cranes.
2. Mobile Cranes.
3. Tower Cranes.

* Corresponding author. doraid@just.edu.jo

Few studies exist on crane selection such problem as compared to its scale of use and importance. Most of these studies have been conducted using data-based systems in order to select the most appropriate crane for the construction. Few existing applications that use knowledge-based systems have been published, namely CRANES, LOCRANE, and SELECTCRANE. Gray and Little presented CRANES as a knowledge-based system designed to configure cranes according to the site conditions, [1]. It evaluates the least cost option to be selected through optimization techniques. The solution of CRANES is restricted to large buildings which require the coordination of more than one crane, [5].

Another knowledge based system called LOCRANE was developed to assist the construction planner in selecting and locating a crane for construction sites [5]. In LOCRANE, the system asks the user to input all the information related to the building geometry and the possible application for the proposed crane. After all the needed information is entered, the system outputs the most appropriate alternative from the set of the available cranes.

SELECTCRANE is another knowledge-based expert system which was developed to assist the contractor in selecting the type and then the configuration of the best cranes, [6]. The user provides the system with the expected weights, dimensions and lift radii of the heaviest loads, wind speed, the rental charges and other project information. That done, SELECTCRANE will then provide the user with the recommended type of cranes. Geometrical databases have been built to help in this task as well. Proposed by Moselhi et al. [7], interesting number of features have been entailed such as relational databases designed to store the cranes' geometry-related variables.

Fuzzy logic and neural based algorithms have been implemented to get solutions for such problem too, [4, 8]. In addition, some optimization techniques were studied to model such problem, [2]. However, most of these techniques rely on geometrical constraints related to the physical site conditions while disregarding the importance of the different factors comprehended previously.

Regarding the cane software, a number of computer systems have been developed for the crane selection process [3, 5, 9, 10]. Most of these systems depend on database driven systems with less intelligence in making the decision and selection. Recently, trends have been focused towards Multi Criteria Decision Making approaches (MCDM) such as the Analytical Hierarchy Process (AHP). AHP helps capture both subjective and objective assessment measures of the alternative options available, thus reducing bias in decision making. AHP was not used on the extent of carne selection, rather, the few studies that implemented the AHP were held to determine the most suitable equipment and material used in construction, [11, 12, 16, 17].

The paper is organized as follows: the subsequent section explains the analytical hierarchy process. Next in section 3, the AHP crane selection model is illustrated. Later in section 4, a sensitivity analysis is presented followed by the conclusions in sections 5.

2. Analytical Hierarchy Process (AHP)

In this work, AHP is used to find the most suitable crane in a construction process. AHP is a widely used multi-criteria decision making tool. Unlike the conventional methods, AHP uses pair-wise comparisons which allow verbal judgments and enhances the precision of the results. The pair-wise comparisons are used to derive accurate ratio and scale priorities. Developed by Thomas Saaty [13], AHP provides a proven, effective means to deal with complex decision making and can assist in identifying and weighing criteria, analyzing the data collected and expediting the decision-making process.

AHP helps capture both subjective and objective evaluation measures, providing a useful mechanism for checking the consistency of the evaluations thus reducing bias in decision making, [14]. When making complex decisions involving multiple criteria, the first step is to decompose the main goal into its constituent sub-goals or sometimes called objectives, progressing from the general to the specific. In its simplest form, this structure comprises a goal, criteria or objective and alternative level. Each set of criteria would then be further divided into an appropriate level of detail, recognizing that the more criteria included, the less important each individual criterion may become as illustrated Fig. 1.

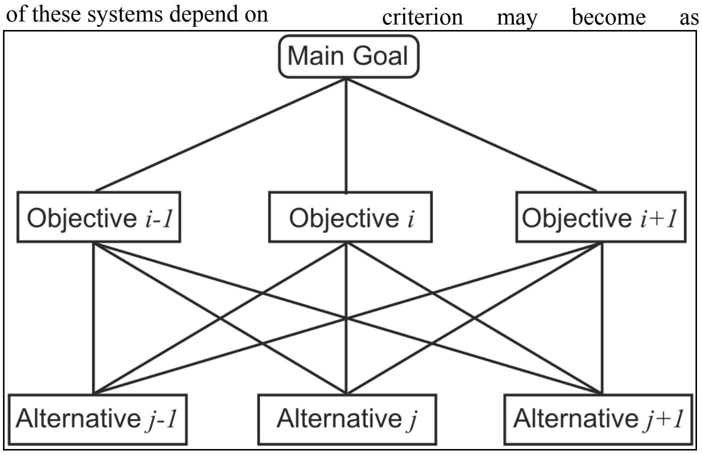

Fig. 1: AHP hierarchy of goals, objectives and alternatives.

Generally, the main goal is laid on the top hierarchy while the decision alternatives are at the bottom. Between the top and bottom levels reside the relevant attributes of the decision problem such as the selection criteria and objectives. Next, relative weights to each item in the corresponding level are assigned. Each criterion has a local (immediate) and global priority. The sum of all the criteria beneath a given parent criterion in each layer of the model must equal one. The global priority shows alternatives relative importance within the overall model.

After the criteria factors are identified, scoring of each level with respect to its parent is carried out using a relative relational basis by comparing one choice to another. Relative scores for each choice are computed within each leaf of the hierarchy. Scores are then synthesized through the model, yielding a composite score for each choice at every layer, as well as an overall score.

This relative scoring within each level will result in a matrix of scores, say $a(i, j)$. The matrix holds the expert judgment of the pair-wise comparisons. However, the judgment should be consistent. Therefore, inconsistency test is required to validate the expert knowledge. The inconsistency measure is useful for identifying possible errors in judgments data entry as well as actual inconsistencies in the judgments themselves.

Inconsistency measures the logical inconsistency of the expert judgments. For example, if we were to say that "*A*" is more important than "*B*" and "*B*" is more important than "*C*" and then say that "*C*" is more important than "*A*" we are not being consistent. A somewhat less inconsistent situation would arise if we would say that "*A*" is 3 times more important than "*B*", "*B*" is 2 times more important than "*C*", and that "*C*" is 8 times more important than "*A*".

In general, the inconsistency ratio should be less than 0.1 or so to be considered reasonably consistent. Particularly, a matrix $a(i, j)$ is said to be consistent if all its elements follow the transitivity and reciprocity rules below:

$$a_{i,j} = a_{i,k} \cdot a_{k,j} \tag{1}$$

$$a_{i,j} = \frac{1}{a_{j,i}} \tag{2}$$

Where i, j and k are any alternatives of the matrix, [14]. For instance if you feel that "A" is 3 times more important than "B", then "B" should be 1/3 times more important than "A". The relational scale used in ranking is presented in Table 1.

Table 1: AHP importance scale, [14].

For any pair of objectives *i, j*:

Score	**Relative importance**
1	Objectives *i* and j are of equal importance.
3	Objective i is weakly more important than j.
5	Objective i is strongly more important than j.
7	Objective i is very strongly more important than j.
9	Objective i is absolutely more important than j.

Note: 2, 4, 6, 8 are intermediate values.

The pair-wise comparison matrices can also be represented as:

$$A = \begin{bmatrix} a_{11} & \cdots & a_{1n} \\ \vdots & \vdots & \vdots \\ a_{n1} & \cdots & a_{nn} \end{bmatrix} = \begin{bmatrix} w_1/w_1 & \cdots & w_1/w_n \\ \vdots & \vdots & \vdots \\ w_n/w_1 & \cdots & w_n/w_n \end{bmatrix} \tag{3}$$

For a consistent matrix, we can demonstrate that:

$$A = \begin{bmatrix} w_1/w_1 & \cdots & w_1/w_n \\ \vdots & \vdots & \vdots \\ w_n/w_1 & \cdots & w_n/w_n \end{bmatrix} \times \begin{bmatrix} w_1 \\ \vdots \\ w_n \end{bmatrix} = n \begin{bmatrix} w_1 \\ \vdots \\ w_n \end{bmatrix} \tag{4}$$

Or in a matrix form:

$$A \cdot w = nw \tag{5}$$

where **A** is the comparison matrix , **w** is the eigenvector and n is the dimension of the matrix. The equation above can be treated as an eigenvalue problem. For a slightly inconsistent matrix, the eigenvalue and the eigenvector are only slightly modified [15]. Proved in [13], Saaty demonstrated that for consistent reciprocal matrix, the largest eigenvalue is equal to the number of comparisons, or $\lambda_{max} = n$. Then he gave a measure of consistency, called Consistency Index as a deviation or a degree of consistency using the following formula:

$$CI = \frac{\lambda_{\max} - n}{n - 1} \tag{6}$$

Knowing the Consistency Index, the next question is how do we use this index? Again, the research in [13, 14] proposed to use the index by comparing it with the appropriate random consistency index through picking randomly generated reciprocal matrix using the scale: 1/9, 1/8, …,1, …, 8, 9 and then get the random Consistency Index. The Average Random Consistency Index of a sample size of 500 matrices is shown in the table below:

Table 2: Random index (RI) for the factors used in the decision making process.

n	1	2	3	4	5	6	7	8	9	10	11	12
RI	0	0	0.58	0.9	1.12	1.24	1.32	1.41	1.45	1.49	1.51	1.58

Proposed by [13], a Consistency Ratio is a comparison between Consistency Index and Random Consistency Index, or in formula:

$$CR = \frac{CI}{RI} \tag{7}$$

If the value of Consistency Ratio is smaller or equal to 10%, the inconsistency is acceptable. Alternately, if the Consistency Ratio is greater than 10%, the subjective judgment should be revised.

3. 3. Analytic Hierarchy Process Based Crane Selection Model

Crane selection is a time consuming process that requires extensive data management. Most of the present systems even might have good database, they are deficient in the support of an expert knowledge based decision making. Comprehensive database provides information about crane configurations, their lift capacity settings, and rigging equipment. Yet, the selection task stays vulnerable with the lack of some intellect in the process. Although crane manufacturers provide data for their cranes, the data is not always consistent and do not follow a standard format. This creates frequent problems for crane users, predominantly when interpolation of loads is carried out through load charts. Upon facing such problem, the users are to make decisions based on job conditions and categories of cranes which may lead to costly mistakes. Early planning in such investment is important. Supported by keen decision making, money and effort can be saved. In this paper, a rational approach is presented which can extract the expert knowledge to be modeled qualitatively to help find the best crane considering multiple criteria factors.

Tabular knowledge-based format of cranes is widely available. Plenty of database systems that hold detailed information about cranes are available. Though, the manipulation of such massive data is not trivial. AHP has proved its performance in converting qualitative measures to quantitative numerics that can help draw a conclusion or make a decision. A knowledge based data for crane selection was provided by [6]. The data in general considers the weights, dimensions, the type of lifting to be done, serviceability of the equipment, the site conditions, supporting surfaces, access and stability, working area and others.

Table 3 presents the different factors that affect the selection of a crane, [4]. For example, the site condition criterion includes the following sub-items:

- Soil stability and ground conditions
- Access road requirement and site accessibility.
- Operating clearance.

Table 3: Types of cranes and the factors affecting their selection, [4].

Factors	Mobile Cranes	Tower Cranes	Derrick Cranes
1. Building Design • Building Height	Adequate for all types of structures (up to 107 m)	Preferable for high-rise (over 107 m).	Preferable for high-rise and apartment buildings
• Project Duration	Used for shorter projects duration (less than 4 months).	Used when crane requirement is for long term m a specific.	Can be used for both long term and short term projects.
2. Capability • Power Supply	Usually powered by diesel engines.	Usually electrically powered (requires power supply)	Usually powered by diesel engines.
• Load lifting frequency.	Used when lift frequency is sporadic.	Preferred when lift frequency is high	Used if lift frequency is not a major consideration or no other viable alternative crane type exists
• Operators Visibility	Usually not good and fair for smaller units.	Better	Depends on the location.
3. Economy • Cost of move in, setup, and move out	Not expensive.	Expensive to set up because it requires a foundation and possibly bracing to the structure being erected	Cheaper than mobile and tower cranes.
• Cost for rent	Usually cheaper if required for projects of short duration (less than 4 months)	Usually costs less for the long term duration (Greater than 4 months).	Cheaper to rent and cheaper to buy.
• Productivity	Not very productive.	Much more productive than mobile units.	Least productive
4. Safety • Initial Planning and Engineering	Details are not very much needed, only job site has to be examined for adequate crane maneuverability.	Extensive planning is needed to provide the crane with appropriate foundation.	Not very detailed
• Safety	Not considered to be very safe due to lack of safety devices or limited switches to prevent overloading.	Considered to be very safe due to the presence of limit switches.	Not considered to be safe
5. Site Conditions • Soil Stability and Ground Conditions	Can operate in muddy terrain but requires good ground conditions.	Can operate where ground conditions are poor.	Used when a ground condition does not allow the use of mobile or tower crane.
• Access road requirement and site accessibility.	Requires access to and from lifting position.	Preferred when poor accessibility prevails since tower cranes are brought to site disassembled.	Minimum site accessibility and access road conditions are adequate since derricks are always dismantled into smaller units for transit
• Operating Clearance	Needs adequate operating clearance.	Used when site is constricted or congested.	Used when clearance is Inadequate for the other units and sufficient space is unavailable for the erection of a tower foundation or base

The main goal of the presented hierarchical model is to select the best crane that will serve the construction process in a fairly optimized manner. This is performed through matching the effect of the tree of sub-goals according to their weights of importance. The following criteria items are to be considered:

- Building Design
- Capability
- Economy
- Safety
- Site condition.

Three alternative cranes are selected for this study, namely: Tower, Derrick, and Mobile cranes. Fig. 2 shows the developed hierarchical structure of the problem in which the first level has the goal of selecting the optimal crane type. The second level consists of five criteria, under which there are further sub-criteria. The last level of the hierarchy comprises of the three alternatives of the available crane types.

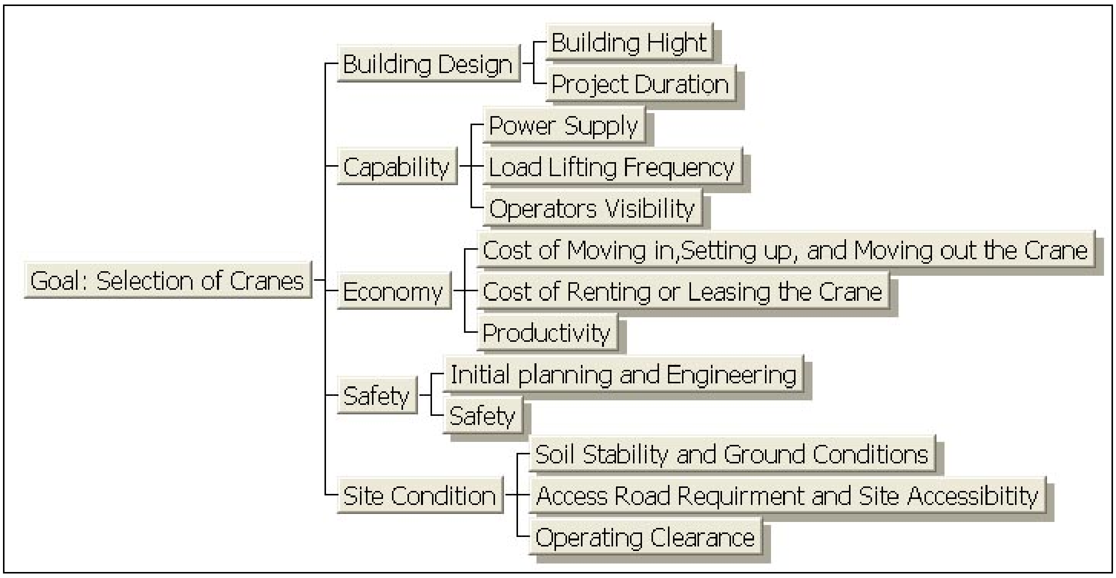

Fig. 2: AHP crane selection hierarchy.

As explained earlier, a set of pair-wise comparison matrices are developed for all of the levels of the hierarchy. An element in the higher level is assumed to be the governing element for those in the lower level of the hierarchy. The elements in the lower level are compared with respect to each other according to their effect on the governing element above. This yields a square matrix of judgments. The pair-wise comparison is performed on the basis of how an element dominates the other and the judgments are entered using Saaty's 1–9 scale. An element compared with itself is always assigned the value of "1", so the main diagonal entries of the pair-wise comparison matrix are all "1".

The expert (designer) begins by comparing pairs of main criteria (factors) with respect to the main goal by assigning importance. There will be $n(n-1)/2$ comparisons. Expert Choice™ software package was used to carry out such comparison. Verbal assessment is used to help the expert understand and summarize his knowledge efficiently. For instance, considering the capability factor in Fig. 2 under which $n = 3$, three questions need to be answered by the expert. Typical question forms of this level may be put across as follows:

- How more important is the Power Supply relative to Load Lifting Frequency from the capability standpoint.
- How more important is the Power Supply relative to Operators Visibility from the capability stand point.
- How more important is the Load Lifting Frequency relative to Operators Visibility from the standpoint of capability.

A scale of verbal assessments is used to answer the above survey, namely: Extreme, Very strong, Strong, Moderate and Equal importance along with their corresponding reciprocal scale of importance. Table 4 presents the surveyed numbers for the above factor and its siblings.

Table 4: Pair-wise comparison matrix for different criteria.

Criterion	power supply	Load lifting frequency	Operators visibility
power supply	1	4	5
Load lifting frequency	1/4	1	3
Operators visibility	1/5	1/3	1

Note that the three questions above are essentially enough to fill the above matrix as a result of the transitivity and reciprocity rules stated in equations 1 and 2. Now if the columns of the above table are normalized and the resulting rows are averaged we get the corresponding weights of each factor as illustrated below:

$$\begin{pmatrix} 0.69 & 0.75 & 0.56 \\ 0.17 & 0.19 & 0.33 \\ 0.14 & 0.06 & 0.11 \end{pmatrix}$$

Hence, the row averages are $(0.67 \quad 0.23 \quad 0.10)^T$. Note that the same weights were found using Expert Choice as shown in Fig. (3). The largest eigenvalue λ_{max} of the matrix in Table 4 = 3.0858. The random consistency index of a 3-factor matrix = 0.58 as provided in Table 2, and therefore, the calculated *CI* is equal to 0.075 ≈0.08. The same result is found using the software package as demonstrated for this particular criterion in Fig. 3. Clearly, as stated before, a *CI* ratio that is less than 10% is acceptable and the judgments are said to be consistent.

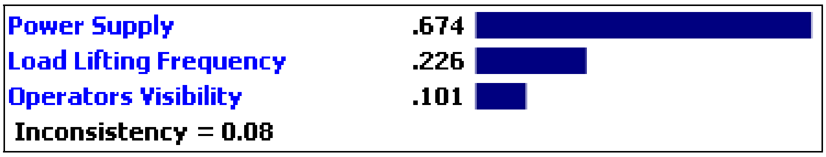

Fig. 3: The contribution of sub-criteria to the main criterion (the capability).

Likewise, the main goal level is presented in Table 5. Here, the maximum eigenvalue is 5.3038 which results in a *CI* value of ≈0.09. The ratio is still acceptable and the judgments are undoubtedly consistent.

Table 5: Pair-wise comparison between main criteria.

	Building Design	Capability	Economy	Safety	Site Condition
Building Design	1	4	2	1/4	1/2
Capability	1/4	1	2	1/4	1/4
Economy	1/2	1/2	1	1/4	1/3
Safety	4	4	4	1	4
Site Condition	2	4	3	1/4	1

Fig. 4 presents the ratio of each criterion, where safety is evidently the most important factor in the presented case study with a total aggregate weight of 0.476. Conversely, the economy factor is shown to be the least important carrying a weight of 0.070.

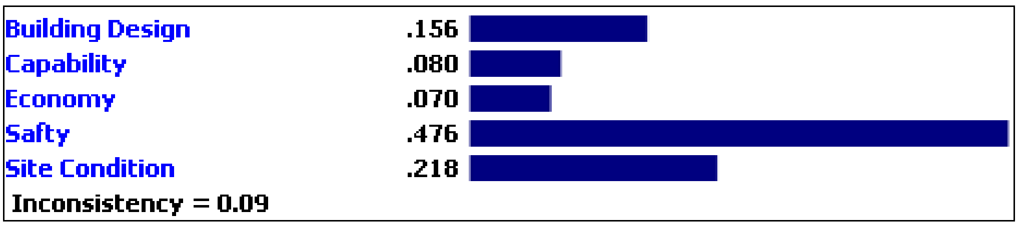

Fig. 4: Resulting contribution of main criteria to main goal.

4. Model Sensitivity Analysis:

Finally, a sensitivity analysis is held to show the effect of altering different parameters of the model on the choice of the right crane. First, the current values of the model are presented according to the pair-wise comparison that has been carried out by the experts in the construction fields. Fig. 5 demonstrates the current weights of each factor. Obviously, the results are in favor of the Tower Cranes. Now that the best crane type has been identified, how would the model respond to any changes in the weights of the listed factors?

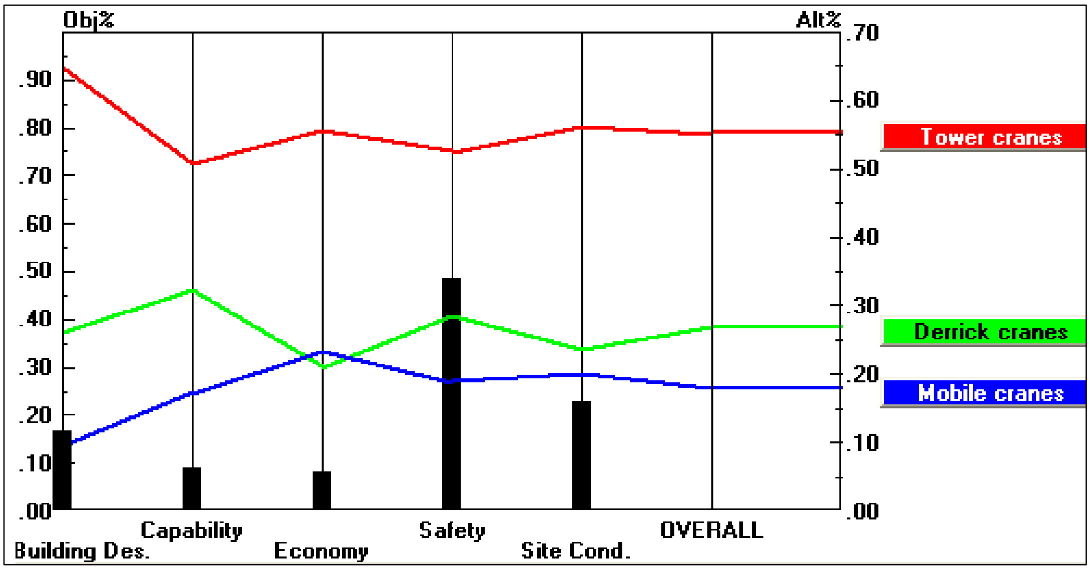

Fig. 5: The sensitivity graph of the main factors with respect to the main goal.

First, consider the building design. By increasing the share of this factor to an extreme of 90% of the main goal, leaving 10% for the others while keeping the proportionality between each, it has been noticed that the model is still in favor of The tower cranes with a score of 63.6%, followed by the Derrick and lastly the Mobile cranes. The same conclusion can be drawn for the capability factor, where the tower cranes stay as the best choice with a score of 51.1%, Fig. 6 and 7.

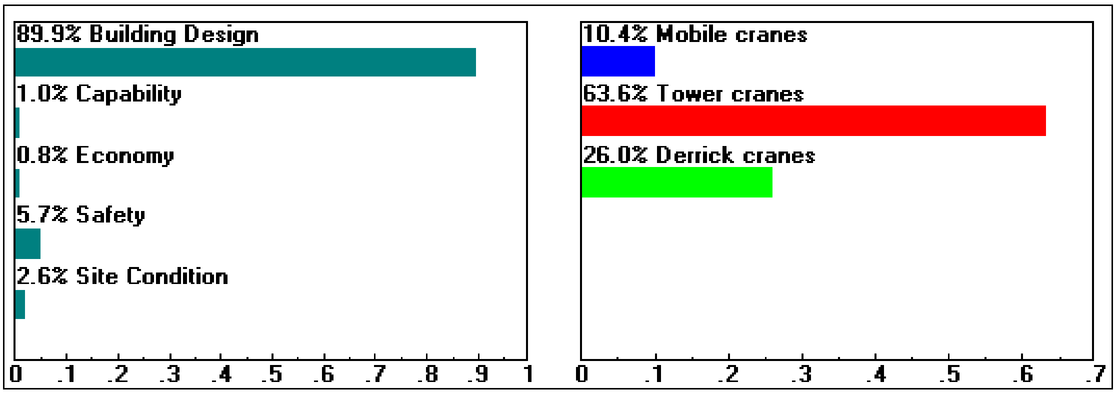

Fig. 6: Sensitivity analysis of the building design factor, the new assigned weights (left) and the resulting scores of the alternatives (right).

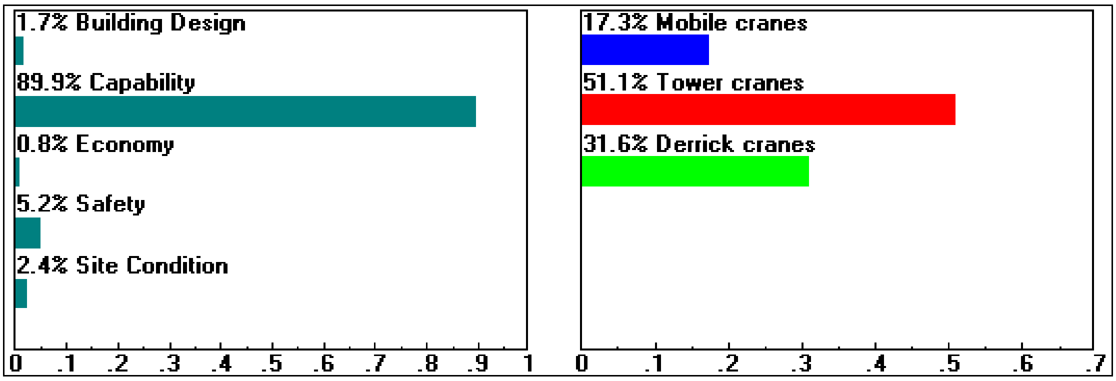

Fig. 7: Sensitivity analysis of the capability factor, the new assigned weights (left) and the resulting scores of the alternatives (right).

The sensitivity analysis of the economy factor still demonstrates the tower cranes as the best scorers (55.6%), however, as more weight is assigned, the mobile cranes will tend to have advanced rank among the others, Fig. 8. The result is fairly reasonable since the installation cost in mobile cranes is significantly less than the other candidates.

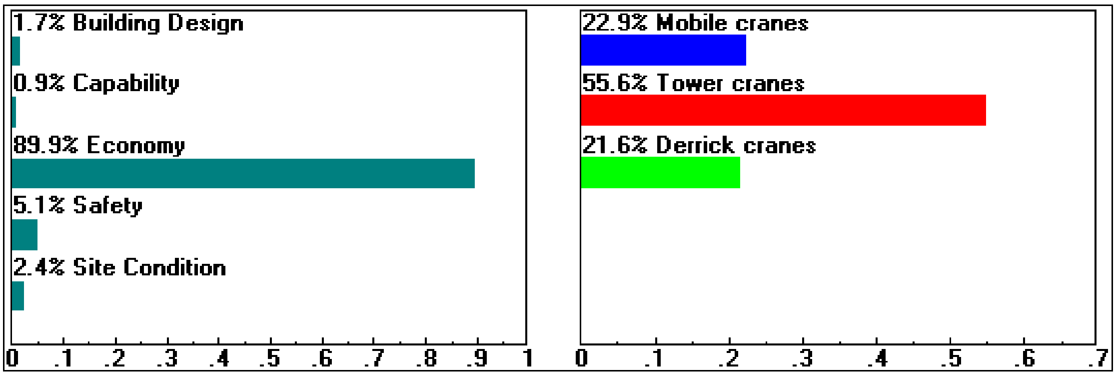

Fig. 8: Sensitivity analysis of the economy factor, the new assigned weights (left) and the resulting scores of the alternatives (right).

Similar analysis is held for the safety and site condition. The results show that the tower cranes are always in the lead with a persistent score beyond 50%, followed by the Derrick and lastly the Mobile type. Even at almost equal weights in Fig. 9, still, the Tower cranes will score higher than 50% leaving the Derrick and Mobile cranes in the second and third ranks respectively.

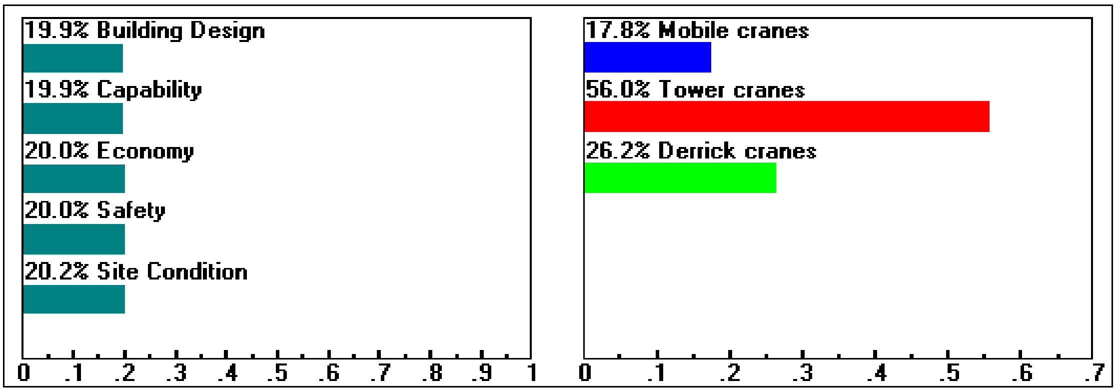

Fig. 9: Sensitivity analysis with equal weight for all factors. The new assigned weights (left) and the resulting scores of the alternatives (right).

The sensitivity analysis presented here demonstrates how consistent the decision is. The choice of the crane remain the same even with significant changes on the criteria weights, which can be justified by the consistent judgments made between the siblings of the parent goal and the pair-wise comparisons. Frankly, AHP analysis demonstrates an efficient knowledge based approach to help quantify experts' knowledge to qualitative analysis that help in multi-criteria decision making.

The best crane choice in this case study was the Tower crane. Fig. 10 presents the scores of each crane with a corresponding inconsistency of 0.07. Tower cranes are known for their safety from the practitioners' perspectives. Notice that in Table 5 the safety has been assigned higher importance relative to the other factors where the safety contributes for 80% of its parent criterion whereas the initial planning and engineering is only 20%.

Fig. 10: Final ranking of alternatives.

Finally, a complete hierarchy of goals and objectives with the corresponding aggregate weights is shown in Fig. 11. Once again, the safety factor contributes for the most weight in the hierarchy.

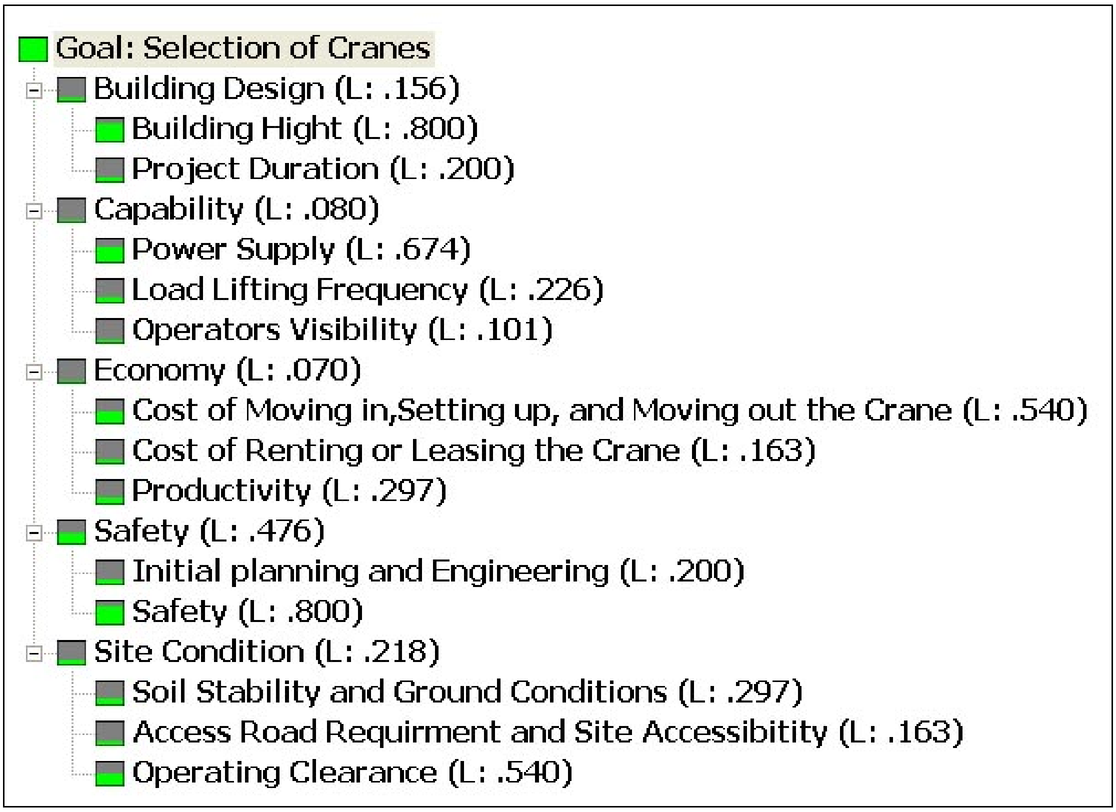

Fig. 11: Importance of each criterion with respect to the main goal and parents.

5. Conclusion

It was observed that the developed analytic hierarchy process (AHP) expert model works adequately and yields acceptable results as well as dragging accurate decisions in crane selection for a construction site. It was made clear from the output of Expert Choice™ for each of the crane types, that most of the area of the AHP priority stack is occupied by safety and site condition criteria, thus, showing the desired dominance of these two criteria in the selection process. The developed model certainly eases the decision maker's mission of choosing the quantitative weights and making further calculations and, thereby, leaves the decision makers less susceptible to human errors. Moreover, this approach does not require the decision makers to have any in-depth technological knowledge regarding the available specification of crane types and their capabilities.

The pair-wise assessment through the verbal scaling made it easy for the expert to disseminate his/her comprehension and eventually reveal more representing knowledge and decisions. The above application of AHP theory is a step toward the elimination of bias or prejudice in the judgment of an expert, since the steps leading to the judgment are made explicit via relational assessment. This also helps uncover any gap in the expert's thinking in regard to qualitative factors in crane selection which may not have been considered.

References

[1] Gray, C. and Little, J., A systematic approach to the selection of an appropriate crane for a construction site, Construction Management and Economics, Vol. 3, 121–144, 1985.

[2] Mohamed Al-Hussein, Sabah Alkass and Osama Moselhi, Optimization algorithm for selection and on site location of mobile cranes, Journal of Construction Engineering and Management, Vol. 131, No. 5, 579-590, 2005.

[3] Zhang, P., Harris, F.C., Olomolaiye, P.O. and Holt, G.D., Location optimization for a group of tower cranes, Journal of Construction Engineering and Management, , Vol.125, No.2, 115-122. 1999.

[4] Awad S. Hannaa, Wafik B. and Lotfallah B., A fuzzy logic approaches to the selection of cranes, Automation in Construction, Vol. 8, No. 5 , 597–608, 1999.

[5] Warszawski, A., Expert systems for crane selection. Construction Management and Economics, Vol. 8, 179–190, 1990.

[6] Hanna,A.S., Selectcrane: An Expert System for Optimum Crane Selection, Proc.1st Congress on Computing in Civil Engineering, Washington, DC, 958–963. 1994.

[7] Osama Moselhi Sabah Alkassand Mohamed Al-Hussein. "Innovative3D-modelling for selecting and locating mobile cranes", Engineering, Construction and Architectural Management, Vol. 11, No. 5, 373–380. 2004

[8] Anil Sawhney and André Mund, Adaptive Probabilistic Neural Network-based Crane Type Selection System" J. Constr. Engrg. and Mgmt., Vol. 128, No.3, 265-273, 2002.

[9] Al-Hussein, M., Alkass, S. and Moselhi, O., An algorithm for mobile crane selection and location on construction site, Construction Innovation Journal, Vol.1, 92-105, 2001.

[10] Al-Hussein, M., Alkass, S. and Moselhi, O., 3D animation for planning cranes operation, Proceeding of the 16th International Symposium on Automation and Robotics in Construction (ISARC), Spain, 151-156, 1999.

[11] Aviad Shapira, M.ASCE and Marat Goldenberg, "AHP-Based Equipment Selection Model for Construction Projects", Journal of Construction Engineering and Management, Vol. 131, No. 12, 1263-1273, 2005.

[12] Fikri Dweiri and Faris M. Al-Oqla, Material selection using analytical hierarchy process, Int. J. Computer Applications in Technology, Vol. 26, No. 4, 2006.

[13] Saaty, T.L. The Analytical Hierarchy Process, McGraw-Hill, New York, 1980.

[14] Ishizaka Alessio and Lusti Markus, An Intelligent Tutoring System for AHP, Proceedings of the 9th International Conference on Operational Research KOI 2002, Trogir, 215-223, 2003.

[15] Saaty, T. L., Decision-making with the AHP: Why is the Principal Eigenvector necessary? In: Klaus Dellmann (Ed.), Proceedings of the Sixth International Symposium on the Analytic Hierarchy Process, ISAHP 2001, 383-396, Bern, 2001.

[16] Mohammad H. Vahidnia, Ali A. Alesheikha and Abbas Ali Mohammadia. Hospital site selection using fuzzy AHP and its derivatives, Journal of Environmental Management. Vol. 90, Issue 10, 3048-3056, 2009.

[17] Tsung-Han Chang, Tien-Chin Wang. Using the fuzzy multi-criteria decision making approach for measuring the possibility of successful knowledge management. International Journal of Information Sciences, Vol. 179, Issue 4, 355-370, 2009.

[18] Sandip D. Shinde. Standardization of Jib Crane Design by "F.E.M.Rules" and Parametric Modeling, International Journal of Recent Trends in Engineering, Vol. 1, No. 5, 2009.

[19] Cheng Zhang, Amin Hammada and Homam Albahnassi. Path Re-Planning of Cranes Using Real-Time Location System. Automation and Robotics applications - 26th INternational Symposium on Automation and Robotics in Construction (ISARC2-09), 412-420, 2009.

JJMIE

Volume 4, Number 5, November 2010
ISSN 1995-6665
Pages 579 - 590

Jordan Journal of Mechanical and Industrial Engineering

Reduction of Wastages in Motor Manufacturing Industry

S. P. Vendan [*], K. Sakthidhasan

Department of Mechanical Engineering ,P.S.G College of Technology Coimbatore, India.

Abstract

Lean manufacturing appears to hold considerable promise for addressing a range of simultaneous, competitive demands including high levels of process and product quality, low cost and reductions in lead times. This research addresses the application of lean manufacturing concepts to the continuous production sector with a focus on the motor manufacturing industry. The goal of this research is to investigate how lean manufacturing tools can be adapted from the discrete to the continuous manufacturing environment. This paper presents lean manufacturing as a leading manufacturing paradigm applied in many sectors. The fundamental focus on lean production is the systematic elimination of non-value added activity and waste from the production process. The implementation of lean principles and methods results in improved system and surrounding performance. Value stream mapping is used to first map the current state used to identify sources of waste and to identify lean tools to eliminate this waste. The future state map is then developed for a system with lean tools applied to it. To quantify the benefits gained from using lean tools and techniques in the value stream mapping, a detailed simulation model is developed and a designed experiment is used to analyze the outputs of the simulation model for different lean configurations. This paper demonstrates the implementation of lean philosophy through layout modification.

Keywords: Lean manufacturing, layout, value stream mapping, witness, VIPPLANOUT, Bottleneck.

1. Introduction

Lean is a popular fact that JIT system started in the initial years after the World War II in Japan for the Toyota automobile system. Toyoda family in Japan decided to change their automatic loom manufacturing business to the automobile business. But they had few problems to overcome. They could not compete with the giants like Ford in the foreign markets. Therefore Toyota had to depend upon the small local markets. They also had to bring down the raw materials from outside. Also they had to produce in small batches. They haven't had much of capital to work with. Therefore capital was very important. With these constrains Taiichi Ohno took over the challenge of achieving the impossible. With his right hand man Sheigo Shingo for next three decades he built the Toyota production system or the Just In Time system.

Long production runs, big backlogs and long lead times are fast becoming operating styles of the past. Flexibility and quick response must become the norm. The driving force behind this need is customers who increasingly expect short lead times for products configured exactly as specified and delivered on time, every time. The trend of quick-response, no-excuses delivery has put many manufacturers in the uncomfortable position of having to conform or lose business to a competitor who has developed short cycle time capabilities. To meet competitive requirements and reduce costs, many manufacturers are turning to lean manufacturing techniques to drastically cut cycle time and increase their competitive edge.

Lean operating principles began in manufacturing environments and are known by a variety of synonyms; Lean Manufacturing, Lean Production, Toyota Production System, etc. It is commonly believed that Lean started in Japan (Toyota, specifically), but Henry Ford had been using parts of Lean as early as 1920's, as evidenced by the following quote: "One of the most noteworthy accomplishments in keeping the price of Ford products low is the gradual shortening of the production cycle. The longer an article is in the process of manufacture and the more it is moved about, the greater is its ultimate cost." [1].

In order to set the groundwork for this paper, let's begin with the definition of Lean, as developed by the National Institute of Standards and Technology Manufacturing Extension Partnership's Lean Network. A systematic approach of identifying and eliminating waste through continuous improvement, flow the product at the pull of the customer in pursuit

* Corresponding author. spvendann@yahoo.com

of perfection. Keeping in mind that Lean applies to the entire organization. Although individual components or building blocks of Lean may be tactical and narrowly focused, and achieve maximum effectiveness by using them together and applying them cross-functionally through the system.

In its most basic form, lean manufacturing is the systematic elimination of waste from all aspects of an organization's operations, where waste is viewed as any use or loss of resources that does not lead directly to creating the product or service a customer wants when they want it. In many industrial processes, such non-value added activity can comprise more than 90 percent of a factory's total activity. The objective is to make the production flow through the system quicker and in more predictable manner. Some of the activities to improve the production environment are discussed below. The intent is to eliminate waste thereby permitting better wages for workers, higher profit for owners and better quality for customer. Types of wastes, effects of waste, using lean tools as explain to the following table 1.Value stream mapping is a set of methods to visually display the flow of materials and information through the production process. The objective of value stream mapping is to identify value-added activities and non value-added activities.

Value stream maps should reflect what actually happens rather than what is supposed to happen so that opportunities for improvement can be identified. Value Stream Mapping is often used in process cycle-time improvement projects since it demonstrates exactly how a process operates with detailed timing of step-by-step activities. It is also used for process analysis and improvement by identifying and eliminating time spent on non value-added activities.

Lean Manufacturing is a buzzword. More often it is used with the terms like benefits, cost reduction, lead-time reduction etc. but if you have not started implementing lean manufacturing yet and if you have not started benefiting from lean manufacturing yet, you will need some numbers to be motivated. We shall look into some quantified benefits of lean manufacturing where the principles of lean are implemented successfully.

2. Background

2.1. Lean Manufacturing Implementation

Lean philosophy implementation in a forging company: implementing lean manufacturing in forging industry and the methodology of implementation of lean tools. Due to increased customer expectations and fierce global competition, the Indian forging industries are desperately trying to improve productivity at lower cost and still retain excellent product and service quality. In this paper, the effectiveness of lean principles is substantiated in a systematic manner with the help of various tools, such as value stream maps, Taguchi's method of parameter design [2].

The development of a survey instruments to assess the implementation of lean practices within an organization. The results of a literature review, which was used to identify lean manufacturing practices and existing lean assessment tools, are presented. The findings of this review were synthesized to develop an instrument to assess both the number and the level of implementation of a broad range of lean practices in an organization. As part of a larger research project, an exploratory study was completed using the survey. A cross section of electronic manufacturers in the Pacific Northwest was used for the exploratory study. Analysis of the survey results from the exploratory study are summarized in this paper to illustrate how the survey can be used to understand what factors might contribute to the implementation of lean practices [3]. In the exploratory study completed, it was found that while electronic manufacturers have implemented a broad range of lean practices, the level of implementation does vary and may be related to economic, operational, or organizational factors [4].

The concepts of lean manufacturing can be successfully transferred from the manufacture of cars and electrical goods to software development. The key lean concept is to minimize work in progress, so quickly forcing any production problems to get sequence solution. Production is then halted to allow each problem with the system producing the goods, to be permanently corrected. While frustrating at first, the end result is very high levels of productivity and quality. Lean software development indicates that software quality problems are often the result of deeply embedded organizational habits of recruitment, retention and motivation. To obtain organizational change there is a need for fast results from low cost actions. Change requires motivation, which is triggered and sustained by results. The lean technique has demonstrated that it can go right to the core of the problems of motivation, quality assurance and staff evaluation [5].

Lean manufacturing appears to hold considerable promise for addressing a range of simultaneous, competitive demands including high levels of process and product quality, low cost and reductions in lead times. These requirements have been recognized within the aerospace sector and efforts are now well established to implement Lean practices. Lean manufacturing was initiated within the automotive sector. A Lean implementation case comparison examines how difficulties that arise may have more to do with individual plant context and management than with sector specific factors [6].

This session discusses lean implementation and challenges faced while implementing lean in various environments. The lean implementation in forging company, aerospace sector, electronics manufacturers and software development are discussed.

2.2. Design of Lean tool

Traditional costing systems consider the accumulation of costs, but not their timing. Value stream mapping presents a good picture of the time consumed and operations performed for the production of a product within a manufacturing facility, but it does not track the accumulation of costs. The cost–time profile (CTP) is a tool that follows the accumulation of cost in the manufacturing of a product through time; and it finds the cost–time investment (CTI), which is an indicator of the use of resources in the manufacturing of a product through quantities and timing. In this paper, the expected impact of Lean implementations on the CTP and CTI is discussed. The CTP is proposed as a useful tool for the evaluation of the improvements achieved by the implementation of Lean tools and techniques [7].

The value stream analysis was carried out by breaking down each step into a series of activities, the time taken for each activity was recorded, and each activity was given a designation to indicate whether it added value. Value-add activities were designated as operation, while non-value add activities were categorized as 'delay' (including queuing and rework), 'transport' (of material or information) or 'inspection'. Supporting information was also collected, such as numbers of people involved, any discussion required, use of equipment and systems, and problems encountered. This analysis enabled improvement opportunities specific to each process area to be identified.

Lean manufacturing appears to hold considerable promise for addressing a range of simultaneous, competitive demands including high levels of process and product quality, low cost and reductions in lead times. These requirements have been recognized within the aerospace sector and efforts are now well established to implement Lean practices. Lean manufacturing was initiated within the automotive sector. However, since the publication of the influential book, The Machine That Changed the World [8], there has been a range of documented cases of Lean implementation in a variety of sectors. Despite this evidence, the perception remains that Lean manufacturing is to some degree, an 'automotive idea' and difficult to transfer to other sectors especially when there are major differences between them. In this paper we discuss the key drivers for Lean in aerospace and examine the assumption that cross- sector transfer may be difficult. A Lean implementation case comparison examines how difficulties that arise may have more to do with individual plant context and management than with sector specific factors [9].

These papers investigate the importance of the resource cost of resource usage with the time line in value stream mapping. This paper discusses the traditional costing system for calculate the resource usage. The paper motivates me to analyze further feasible design alternatives.

2.3. Summary of Literature Survey

Lean manufacturing has served the manufacturing sector with speed and quality. Those papers investigate the existing scenario of the lean philosophy in various sectors. The paper also reveals the challenges faced while implementing in the diverse environment. During the course of literature survey, there is scope for applying lean tools in any industry.

3. Objective

Objective of our project is to demonstrate systematically how lean manufacturing tools used appropriately so that industry can eliminate waste. Hence better inventory control, better product quality, and better overall financial and operational procedure can be achieved. To study of opportunities for continuous improvement (KAIZEN) and Conducting VE study for cost reduction in assembly line. From the figure.1 is to explain the Objective of lean implementation

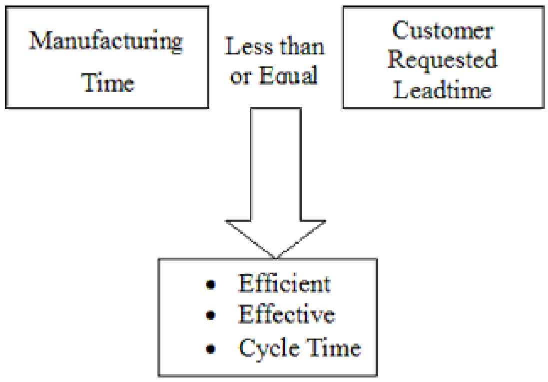

Figure 1 Objective Flowchart

4. Methodology

Getting started with an effective program to implement lean manufacturing requires careful planning, design and execution of the business changes needed to achieve the desired improvement goals. Implementation should not begin unless top management is solidly championing the effort with an understanding that many business processes must be changed. Starting with a pilot product line or another contained area of the business is a big help to "proof" your concept and methodology.

Organize and plan for Lean manufacturing with executive champion.

- Conduct extensive education
- Value stream map administrative, engineering and production processes
- Develop concept for lean manufacturing pilot
- Establish improvement targets
- Develop time-phased implementation Plan
- Present lean manufacturing pilot concept and plan to management
- Obtain management approval and commitment

- Train all employees involved in pilot
- Implement pilot

The implementation of lean concept is step by step process. Implementation steps are explained in the flowchart as shown in the Figure 2.Current state process of assembly layout in a motor manufacturing company is analyzed and current state value stream mapping is plotted (drawn). With the help of VSM bottle neck operations at machines and the nature of wastes (transportation time, distance, and work in process) are identified using calculations. Wastage type is identified and evaluated. A new layout model is developed using VIP plan out.

4.1. Selection of Critical Shop Floor

The first step in this methodology is selection of the critical Shop floor. All the production environments were studied. Assembly shop was reflecting the most number of defects and was not meeting the customer demands. So the assembly shop floor was selected as the critical shop floor.

5. Value stream mapping

A manufacturing system operates with timing of step-by step activities. The various steps in implementation of VSM are shown in Figure 3 and are discussed

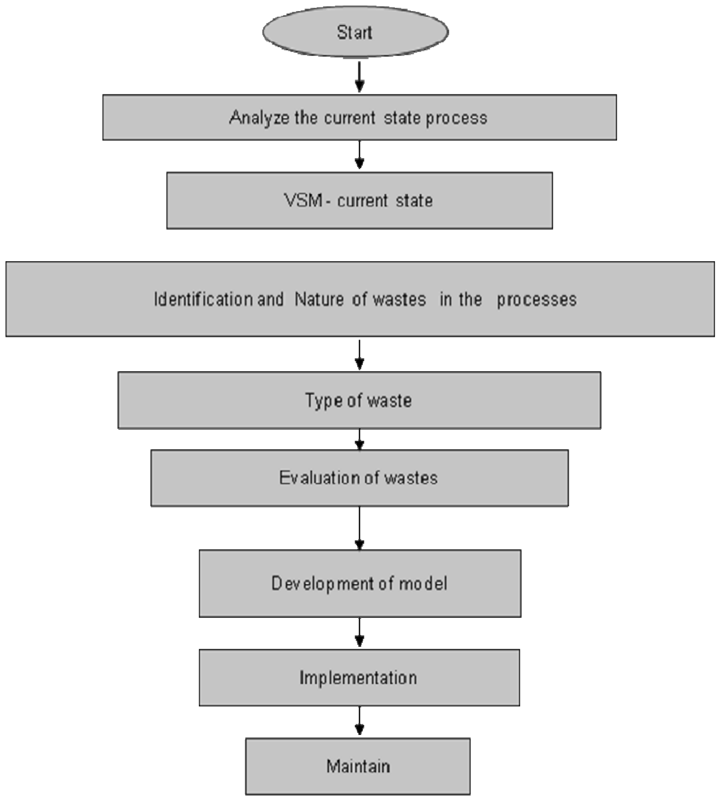

Figure 2 Methodology Flowchart

in the following sections. The process analysis is carried out by collecting the data from various enquiries with expertise in shop floor, workers and directly participating in measuring the time of various processes [2].

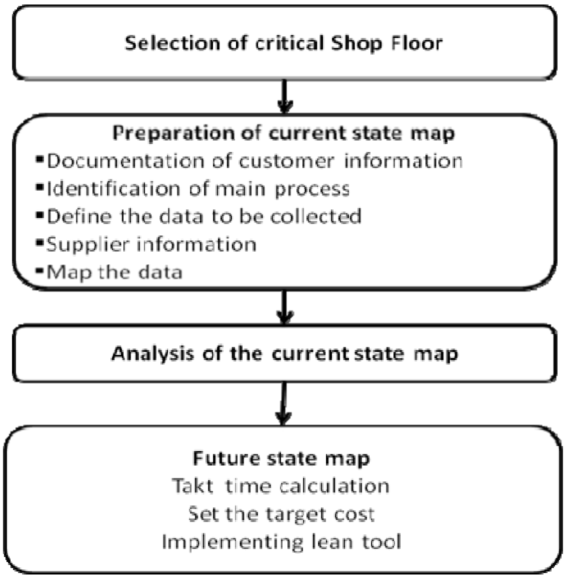

Figure 3 VSM Implementation flowchart

5.1. Preparation of Current State Map

Interaction with the industry the information of the customer's requirement. The company has a wide range of customer requesting for a wide range of product from BN56, BN63, and BN73 (induction motor). Requirement of motors are 15000 motors/month.

- Identification of Main Processes

Quick walk through the shop floor (gemba) helps to identify the main process. The main process involved in assembly shop floor is heating motor body and pressing stator, wiring & testing ,outer diameter turning ,inspection ,excess wire cutting & inserting contact pins, high voltage testing, rotor & cover assembly, quality testing, painting ,fan fixing, packing.

- Define the Data to be collected

The data in the data box serves to track down the opportunity for improving the collection of appropriate data benefits in quick tracking of the opportunities. The data box envelopes the following data like cycle time, change over time, up time and available time. The inventory triangle envelopes two data work in process between each process and respective inventory.

Table 2. VSM input data

Customer Order	15000(per month)
Demand	600(per day)
Working Hours	One Shift 8 Hours (per day)
Break	One Hour (per day)
Raw Materials	Every 15 Days

Table 3 . Process cycle time

Process	Cycle time (sec)
Heating motor body & pressing stator	87
Testing	24
Drilling & turning	71
Inspection	10
Excess wire cutting	47
Fixing terminal board	120
High Voltage testing	22
Rotor & cover fitting	135
Quality testing	80
Painting	45
Fan Fixing	80
Packing	60

5.2. TAKT Time: A Benchmark for Process Pace

Takt demonstrates the rate at which the customer buys the product. TAKT reflects the frequency at which the product has to come out of the manufacturer to meet the customer demand. From Figure 4 Takt time is calculated by dividing available working time per shift (in sec) with the customer demand per shift.

TAKT Time of 42 seconds represents, every motor has to be completed in every 42 seconds. The current state map sights out that the Fixing terminal board & 7nserting contact pins, rotor & cover assembly processes takes 78 Seconds and 93 Seconds more than the Takt time. In order to address the problem layout modification was carried out.

Available Time =Working hours – Breaks= (8 x 60x 60) – (1 x 60 x60) = 25200 sec

$$TAKT\ Time = \frac{Available\ working\ time\ per\ shift}{Customer\ demand\ per\ shift}$$

$$TAKT\ Time = \frac{25200}{600}$$

TAKT time = 42 seconds
Demand=15000 motor/month
Demand per shift=600motor.

5.3. Process improvement (Removing Bottlenecks)

Improvements in quality, flexibility and speed are commonly required .The following lists some of the ways that processes can be improved.

- Rearranging the layout to eliminate large amounts of inventory between operations
- Add additional resources to increase capacity of the bottleneck (an additional machine can be added in parallel to increase the capacity)
- To improve the efficiency of the bottleneck activity
- Minimize non-value adding activities(decrease cost, reduce lead time)
- Eliminating the batching and moving to one piece flow

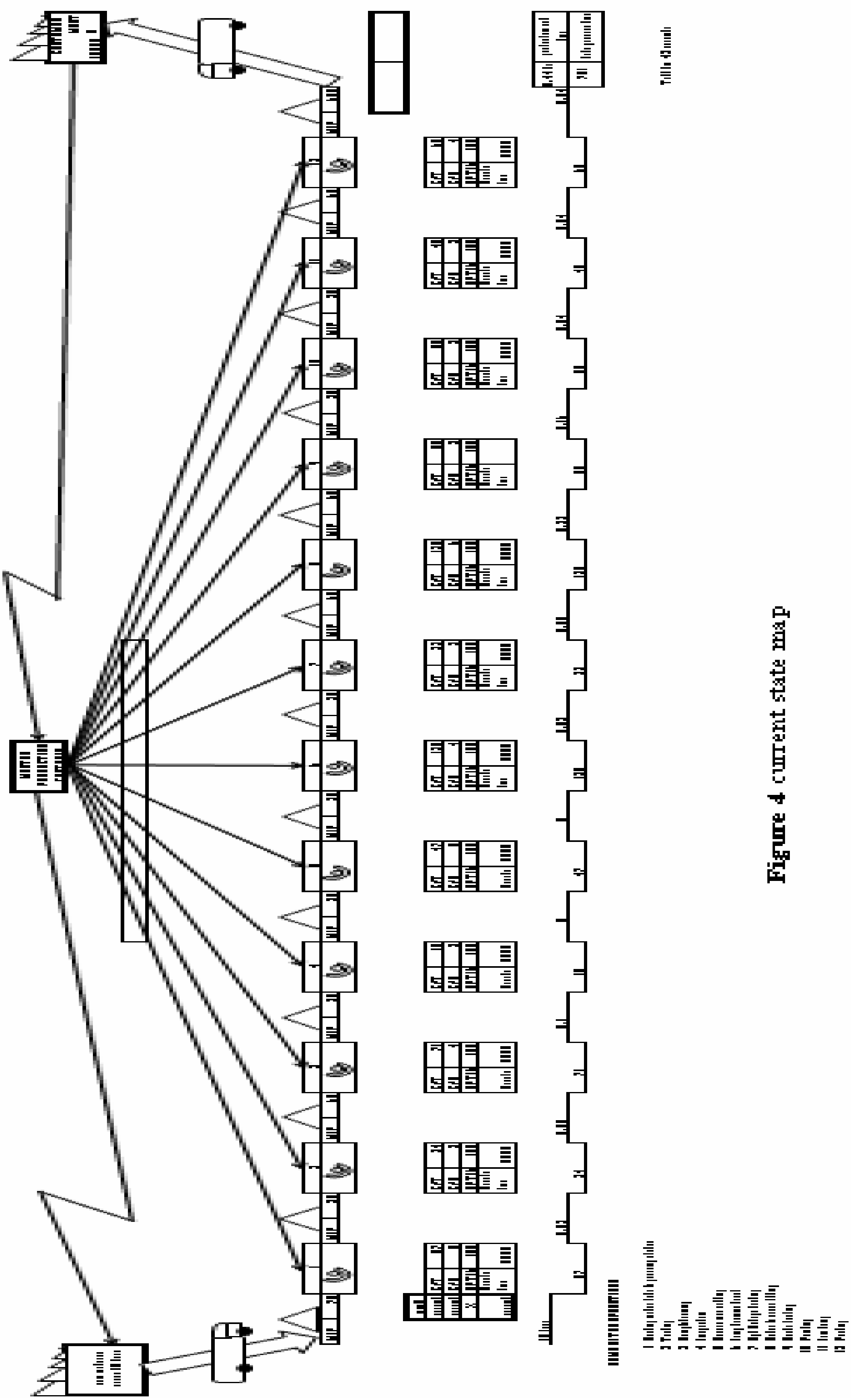

Figure 4 current state map

6. Layout modification

6.1. Current layout

The current layout motor manufacturing assembly operation. The assembly layout is shown in the Figure 5. From the Figure 5 The flow of materials are from oven to heating aluminum body and pressing stator. Then the part is moved to wiring and testing. After testing the body face in and out are done in separate workstation. Then it is passed to inspection, fixing terminal board, HV testing, rotor and cover assembly and it is tested again and painted. Fan is fixed and finally packing is done

In the industry they use batches as 50 parts. Though worker working in first assembly process of heating body and pressing stator finishes his the daily demand in shift time, the worker working in assembly process of packing, painting could not able to finish their work in shift time. Due to which extra transportation time, waiting time affects entire assembly process to meet daily demand. Similarly the part from oven takes more transportation time due to present layout in the process.

6.2. Witness model

The current layout of witness model is shown in Figure 6. From that model it has found out average machine time, average buffer size time, and number of operations. The witness model, to enter the number of machines or operations, cycle time of the each operation, part moving direction (push, pull direction) and to define the number of buffers, buffer size and to select place of each buffer. All data should be enter and to getting the current layout model. The output of the witness model is shown in table 3 and table 4.The table 3 to explain the machine statistics like % idle, %busy, number of operations. The table 4 to explain the buffer statistics like total input, total output, average buffer size and average machine time

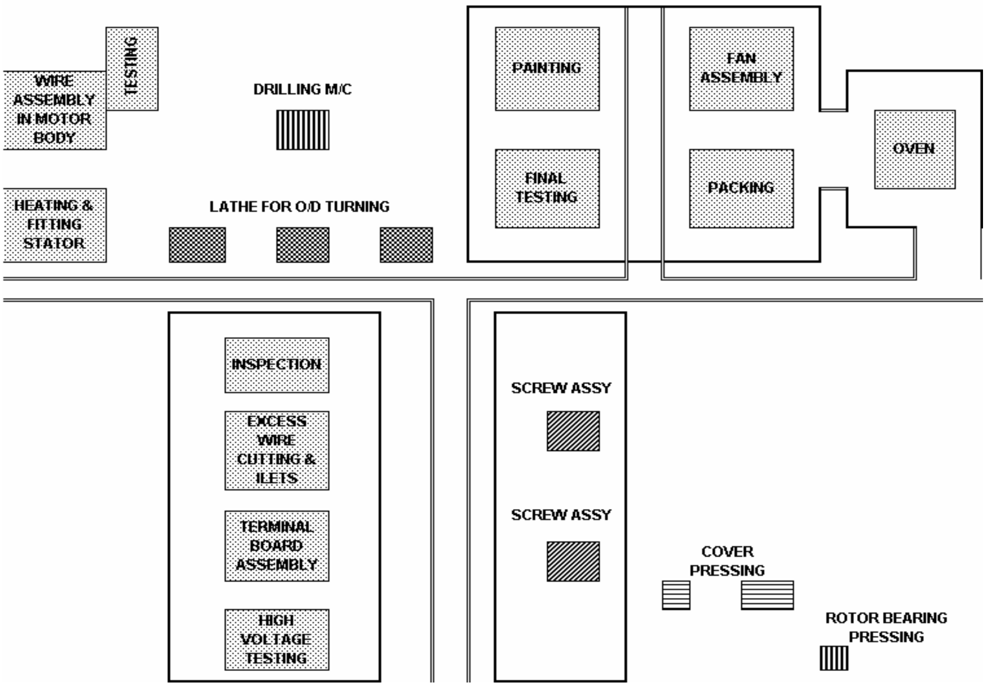

Figure 5 Current layout

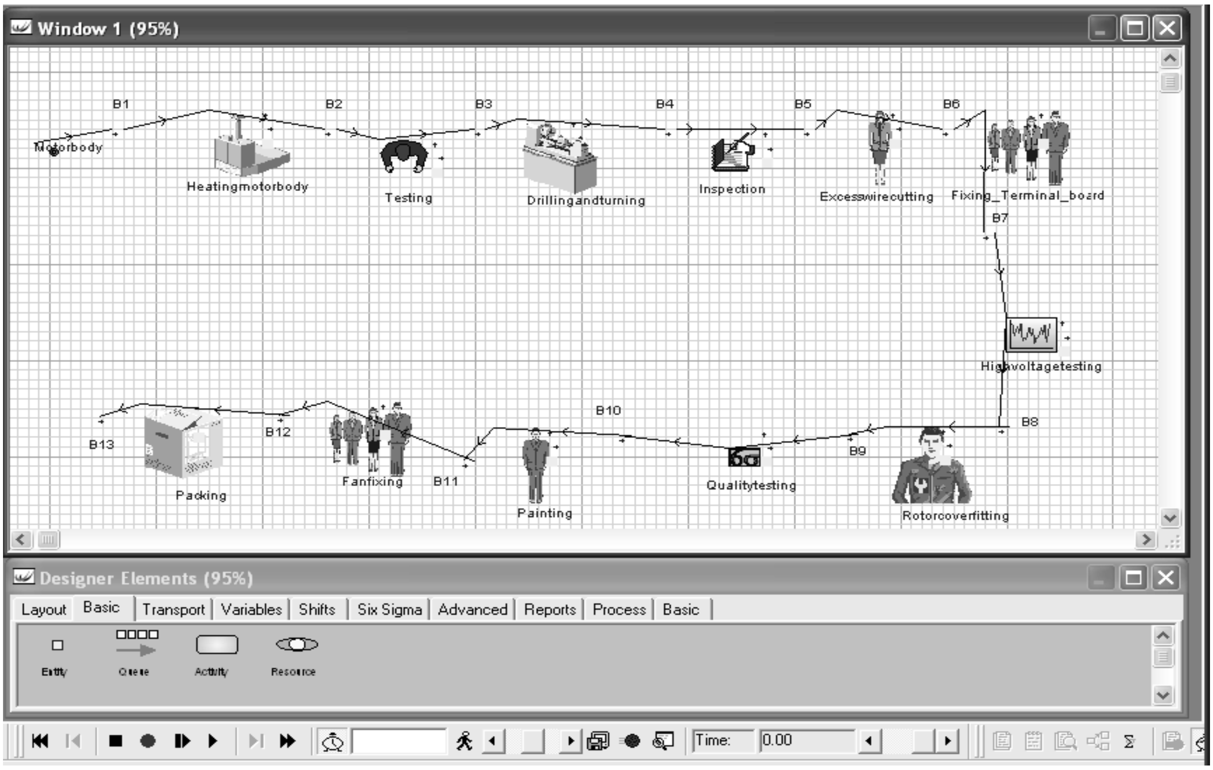

Figure 6 Witness model Assembly layout

Table 3. Current layout performance table: Machine Statistics

WITNESS

Machine Statistics Report by On Shift Time

Name	% Idle	% Busy	% Filling	% Emptying	% Blocked	% Cycle Wait Labor	% Setup	% Setup Wait Labor	% Broken Down	% Repair Wait Labor	No. Of Operations
Heatingmotorb	0.00	100.00	0.00	0.00	0.00	0.00	0.00	0.00	0.00	0.00	450
Testing	72.45	27.55	0.00	0.00	0.00	0.00	0.00	0.00	0.00	0.00	450
Drillingandturni	18.61	81.39	0.00	0.00	0.00	0.00	0.00	0.00	0.00	0.00	449
Inspection	88.55	11.45	0.00	0.00	0.00	0.00	0.00	0.00	0.00	0.00	449
Excesswirecut	46.20	53.80	0.00	0.00	0.00	0.00	0.00	0.00	0.00	0.00	448
Fixing_Termina	0.61	99.39	0.00	0.00	0.00	0.00	0.00	0.00	0.00	0.00	324
Highvoltagetes	81.82	18.18	0.00	0.00	0.00	0.00	0.00	0.00	0.00	0.00	324
Rotorcoverfitti	0.97	99.03	0.00	0.00	0.00	0.00	0.00	0.00	0.00	0.00	287
Qualitytesting	41.44	58.56	0.00	0.00	0.00	0.00	0.00	0.00	0.00	0.00	287
Painting	41.64	58.36	0.00	0.00	0.00	0.00	0.00	0.00	0.00	0.00	286
Fanfixing	67.17	32.83	0.00	0.00	0.00	0.00	0.00	0.00	0.00	0.00	286
Packing	56.36	43.64	0.00	0.00	0.00	0.00	0.00	0.00	0.00	0.00	285

Table 4. Current layout performance table: Buffer Statistics

WITNESS

Buffer Statistics Report by On Shift Time

Name	Total In	Total Out	Now In	Max	Min	Avg Size	Avg Time	Avg Delay Count	Avg Delay Time
B1	1451	451	1000	1000	0	989.68	26741.93		
B2	450	450	0	1	0	0.00	0.00		
B3	450	450	0	1	0	0.00	0.00		
B4	449	449	0	1	0	0.00	0.00		
B5	449	449	0	1	0	0.00	0.00		
B6	448	325	123	123	0	61.21	5356.82		
B7	324	324	0	1	0	0.00	0.00		
B8	324	288	36	36	0	17.80	2153.94		
B9	287	287	0	1	0	0.00	0.00		
B10	287	287	0	1	0	0.00	0.00		
B11	286	286	0	1	0	0.00	0.00		
B12	286	286	0	1	0	0.00	0.00		
B13	285	0	285	285	0	139.97	19255.42		

6.3. Performance table

From the current process layout to Identification of the wastes such as transportation distance (total process), inventory between the processes and part waiting time are reflected in the table 5.

Table 5 Current layout Wastages

Waste	Units
Transportation	140 meters
Inventory	45 parts
Part waiting time	250 seconds

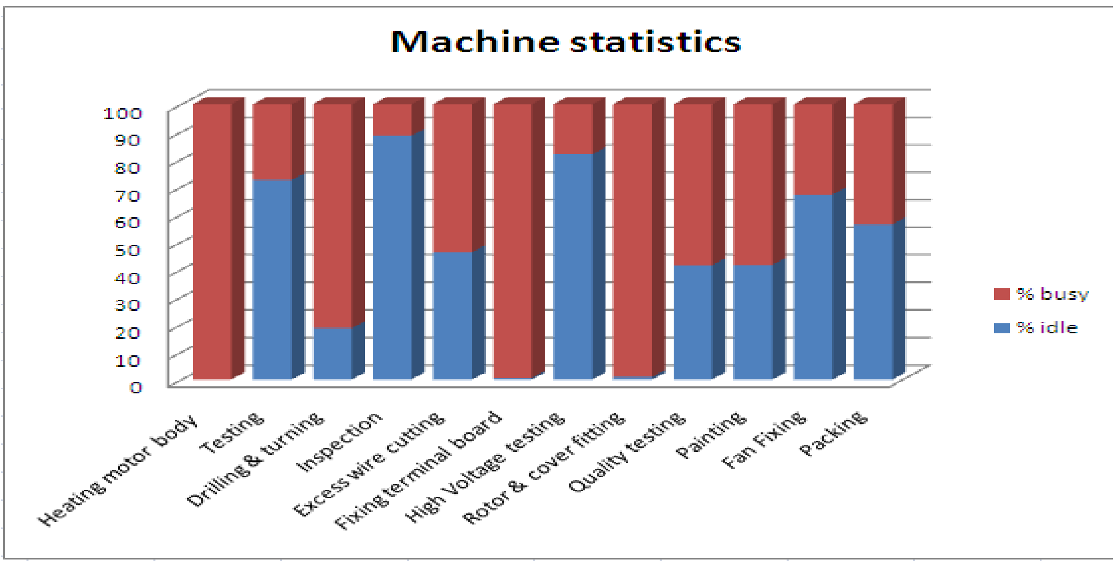

Figure 7 Machine Statistics

From the Figure 7 to explain that the percentage of machine utilization. The machine utilization value is given by table 3.The first machine is 100% busy, the second machine is 74.45% busy and 27.56% idle, like that all machine performance as shown in the figure 7.If the fixed terminal board and rotor cover fitting is 99.3% busy. To increase the machine utilization and to increase the productivity.

6.4. Modified layout

The optimized layout is show in figure 8. This layout modified using VIPPLANOPT software. The objective of modified layout is to minimize the transportation cost, inventory between the process and part waiting time.

From figure 9 to explain the transportation distance between machine to machine. Those distances are based on new modified layout. This layout modified using VIPPLANOPT software. For example the distance between 1'st machine and 2'nd machine is 51.6meters, like that calculate to total modified layout distance is 75.6meters

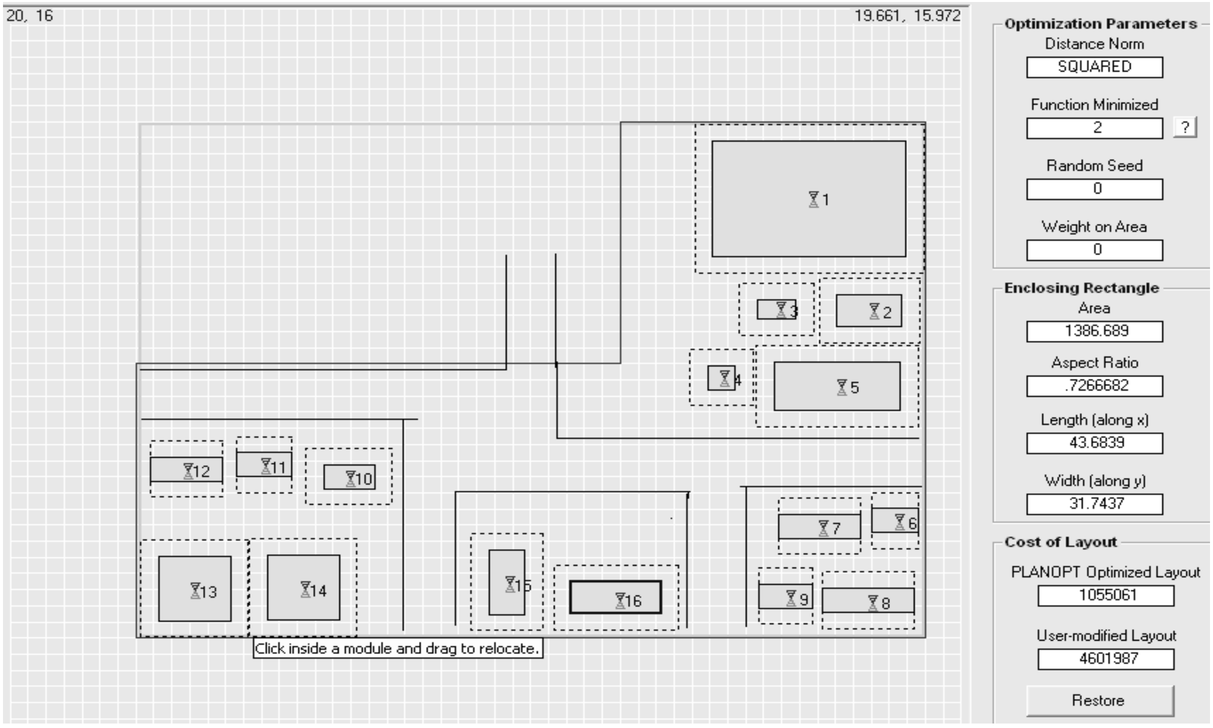

Figure 8 VIP layout model

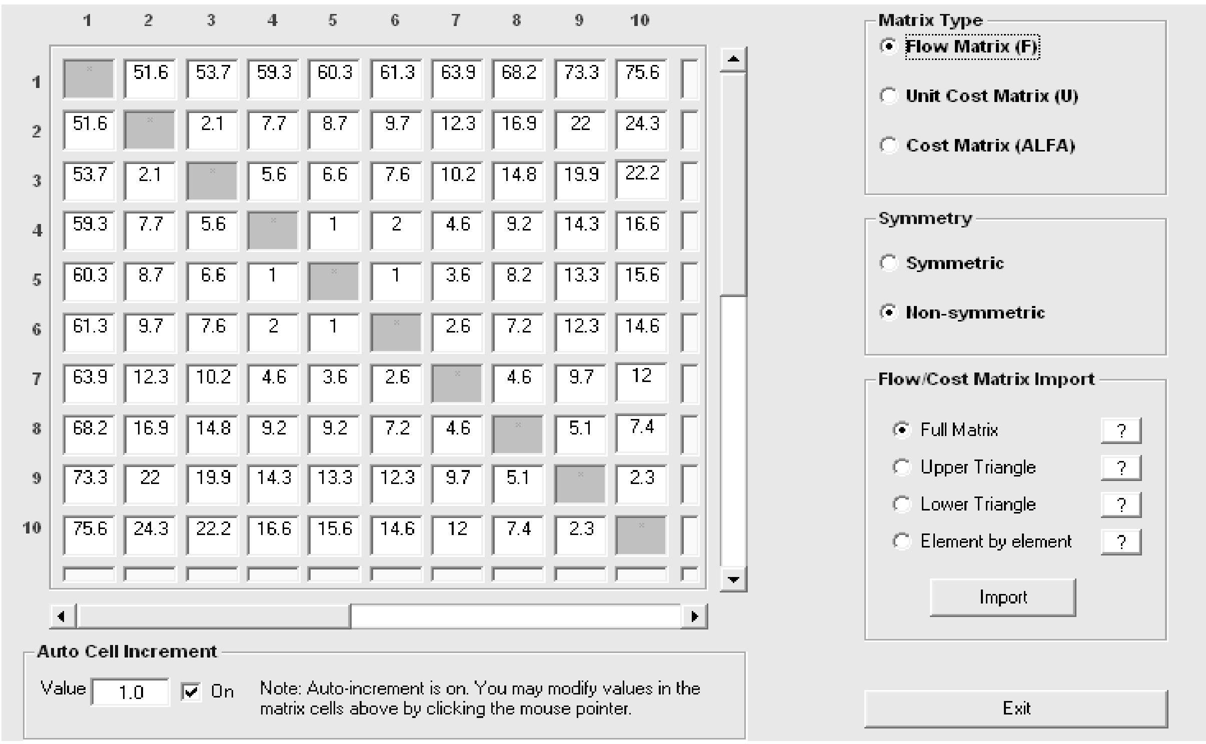

	1	2	3	4	5	6	7	8	9	10
1		51.6	53.7	59.3	60.3	61.3	63.9	68.2	73.3	75.6
2	51.6		2.1	7.7	8.7	9.7	12.3	16.9	22	24.3
3	53.7	2.1		5.6	6.6	7.6	10.2	14.8	19.9	22.2
4	59.3	7.7	5.6		1	2	4.6	9.2	14.3	16.6
5	60.3	8.7	6.6	1		1	3.6	8.2	13.3	15.6
6	61.3	9.7	7.6	2	1		2.6	7.2	12.3	14.6
7	63.9	12.3	10.2	4.6	3.6	2.6		4.6	9.7	12
8	68.2	16.9	14.8	9.2	9.2	7.2	4.6		5.1	7.4
9	73.3	22	19.9	14.3	13.3	12.3	9.7	5.1		2.3
10	75.6	24.3	22.2	16.6	15.6	14.6	12	7.4	2.3	

Figure 9 Transportation distance

7. Conclusion

From this paper it was inferred that VSM is an ideal tool to expose the waste and to identify improvement areas. In this paper the effectiveness of lean principle is substantiated in a systematic manner with the help of simulation softwares in a systematic manner. Availability of information such as material and money flow which facilitate and validate the decisions to implement lean manufacturing. This can also motivate the organization during the actual implementation in to obtain the desired benefits. The results from these simulation software show that there can be much improvements to be made in the manufacturing of motors. It helps the companies to reach their ultimate goal of sustainability and profitable growth in the future.

References

[1] Roberto Panizzolo. 'Applying the lessons learned from 27 lean manufacturing. The relevance of relationships management'.Int .J.Production Economics. Vol 55, 1998, 223-240

[2] Ajit Kumar Sahoo, N K Singh., Ravi Shankar., M K Tiwari., 'Lean philosophy: implementation in a forging company'. Int J Advanced Manufacturing Technology . 2008.

[3] Clark, K. B. Managing technology in international competition: The case of product development in response to foreign entry. International Comprtitiveness. Eds. M. Spence and H. A. Hazard, Ballinger, 1988, 27-74.

[4] Toni L. Doolen and Maria E. Hacker, 'A Review of Lean Assessment in Organizations: An Exploratory Study of Lean Practices by Electronics Manufacturers'. journal of manufacturing systems Vol.24, No-1, 2005.

[5] Peter Middleton, 'Lean Software Development: Two Case Studies' Software Quality Journa, Vol. l 9, 2001, 241–252.

[6] Askin R G and Goldberg J B., 'Design and Analysis of Lean Production System' John Wiley and Sons Inc., 2003.

[7] Leonardo Riveraa, F. Frank Chen, 'Measuring the impact of Lean tools on the cost–time investment of a product using cost–time profiles', Robotics and computer integrated manufacturing Vol. 23, 2007, 684-689.

[8] Womack JP, Jones D., 'The machines that changed the world'. New York, NY: Rawson Association., 1990.

[9] Crute, V., Ward, Y. Brown, S. And Graves A., "Implementation lean in aerospace challenging the assumption and understanding the challenges", Technovation, Vol. 23, 2003, 917-928.

JJMIE

Volume 4, Number 5, November 2010
ISSN 1995-6665
Pages 591 - 596

Jordan Journal of Mechanical and Industrial Engineering

Surface Retorting of Jordanian Oil Shale and Associated CO_2 Emissions

Jamal O. Jaber*, Taiseer M. Abu-Rahmeh, Aiman Alawin, N.Al-Kloub

Department of Mechanical Engineering, Faculty of Engineering Technology Al-Balqa' Applied University, Amman, Jordan

Abstract

In this study, two oil shale samples, from two different deposits in Jordan, have been pyrolysed using a thermogravimetric analyser (TGA). The controlling parameters studied were the final pyrolysis temperature and the influence of the heating rate as well as type of purge gas employed on the process of thermal degradation of the shale sample. It is found that there are two main steps of samples' weight loss. The first one is due to conversion of organic matter to oil and gas which occurred within the temperature range of between 250 to 550 °C, while the second step represents weight loss due to carbonate decomposition releasing CO_2 and occurred at approximately higher temperature of more than 550 °C for examined samples. In directly heated systems additional quantities of CO_2 will be produced due to combustion of residual carbon in order to provide needed heat for the retorting process. Therefore, surface retorting processes aiming to produce crude shale oil from raw oil shale will release higher rates of CO_2 emissions to the environment compared with production of conventional or other synthetic fuels.

Keywords: Oil Shale, Surface Retorting, Co_2 Emission, Jordan.

1. Introduction

The proven reserves, in the central region of the Jordan, are huge (i.e. exceeding $5x10^{10}$ tonnes of oil shale) with an average organic content of between 9 and 13% by weight (which would yield ~$5x10^9$ tonnes of shale oil) [1-5]. Yet there is a dearth of information available about the pyrolysis of Jordanian oil shales, because there has been only little interest in developing such resource. The main reasons for this are that the majority of the deposits are relatively lean and located in remote regions, where, at best, only a limited industrial infrastructure exists. Equally important is the poor knowledge of their full extent and exact characteristics. Moreover, the prevailing relatively low unit-prices for crude oil on the international market have discouraged entrepreneurs from making investments to exploit these oil shale resources.

In the literature, the kinetics of the thermal decomposition of various oil shales, from different regions of the world, have been investigated and various suggestions as to the decomposition mechanisms have been reported [6-21]. Many thermogravimetric studies have been carried out under isothermal conditions (for which the rates of reaction are determined at constant temperatures), but this method involves some inaccuracies. It is more accurate to use a non-isothermal method to determine the kinetic parameters of the pyrolysis process, employing a TGA apparatus, with the sample heated at a constant rate and recording its weight change. This is mainly because of the shorter experimental times and the fewer encountered difficulties (e.g. the initial heating-up period in isothermal methods). But the principal reason for their popularity in the field of oil shale pyrolysis is that it more closely simulates the conditions expected in commercial-scale oil shale retorting systems. Thus, such a technique for determining the reaction kinetics, such as the activation energy, has been preferred by many researchers. Hence, the kinetics of thermal degradation of a small shale particles specimen can be obtained using a TGA apparatus, which records the changes of a small shale sample with time. Consequently, this can be used to determine the characteristics of devolatilisation as well as kinetic parameters [6,12,17,19-23]. The behaviour of oil shale pyrolysis is considered to be complicated because the shale is a complex mixture of kerogen and wide range of minerals. Also, the shale oil produced by pyrolysis is the result of several physical and chemical reactions occurring simultaneously in series and parallel, while the TGA apparatus measures the overall weight loss due to these reactions. Hence, the TGA provides only general information about the overall reaction kinetics.

However, a large number of researchers have studied the influence of pyrolysis temperature and heating rate on oil shale decomposition used TGA apparatus . For example, Haddadin and Mizyed [6], Dogan and Uysal [19] and Ahmad and Williams [20] have investigated the influence of final pyrolysis temperature and reported greater weight losses, from the oil shale specimens, as the temperature was increased. Skala et al., [11], Drescher [21], Lee et al., [22], Rajeshwar [23] and Campbell et al, [24] concluded that there was a systematic shift of the region in which the maximum rate of weight loss ensues towards higher temperatures for higher heating rates. The present investigation is an experimental study using a TGA apparatus (under non-isothermal conditions) to determine the kinetics of the pyrolysis process for two Jordanian oil shales (i.e. from the Ellujjun and Sultani deposits) in relation to the heating rate, final temperature and purge gas employed. Also carbonate ($CaCO_3$) decomposition rates are determined at temperatures higher than desired retorting temperature.

* Corresponding author. jojaber@gmail.com

2. Experimental Equipment and Procedure

2.1. Shales used

Oil shale samples, from the Ellujjun and Sultani deposits, were supplied by the Natural Resources Authority (Amman, Jordan), but details of the sampling method used were not provided. The two samples of raw oil shale received were crushed, separately, by a jaw crusher and then, without further treatment, sieved in order to obtain samples of the required particle size. These oil shales have been examined in a preliminary pyrolysis study, using a fixed bed retort, reported previously [25].

2.2. Experimental apparatus

Kinetic data were obtained using a Shimadzu Model-50 Series TG Analyser, with N_2 or CO_2 (supplied at a constant rate of ~$5x10^{-5}$ m^3 min^{-1} at normal conditions) employed as the purge gas. The TGA apparatus permits the continuous measurement of sample weight as a function of temperature, and provision is made for an electronic differentiation of the weight signal to give the rate of weight loss, with high accuracy of ±0.1%. In this investigation, TGAs were used to determine the effects of heating rate and final temperature on the weight loss of the oil shale sample.

Pyrolysis was carried out non-isothermally using a sample of about$15x10^{-6}$ kg, placed in the alumina crucible, which was then put on the sample pan hanging down in the reaction tube, where the atmosphere could be controlled. The furnace tube was raised to close the system, and the start button depressed. The pre-programmed control unit regulates all the automatic functions of the recorder (e.g. the continuous change in the mass of the sample is measured), as well as the temperature programming of the furnace. Finally, and after the furnace temperature had achieved its set value, the sample was allowed to cool to room temperature. All experiments were repeated in order to minimize experimental uncertainty and cross-checking obtained results, and where significant variance was found the test a third test was conducted in order to confirm results. But it should be noted that due to the fact that oil shale is not homogeneous material, a slight difference in final results would be inevitable. Table 1 lists the main conditions employed during this experimental investigation.

Table 1. Main experimental conditions

Sample grain size (mm)	< 0.85
Heating rate (K min^{-1})	20
Final temperature (°C)	400-900 (and 1000 in the case of CO_2)
Gas carrier	N_2 or CO_2

3. Results and Discussion

A typical variation of the percentage conversion with temperature (i.e. the TGA curve) is shown in Fig. 1, while Fig. 2 shows the differential weight loss (i.e. the DTG) profile for the Ellujjun and Sultani shales. The rate of weight loss, due to conversion of the organic matter, is clearly related to the pyrolysis temperature: the higher the final temperature, the greater the weight loss. This is because, at high temperatures, the pyrolysis process proceeds faster.

The DTG figure demonstrates clearly that there are three steps of the mass-loss profile. The pre-heating phase, being below 200 °C, corresponds with the loss of the interlayer water from the clay minerals and the decomposition of nahcolite as well as the physical changes (i.e. is the softening and molecular rearrangement associated with release of gases) in the kerogen prior to its decomposition to bitumen as shown in Fig. 3 [26]. It is clear, from Fig. 3, that kerogen undergo two steps reaction: the 1st step involves some changes and conversion of light matter and in the 2nd step bitumen is decomposed into oil and gases. The loss of hydrocarbon material took place during the second stage (i.e. between 200 and 600 °C).

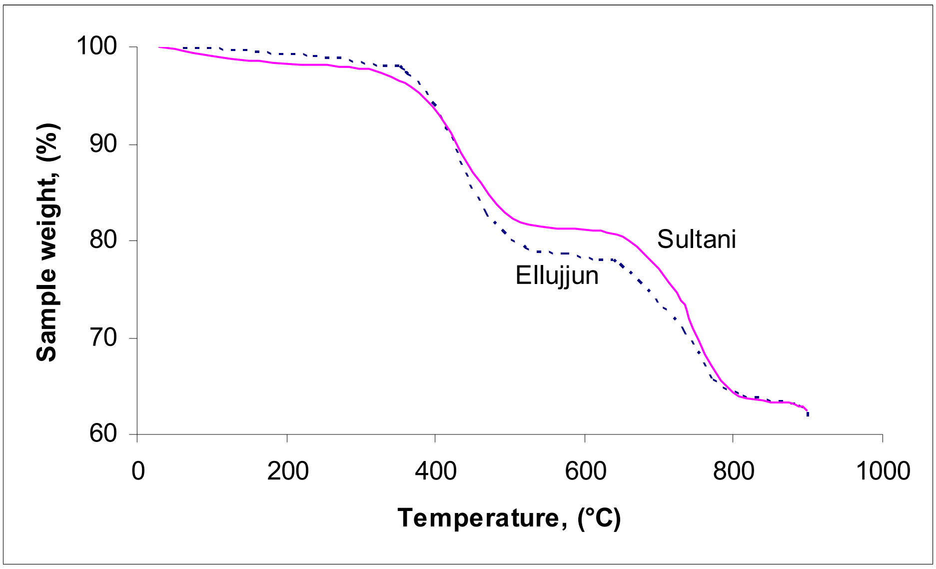

Fig. 1. TG profiles of the Ellujjun and Sultani oil shales (in N_2, h = 20 K min^{-1})

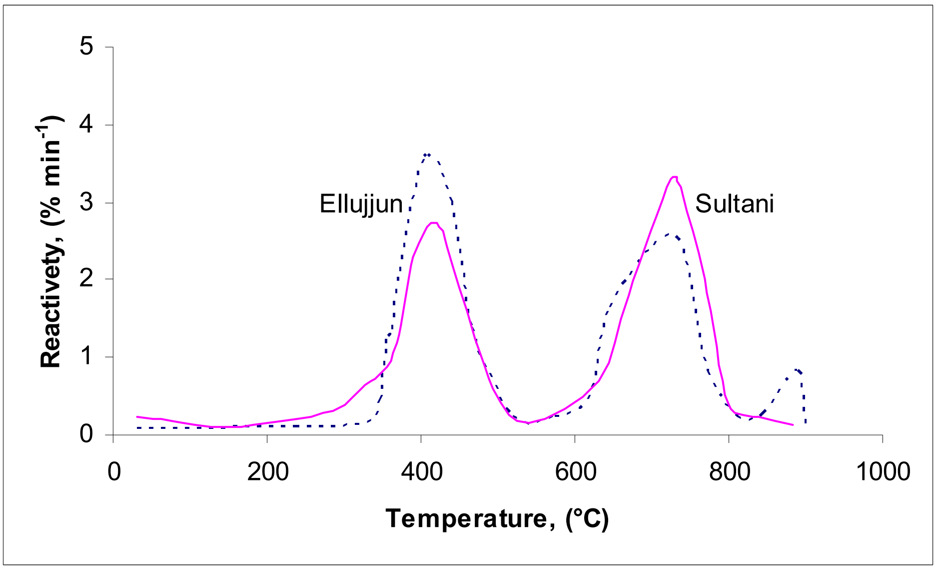

Fig. 2. DTG of the Ellujjun and Sultani oil shales

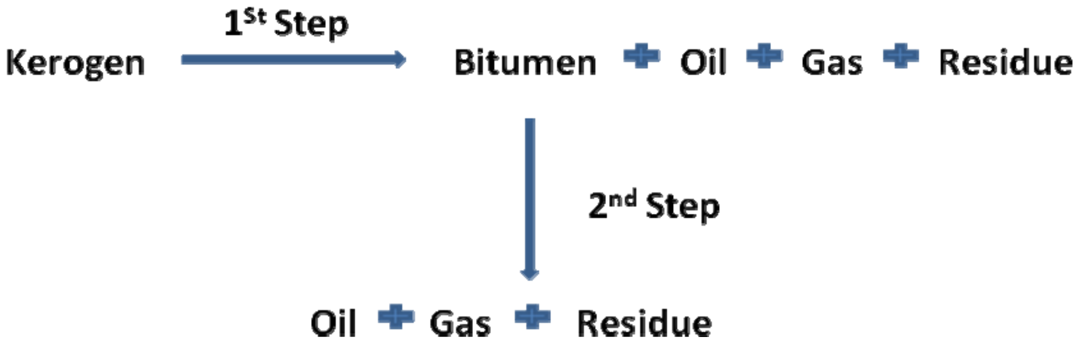

Fig. 3. Mechanism of thermal decomposition of oil shale particles

It is evident that the major pyrolysis peak is a singular one and the extractable organic contents, within the temperature range of 200 to 500 °C, are approximately 21 and 17% of the original sample weight for the Ellujjun and Sultani shales, respectively. Previously, it had been observed, from fixed-bed pyrolysis tests, that water starts emerging from the oil shale sample within the temperature range of 120 to 160 °C, and the devolatilization in the oil shale started at temperatures as low as 250 °C and continued up to approximately 500 °C [4,25]. The third stage, which occurred at higher temperatures exceeding 600 °C, is due to the decomposition of the carbonate (i.e. calcite and dolomite). The sample's continued loss of weight, as the temperature was increased above 600 °C, could be attributed to the possibility of continued pyrolysis, as well as the presence of CO_2 (which evolved as a result of carbonate decomposition) and which reacts with the residual char, through the Boudouard reaction, so forming carbon monoxide.

The two shales exhibit qualitatively the same patterns of thermal degradation when the pyrolysis temperature was raised over the studied range. But it is evident, within experimental error, that during the pyrolysis phase alone, the Ellujjun sample exhibits approximately a 30% higher weight loss compared with the Sultani oil shale: the latter lost about 17% of its initial weight when N_2 was used to purge the furnace and 18% in the case when CO_2 was employed as the sweeping gas. In general, within experimental error, a slightly greater weight loss occurred from the shale sample as a result of using CO_2 instead of N_2 to purge the TGA system. This is because CO_2 is more reactive than N_2 due to the presence of alkali metals, which are very effective in the CO_2 and/or H_2O reactions with carbon [27-29]. The increase in the amount of shale decomposed with increasing temperature is greater between 200 and 550 °C than for temperatures exceeding 550 °C. This is due to the fact that the optimal temperature for maximizing oil shale retorting is around 550 °C.

The singular step thermal decomposition behavior of Jordanian oil shales is similar to those observed for various shales, such as those from Colorado [30], Ohio, West Virginia and North Carolina [22] all in the USA, Aleksinac and Knjazevac in Yugoslavia [17], Beypazari in Turkey [19], Kark, Dharangi and Malgeen in Pakistan [20] and Attarat in Jordan [4]. The conclusions derived from this study concerning the Ellujjun oil shale are in full agreement with those reported by other researchers [6]. Whatever the shape of the decomposition profile (i.e. single or double stage), oil shale pyrolysis studies indicate that the conversion of kerogen into shale oil is a two-stage process. In the first, decomposition of the kerogen to pyrolytic bitumen occurred and then, in the second, decomposition of the bitumen to products ensued [15,19,24]. However, the mechanism for the thermal decomposition of oil shale is complex and involves a series of parallel reactions.

4. Predicted GHG Emissions from Retorting Unit

Major gas emissions from oil shale processing plants are particulates, nitrogen oxides, sulfur oxides and carbon dioxide: the relative amounts emitted increase as the thermal efficiency decreases. Much concern has been expressed recently over the "excessive greenhouse effect", where the increased concentrations of CO_2 in the atmosphere resulting from the burning of fossil fuels are leading to global increases in air temperature and long-term climatic changes. The burning of hydrocarbon fuels with the high hydrogen/carbon ratios (i.e. as with natural gas) would reduce CO_2 emissions per unit of heat (or other form of energy) produced. However, this is not the case with synthetic fuels, where the total amount of CO_2 generated must include that portion released during their manufacture – see Table 2 [31]. So, in shale oil production or oil shale direct combustion, there are additional releases of CO_2 due to the decomposition of the carbonates that are present in the raw shale. Thermal decomposition occurs at high rates at ≥ 500°C: therefore it is not expected to be significant for the indirectly-heated retorting process. However, it is an important source in the directly-heated retorts as well as in some in-situ retorting methods, because the temperature in the combustion zone would then be in the range of 700 to 1100 °C. This would generate more quantities of such emissions due to the combustion of residual carbon remained in the retorted shale. Although CO_2 is potentially a pollutant of global concern, its emission is not controlled by the present air quality and pollution standards which are imposed on air emissions in most countries. As for the oil shale combustion process, a relatively-high temperature (i.e. on average ~800 (±50) °C in the case of fluidized-bed combustors and about 1300 (±100) °C for pulverized oil shale combustion) are necessary in order to ensure complete oxidation of the CO and various HC species. Consequently, decomposition of the carbonate content occurs, but only a small percentage (i.e. ≤ 10% of the total) of this decomposition is desirable for the capture of the sulfur oxides (i.e. mainly SO_2).

Table 2. CO_2 produced in the synthetic fuels' manufacturing processes and burning of fuel (mol CO_2 per MJ of product)

Fuel	*Manufacture*	*Combustion*	*Total*
C	-	2.54	2.54
CH_2	1.36	1.61	2.97
CH_4	2.17	1.25	3.42
CH_3OH	1.92	1.57	3.49

It is hard to estimate with certainty the rates of CO_2 that would be produced by any proposed oil shale project, unless technology and capacity are known. However, it is predicted that, if one quarter only of the carbonate content of the raw shale is decomposed, this would be responsible for emitting approximately 20-25% more CO_2 than from the combustion process alone. Such an endothermic decomposition reaction would consume approximately 5-8% of the total heat released during the combustion process [32]. This is unfavorable from the flue-gas emissions point-of-view, but simultaneously the decomposed carbonates will produce a pozzolanic ash, which is desirable for improving the characteristics of the spent shale in order for it to be used later as a raw material in the construction and cement industries or for safe disposal. Also from the environmental side, increasing rates of CO_2 emission is not favorable due to its contribution to climate change and global warming effects.

5. Conclusion

For both oil shale samples tested, the conversion of kerogen is totally dependent on the final pyrolysis temperature: the higher the final temperature, the greater the weight loss from each sample. Using CO_2 instead of N_2 to purge the TGA system led to a slight increase in the weight loss from the oil shale sample. The principal conclusion of this study is that both of Ellujjun and Sultani oil shale samples' behaviour can be described as a singular reaction phase over the studied temperature range. The second stage, which occurred at higher temperatures exceeding 600 °C, is due to the decomposition of the carbonate. In real oil shale projects, it is expected that GHG emissions would be higher due to many reasons, e.g. mining activities, combustion of residual carbon and transportation of raw oil shale and finished products.

References

[1] Jaber, J.O. and S.D. Probert, Exploitation of Jordanian oil shales. *Applied Energy*, Vol. 58, 1997, 161-175.

[2] Jaber, J.O. and S.D. Probert, P.T. Williams, M. Tahat, Gasification potential and kinetics of Jordanian oil shales using CO_2 as the reactant gas. *Energy Sources*, Vol. 22, 2000, 573-585.

[3] Jaber, J.O. and M. Mohsen, Behaviour of two Jordanian oil shales at drying. *Oil Shale*, Vol. 18, 2001, 47-55.

[4] Jaber, J.O., M. Abu-Qudis, and S. Sawalha, Kinetics of pyrolysis of Attarat oil shale by thermogravimetry. *Oil Shale*, Vol. 22, 2006, 51-63.

[5] Anon, Natural Resources Authority, Annual Reports 1985→2005, Amman, Jordan.

[6] Haddadin, R.A. and F.A. Mizyed, Thermogravimetric analysis kinetics of Jordan oil shale. *Industrial Engineering Chemistry, Process, Design and Development*, Vol. 13, 1974, 332-336.

[7] Braun, R.L. and A.K. Burnham, Kinetics of Colorado oil shale pyrolysis in a fluidised bed reactor., Vol. 65, 1986, 218-222.

[8] Koseoglu, R.O. and C.R. Phillips, Kinetic models for the non-catalytic hydrocracking of Athabasca bitumen., Vol. 67, 1988, 906-915.

[9] Skala, D., H. Kopsch, M. Sokic, H.J. Neumann, and J.A. Jovanovic, Kinetics and modelling of oil shale pyrolysis., Vol. 69, 1990, 490-496.

[10] Yang, H.S. and H.Y. Sohn, Effect of reduced pressure on oil shale retorting: kinetics of oil generation. *Industrial and Engineering Chemistry Process Design and Development*, Vol. 24, 1985, 265-270.

[11] Skala, D., H. Kopsch, M. Sokic, H.J. Neumann, H.J. and J.A. Jovanovic, Thermogravimetrically and differential scanning calorimetrically derived kinetics of oil shale pyrolysis,Vol. 66, 1987, 1185-1191.

[12] Williams, P.F.V., Thermogravimetry and decomposition kinetics of British Kimmeridge clay oil shale. , Vol. 64, 1985, 540-545.

[13] Li, S. and J. Qian, Study of the pyrolysis of Maoming oil shale lumps., Vol. 70, 1991, 1371-1375.

[14] Campbell, J.H., G.H. Koskinas, and N.D. Stout, Kinetics of oil generation from Colorado oil shale. *,Vol.* 57, 1978, 372-376.

[15] Granoff, B. and H.E. Nuttall, Pyrolysis kinetics for oil shale particles. ,Vol. 56, 1977, 234-240.

[16] Braun, R.L. and A.J. Rothman, Oil shale pyrolysis: kinetics and mechanism of oil production. ,Vol. 54, 1975, 129-131.

[17] Skala, D., M. Sokic, H. Kopsch, Oil Shale Pyrolysis: A new approch to the kinetic investigation of different kerogen type samples. *Thermochimica Acta*, Vol. 134, 1988, 353- 358.

[18] Thakur, D.S., E.S. Wilkins, and H.E. Nuttall, 1984. Thermal degradation of shale oils: kinetics of vapour phase oil degradation. *,Vol.* 63: 401-407.

[19] Dogan, O. and B.Z. Uysel, Non-isothermal pyrolysis kinetics of three Turkish oil shales. *,Vol.* 75, 1996, 1424-1428.

[20] Ahmad, N. and P.T. Williams, 1998. Influence of particle grain size on the yield and composition of products from the pyrolysis of oil shales. *Journal of Analytical and Applied Pyrolysis* 46: 31-49.

[21] Drescher, E.A., C.A. Bassil, and E.J. Rolinski, The kinetics of the thermal decomposition of Green River oil shale by thermogravimetric analysis, in Alternative Energy Sources V, Part D: Biomass/Hydrocarbons/Hydrogen, Ed. Veziroglu T. N., 1983, Elsevier Science Publishers, Amsterdam, Holland, 1983.

[22] Lee, S., M.E. Polasky, and. R. Joshi, Pyrolysis kinetics of various Eastern shales in nitrogen and carbon dioxide atmospheres, 1983 Eastern Oil Shale Symposium, University of Kentucky, 13-16 November, Kentucky, USA, 1983.

[23] Rajeshwar, K., The kinetics of the thermal decomposition of Green Revir oil shale kerogen by non-isothermal thermogravimetry. *Thermochimica Acta*, Vol. 45, 1981, 253-263.

[24] Campbell, J.H., G.H. Kosinas, T.T. Coburn, and N.D. Stout,. Dynamics of oil generation and degradation during retorting of oil shale blocks and powders, Proceedings of the 10th Oil Shale Symposium, 1977, Colorado School of Mines, Golden, Colorado, USA, 1977.

[25] Jaber, J.O., S.D. Probert, and P.T. Williams, Evaluation of oil yield from Jordanian oil shales. *Energy* , vol. 24, 1999, 761-781.

[26] Burnham, A.K., B.E. Huss, and M.F. Singleton, 1983. Pyrolysis kinetics for Green River oil shale from the saline zone. *,Vol.* 62: 1199-1204.

[27] Burnham, A.K., C.T. Stubblefield, and J.H. Campbell, Effects of gas environment on mineral reactions in Colorado oil shale. ,Vol. 59, 1980, 871-877.

[28] Dror, Y., S. Marian, and M. Levy, Pyrolysis/g.c. of oil shales and coal. ,Vol. 64, 1985, 406-410.

[29] Li, S. and Cheng, Y., Catalytic Gasification of gas-coal char in CO_2, Vol. 74 , 1995, 456-458.

[30] Weitkamp, A.W. and L.C. Gutberlet, 1970. Application of a microretort to problems in shale pyrolysis. *Industrial and Engineering Chemistry, Process Design and Development* 9: 386-395.

[31] Probstein, R. and R. Hicks. *Synthetic Fuels,* International Student Edition, McGraw-Hill International Book Company, Tokyo, Japan, 1982.

[32] Wallman, P., Co-production of Oil and Electric Power from Colorado Oil Shale. Energy, Vol. 17, 1992, 313-319.

JJMIE

Volume 4, Number 5, November 2010
ISSN 1995-6665
Pages 597 - 604

Jordan Journal of Mechanical and Industrial Engineering

Real Time Compensation of Machining Errors for Machine Tools NC Based on Systematic Dispersion

M. RAHOU , A. CHEIKH , F. SEBAA

Automatic Control Laboratory, Department of Mechanical Engineering Faculty of Sciences Engineering, Abou Bakr Belkaid University , 13000 Tlemcen ALGERIA

Abstract

Manufacturing tolerancing is intended to determine the intermediate geometrical and dimensional states of the part during its manufacturing process. These manufacturing dimensions also serve to satisfy not only the functional requirements given in the definition drawing, but also the manufacturing constraints, for example geometrical defects of the machine, vibration and the wear of the cutting tool. In this paper, an experimental study on the influence of the wear of the cutting tool (systematic dispersions) is explored. This study was carried out on three stages .The first stage allows machining without elimination of dispersions (random, systematic) so the tolerances of manufacture according to total dispersions can be identied. In the second stage, the results of the first stage are filtered in such way to obtain the tolerances according to random dispersions. Finally, from the two previous stages, the systematic dispersions are generated. The objective of this study is to model by the least squares method the error of manufacture based on systematic dispersion. Finally, an approach of optimization of the manufacturing tolerances was developed for machining on a CNC machine tool

Keywords: Compensation, Modeling, Manufacturing Tolerance, Machine Tool, Time Real

1. Introduction

Manufacturing tolerancing is intended to determine the intermediate geometrical and dimensional states of the part during its manufacturing process. These manufacturing dimensions also serve to satisfy not only the functional requirements given in the definition drawing, but also the manufacturing constraints, for example geometrical defects of the machine, vibration and the wear of the cutting tool…

Many research works were treated the tolerancing problem with different approaches, Rong and Bai [1] analyzed a dependent relationship of operational dimensions to estimate machining errors in terms of linear and angular dimensions of a workpiece. Cai et al. [2] proposed a method to conduct a robust fixture design to minimize workpiece positional errors as a result of workpiece surface and fixture setup errors. Djurdjanovic and Ni [3] developed procedures for determining the influence of errors in fixtures, locating datum features and measurement datum features on dimensional errors in machining. These studies were conducted when a static case was assumed.

Kim and Kim [4] have developed a volumetric error model based on 4x4 homogenous transformations for generalized geometric error. Eman and Wu [5] have developed error model accounts for error due to inaccuracies in the geometry and mutual relationships of the machine structural elements as well as error resulting from the relative motion between these elements. Kakino et al. [6] have measured positioning errors of multi-axis machine tools in a volumetric sense by Double Ball Bar (DBB) device. Takeuchi and Watanabe [7] have shown five-axis control collision free tool path and post processing for NC-data.

In the work of [8], the authors present an experimental semi study of the vibratory behavior of the cutting tool golds of the operation of slide-lathing, is the object to show that it is possible to consider the roughness average of the part machined starting from displacement resulting from the nozzle of the tool. In the work of [9] a study was presented on the influence of the position of the cutting tool on dynamic behavior in milling of thin walls, and in work of [10,11,12], authors thus illustrate the influence of the trajectory of the cutting tool on the surface quality tolerances of manufacture for machining on the machine tool has numerical control.

* Corresponding author. am_rahou@yahoo.fr

2. Sources of errors

Before we look at how the task of error compensation can be achieved, we need to clearly understand what we mean by accuracy and error. Accuracy could be defined as the degree of agreement or conformance of a finished part with the required dimensional and geometrical accuracy [13]. Error, on the other hand, can be understood as any deviation in the position of the cutting edge from the theoretically required value to produce a workpiece of the specified tolerance. The extent of error in a machine gives a measure of its accuracy; that is the maximum translation error between any two points in the work volume of the machine. This of course depends on the resolution of the system. Positioning can never be more accurate than this as there will be no further feedback to improve the positioning within this range. However, more important than system resolution, are the errors that occur between the measurement point and the feedback point [14]. The best way to keep track of the errors is to formulate an error budget. An error budget allocates resources among the different components of a machine. It is a system analysis tool used for the prediction and control of the total error of a system. An error budget basically addresses two fundamental issues. One involves obtaining the influence of different sources of error (the individual members of the kinematic chain of the machine tool) on the accuracy of the machine. The other involves taking a set of specifications and determining the permissible level of each source so that some criterion like cost etc., is optimised [15]. Errors can be classified into two categories namely quasi-static errors and dynamic errors. Quasi-static errors are those between the tool and the workpiece that are slowly varying with time and related to the structure of the machine tool itself. These sources include the geometric/kinematic errors, errors due to dead weight of the machine's components and those due to thermally induced strains in the machine tool structure. Dynamic errors on the other hand are caused by sources such as spindle error motion, vibrations of the machine structure, controller errors etc. These are more dependent on the particular operating conditions of the machine. Quasistatic errors account for about 70 percent of the total error of the machine tool and as such, are a major focus of error compensation research. Once the individual error components have been identified, the next step in the problem of error budgeting is to determine the optimal level of these errors so that the cost factor is minimised [15].

In general, a machining centre consists of a bed, column, spindle and its slide and the various linear and/or rotary axes. Each of these elements contributes to the total error of the system that is represented by the error budget. Errors can broadly be classified as:

a) Geometric errors of machine components and structures
b) Kinematic errors
c) Errors induced by thermal distortions
d) Errors caused by cutting forces including
   (i) by gravity loads
   (ii) by accelerating axes, and
   (iii) by the cutting action itself
e) Material instability errors
f) Machine assembly-induced errors
g) Instrumentation errors
h) Tool wear
i) Fixturing errors and
j) Other sources of errors like servo errors of the machine (following errors and interpolation algorithmic errors) [16,17,18].

2.1. Geometric and kinematic errors

Geometric errors are those errors that are extant in a machine on account of its basic design, the inaccuracies built-in during assembly and as a result of the components used on the machine.

As such, they form one of the biggest sources of inaccuracy. These errors are concerned with the quasi-static accuracy of surfaces moving relative to one another. Geometric errors can be smooth and continuous or they could exhibit hysteresis or random behaviour. These errors are affected by factors like surface straightness, surface roughness, bearing pre-loads etc. Geometric errors have various components like linear displacement error (positioning accuracy), straightness and flatness of movement of the axis, spindle inclination angle, squareness error, backlash error etc [17]. Kinematic errors are concerned with the relative motion errors of several moving machine components that need to move in accordance with precise functional requirements. These errors are particularly significant during the combined motion of different axes as in the case of gear hobbing or profile machining where co-ordination of rotary with respect to linear axes or linear with respect to linear axes is of prime importance. Such errors occur during the execution of linear, circular or other types of interpolation algorithms and are more pronounced during actual machining.

2.2. Thermal errors

Another principal cause for inaccurate workpieces is error due to improper tool positioning on account of thermal deformation. It is well understood that errors due to thermal factors account for 40–70% of the total dimensional and shape errors of a workpiece in precision engineering [19]. Six sources of thermal influence are identified: (i) heat from the cutting process, (ii) heat generated by the machine, (iii) heating or cooling provided by the cooling systems, (iv) heating or cooling influence of the room, (v) the effect of people and (vi) thermal memory from any previous environment [19]. Critical among these sources is heat generated by the machine. Continuous running of the machine causes heat to be generated at the moving elements as a result of frictional resistance, at the motors, in pumps etc [20]. This heat causes relative expansion of the various elements of the machine tool leading to inaccurate positioning of the cutting tool tip.

Consequently errors due to spindle growth, thermal expansion of the ballscrews and thermal distortion of the column are generated at the tool tip. As heat generation at contact points is unavoidable, this source of error is one of the most difficult to eliminate completely. In the manufacture of precision components error due to thermal deformation of the machine elements plays a vital role in limiting the accuracy of the part produced.

2.3. Cutting-force induced errors

The dynamic stiffness of all the components of the machine tool (namely the bed, column, etc.) that are within the force–flux flow of the machine is responsible for errors caused as a result of the cutting action. This is one of the major sources of error in metal-cutting machines as the force involved in the cutting action is considerable. As a result of the forces, the position of the tool tip with respect to the workpiece varies on account of the distortion of the various elements of the machine. Depending on the stiffness of the structure under the particular cutting conditions, the accuracy of the machine tool would vary. Thus, for a machine with a given stiffness a heavy cut would generally produce more inaccurate components than a light cut.

2.4. Other errors

Other errors like tool wear and fixturing errors add to the overall inaccuracy of the machined component. Errors in fixturing are caused by fixture set-up and geometric inaccuracies of the locating elements and by fixture flexure. In cases where the workpiece is restrained by a small area of contact with the fixture, the errors due to deformation or lift-off of the workpiece could cause significant errors. Workpiece displacement is dependent on several factors like position of the fixturing elements, clamping sequence, clamping intensity, type of contact surface etc. Thus workpiece displacement could be a significant source of machine error.

3. Systematic dispersion

Systematic dispersion is due primarily to the wear of the cutting tool between the realization of the first part and the last part of a given series (Figure1).

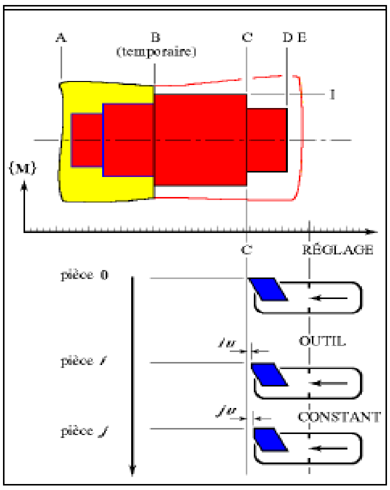

Figure 1: Wear of tool [22]

The wear of the tool leads us to make an experimental study which makes it possible to show the influence of systematic dispersion on the manufacturing tolerances.

4. Procedure of the tests

It is difficult, if not impossible; to obtain manufacturing tolerances while being limited only to systematic dispersions. For this reason, it is necessary to take into account all dispersions. In order to achieve this goal, there are three stages:

1st stage:

The machining of the parts is done without the elimination of dispersions (random, systematic) so that one finds the manufacturing tolerances according to total dispersions.

2nd stage:

The results of the first stage were filtered in such way that one only finds the tolerances of manufacture according to random dispersions.

3rd stage:

From the two previous stages, we compute the systematic dispersions.

5. Conditions of the tests

We have machined 40 parts, C35 matter, on lathe with numerical control using a facing tool with standard brought back pastille “J11ER”

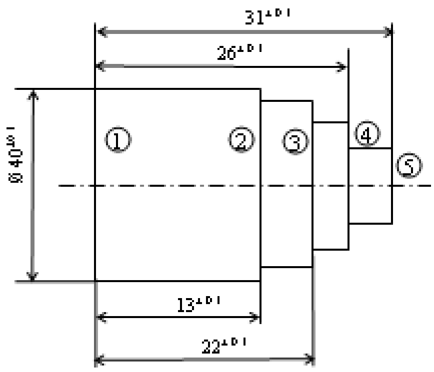

Figure 2: Design drawing of the workpiece.

We place the test in the following conditions:

- The wear of the tool is a linear function;
- Thermal balance is reached;
- Geometrical dispersion is immersed in random dispersion;
- The machining of surface 1 is carried out under phase with the same tool;

6. Stages of manufacture

After having presented the procedure, let us detail the three stages of the study:

6.1. First stage

Starting from a crude, we carried out 5 surfaces on a lathe white numerical control, (Figure 3), by respecting the following parameters of the cut:

- Cutting speed: Cs = 80 m/mn;
- Speed in advance: F = 0.05 mm/tr;
- machining without lubrication;
- Depth of cut = 2 mm;

A program of machining was developed under a language FANUC (Figure3), for the realization of these tests

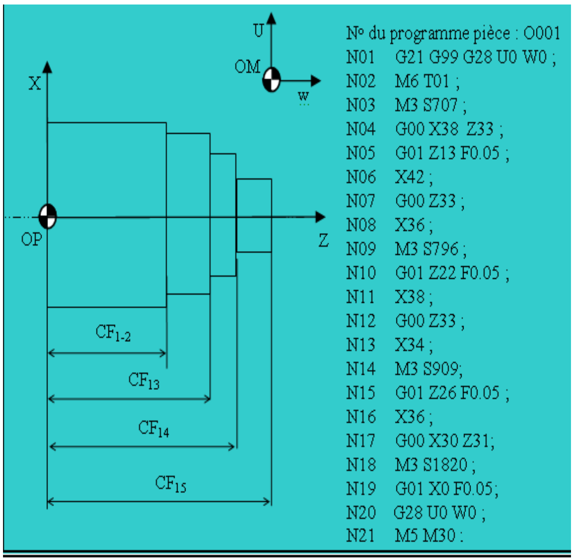

Figure 3: Sketch of turning phase

On each part of the series, we measures dimensions d12, d13, d14, d15 and we calculates d23.

From the *equations (1), (2) and (3)*, we gives the statistical results (the average X, the standard deviations σ_{ij} and ΔCF_{ij}) illustrated in Table 1

Table 1: Statistical Results of the 1st stage

	X (mm)	δ (mm)	ΔCFij (mm)
d12	13.0052	3.489 10-2	2.093 10-1
d13	22.0074	2.860 10-2	1.716 10-1
d14	26.0076	3.199 10-2	1.917 10-1
d15	31.0141	2.685 10-2	1.611 10-1
d23	9.0020	3.369 10-2	2.021 10-1

$$\bar{x} = \frac{1}{N}\sum_{i=1}^{N} n_i \; x_i \tag{1}$$

$$v(x) = \sum_{i=1}^{N} \frac{n_i}{N}(x_i - \bar{x})^2 \tag{2}$$

$$\sigma = \sqrt{v(x)} \tag{3}$$

The system (5), is deduced by the *equation (4)*

$$\Delta CF_{ij} = \Delta l_i + \Delta l_j \tag{4}$$

$$\begin{cases} \Delta CF_{12} = \Delta l_1 + \Delta l_2 \\ \Delta CF_{13} = \Delta l_1 + \Delta l_3 \\ \Delta CF_{14} = \Delta l_1 + \Delta l_4 \\ \Delta CF_{25} = \Delta l_2 + \Delta l_5 \\ \Delta CF_{23} = \Delta l_2 + \Delta l_3 \end{cases} \tag{5}$$

The resolution of the *system (5)* leads to the *solutions (6)*:

$$\begin{cases} \Delta l_1 = 8.949 \quad 10^{-2} \text{ mm} \\ \Delta l_2 = 1.200 \quad 10^{-1} \text{ mm} \\ \Delta l_3 = 8.221 \quad 10^{-2} \text{ mm} \\ \Delta l_4 = 1.029 \quad 10^{-1} \text{ mm} \\ \Delta l_5 = 7.199 \quad 10^{-2} \text{ mm} \end{cases} \tag{6}$$

The results (6) represent total dispersions.

6.2. Second stage

In this stage, *formula (7)* was used to filter dimensions of the first stage.

$$da_{ij} = dt_{ij} - \frac{\Delta CFs_{ij}}{N} i \tag{7}$$

ΔCFs_{ij} : The variation of the dimensions manufactured with systematic dispersion;
da_{ij} : Filtered dimensions;
dt_{ij} : Dimensions according to total dispersion;
i : Number of test;
To calculate Δs_{ij} , we trace for each dij the graphs (dij (N)) and average lines, Figure (4-8).

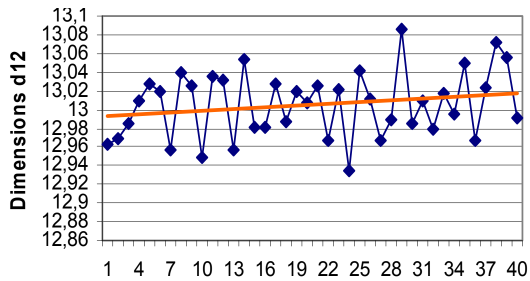

Figure 4: Graph of dimensions d12

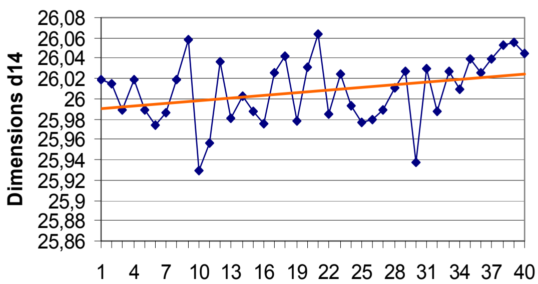

Figure 5: Graph of dimensions d14

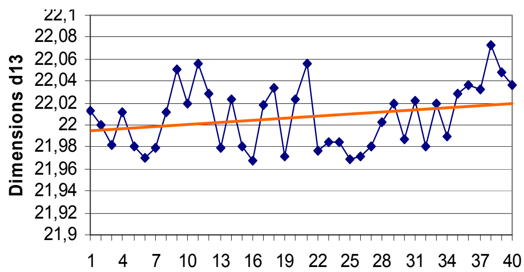

Figure 6: Graph of dimensions d13

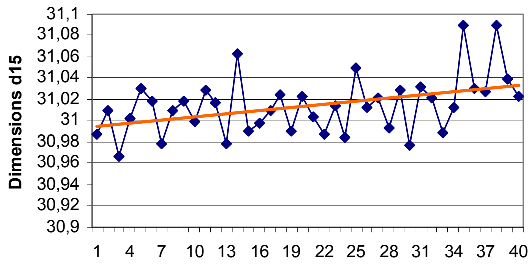

Figure 7: Graph of dimensions d15

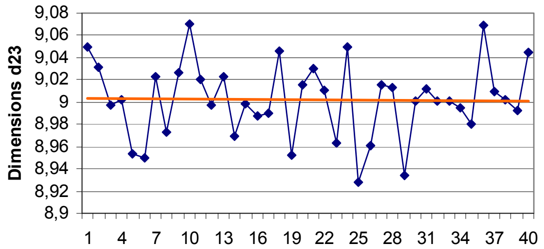

Figure 8: Graph of dimensions d23

The variation of manufacture, expression (8), is given according to the average line tangent a_{ij} and of the tests number N.

$$\Delta CFs_{ij} = a_{ij}.N \tag{8}$$

The resolution of the *system (8)* gives the results of ΔCFs_{ij} ,represented by *(9)*.

$$\begin{cases} \Delta CFs_{12} = 2.656\ \ 10^{-2}\ \text{mm} \\ \Delta CFs_{13} = 2.508\ \ 10^{-2}\ \text{mm} \\ \Delta CFs_{14} = 3.428\ \ 10^{-2}\ \text{mm} \\ \Delta CFs_{15} = 3.816\ \ 10^{-2}\ \text{mm} \\ \Delta CFs_{23} = 0.169\ \ 10^{-2}\ \text{mm} \end{cases} \tag{9}$$

From the *equation (7)* and the *system (9),* calculation gives new dimensions (da_{ij}) .

Table 2 represents the statistical results calculated starting from the *equations (1), (2) and (3)*

Table 2: Statistical results of the 2nd stage.

	X (mm)	δ (mm)	ΔCFaij (mm)
da12	12.992	3.403 10-2	2.041 10-1
da13	21.995	2.767 10-2	1.661 10-1
da14	25.991	3.042 10-2	1.825 10-1
da15	30.995	2.448 10-2	1.469 10-1
da23	9.003	3.369 10-2	2.021 10-1

According to the *equation (10),* there is the system of expressions (11)

$$\Delta CFa_{ij} = \Delta la_i + \Delta la_j \tag{10}$$

$$\begin{cases} \Delta CFa_{12} = \Delta la_1 + \Delta la_2 \\ \Delta CFa_{13} = \Delta la_1 + \Delta la_3 \\ \Delta CFa_{14} = \Delta la_1 + \Delta la_4 \\ \Delta CFa_{25} = \Delta la_2 + \Delta la_5 \\ \Delta CFa_{23} = \Delta la_2 + \Delta la_3 \end{cases} \tag{11}$$

The resolution of the *system (11)* leads to the *solutions (12)* :

$$\begin{cases} \Delta a_1 = 8.379\quad 10^{-2}\ \text{mm} \\ \Delta a_2 = 1.199\quad 10^{-1}\ \text{mm} \\ \Delta a_3 = 8.200\quad 10^{-2}\ \text{mm} \\ \Delta a_4 = 9.824\quad 10^{-2}\ \text{mm} \\ \Delta a_5 = 6.279\quad 10^{-2}\ \text{mm} \end{cases} \tag{12}$$

The result of system (12) represents random dispersions.

6.3. Third Stage

In this stage we trace the graphs of the dimensions filtered (daij) according to many tests (N).

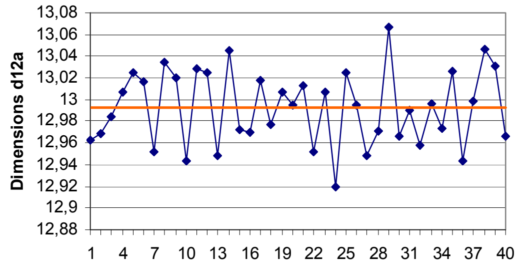

Figure 9: Graph of dimensions da12

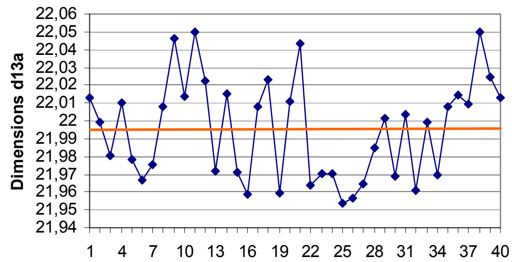

Figure 10: Graph of dimensions da13

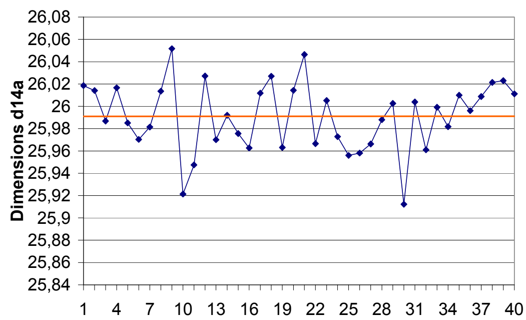

Figure 11: Graph of dimensions da14

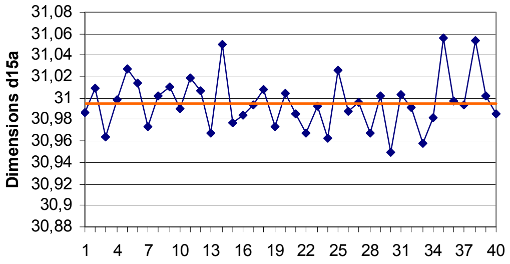

Figure 12: Graph of dimensions da15

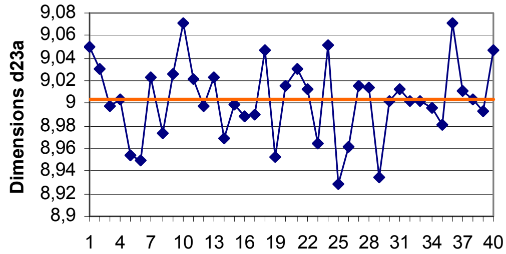

Figure 13: Graph of dimensions da23

According to figures' (9), (10), (11), (12), (13), we notice that the tangents are equal to zero. Therefore filtering is made completely. The replacement of the equation *(13)* in the *system (14),* leads to the *system (15).*

$$\Delta CFs_{ij} = \Delta s_i + \Delta s_j \qquad (13)$$

$$\begin{cases} \Delta CFs_{12} = 2.656 \ \ 10^{-2} \text{ mm} \\ \Delta CFs_{13} = 2.508 \ \ 10^{-2} \text{ mm} \\ \Delta CFs_{14} = 3.428 \ \ 10^{-2} \text{ mm} \\ \Delta CFs_{15} = 3.816 \ \ 10^{-2} \text{ mm} \\ \Delta CFs_{23} = 0.169 \ \ 10^{-2} \text{ mm} \end{cases} \qquad (14)$$

$$\begin{cases} \Delta s_1 = 2.497 \quad 10^{-2} \text{ mm} \\ \Delta s_2 = 0.158 \quad 10^{-2} \text{ mm} \\ \Delta s_3 = 0.00105 \quad 10^{-2} \text{ mm} \\ \Delta s_4 = 0.931 \quad 10^{-2} \text{ mm} \\ \Delta s_5 = 1.319 \quad 10^{-2} \text{ mm} \end{cases} \qquad (15)$$

The results of *system (15)* represent systematic dispersion.

7. Interpretation

Table 3 presents a recapitulation of the results of the dispersions calculated in the three stages.

Table 3: Results of calculated dispersions.

	Total dispersion (mm)	Random dispersion (mm)	Systematic dispersion (mm)
Surface 1	$0.895\ 10^{-1}$	$0.837\ 10^{-1}$	$2.497\ 10^{-2}$
Surface 2	$1.200\ 10^{-1}$	$1.199\ 10^{-1}$	$0.158\ 10^{-2}$
Surface 3	$0.822\ 10^{-1}$	$0.819\ 10^{-1}$	$0.105\ 10^{-3}$
Surface 4	$1.029\ 10^{-1}$	$0.982\ 10^{-1}$	$0.931\ 10^{-2}$
Surface 5	$0.719\ 10^{-1}$	$0.627\ 10^{-1}$	$1.319 10^{-2}$
Summon	$4.667\ 10^{-1}$	$4.462\ 10^{-1}$	$0.490\ 10^{-1}$

In figure 17 the graph of total dispersion is almost confused with the graph of random dispersion. The influence of systematic dispersions on the tolerances of manufacture is minimal Compared to random dispersions.

The greatest value of systematic dispersions (Figure 14) is on surface 1 used like reference surfaces, due to the influence of the machined surfaces 2, 3, 4, 5, and the grinding problem of the tool.

On the other hand the greatest value of random dispersions (Figure 15) is on the level of surface 2, then surface 4. The order of surfaces is not imperative; it has a relationship to the setting in position of the part in the chuck, the quality of tightening (manual or pneumatic) or the stop materializing the fifth point of isostatism. The smallest value is at the level of surface 3, since the latter is between two machined surfaces characterized by a small machining length.

The values of systematic dispersions are very small relative with total dispersion. The sum of the values of systematic dispersions is about 10% of the sum of total dispersions. Therefore random dispersion accounts for 90% of total dispersion.

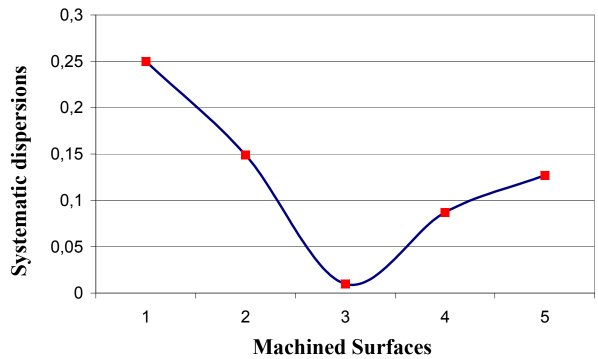

Figure 14: Systematic dispersions according to the machined surfaces.

Figure 15: Random dispersions according to the machined surfaces.

Figure 16 represents the evolution of total dispersions according to the machined surfaces.

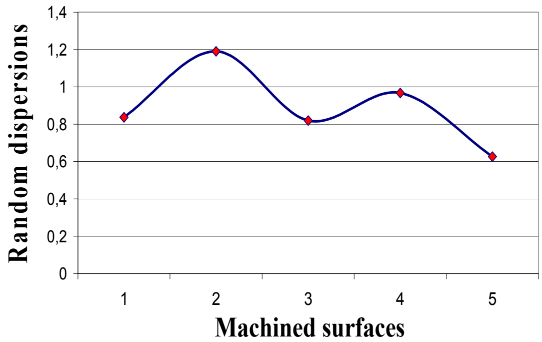

Figure 16: Total dispersions according to the machined surfaces.

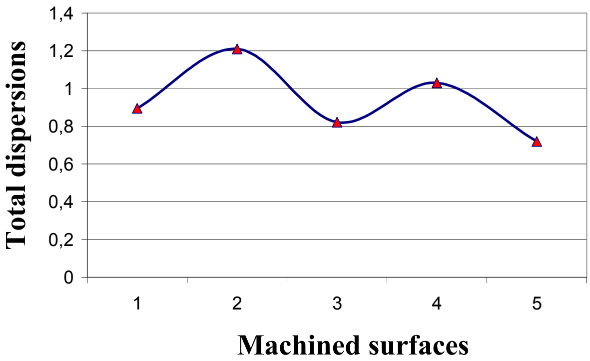

Figure 17 illustrates a comparison between total dispersions and random dispersions.

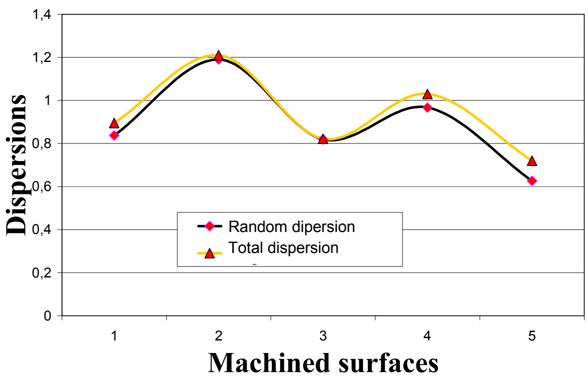

Figure 17: Comparison enters total and random dispersions.

Figure 18 illustrates the percentage between the sum of the values of systematic dispersions and the sum of the values of total dispersions.

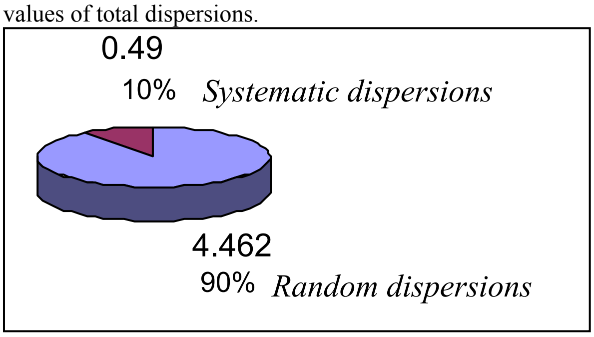

Figure 18: Statistical representation by sector between systematic dispersion and random dispersion.

8. Errors modeling

In this part, a modeling of the errors of dispersions was worked out by the least squares method to develop two models of correction of the tolerances. In the first model, *equation 16*, we can calculate tolerances of manufacture due to systematic dispersion according to the machined length. In the second model, *equation 17*, we can calculate tolerances of manufacture according to the machined length

$$IT = 6{,}5.10^{-4}\ \sqrt[3.5]{D}\ +\ 1{,}3.10^{-5}.D\ + 1{,}2.10^{-5} \qquad (16)$$

$$IT\ = 0.05\ \ \sqrt[3.5]{D}\ \ +\ \ 10^{-3}.D\ \ + 10^{-3} \qquad (17)$$

After the integration of tolerancing models in the numerical command control program, the new statistical results are given by the Table 4 .

According to the results, the variations of manufacture (tolerance of manufacture) were decrease by 55 % .

Table 4: Statistical Results.

	X (mm)	δ (mm)	ΔCFij (mm)
d12	13.0022	0.01958	0.11748
d13	22.0024	0.01867	0.11202
d14	26.0016	0.01874	0.11244
d15	31.0031	0.01685	0.1011
d23	9.0002	0.02269	0.13614

9. Conclusion

In this work, a step centered on three stages, was presented to calculate dispersions of machining and their influence on the intervals of tolerances. The influence of systematic dispersion accounts for 10% of the total discrepancies under the conditions normal and between 25% and 35%, if the parameters of cut or the cutting tool are badly selected.

The relative value of 10% of the tolerance is very important especially in work in series; because the wear of the tool influences the dimensions of adjustment. An error about the micron influences the overall costs of the end product and risk to guarantee the competitiveness of the product on the market.

Two models of compensation the error in the tool machine numerical control were developed, the first models it is the calculation of systematic dispersion according to the machined length; for the second it is the calculation of the tolerances of manufacture (total dispersions) according to the machined length. These models allowed us optimize the manufacturing dimensions , that is to say by integration in the command balls or in the machining programming

References

[1] Rong Y, Bai Y Machining accuracy analysis for computer-aided fixture design verification. J Manuf Sci Eng, Vol. 118, 1996, 289–300.

[2] Cai W, Hu SJ et al A variational method of robust fixture configuration design for 3-D workpieces. J Manuf Sci Eng , Vol. 119, 1997, 593–602.

[3] Djurdjanovic D, Ni J Dimensional errors of fixtures, locating and measurement datum features in the stream of variation modeling in machining. J Manuf Sci Eng Trans ASME, Vol. 125, No. 4, 2003, 716–730.

[4] K. Kim, M.K. Kim, Volumetric accuracy analysis based on generalized geometric error model in multi-axis machine tools, Mech. Mach. Theory, Vol. 26 , No.2, 1991, 207–219.

[5] K.F. Eman, B.T. Wu, A Generalized error model for multi-axis machines, Annals of the CIRP Vol. 36 , No. 1, 1987, 253–256 .

[6] Y. Kakino, Y. Ihara, A. Shinohara. Accuracy Inspection of NC Machine Tools by Double Ball Bar Method. Hanser Publishers, Munich, Germany 191, 1993.

[7] Y. Takeuchi, T. Idemura, Generation of five-axis control collision free tool path and post processing for NC-data, Annals of the CIRP Vol. 41, No. 1, 1992, 539–542 .

[8] N .Ouelaa, N .Kribes , A .Rezaiguia, M.A Yallese Etude semi-expérimentale du comportement vibratoire de l'outil de coupe lors de l'opération de chariotage " 5th internationale conference cpi 2003 Rabat

[9] T. Vincent, A .Lionel, D. Gilles, C .Gilles Influence de la position de l'outil sur le comportement dynamique en fraisage de parois minces " , Mécanique & Industries, Vol. 6, 2005, 403–410 .

[10] L. Sotiris,C .Andreas. Nearchoub A CNC machine tool interpolator for surfaces of cross-sectional design " Robotics and Computer-Integrated Manufacturing, Vol. 23, 2007, 257–264 .

[11] L. Andre , S .Klaus Investigation of tool path interpolation on the manufacturing of die and molds with HSC technology" Journal of Materials Processing Technology Vol. 179, 2006, 178–184

[12] Eing-Jer Wei, Ming-Chang Study on general analytical method for CNC machining the free-form surfaces" Journal of Materials Processing Technology, Vol. 168, 2005, 408–413

[13] J. Jedrzejewski, W. Modrzycki, Intelligent supervision of thermal deformations in high precision machine tools, Proc. 32nd Int. MATADOR Conf, Manchester, UK, 1997, pp. 457–462.

[14] T.J. Morris, The REAL Accuracy of machine tools, Proc. 3rd Int. Conf. on Laser Metrology and Machine Performance — LAMDAMAP, 1997, 113–122.

[15] C.J. Evans, R.J. Kocken, Self-calibration: reversal, redundancy, error separation and absolute testing, Annals of the CIRP Vol. 45, No. 2, 1996, 617–632.

[16] M.A. Donmez, A general methodology for machine tool accuracy enhancement: theory, application and implementation, PhD dissertation, Purdue University, 1985.

[17] J. Ni, CNC machine accuracy enhancement through real-time error compensation, ASME Trans Journal of Manufacturing Science and Engineering , Vol. 119, 1997, 717–724.

[18] A.H. Slocum, Precision Machine Design, Prentice Hall, 1992.

[19] J. Bryan, International status of thermal error research, Annals of the CIRP Vol. 39 , No. 2, 1990, 645–656.

[20] R. Venugopal, Thermal effects on the accuracy of numerically controlled machine tools, PhD dissertation, Purdue University,. (1985)

[21] P. BOURDET, Chaînes de cotes de fabrication (Méthode des delta l): deuxième partie Mode opératoire" L'ingénieur et le Technicien de l'Enseignement Technique, ENS, Cachan. 2003.

[22] Guy M. CLOUTIER, FAO et Machines-Outils simulation d'usinage", Mec4510, ENS, Cachan. 2002.

JJMIE

Volume 4, Number 5, November 2010
ISSN 1995-6665
Pages 605 - 614

Jordan Journal of Mechanical and Industrial Engineering www.jjmie.hu.edu.jo

Ballistic Impact Fracture Behaviour of Continuous Fibre Reinforced Al-Matrix Composites.

Al-Hamdan Ali*, Yassin L. Nimir, Ramadan J. Mustafa

Faculty of Engineering, Mechanical Engineering Department, Mu'tah University, Jordan.

Abstract

The materials response under high energy impact loads was studied using a gas gun. The projectiles were pins 1.2-1.5 mm in diameter and weighing 0.347-0.435 g. The projectile velocity was in the range 100–1300 m/s. The remnant load carrying capability of composite samples after high velocity impact tests was measured to quantify high energy impact induced microstructural damage. The composites retained some of their load bearing capacity even after penetration of the projectile, since structural damage caused by projectiles remained localised, preventing catastrophic failure, particularly for continuous fibre reinforced Al_{pure} matrix composites. Penetration by the projectile occurred at impact energy of about 62-65 J for the conditions investigated. The experimental findings show that the energy absorbing capacity of such composites and their ability to withstand a given blow are largely functions of fibre type and greatly influenced by the matrix ductility, fibre-matrix interfacial bonding and volume fraction of reinforcing fibre. Understanding crack propagation and damage development under high energy impact loads may open new opportunities for the use of these composites in lightweight armour applications.

Keywords: Fracture Behaviour, Composite materials, Fibre reinforced, Ceramic matrix, Metal matrix, High energy impact, High velocity.

1. Introduction

Since the 1960's, considerable interest has been given to metal-ceramic laminated composites armours because of their unique combination of strength, fracture toughness, high hardness and low density that make them ideal candidates for light weight protective systems [1-19]. At present they are developed to replace conventional matrix alloys and ceramic materials in specifically required engineering components. Very little work has been done on examining the impact response of ceramic fibre reinforced metal matrix composites at impact velocities above 500 m/s. Cantwell and Morton [5] have shown that the response of a Carbon fibre reinforced composites to low and high velocity impact loading was quite different. On the one hand, for low velocity impact, the size and shape of the panel determined its energy absorbing capability. Whereas, the high velocity projectiles induced a localised response in the target that did not depend on the real size of the target. Cantwell et al. [21] have previously shown that below an impact energy of 50 J, the energy absorbed by 3 mm and 6 mm plates dropped off and appeared to approach an asymptotic level. For a 6- mm thick CFRP composite panel, the level of damage also appeared to drop off and approached a constant level whereas with the 3 mm target the level of damage appeared to be constant regardless of the impact energy. The observed constant level of damage in the 3 mm panel was probably due to the fact that the level of damage had already plateaued before the minimum impact velocity used in these experimental trials was reached. Indeed, Lee and sun [20] have shown that the drop off in a real damage occurred at an impact energy of 20 J for 4 and 5-mm diameter spheres impacting a 2-mm thick graphite/epoxy laminates. This was at much lower impact energy than was tested in [5]. Recent studies [3, 12, 18] on impact response of a variety of carbon-fibre-based laminates at velocities between 150 and 1000 m/s. In their work, they employed embedded PVDF stress gauges and constantan strain gauges to assess the stress and strain response of the

* Corresponding author: Hayajneh@mutah.edu.jo

materials when subjected to impact and penetration. They found that the maximum stress generated in the CFRPs depended on the nature of the reinforcing fibres. Further, they noted that above a critical measured stress, the fracture of the CFRP was ‘‘fluid-like’’ in that comminution of the material had occurred. They also observed, what they described as a ‘‘fluid-like’’ failure of the laminate. Notably, they showed that there was no clear difference in the energy absorbing abilities between cross-ply specimens and specimens consisting of a five-harness woven cloth. They also showed that the delamination width depended on impact energy. Here they showed that the maximum damage inflicted by the projectile at the ballistic limit was produced at normal incidence [3]. Furthermore, below the ballistic limit, the extent of damage for normal impact was larger than that for the oblique impact. However, the extent of damage at higher velocities appeared to be greater for oblique impacts. The objective of this study was to experimentally examine the response of a range of performs of continuous Silicon Carbide (SiC), high strength (HS) Carbon, and tungsten fibre reinforced Al_{pure} and Al-Si-Mg metal matrix materials under high energy impact loads using a gas gun. The remnant load carrying capability of composite samples after the high velocity impact tests was measured to quantify the high energy impact induced failure.

2. Experimental methodology

2.1. Materials

The composite materials utilized in this study were made from unidirectionally infiltrated 99.95% commercially pure aluminium Alpure and aluminium alloy(6061) Alalloy matrix into performs of continuous high strength carbon (H.S.C), tungsten (w), and Silicon Carbide (SiC) fibres, and the mechanical properties of the constituents are shown in table 1-3. The composite material was manufactured by a liquid infiltration technique, Detailed information of the constituents and processing conditions can be found in [10-12]. Fibre volume fractions of unidirectional specimens were determined by optical numeric volume fraction analysis (ONVF) technique which is described in details in [13], and the analysis indicated that the volume fraction of fibres was consistent from plate to plate, with a volume fraction of 45%±3% for all composites.

The type and geometry of the test specimens were dictated by the size and quantity of the fabricated materials plates produced. Using a diamond saw, specimens with dimensions 75 x 10 x 3 mm were then cut from unidirectional material plates.

Table (1): Properties of the selected continuous fibre reinforcement, [9,2014,21]

Properties	High Strength Carbon fibre(H.S.C)	Silicon Carbide fibre (SiC)	Tungsten (w)
Fibre Diameter, μm	7-30	12-20	10-150
Density, Mg/m^3	1.75-1.9	2.5	19.2
Young's Modulus, GPa	230-270	190-200	400
Poisson's Ratio (v)	0.2	0.25	-
Tensile Strength, GPa	3-4.8	2.5	2.5
Failure Strain, %	1.1	-	-
Thermal Expansivity, $10^{-6} K^{-1}$	(-0.4)-(-1.2)	4.5	5
Thermal Conductivity, $Wm^{-1}K^{-1}$	24	-	-

Table (2): Chemical composition of Al (1100) and Al (6061) matrix materials by weight percentage, [8].

Alloy	Si	Mg	Cu	Ti	Fe	Mn	V	Cr	Zn	Be	Other elements
Al(1100)	0.25	0.05	0.05	---	0.04	0.05	0.05	---	---	---	0.03
Al(6061)	0.76	0.92	0.22	0.1	0.28	0.04	0.01	0.07	0.06	0.003	0.45

Table (3): Mechanical properties of Al (1100) and Al (6061) matrix materials, [8].

Material	E (GPa)	σtensile (MPa)	σyield (MPa)	Strain to failure (%)	Poisson ratio (v)
Al(1100)	69	90	34	50-70	0.33
Al(6061)	72	310	275	12	0.33

2.2. High energy impact test and evaluation

High energy impact tests were carried out by impacting composite specimens of dimensions 75 mm 10 mm 3 mm with projectiles of varying velocities using a laboratory gas gun. The diameters of the 2024Al projectiles are in the range 1.22–1.28 mm, and weighing 0.347-0.435g. The projectile velocity range during this investigation was 100-1350 m/s with normal angle. The samples were mechanically clamped to a steel sample holder without a backing plate. The gun employed for this study was a single stage laboratory gas gun capable of firing spherical or cylindrical projectiles with diameters up to 1-12 mm at velocities up to 2500 m/s. A detailed description of the facility used is given by McQuillan [7] and a schematic diagram of the gas gun is shown in Figure 1. The gun uses compressed nitrogen gas to fire the projectile and is operated by a bursting-diaphragm firing mechanism. The compressed gas is transferred from the cylinder to the gas reservoir (on one end of the barrel), which is joined to a breech adaptor. A suitable diaphragm is placed between the barrel and the breech adaptor. The pressure in the reservoir causes the diaphragm to rupture, shooting the projectile through the barrel. The velocity of the projectile is controlled by the pressure, which is required to burst the diaphragm.

The macroscopic damage of the samples after impacts was recorded using a digital camera (Olympus D-510). At least five samples for each testing condition were considered; with the impression left by the high velocity impact was placed in the centre of the sample. As-received and impacted samples were tested on a universal testing machine using a 4-point flexure fixture with 30-mm inner and 60-mm outer spans. Each specimen was placed in the fixture such that its impacted side was under tension and the point of impact was located in the centre of the inner spans. Tests were conducted at a speed of 1 mm/min using a 50 kN load cell. On the basis of data obtained during the 4-point bending tests, Young's modulus was calculated using the following relation:

$$E = \frac{F l_0^2 l_1}{16 J y_o} \tag{1}$$

where,

$$J = \frac{bh^3}{12} \tag{2}$$

with: b, width of sample; h, height of sample; l_1 = 15 mm; l_o = 30 mm; F, maximum load and y_o, deflection at load F, measured using transducers. From the load–deflection curves the load for fracture initiation was recorded. A digital camera (Olympus D-510) was used to document the macroscopic deformation of the sample during 4-point flexure strength test. Fracture surfaces of selected samples were observed by scanning electron microscopy (SEM).

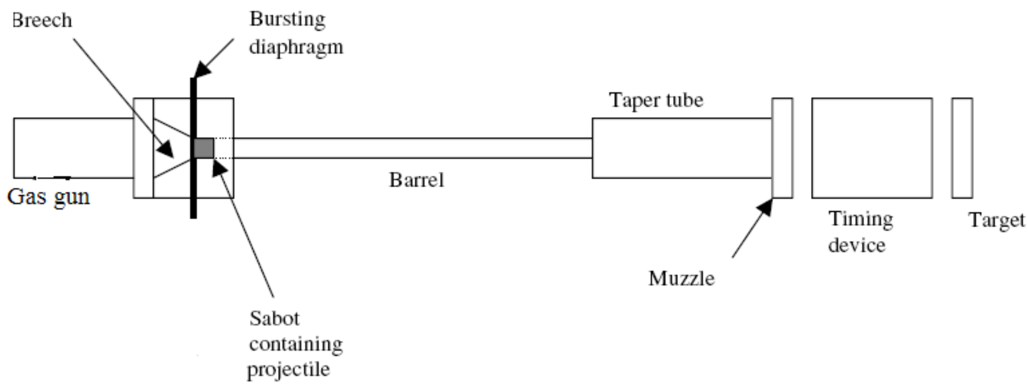

Figure 1 Schematic diagram of the testing apparatus used for the high energy impact tests.

3. Results and Discussion

3.1. High velocity impact resistance and damage

Low energy impacts are associated with delamination damage in fibre reinforced composite materials, and this inter-laminar debonding primarily may reduce the local bending stiffness and thus can affect the bending and buckling behaviour of the structure, by inducing further delamination growth which can lead to overall global weakening of the structure. Such damage has been reported [15-21] to cause as much as a 40% reduction in static and fatigue strength. The results obtained for continuous fibre reinforced Al_{pure} and Al_{6061} matrix composites, when subjected to low energy projectile impacts, demonstrated a typical composite behaviour with the samples remaining in one piece despite some localised damage, Figure 2(a) shows the macroscopic damage caused by a projectile having impact energy of 17.25 J wherein a considerable number of fibres fracture, pulling-out on the front face of the sample can be seen.

Owing to the relatively low impact energy, the sample was not penetrated during this impact.

As impact energy increases, debonding coupled with fibre fragmentation, as in Figure 2(b) for a sample impacted with a projectile of 75.25 J energy, has occurred, with penetration of the projectile through the samples. This and Traces of force versus time of six impact events with incremental incident energies for W-Al_{pure} composite material, and force versus time histories and damage progression for unidirectional C-Al_{pure} shown in figures 3 and 4, respectively,. The samples for continuous fibre reinforced Al_{pure} stayed in one piece and with less damage compared to that of fibre reinforced Al_{6061}, as in Figure 5, this is possibly due to the presence of ductile matrix and a low fibre-matrix interfacial strength, giving rise to energy absorption mechanisms during high energy impact loads. However, due to the complex nature of the metal matrix composite microstructure, post-impact microscopic examination of the impacted surface did not reveal much structural detail. High energy impact [19-29] is defined by the energy required for a projectile to penetrate the rear face of the composite plate, however, from the results obtained for high energy impact seemed that the structural damage was highly localised around the point of impact, and the localised delamination and damage below the surface were easily detected by ultrasonic C-scan, as shown in Figure 6.

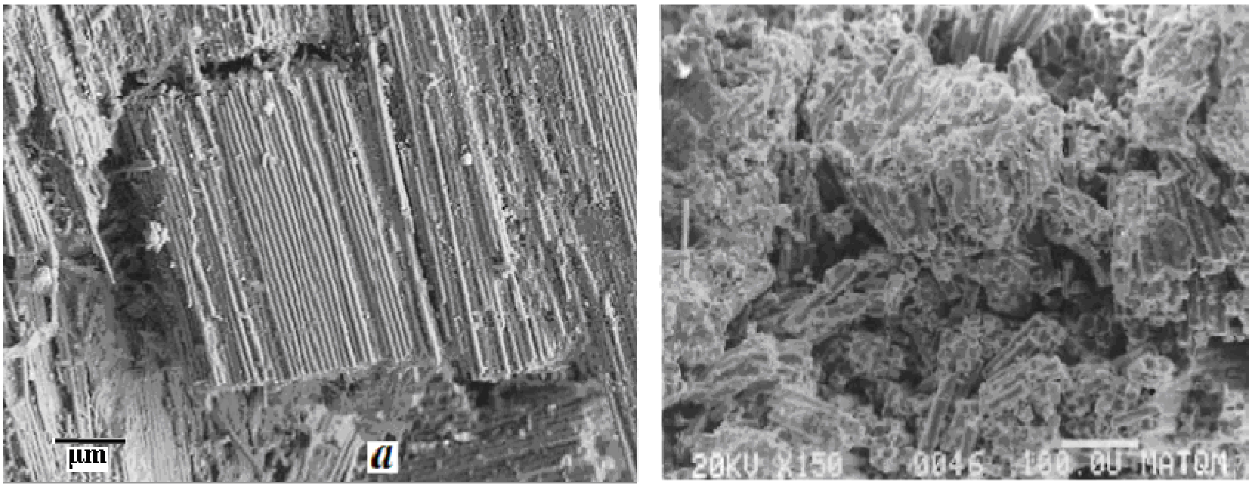

(a) *magnification of a*

Figure 2(a) Micrographs showing the macroscopic damage of SiC-Al_{pure} matrix composite after high velocity impact test at impact energy of 17.25J

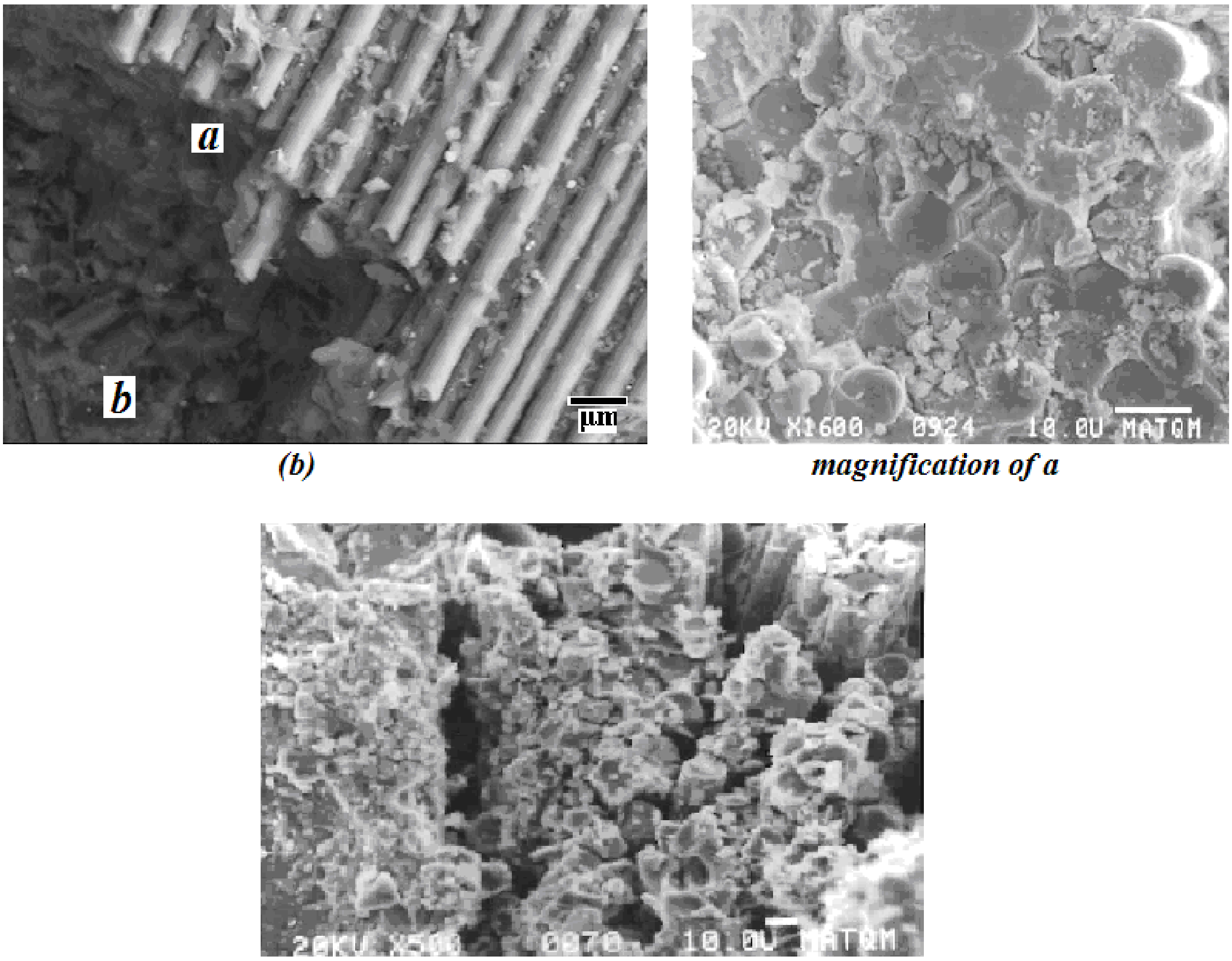

(b) *magnification of a*

magnification of b

Figure 2(b) Micrographs of high energy impacted area (75.25J), showing debonding coupled with fibre fragmentation of C-Al_{pure} composite material, and the higher magnification of area a and b.

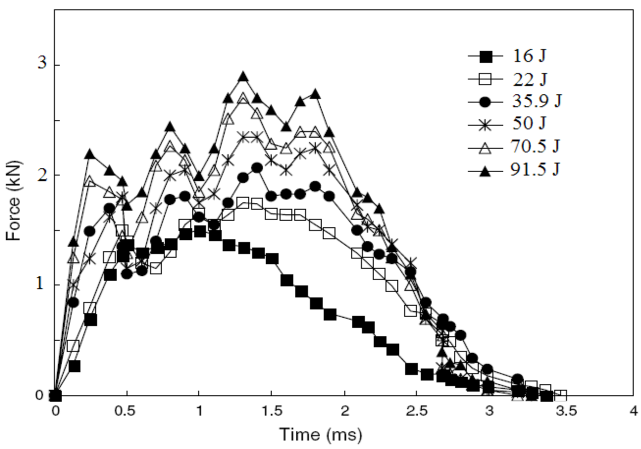

Figure 3(a) Force versus time traces of six impact events with incremental incident energies for w-Al_{pure} composite material.

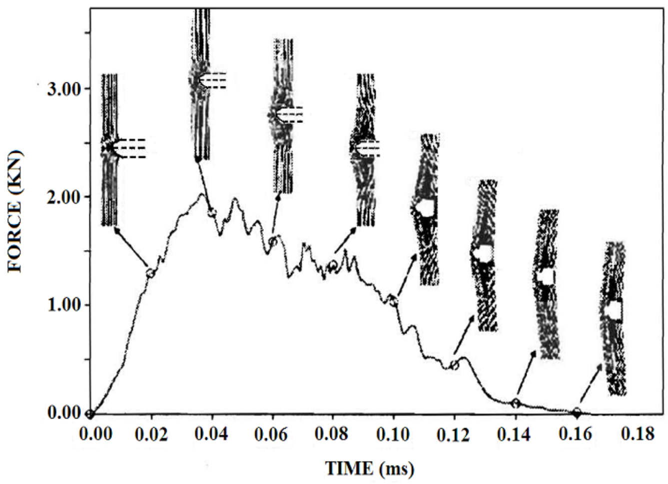

Figure 3(b) Force versus time histories and damage progression for w-Al_{pure} composite material, at an impact velocity of 670 m/s by 2024Al projectile.

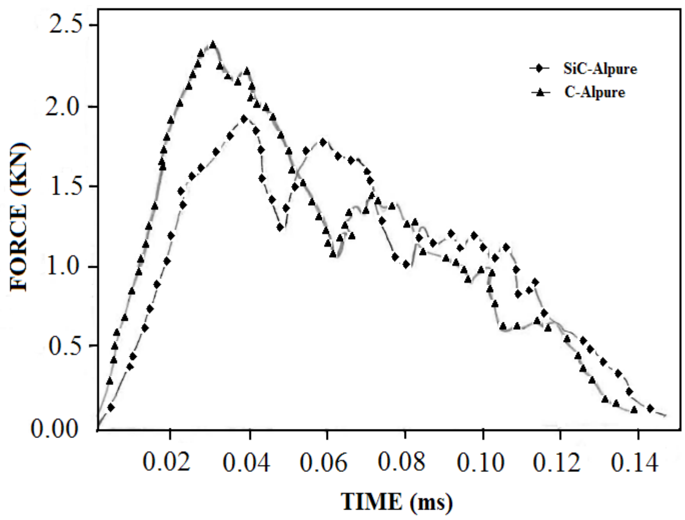

Figure 4 Force versus time histories for C-Al_{pure} and SiC-Al_{pure} composite material, at an impact velocity of 700 m/s by 2024Al projectile.

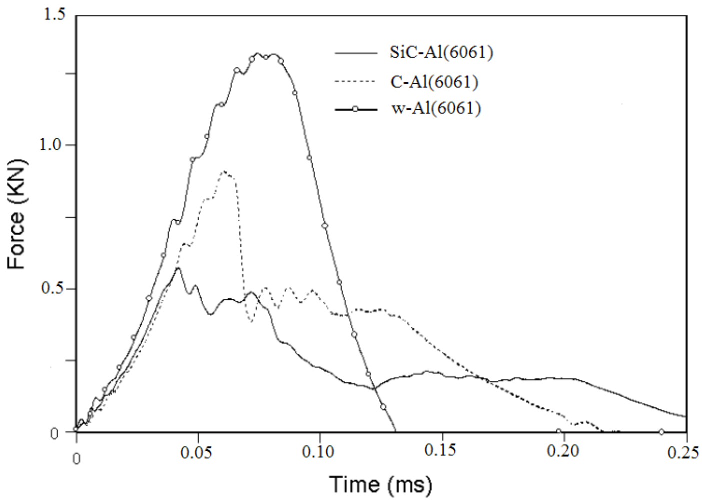

Figure 5 Force versus time histories for C-Al_{6061}, SiC-Al_{6061} , and w-Al_{6061} composite material, at an impact velocity of 700 m/s by 2024Al projectile.

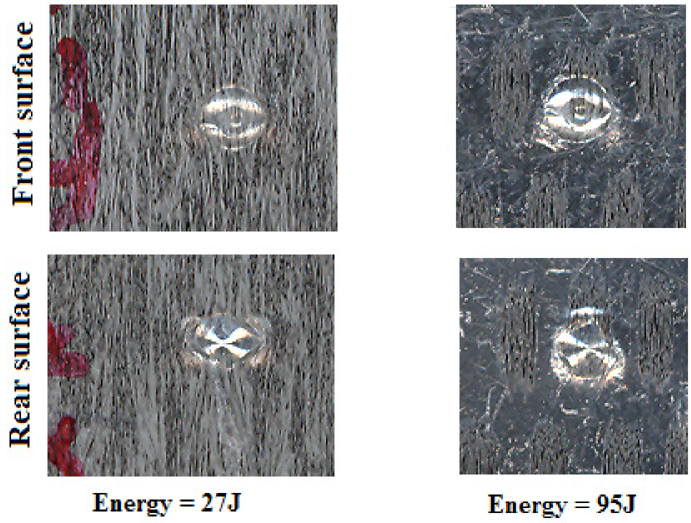

(a) SiC-Al_{6061} (b) SiC-Al_{pure}

Figure 6(a) Insitu observations on the front and rear surface of specimens SiC-Al_{6061} and SiC-Al_{pure} composite materials.

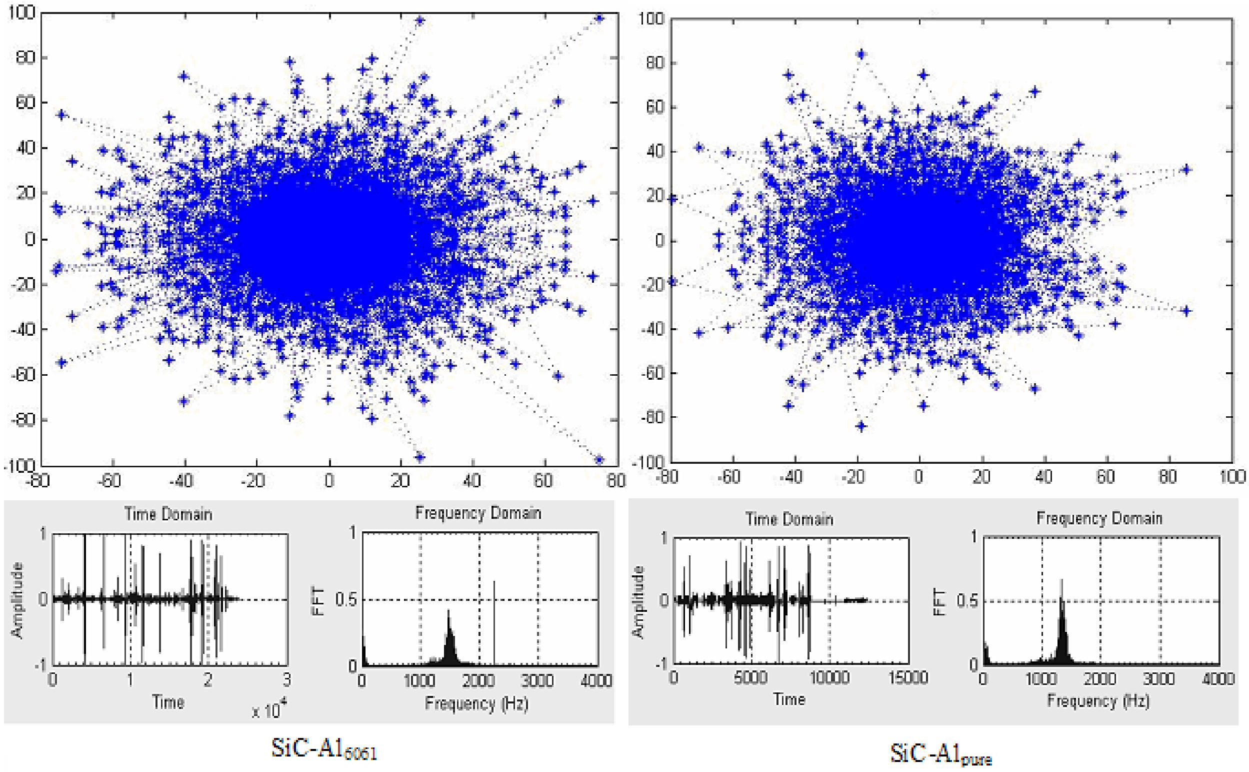

Figure 6 (b) C-scan plot of figure 6 (a) of impact sites on SiC-Al_{6061} and SiC-Al_{pure} composite material, impacted at 173.5 J, showing distinct craters concentration sites.

In order to assess the effects of high velocity impact energy on microstructural damage and on structural integrity of the composite, the damaged samples were subjected to 4-point flexural strength test. Fig.7 shows load–displacement curves for as-received (a), and impact damaged samples(b), (impact energy 85.01 J). with the impression left by the high velocity impact was in the centre of the sample. As expected, the composite under investigation does not fail catastrophically, even after having been substantially damaged by the impact of projectiles. Instead, the material retains its load bearing capacity after the commencement of failure (penetration of the projectile). This behaviour is in agreement with literature reports [3,5,28] on continuous fibre reinforced glass–epoxy matrix composites. Fig. 8 documents the high level of deformation achieved during 4-point flexural strength test in a sample of SiC-Al_{pure} , that had been impacted at an energy of 27.76 J. The sample did not break into two fragments, demonstrating a true composite, ''pseudo-plastic'' behaviour.

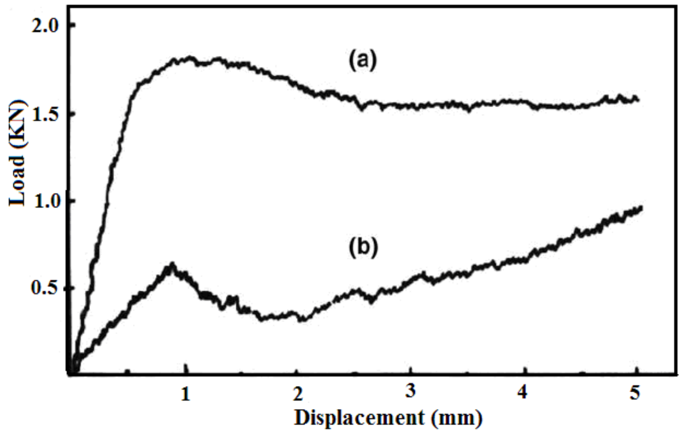

Figure 7 Load-displacement curves for: (a) as received and (b) impact damaged samples in 4-point flexural test for SiC-Al_{6061} composite material impacted at 85.01 J.

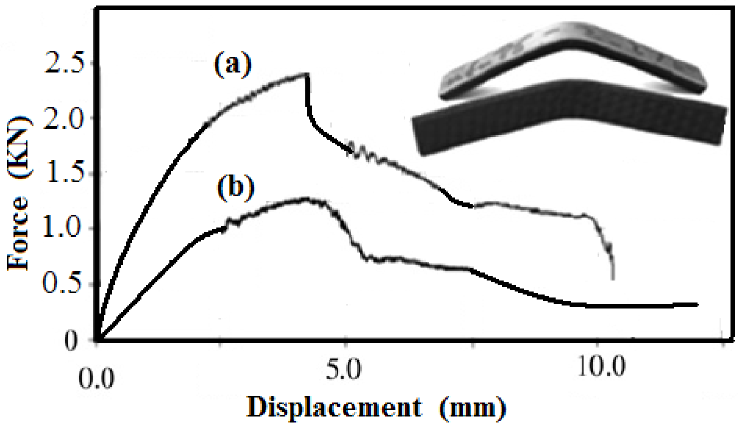

Figure 8 Load-displacement curves for: (a) as received and (b) impact damaged samples in 4-point flexural test for of SiC-Al_{pure} composite material impacted at 27.76 J. showing ''pseudo-plastic'' behaviour.

A plot of relative Young's modulus as a function of impact energy is presented in Fig.9 (a and b). A decrease in elastic modulus after high energy impact for all fibre reinforced Al_{pure} composite materials were observed up to the point of (62-65 J impact energy), whereas, the fibre reinforced Al_{6061} composite materials were observed up to the point of (15.6-27.76 J impact energy) where structural damage is maximum. Samples impacted with higher energy projectiles show an increase in Young's modulus, particularly for fibre reinforced Al_{pure} matrix composites, indicating less structural damage. This is in accordance with the existing understanding that structural damage under high velocity impact increases to a point where impact energy is just sufficient to cause penetration as observed, in polymer and glass–ceramic matrix composites [28,29].

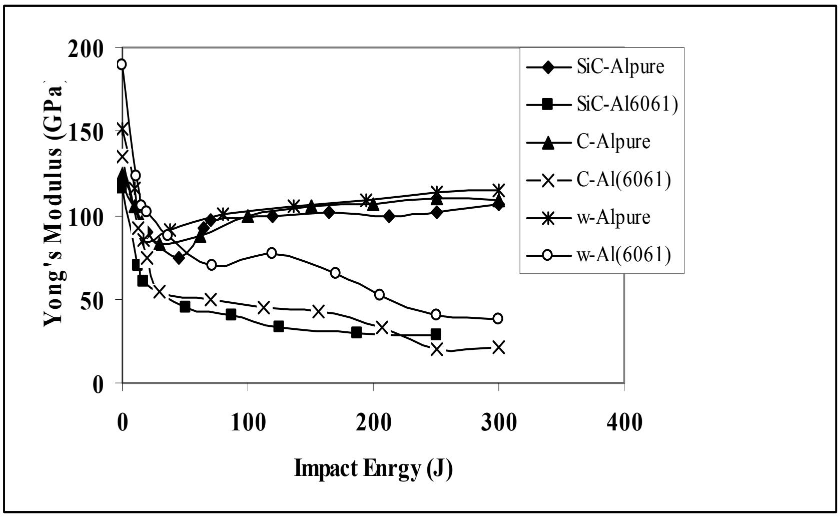

(a)

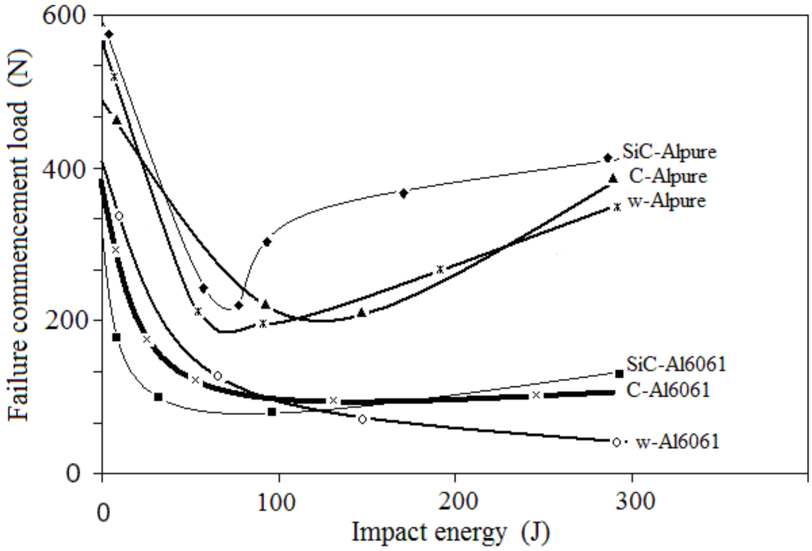

(b)

Figure 9(a) Elastic modulus and (b) fracture load of high velocity impacted Continuous fibre reinforced A_{pure} and Al_{6061} matrix composites as a function of impact energy. The values shown are averages of five measurements and the relative error was in all cases <10%.

The observed continuous decrease of Young's modulus with increasing impact energy of projectile (below 15.5 J), as in Fig.9 (a and b), which is related to the cumulative development of microstructural damage in the sample, may be analysed by considering a model linking elastic constants, macrocracking density, and matrix ductility. Assuming that macrocracking in the matrix is the dominant damage mechanism, the approach proposed by Silva MAG and S Ryan [24,26] for the elastic modulus of a cracked body could be appropriate, which introduces a damage parameter based on area and perimeter of uniformly distributed cracks. However the damage introduced in the present composites under increasing impact energy may involve more complex mechanisms than purely matrix micro or macrocracking, including matrix ductility, fibre-matrix interfacial debonding, localised multifracture of fibres, and fibre pullout. Thus a predictive model for the high energy impact behaviour of the present composites must take into consideration the complex microstructure of the composites and the effect of matrix ductility and interfaces. The formulation of such a model is beyond the scope of the present experimental study. Considering the failure commencement load as an indicator of residual strength of the composite, it was found that this reaches a minimum value when the impact energy is just below that required for penetration of the projectile (Fig. 9(b)). Further increase in high impact energy after penetration of the sample by the projectile results in increase of the load carrying capability of the composite, due to less microstructural damage being introduced in the sample. This behaviour is in general agreement with the literature on high velocity impact resistance of composite materials [23,28,29].

4. Conclusion

Ceramic fibre reinforced Al_{pure} and Al_{6061} metal matrix composites, when subjected to high velocity impact loading by firing metallic cylindrical projectiles, retain some of their load bearing capacity after penetration by the projectile. This is due to the fact that structural damage caused by projectiles remains localised preventing catastrophic failure. For the conditions of the present tests, penetration by the projectile occurs at impact energy of about 17.5-27.5 J and 62-65 J for fibre reinforced Al_{6061} and Al_{pure} metal matrix composites, respectively, which indicates that there is a limiting value for the material to be useful in high energy impact armour applications when it is used on its own (without backing layers).

References

[1] Børvik T, Langseth M, Hopperstad OS, Malo KA. Perforation of 12 mm thick steel plates by 20 mm diameter projectiles with flat, hemispherical and conical noses Part I: experimental study. Int J Impact Eng 2002;27:19–35A study of fragmentation in the ballistic impact of ceramics. Int J Impact Eng 1994;15:605–18.

[2] Roy T, Chakraborty D. Delamination in hybrid FRP laminates under low velocity impact. J Reinf Plast Compos , Vol. 25, No. 18, 2006; 1939–56.

[3] Lopez-Puente J, Zaera R, Navarro C. Experimental and numerical analysis of normal and oblique ballistic impacts on thin carbon/epoxy woven laminates. Compos Part A Appl Sci, Vol. 39, 2008, 374–87.

[4] Millett JCF, Bourne NK, Meziere YJE, Vignjevic R, Lukyanov A. The effect of orientation on the shock response of a carbon fibre-epoxy composite. Compos Sci Technol, Vol. 67, 2007, 3253–60.

[5] Cantwell WJ, Morton J. Comparison of the low and high velocity impact response of CFRP. Composites , Vol. 20, No. 6, 1989, 545–51.

[6] Silvestrov VV, Plastanin AV, Gorshkov NN. Hypervelocity impact on laminate composite panels. Int J Impact Eng , Vol. 17, 1995, 751–62.

[7] McQuillan F. PhD Thesis, Imperial College, University of London; 1992.

[8] American Society for Metals, "Properties and Selection: Nonferrous alloy and pure metals", Metals Handbook, 9th edition, Vol.2, 1979, 63 and 161.

[9] Ming Yang, V.D. Scott and R.L.Trumper, "The role of interface on the mechanical behaviour of carbon fibre reinforced aluminium alloy composites". Metal Matrix Composites, 2nd Conference, the Royal Society, U.K, 1989.

[10] F.M.Hosking, F.Folgar-Portillo, R.Wunderlin, And R.Mehrabian, in "Composite of Aluminium alloys; Fabrication and Wear Behaviour", J. Mat. Sci., 17, 1982, 477-98.

[11] R. L. Trumper, P. J. Sherwood and A.W. Cifford, in "Metal Matrix Composites", Proc. 1st Conf. on 'Materials in Aerospace, 2-4 April, 1985, The Institute of Metals, London, 20.1-20.15.

[12] R. L. Trumper, and V. D. Scott, in "Cast microstructures in fibre reinforced metals", 7th International Conference on the materials revolution through the 90's, paper 27, 1989.

[13] M. C. Waterbury and L. T. Drzal, in "Determination of fibre volume fraction by optical numeric volume fraction analysis", J. Reinforced Plastics and Composites, Vol. 8, 1989, 627-636

[14] Schonberg WP. Key Engineering Materials 1998;141–143:573–84.

[15] George PE, Dursch HW. NASA Technical Reports Accession ID: 94N31036, Document ID: 19940026531; 1993.

[16] Tennyson RC, Lamontagne C. Hypervelocity impact damage to composites. Composites Part A , Vol. 31, 2000, 785–94.

[17] Übeyli M, Yıldırım RO, Ögel B. Investigation on the ballistic behavior of Al2O3/Al2024 laminated composites. J Mater Process Technol Vol. 196, 2008, 356–64.

[18] Übeyli M, Yıldırım RO, Ögel B. On the comparison of the ballistic performance of steel and laminated composite armours. Mater Design 2007;28(4):1257–62.

[19] Wang B, Chou SM. The behavior of laminated composite plates as armour. J Mater Process Technol , Vol. 68, 1997, 279–87.

[20] Lee S-WR, Sun CT. Dynamic penetration of graphite/epoxy laminates impacted by a blunt-ended projectile. Compos Sci Technol, Vol. 49, 1993, 369–80.

[21] Cantwell WJ, Morton J. Impact perforation of carbon fibre reinforced plastics. Compos Sci Technol 1990;38:119–41

[22] Woodward RL, Gooch Jr WA, O'Donnell RG, Perciballi WJ, Baxter BJ, Pattie SD. A study of fragmentation in the ballistic impact of ceramics. Int J Impact Eng, Vol. 15, 1994, 605–18.

[23] Naik NK, Shirirao P, Reddy BCK. Ballistic behaviour of woven fabric composites: formulation. Int J Impact Eng, Vol. 32, No. 9, 2006, 1521–2.

[24] Silva MAG, Cismas-iu C, Chiorean CG. Numerical simulation of ballistic impact on composite laminates. Int J Impact Eng, Vol. 31, No. 3, 2005, 289–306.

[25] Berthelot JM, Sefrani Y. Longitudinal and transverse damping of unidirectional fibre composites. Compos Struct , Vol. 79, 2007, 423–31.

[26] Ryan S, Schaefer F, Riedel W. Numerical simulation of hypervelocity impact on CFRP/Al HC SP spacecraft structures causing penetration and fragment ejection. Int J Impact Eng, Vol. 33, 2006, 703–12.

[27] Tanabe Y, Aoki M, Fujii K, Kasano H, Yasuda E. Fracture behavior of CFRPs impacted by relatively high-velocity steel sphere. Int J Impact Eng, Vol. 28, 2003, 627–42.

[28] Fujii K, Aoki M, Kiuchi N, Yasuda E, Tanabe Y. Impact perforation of CFRPs using high-velocity steel sphere. Int J Impact Eng, Vol. 27, 2002, 497–508.

[29] Strassburger E, Lexow B, Ashuach H, Yeshurun Y, Bar-Ziv S, Hachamo Y, Gedon H. Impact on ceramic-metalcomposites-ballistic resistance and fracture behavior Proceedings of the 20th Symposium on Ballistics, Orlando, FL, USA, 2002. 8pp.

JJMIE

Volume 4, Number 5, November 2010
ISSN 1995-6665
Pages 615 - 628

Jordan Journal of Mechanical and Industrial Engineering

Numerical Simulation and Performance Evaluation of Stirling Engine Cycle

M. Tarawneh [a,*], F. Al-Ghathian[b], M. A. Nawafleh[c], N.Al-Kloub[d]

[a] Department of Mechanical Engineering, Mutah University, Karak, Jordan

[b,d] Department of Mechanical Engineering, Al-Balqa' Applied University, Amman, Jordan

[c] Department of Civil Engineering, Al-Hussein Bin Talal University, Ma'an, Jordan

Abstract

A thermodynamic based model was developed. The influences of thermo-physical parameters on the Stirling engine performance were investigated. The analysis is mainly performed inside the compression and expansion cylinders. The instantaneous temperatures of the working fluid inside the engine cylinders, and the interconnected heat exchangers were investigated. The system of governing equations (mass and energy) was developed and employed to investigate the variations of all the process parameters. The step-by-step crank angle intervals were applied to investigate the pressure, temperature, volume, mass flow, and convective heat transfer during the compression and expansion processes. Losses of mass due to the leakage, and energy losses were investigated under the adopted working conditions and phase difference. Variation of work generation due to the leakage of gas through the clearance between the piston and cylinder was evaluated. The numerical solution was adequately performed with a large number of iterations and for each angular interval. A noticeable stable evolutional behavior of the simulated parameters was observed. The stable evolutional behavior of the simulated parameters confirms the model suitability, the capability of pointing out the engine performance, and the capability of converting the thermal energy into useful mechanical work. Additionally, the use of other related correlations ensures the model accuracy, while the resulted small differences are within the expected ranges. In comparison with similar studies, the calculation procedure can be used to investigate the engine performance under different operating conditions.

Keywords: Bio-Diesel; Stirling Engine; Hot Expansion; Cold Compression; Gas Leakage; Polytropic.

Nomenclature

A: Area [m^2]
B.D.C: Bottom Dead Center
c: compression
C.A: Crank angle
c.c: Crank case
c_P, cv: Specific heats [J/Kg.k]
D: Diameter [m]
d: expansion
E, e: Total energy [KJ]
f_c: Cyclic frequency [H_Z]
H, h: Enthalpy [KJ]
$\dot{m}$: Mass flow rate [kg/s]
m : Mass of gas [kg]
n: Polytropic exponent
P: Power [KW]
p: pressure [N/m^2]
Q: Heat transfer [KJ]
R: Gas particular constant [J/Kg.k]
S: Stroke [m]
S_p: Mean piston speed [m/s]
T: Temperature [K]
T.D.C: Top Dead Center
T_H: High Temperature [K]
T_L: Lower temperature [K]
W: Work [KJ]
V_S: Swept volume [dm^3]
t: Time [s]
δ : Clearance between piston and cylinder [m]
ρ : Gas density [kg/m^3]
η_{cycle} : Cycle efficiency [%]
λ : Thermal conductivity [W/m K]
ν : Dynamic viscosity [Ns/m^2]
ω : Angular velocity [rpm]
θ : Crank angle (C.A)

* Corresponding author. tatmuf@mutah.edu.jo

1. Introduction

Robert Stirling invented Stirling engine in 1816. Engines based on his invention were built in many forms and sizes. The new materials, developments, and models are the keys of the success for this engine. The increased interest in Stirling engines is due to several important advantages over the classical engines, Stirling engines are simple in design, easily operated and externally heated. They operate on a closed regenerative thermodynamic cycle using compressed gases. In comparison with the internal combustion engines, Stirling engines are more attractive, because they offer several important advantages over the traditional internal combustion engine. If the fuel combustion is considered as the fueling heat for this engine, the Stirling engine appears to be more clean and efficient engine, because the combustion is performed externally and the possibility of controlling the amount of oxygen will result in getting a complete combustion, and less fuel consumption with lower pollution. Unlike the internal combustion engine with greater difficulty of controlling the amount of oxygen needed for a complete combustion [1,2]. The demands for clean environment and energy saving can be satisfied [3]. The ability to use a wide variety of cheapest and available thermal sources of energy such as: sources of renewable energy, biomass, biogas, waste heat recovery, and fossil fuel which meet the effective use and saving of energy [4]. Unfortunately, the real Stirling engine suffers from significant losses and disadvantages; flow loses, gas leakage, heat losses, the negative influence of dead volume, and the poor reputation of the heat exchangers under a continuous heat transfer at higher temperature and pressure.

Once these disadvantages are minimized or eliminated, the Stirling engine solution becomes more attractive due to its adaptability to the new demands and operational standards. The reported literature review with valuable base line information, important developments, and performance optimization about Stirling engines have been reviewed and evaluated [5,6]. Usually, the design point of the engine will be between the limits of maximum efficiency and maximum power output. Several authors have studied the thermodynamic performance, and evaluated the effects of different losses on the engine performance. The first classical analysis of Stirling-cycle engine was performed Schmidt [7]; he obtained a theory that provides sinusoidal volume variations in the compression and expansion spaces, and uniform pressure through the system. Considerable efforts have been made to develop and improve the Schmidt analysis. Urieli et al. [9] improved the analysis to cover the effects of leakage, heat losses, and flow losses, indicated work for all the configurations of Stirling engine. Fenkelsein [10] provide the nodal thermodynamic analysis. In this analysis the engine was divided into 13 sub-volumes, the temperature variation at sub-volumes is calculated with differential time intervals by the first law of thermodynamics. Several investigators applied the nodal analysis; they studied the effect of different losses on basis of the nodal analysis. Intensive research works, developments, analysis, and simulation methods were applied to improve the engine cycle performance [11-16]. Petrescu [17] presented a method based on the first law of thermodynamics for calculating the efficiency and power output; they showed that the significant reduction in the engine performance is due to the non-adiabatic and incomplete heat regeneration. The effects of pressure drop due to the mechanical and fluid friction in heat exchangers, the energy losses due to internal and external conduction between the hot and cold parts, and the shuttle effect were studied [3,4] A thermodynamic analysis to investigate the effect of dead volumes on the engine network, and the heat transfer efficiency [18]. The significant amount of lost power is directly related to the lost mass and gas leakage through the clearance between the piston and cylinder [4, 15].

In this paper, the greatest interest was focused on developing a precise and practical numerical simulation, to adequately investigate the operational behavior of the working fluid (hot air) inside the compression and expansion engine cylinders. The proposed thermodynamic model, with the appropriate data input related to the design and operational characteristics, is primarily based on solving the system of governing (mass and energy balance equations). The step-wise basis of the angular increments or intervals was applied over whole the engine operating cycle. The evolutional behavior of the simulated parameters during the hot expansion, and the cold compression of the gas inside the engine cylinders are presented. The same results could be obtained when applying the time or spatial variation methods. Finally, the model was developed; the obtained results of the simulated properties were compared with similar studies [12,14,15,16]. The results are graphically presented on a proper performance curves. The remarkable degree of stability of the gas evolutional behavior was observed during the compression and expansion processes. The resulting indicated performance parameters demonstrate the engine capability of converting the thermal energy into a useful mechanical work.

2. Thermodynamics of Stirling cycle engine

2.1. The ideal cycle engine

Stirling engines are classified into three main configurations (alpha, beta, and gamma). They have the same thermodynamic cycle; but each configuration has its particular mechanical design [5]. Alpha-type is the simplest configuration; it consists of two pistons placed in separate cylinders and mounted on the same crankshaft. The phase difference between both cylinders is 90º crank angles, resulting to have a pure sinusoidal reciprocating motion. The ideal cycle of Stirling engine consists of four processes, namely isothermal compression and expansion, and isentropic heat addition and rejection processes. The engine cycle invented by Robert Stirling presented on PV and TS diagrams as shown in Figure 1 [5]. The expansion and compression cylinders are interconnected via a series of heat exchangers (heater, regenerator, and the cooler).

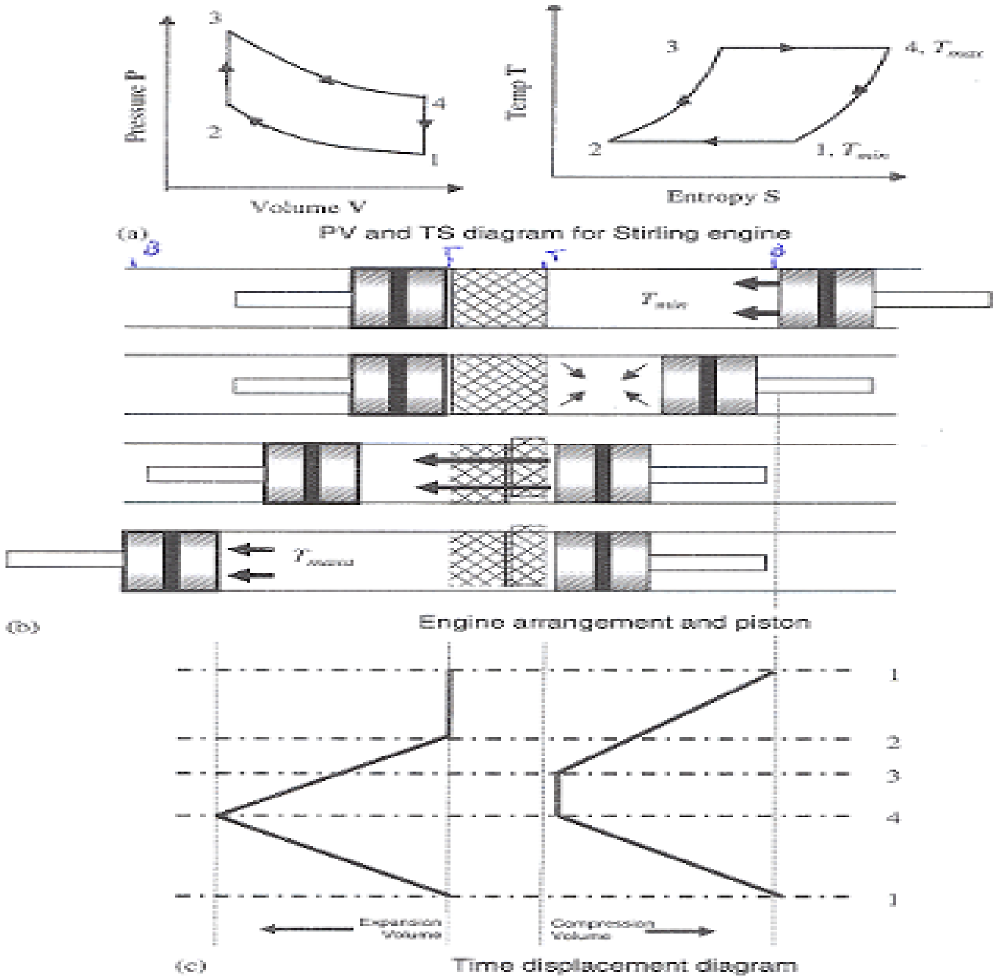

Fig.1. Ideal cycle of Stirling engine

Expansion volume is maintained at the same high temperature of the thermal source (T_H), while the compression volume is kept at low temperature, which is the same temperature of the cold sink (T_C). The regenerator is like a thermal storage; it absorbs and rejects the heat from and to the working fluid. The working gas transports energy from the high temperature heat source to the low temperature heat sink. Hence, work is obtained during one complete cycle. The initial state of the cycle is identified by the position of the crank angle for both pistons. The power piston in the compression volume is maintained at its BDC, and the compression volume is at its maximum, while the pressure and temperature of the working fluid are at their minimum values. The displacer is contained in the expansion volume at its TDC and close to the regenerator. The phase difference between the power piston and displacer is 90º crank angles. In Figure1, both P-V and T-S ideal diagrams, the engine arrangements, and time displacement diagram are clearly shown. The main four ideal processes are:

1-2: Isothermal Compression Process: D*uring this process, the power piston moves from the BDC toward reaching its TDC, helped by the flywheel momentum, and the created partial vacuum in the cold space (cooler) due to the cooling of the working fluid. The total mass of fluid* *is still maintained in the cold space, which follows to be compressed by the power piston. In this process the pressure and temperature of the fluid are increased to their values in state 2. The displacer is still maintained stationary at its TDC.*

2-3: Constant volume regenerative heating: *In this process, the power piston is kept at its TDC close to the regenerator. The displacer starts moving from its TDC away from the regenerator. The volume between both pistons remains constant. The working fluid is forced to pass from the cooler through the regenerator to the heater. The stored heat in the regenerator from the previous cycle is added to the flowing fluid. The temperature is increased and causes the pressure increase to achieve their maximum values (state 3).*

3-4: Isothermal Expansion: *After which the displacer has introduced the working fluid into the hot space, it will be held stationary at its BDC, and the volume, pressure, temperature achieved their maximum values in the expansion space. The power piston being pushed to move back toward its BDC under the increased pressure, it forces the flywheel thus creating a mechanical work.*

4-1: Constant volume regenerative cooling: *Heat is transferred from the fluid and absorbed into the regenerator as a result of flowing through the regenerator from the heater to the cooler and then to the compression space. After which the power piston has reached its BDC, the pressure and temperature start dropping until achieving their initial values (state1).*

2.2. Key factors influencing the cycle engine performance.

Several practical factors affecting the engine performance were reported by various authors. Schmidt [7] performed the first analysis of Stirling engine. However, the working spaces of the real engines have the tendency to be adiabatic rather than isothermal. Fenkelstein [19] performed the first analysis with non-isothermal working spaces, and introduced the concept of conditional temperatures, which depends on the flow direction of the fluid; he assumed that the heat transfer within the working spaces occurs by convection. Using the state equation as well as the laws of energy and mass conservations the analysis was performed. Real engines have many losses. The influence of several practical factors, which causes the real engine to deviate from the ideal one, should be highlighted. Neither heating nor cooling takes place exactly at constant volume or at constant temperature. The working fluid inside the engine cylinders tends to be influenced in an adiabatic rather than isothermal manner. Therefore, the temperature in the compression and expansion spaces will vary over the cycle according to the adiabatic nature. The working fluid should provide high thermal conductivity; high specific heat; low viscosity, and low density. The heat transfer coefficient varies linearly with respect to the local temperatures of the hot components. The heat transfer coefficient must then be determined using the Reynolds analogy, which relates heat transfer to the fluid frictional resistance [20]. Factors governing the performance of a well-designed engine are proportional to pressure, volume, speed and temperature [5,6,17]. A significant effect of friction factor becomes as a function of Reynolds number, the friction factor decreases gradually with the increased value of Reynolds number [21] In real engines, the dead volumes accounts up of 50% of the total internal volume [15]. The increased dead volume within the engine results in reducing the power output [18]. The dead volumes of hot and cold spaces will reduce the engine power and efficiency, and increases the external heat input and output [13]. The leakage of the working fluid is inevitable, this is due to the higher pressure that forces the sealing elements to leak the gas out of the system. Therefore, both pistons need to be perfectly sealed to prevent the leakage tendency [17]. Other important disadvantages related to the flow and energy losses were reported [9,15]

3. Operational principles Design characteristics

The Stirling engine components and operating cycle are shown in Figure 2 [6]. The engine operates on a closed regenerative thermodynamic cycle with a cyclic hot expansion and cold compression. The expansion piston acts as an expander while the compression piston as a compressor. The regenerator is placed between the cooler and a heater with the scope of using the removed heat from the gas during the energy transfer to the cold cylinder. The stored energy in the regenerator is added to preheat the fluid when it is transferred back to the hot cylinder. The gas (air) is initially compressed in the compression space (cold compression), and forced to flow at a uniform rate through the regenerator to recover the stored heat. The maximum working temperature is reached inside the heater, due to the transferred heat from the higher temperature source (T_H) to the fluid. The working gas transports energy from the high temperature heat source to the low temperature heat sink. Hence work is obtained during one complete cycle. Work is exerted to compress the cold working gas, and a useful work is extracted by expanding the gas after it has been heated in order to increase its pressure. Heating and cooling of the gas is achieved by moving the gas back and fourth through the connected heat exchangers (heater, regenerator, and cooler). The deviation between the ideal and real cycles is clearly shown in Figure 3 [6], where the effects of irreversible factors are presented on the pressure-volume diagram (P-V). Alpha-type Stirling engine consists of two separate cylinders with symmetrical geometry. The expansion cylinder is advanced with a 90º crank angles than the compression cylinder. Some valuable conclusions regarding to the effects of the operating parameters were appreciated. An efficient heat transfer to the working fluid can be satisfied by high mass flow rate of the working fluid [12]. The power output of Stirling engine is assumed to be proportional to the increased mean cycle pressure [3]. The high pressure is necessary to reduce the need for high mass flow rate [3,4,22]. The friction factor and flow discharge coefficient are considered as a function of Reynolds number, the fluid friction in the heat exchangers decreases gradually with the increased value of Reynolds number [21]. In this work, the geometrical and operational parameters are tabulated in Table 1.

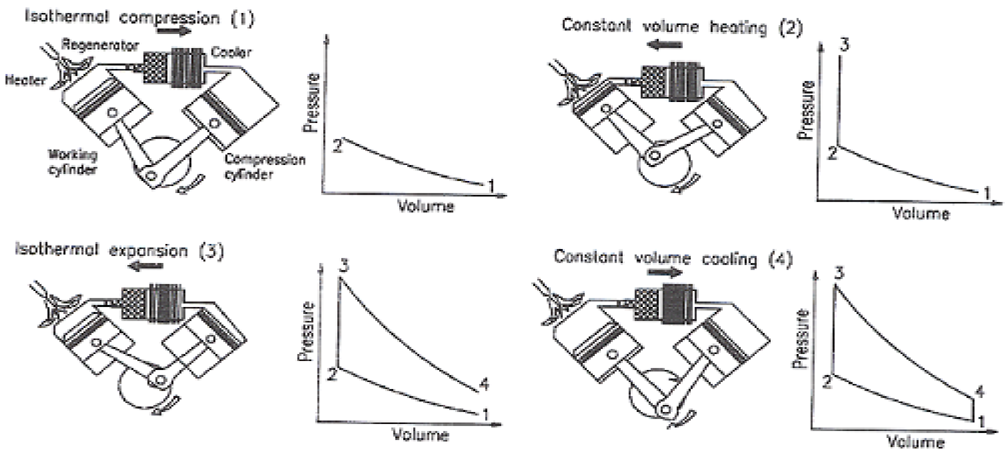

Figure 2. Stirling engine operation principles

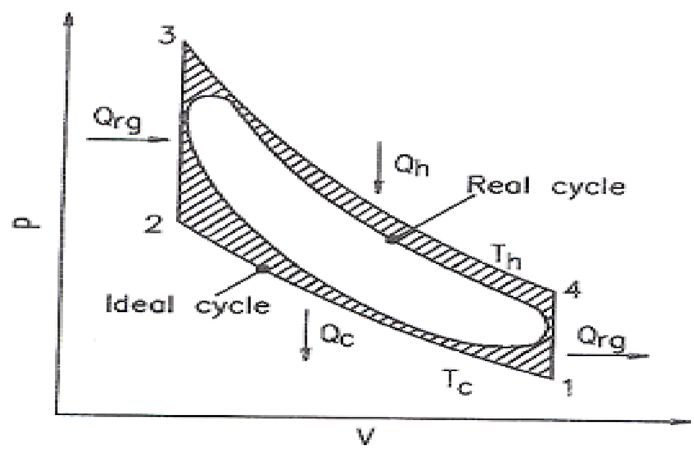

Figure 3. Deviation between the ideal and real cycles of Stirling engine

Table 1. Stirling engine characteristics

Swept volume, $V_S = 1dm^3$	Working fluid is air
Cylinder diameter = 108 mm	Engine speed= 1500 rpm
Stroke length = 108 mm	Initial pressure = 50 bar
Phase angle advance = 90º	Hot source temperature = 1000K
Number of nodal volumes = 72	Low sink temperature = 300 K

The cheap and available air is taken as the working agent, and a pressure of 50 bars is used. The passageway between both cylinders is formed by a number of small tubes; it has relatively a total cross-sectional area of 42.6% of the total frontal cross-sectional area of the piston. The constant discharge coefficient of 70% was taken as a function of Reynolds number. The engine operating cycle is divided into 72 angular intervals or increments; each interval is represented by 0.2º of one full crankshaft rotation. . The difference between two successive intervals is 5º of crank angles. The first step of calculation will be started by setting the initial state and aligning the expansion piston to its (TDC), which corresponds to a crank angle ($\theta_{exp.} = 0$), respectively the swept volume at the initial crank angle ($V_{exp.}$=$1dm^3$). At the same time, the swept volume in the compression cylinder is identified by the position of the compression piston with the crank angle of ($\theta_{comp.} = 270^o$).

4. The Stirling engine model

4.1. Governing equations and assumptions

Modeling activities have major contributions to predict the engine performance over a wide range of design and operating variables, and at different conditions. Modeling is considered as a powerful tool to identify the key controlling variables without having to conduct the costly experiments and tests, or due to the difficulty of performing direct measurements for all the flow parameters and characteristics.

The thermodynamic-based model is formed by the combination between the system of governing equations (mass and energy balance equations), with the time or crank angle increments as the independent variables. In order to accurately evaluate the variation of the simulated parameters, the system of equations was solved on a step-wise spatial variation in each angular interval. Each cylinder is divided into an active swept volume (V_S) and inactive dead volume. The total internal volume occupied by working fluid is divided into a number of small nodal volumes. The first nodal volume is taken in expansion cylinder, and the last nodal volume in the compression cylinder. The other nodal volumes are located in the flow passage between the cold and hot spaces. All the nodal volumes are assumed to be open systems. From the thermodynamic point of view, every cell in an open system is controlled by the periodic condition at the inlet and outlet. Generally, the main thermodynamic assumptions for an open system were adopted to formulate the mathematical model:

- The air is taken as working agent; it behaves as an ideal gas.
- The state of the mass at each does not vary with time
- Total mass in the system does not change with time
- The volume in hot and cold cylinders vary according to the crank angle, while in all the heat exchangers the volume is kept constant
- The gas pressure and temperature does not vary with time at the boundaries of any control volume.
- Uniform working fluid with uniform states of mass at any point throughout the entire control volume.

The engine consists of two cylinders with symmetrical geometry; but they differ in their working conditions. The phase difference between the power piston and displacer is 90º crank angles. The expansion piston is set to be in advance with 90º-phase angle than the compression piston. In this work, the calculation procedure was performed in the expansion cylinder, a cylinder in which heat energy is converted into a useful mechanical work. Therefore, the variations and evolutional behavior of the simulated parameters inside the cylinder are described by solving the system of governing equations on a stepwise basis of crank angle intervals:

The mass balance equation for open control volume:

When the gas leakage from the engine is

$$m_i = m_e \tag{1}$$

considered, it can be calculated by:

$$\frac{\partial m}{\partial t} = \dot{m}_i - \dot{m}_e - \dot{m}_{lost} \tag{2}$$

The mass flow rate of gas leakage through the clearance between the piston and cylinder as due to the bad sealing conditions can be calculated by:

$$m_{leakage} = \frac{\pi D \delta^3}{12 \nu L}(p_{cylinder} - p_{c.c}) \tag{3}$$

The first law of thermodynamics (energy balance) is rearranged into the following form: (equation 4)

$$dQ_{wall} - dW_{\text{intern}} = mde + e_{out}dm_{out} - e_{in}dm_{in} + e_{lost}dm_{lost}$$

Generally, for an open control volume, only the change in enthalpy is considered. The kinetic and potential energies are assumed of negligible effects, because they are small enough. The pressure difference between nodal volumes due to flow friction can be calculated by

$$p = \frac{m_t R}{\sum_{i=1}^{n} V_i / T_I} \tag{5}$$

The temperature variation between two steps of time within a nodal volume is calculated by using the first law of thermodynamics for open system as:

$$\Delta T_i = [h_i A_i (T_{wi} - T_i)\Delta t - \Delta m_i C_v T + E_i - P\Delta V_i)/(m_i C_V) \tag{6}$$

Where E_i, represents the enthalpy flow in or out the nodal volume, and calculated by:

$$E_i = -C_P \frac{T_i + T_{i+1}}{2} \sum_{j=i+1}^{n} \Delta m_j - C_P \frac{T_{i-1} + T_i}{2} \sum_{j=1}^{i-1} \Delta m_j \tag{7}$$

Boundary temperature of flow passage is assumed to be constant with time and varies linearly in flow direction from T_C to T_H. Specific heats are assumed constant. The flow across boundaries is taken as positive in the direction of flow. The influence of flow friction on the mass distribution in the engine, is directly included in the mass balance equation, and it could be using the pressure losses correlations. If $\sum_{j=i+1}^{n} \Delta m_j$ has a negative value, enthalpy flow occurs from the nodal volume i+1 to the nodal volume i. else the enthalpy flow will be from the nodal volume i to the nodal volume i+1. Similarly, if $\sum_{j=1}^{i-1} \Delta m_j$ has a negative value, then enthalpy flow will be from the nodal volume i-1 to the nodal volume i; else the flow of enthalpy will be from the nodal volume i to the nodal volume i-1. Instantaneous values of the mass m_j, in the nodal volumes are calculated using the general state equation of perfect gases. The included terms in equation (6) are the flow of energy (enthalpy) between neighboring control volumes, the convective heat transfer between the gas and metal, and the work as due to the volume variation. The heat transfer between the gas and the internal walls of the cylinders, is assumed take place by convective heat transfer only:

$$dQ_{walls} = h_c A(T_{wall} - T_{gas})d\tau \qquad (8)$$

Different correlations can be used to determine the heat transfer coefficient such as Woschni correlation number 9 or equation number 10 can be applied to calculate the heat transfer coefficient [17,20].

$$h_c = 4.14(1+1.24\bar{S}_p)(p^2T)^{1/3} \qquad (9)$$

$$h_c = 2.1\frac{\lambda}{D}\left(\rho \bar{S}_p \frac{D}{\eta}\right)^3 \qquad (10)$$

both correlations give nearly the same value of the heat transfer coefficient.

The indicated work term is expressed as:

$$dW_{indicated} = pdV - mvdv - dW_{friction} \qquad (11)$$

In equation (11), only work due to the volume variation is considered, while the kinetic energy, and the frictional work are assumed with negligible effects, because of their insignificant effects.

The indicated cyclic work can be expressed as:

$$dW_{indicated} = \frac{p_j + p_{j+1}}{2}(V_{j+1} - V_j) \qquad (12)$$

By considering the polytropic exponent, the indicated work is calculated in each angular interval using the following equation:

$$dW_{indicated} = \frac{n}{n-1}mRT\left[\left(\frac{p+dp}{p}\right)^{\frac{n-1}{n}} - 1\right] \qquad (13)$$

where, n is the polytropic exponent, and it can be determined using with the following equation:

$$n = \frac{kdW_{indicated}}{(k-1)dQ_{wall} + dW_{intern}} \qquad (14)$$

The instantaneous values of the indicated power and heat flux are expressed by:

Power: $P_{inst.,j+1} = \frac{p_{mean,j+1}(V_{j+1} - V_j)}{\Delta\tau}$. (15)

Heat flux: $\dot{Q}_{wall,inst.,j+1} = \frac{dQ_{wall,j+1}}{\Delta\tau}$. (16)

Finally, the numerical program provides the following indicated performance parameters at the end of each operating cycle:

Indicated work per cycle: $W_{indicated} = \oint pdV$ (17)

The work given by the cycle is: $W_{net} = W_{expansion} + W_{compression}$ (18)

where, the work done during the expansion and compression are calculated by considering the volume variation in each cylinder.

$$\frac{dW}{dt} = P_c\frac{dV_c}{dt} + P_d\frac{dV_d}{dt}$$

Indicated power: $P_{indicated} = W_{cycle,indicat.}f_c$. (19)

Where, f_c is the cyclic frequency expressed by: $f_c = \frac{\omega}{2\pi}$ (20)

Heat added from the higher temperature source: $Q_{added} = \oint dQ_{added}$ (22)

Heat rejected to the lower temperature sink: $Q_{rejected} = \oint dQ_{rejected}$ (23)

Indicated cycle efficiency: $\eta_{indicated} = \frac{P_{indicat.}}{Q_{added} f_c} = \frac{Q_{added} - Q_{rejected}}{Q_{added}}$ (24)

Indicated specific heat: $C_{indicat.} = \frac{Q_{added}}{P_{indicated} / f_c}$ (21)

4.2. Particular Aspects of The Model.

Defining the initial state of the fluid inside the cylinder starts the first step of calculation. The thermodynamic based model allows the possibility of calculation all the instantaneous and average values of the key parameters. It is capable to simulate all the processes in proper sequence until making up the engine cycle. It is often required to model the region of interest (engine cylinders) as an open thermodynamic system; such a model is appropriate when the fluid inside the open system is assumed to be uniform at each point in time. Convergence with the cycle simulations occurs within a few iterations. The developed model can be used to calculate all of the instantaneous properties, and the indicated parameters at any working condition. The particular aspects of the model are presented as following:

1. A simplified iterative numerical solution is developed to solve the system of governing equations. The analysis is started at the beginning of the expansion stroke (initial state), and the values of the simulated properties are determined at the starting point of the cycle with the expansion piston at its position of TDC. While the compression piston is still maintained at its BDC. The instantaneous properties are calculated on a step-wise basis of crank angle intervals. The operating cycle should ends with the initial state of the working fluid that was started out. The variables representing mass and energy must be the same at the end and starting points of the cycle. The model should results in a periodic response with less error. In case that the values of the fluid properties at the end state are different than those of the initial state, the iterative solution will continue until the discrepancy is sufficiently small and the converged solution is achieved.
2. Nodal volumes technique provides a precise evaluation of the real effects of non-adiabatic processes. In this work, the working space is divided into 72 of finite volumes, which are sufficiently enough to obtain accurate results. The simulated properties are calculated on a step-wise basis of angular intervals, and over each operating cycle.
3. The initial state of the working fluid at the starting point of the cycle was defined. The key parameters that describe the evolutional behavior of the working fluid inside the engine cylinders were calculated. These parameters include: the cylinder dimensions, dead volumes, sizes and cross sectional areas of the heat exchangers, initial pressure and temperature of the working fluid, temperatures of the hot and cold sources, temperature of the cylinder walls, and the engine rpm.
4. The calculated parameters at the end of the first angular interval are obtained as a function of their values at the beginning of the same angular interval. The first property that will be determined at the starting and end points is the displacement volume. The mass of gas in the cylinder was initially considered as known value. The calculation procedure will continue to point out the other properties such as; the pressure and temperature of the fluid at the start and end of each angular interval, the gas leakage through the clearance between the piston and cylinder. Using the mass balance equation, the available mass that still exists in the cylinder is calculated at the end of each interval. The same procedure will be applied from (1to n angular intervals). The simulated properties at the start of each angular interval are function of (θ_j): V_j, p_j, T_j, ΔW_j, ΔQ_j, m_j, and n_j. While their properties at the end of each angular interval are function of (θ_{j+1}), and their values are: V_{j+1}, p_{j+1}, T_{j+1}, ΔW_{j+1}, ΔQ_{j+1},m_{j+1} and n_{j+1}).
5. The stable evolutional behavior of the main parameters is a good indicator for determining the indicated work and power, and the cycle efficiency. The main parameters are: the gas pressure and temperature in each cylinder and for each moment of calculation, the gas flow rates entering and leaving both cylinders, the transferred heat between the gas and internal walls, and the work transfer from the gas to the drive mechanism. Actually, the calculation procedure was performed with sufficient number of iterations. The resulted stable evolutional behavior of the working fluid ensures the model correctness. The same values of the thermo-physical properties at the end and starting points of the cycle were satisfied.

***4.3.** Model Verification*

A great effort has been made to verify the correctness of the model. The great challenge is related the model capability of computing the amount of gas leakage, and energy losses from the engine. Testing for mass conservation has been made by the sum of gas in all control volumes. Using other correlations ensures correctness of the model as well as the implemented correlation, and checking for possible differences. The differences have been found within the expected ranges. The small differences are due to the effects of four design parameters: temperature ratio, gas leakage, swept volume ratio, and dead volume ratio. The Stirling engine power output is a good indicator for measuring and evaluating the engine performance, and the model accuracy. The Stirling engine power output can be calculated by using different formulas. The simpler approach is to use the Beale formula; this formula requires few design parameters and can be used for various configurations and sizes of Stirling engine. Beale formula considers that the power output of many Stirling engines is roughly proportional to the pressure, swept volume, and speed [5,8]. The relationship between all parameters in this formula is expressed by an empirical formula as called Beale number:

$$P/(p_m f V_P) = \text{Constant.} \tag{22}$$

Walker [23] proposed an approximated Beale formula for all types and sizes of Stirling engines in order to calculate the power output as:

$$P = 0.015 p_m f V_P \tag{23}$$

Where P is the engine power in W, p_m is the mean cycle pressure in bar, V_P is the displacement volume in cm^3, f is the cycle frequency in H_Z.

Walker [23] introduced the temperature ratio and modified Beale formula in order to suit all the real engines, the new correlation is:

$$P = F p_m f V_P \frac{T_H - T_C}{T_H - T_C} \tag{24}$$

The last developed correlation (eq.24) is considered as a powerful tool during the first stages of design, it reflects the effects of the real parameters by providing an experience factor F with a practical value ranged between (0.25-0.35). The indicated power can also be calculated by using other correlation:

$$P_{indicated} = W_{net} f \tag{25}$$

Comparing the obtained results with the ideal isothermal or the adiabatic available models is the best method of verification. Several thermodynamic models were reviewed and evaluated. The comparison with similar thermodynamic models [4,12,15,16] and a good agreement between the results was observed. Nearly, the same values of simulated parameters at the starting and end points of the cycle is an important aspect of the model validity. The converged values of simulated parameters are due to the iterative procedure, and the increased number of computational points, where the total volume was divided into 72 of finite volumes. The resulted stable behavior of the simulated parameters demonstrates the engine capability of converting the heat energy into a useful mechanical work. The model can be used to predict different key parameters under different working conditions, and encourage us to start other investigations in the next future. .

5. Results and Discussion

The evolutional behavior of the simulated parameters was investigated in each cylinder as a function of crank angle variation. These parameters are: pressure, temperature, flow rates in and out of the cylinders, mass of gas in and out, polytropic exponent, convective heat transfer coefficient, transferred heat, work done on and by the system, heat rejection and addition, and the power output. The model validation is investigated by studying the effect different design and operational parameters on the engine performance. The adiabatic expansion and compression of the gas inside the engine cylinders was investigated, The influence of the high temperature (T_H) and the lower temperature (T_L) with respect to their values is evaluated, the effect of hydraulic resistances on the flowing fluid, the significant effect of dimensional parameters such as: the length and diameter of the passageway between both cylinders. Based on the accurate data input, the system of equations was solved iteratively on a step-wise basis of angular increments. The variations of operating parameters are presented on a proper performance curves. A detailed analysis and illustration for each gas variable was performed separately.

5.1. Gas pressure and temperature variations.

The pressure and temperature variations in both cylinders are represented over each operating cycle. In Fig.4 (p-θ) diagram, illustrates the pressure variation in the engine cylinders as a function of crank angle variation. The remarkable observation that could be observed is focused the small differences between the calculated pressures in both cylinders. These differences are due to the friction and other resistances against the flowing fluid in the passageway between the cylinders. The increased number of the interconnected small tubes, and their cross sectional areas are important factors that control the pressure difference. The reduced cross sectional areas of these tubes will increase the pressure difference between the cylinders. The pressure difference between the expansion and compression cylinders having to indicate the pressure losses in both cylinders.

In Fig.5, the temperature variation in the hot and cold cylinders versus the crank angle variation is illustrated. Temperature variation within the nodal volumes is obtained by using the first law of thermodynamics for open systems. The influence of the source temperature (1000K) at which heat is added, and the sink temperature (300K) to which hear is rejected is clearly observed. The maximum temperature and pressure are achieved between 60 and 80º crank angle, this is due the heat added during this period. The temperature and pressure start to decrease at around 90 to 100º of crank angles, this decrease is due to the energy conversion into mechanical work during the expansion process.

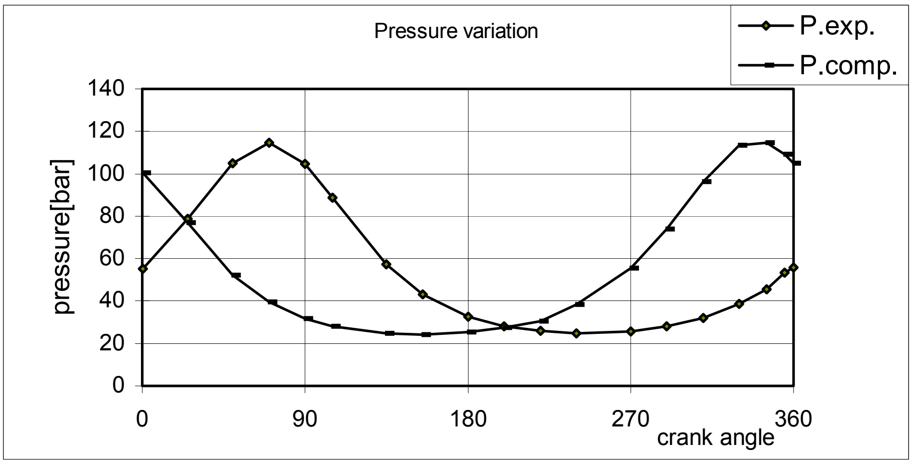

Figure 4. Pressure variation

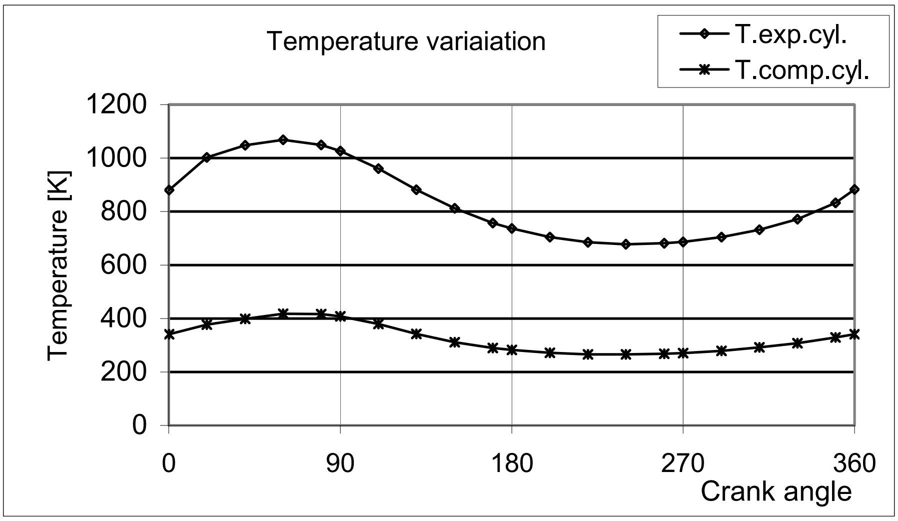

Figure 5. Temperature variation of the working gas

5.2. Mass flow rates and accumulated mass inside the cylinders

The mass transfer between both cylinders depends on various factors. The mass transfer is governed by different factors such as: the cross sectional areas of the pistons (A_P), the pistons speed (S_P) as a function of the engine rpm and stroke length (S), the cross sectional areas of the small pipes in the interconnected passageway, and the density variation between the engine components. The gas density is highly dependent on the operating temperature and pressure. In fact, the mass losses are evaluated as due to the pressure increase. The state equation of ideal gases is employed to calculate the gas density in each crank interval: $p = \rho RT$. Based on the calculated densities, the mass of gas was calculated in each interval. The transferred mass between the cylinders occurs under the effect of pressure difference. The discharge coefficient with a value of 0.7 is considered for all the passages with similar shape. In Fig.6, the flow velocity is illustrated through the variation of the gas entering the expansion cylinder, and the gas leaving the expansion cylinder in Fig. 7. As shown in Figure 6, the gas leakage and mass losses is observed between 15 and 25º Crank Angle, this is mainly due to the high pressure and friction that forces the gas to leak through clearance between the pistons and cylinder. The maximum flow rate was achieved at 70º crank angles. The smoother mass flow rate leaving the expansion cylinder than that entering the cylinder is clearly shown; this is due the reduced pressure. In Fig. 8, the variation of the total mass of the gas in both cylinders versus the crank angle variation is observed with great dependence on the phase difference between the cylinders. it was observed that by lowering the mass of working gas, the temperature of the fluid approaches rapidly the level of hot source temperature after heating. Similarly, the gas approaches the cold temperature sink after cooling. Using the higher pressure or the lower viscosity, or the combination between them could reduce the need for high mass flow rate. As shown in Figure 8, the gas inside the cold cylinder is denser than that in the hot cylinder, except at the angular intervals between (75-145º), as due to the closed position of the piston to the Top Dead Center of the cold cylinder. Actually the total mass in this period is smaller than that in the hot cylinder.

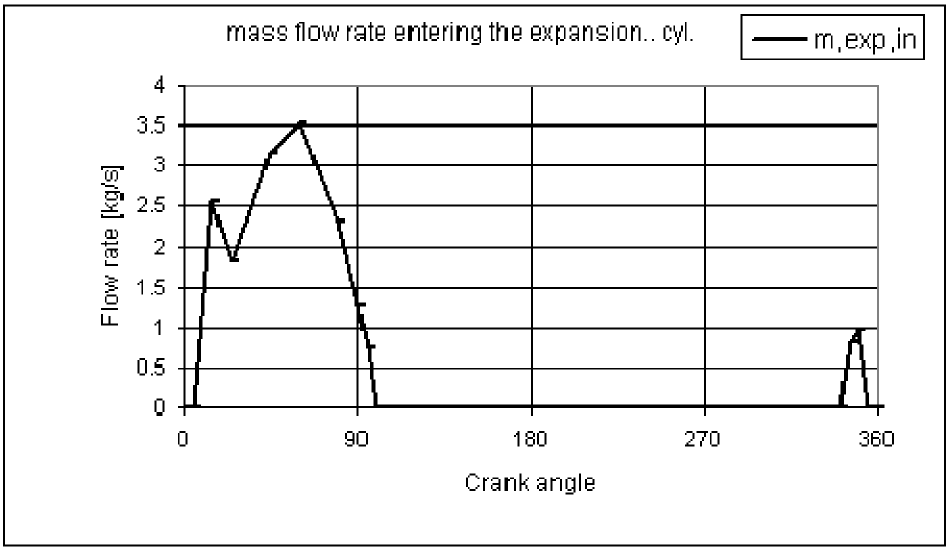

Figure 6. Variation of mass flow rate when entering the expansion cylinder

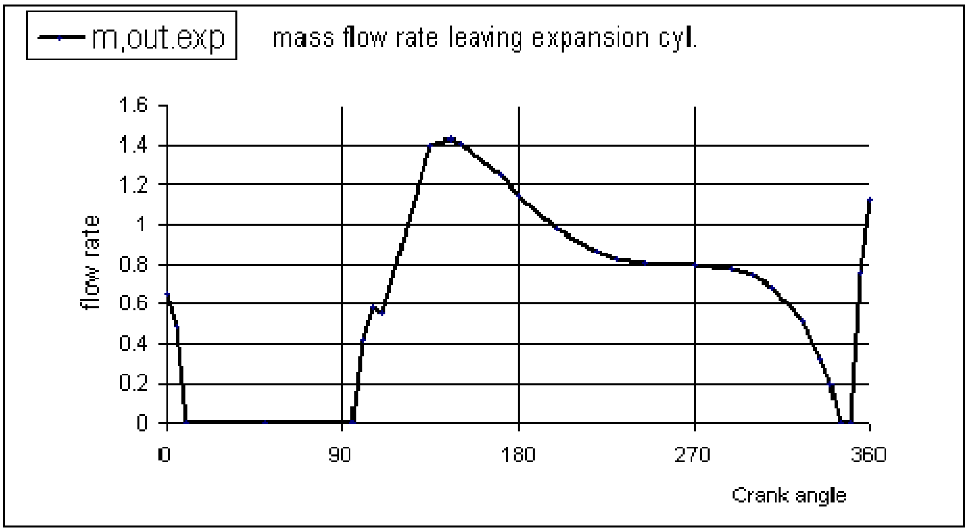

Figure 7. Mass flow rate variations when leaving the expansion cylinder

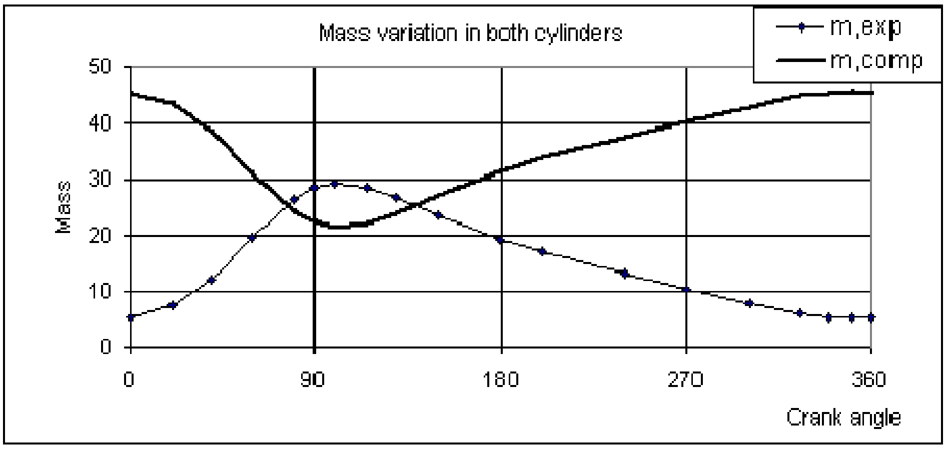

Figure 8. Total mass variation in both cylinders during the adiabatic expansion and compression

5.3. Polytropic Exponent Variation

Practically, in real cycles it is hard to achieve an isothermal behavior. The compression and expansion processes of working gas inside the engine cylinders are associated with the heat and mass transfer, and they are performed with polytropic nature. The work done on or by the system during these processes is expressed by the general expression: (PV^n=constant). The polytropic exponent (n) is assumed to be between the isothermal and adiabatic exponents: 1(isothermal) ≤ n (polytropic) ≤ k (adiabatic). The polytropic exponents were considered and calculated in the hot and cold cylinders under the adiabatic conditions. The polytropic exponent variations versus the crank angle variation are calculated during the hot expansion of the working fluid as shown in Fig.9, and the variation during the cold compression is shown in Fig.10.

$$n_{\exp.(adiab)} = f(\theta_{\exp.})$$

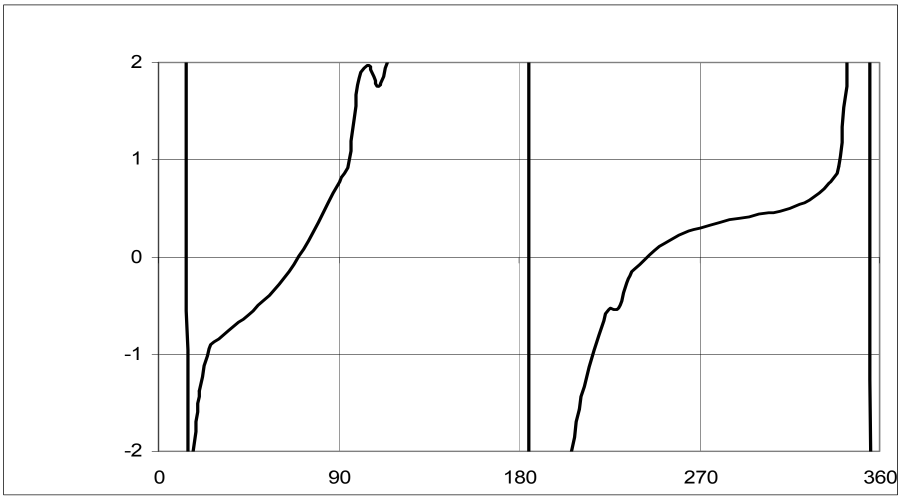

Figure 9.variation of polytropic exponent for the adiabatic expansion of gas inside the hot cylinder.

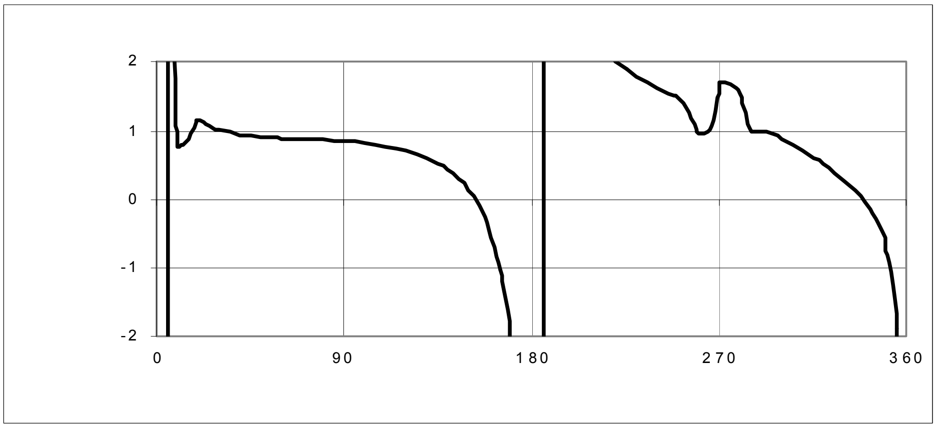

Figure 10. Polytropic exponent variation for the adiabatic compression of the gas inside the cold cylinder

The pronounced variations of this exponent are clearly observed over the total cyclic duration. Practically, the greater variations of the polytropic exponent are observed to occur near the dead centers of both cylinders. The variations of the exponents are primarily provoked by the effect of mass exchange with a slight significance of the heat transfer between the cylinder gas and walls.

5.4. Indicated work per cycle

Several authors demonstrated that the maximum power output of well-developed Stirling engine, is proportionally governed by to the pressure, volume, speed, and temperature. In real engines, the Cooler and heater volumes contribute to large portions of dead volumes; therefore the hot and cold volumes should be as small as possible [18]. The dead volumes accounts up to 50% of the total engine internal volume, they negatively produce an exponential drop in the power output [15,16,18]. In this work, the effect of dead volumes was observed to have a significant reduction on the power output. The optimum dead volume should be accounted to accommodate the necessary heat transfer. The effect gas leakage in real Stirling engines is inevitable; this is due to the higher pressure that forces the sealing elements to leak the gas out of the system. Under the operating pressure a significant power loss was observed to be as a function of gas leakage. Additionally, it was observed that the flow friction consumes significant amount of power from the net engine power. The heat energy is developed and converted into mechanical energy in each operating cycle. The produced work is transferred to the drive mechanism during each operating cycle. Variations of the compression work, expansion work, and network versus the crank angles are presented in Fig.11. The remarkable aspect that can be seen is the similar variation between the compression and expansion works. Another observation that could be detected is the point of origin from which the compression and expansion works are started.

5.5. Evolutional behavior of transferred heat.

The transferred heat from the higher temperature source (1000K) to the gas, and the rejected heat from the gas to the lower temperature sink (300K) are presented against the crank angle variation in Fig.12. Thermal communication between the gas and both reservoirs can be expressed by the instantaneous fluxes of heat within the different cells. The mass flow rate, the specific heat of the working agent and temperature difference between both reservoirs are observed with significant influence on the instantaneous fluxes of heat. The reduced performance of the real Stirling engine was demonstrated as due some deficiencies such as: the non-ideal regeneration, non-isothermal heat transfer, and the non-adiabatic expansion and compression processes. The variations of transferred heat As shown in the figure, the greater amount of heat is added to the flowing mass that enters into the hot cylinder is achieved during the initial period of the gas expansion, during the first quarter of the cycle (90º crank angles).

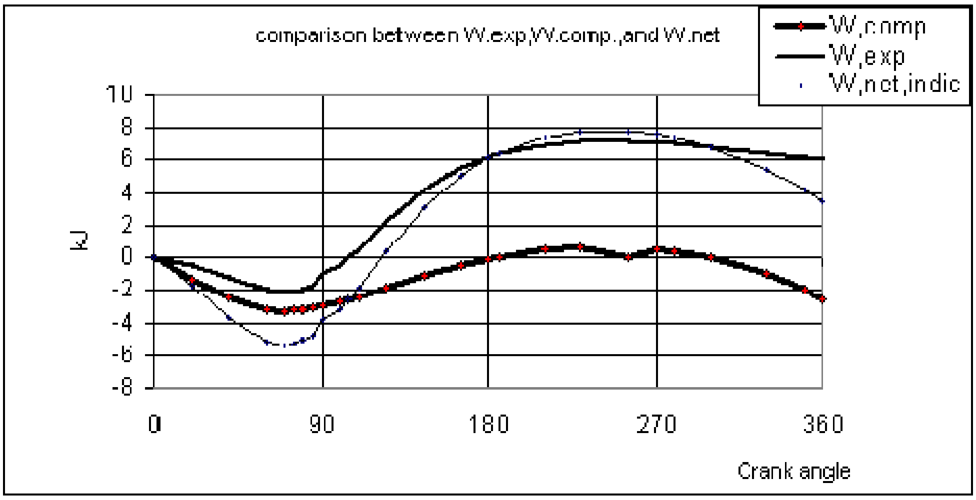

Figure 11. Variations of the work energy versus the crank angles (expansion, compression, and network per cycle.

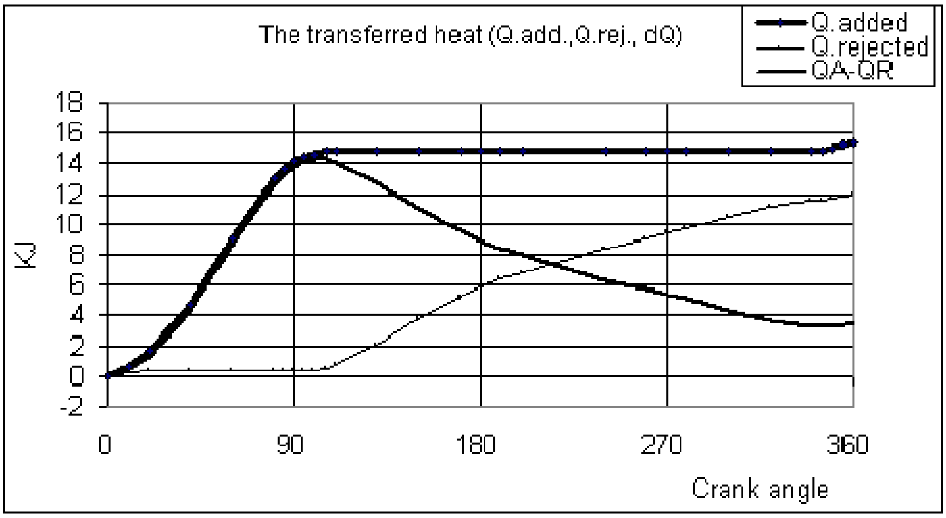

Figure 12. Variations of the transferred heat to and from the gas (Q_{added}, $Q_{\cdot rejected}$, and the heat difference

This is due to the position of heater that is closed to the expansion cylinder. The heat rejection from the working gas is observed with an opposite behavior, the different behavior can be interpreted as due to the effect of gas leakage. Practically, while the cold piston continues moving toward the end point of the compression stroke, the gas which is already heated leaves the compression cylinder back to the hot cylinder without to reject the associated heat.

The effects of mass and heat losses on the engine performance were considered. The obtained results demonstrated that lowering the mass of gas, and minimizing the rejected heat to the surroundings through the cylinder walls could achieve the greater amount of heat. Also, it should be mentioned that the regeneration conditions are much far away than those of the ideal regenerator.

6. Conclusion

In this work, a thermodynamic analysis of Stirling engine was performed. The analysis provides the necessary data for evaluating several operating aspects, which contributes to the improvement of the Stirling engine. The employed model is capable to stabilize all the thermo-physical parameters of the flowing gas between the engine cylinders. The model provides necessary information regarding the irreversible factors, which influence the conversion of thermal energy into a useful mechanical work per cycle. With respect to the gas leakage and phase difference, the variations of simulated parameters were calculated and represented on proper performance curves. The proposed numerical simulation permits including the gas leakage through the clearance between the piston and cylinder. The system of governing equations (mass and energy) equations was iteratively solved in each control volume on a step-wise basis of crank angles. The obtained results show that the lowered performance of the real Stirling engine is related to some deficiencies such as: the non-ideal regeneration, the non-isothermal heat transfer, the gas leakage, and the significant friction associated with the flowing agent through the heat exchangers. The energy losses due to the significant amount of friction associated with the flowing agent through the heat exchangers, and the shuttle effect are additional factors.

It was demonstrated that lowering the charging mass and minimizing the gas leakage could reach the higher thermal efficiency. The working fluid should be with low viscosity to reduce the pumping losses. The higher pressure, or the lower viscosity, or the combination between them could reduce the need for high mass flow rate.

The effect of dead volume in real Stirling engines is unavoidable; it reduces the engine network and thermal efficiency. In real engines, the leakage tendency of the fluid is inevitable and it negatively affects the engine power output, the gas leakage is due to the higher pressure that forces the sealing elements to leak the gas out of the system.

Finally, the obtained stable evolutional behavior is good indicators that encourage the future research and development of finding proper measures to overcome the engine deficiencies. In the next future, a comparison between the adiabatic and non-adiabatic performance will be made using the same model. This comparison will be focused on evaluating the effect of higher temperature source on the work output and engine efficiency under the adiabatic and non-adiabatic conditions, in order to minimize the deviation between the real and ideal cycles. Based on the expected results, the model will be validated against experimental data.

References

[1] J.B.Heywood, Internal Combustion Engines Fundamentals, McGraw-Hill Book Company, 1988.

[2] A. D. Gosman, Flow Processes in Cylinders, in J.H. Horlock, and D.E. Winterbone, The Thermodynamics and Gas Dynamics of Reciprocating Engines, (1986), Vol. II, Oxford University Press

[3] Youssef Timoumi et al. Design and performance optimization of GPU-3 Stirling engines. Energy (2008), 33: 1100-1114.

[4] Youssef Timoumi et al. Performance optimization of Stirling engines. Renewable Energy (2008), 33: 2134-2144.

[5] D.G.Thombare, S.K.Verma, Technological development in the Stirling cycle engines. Renewable and Sustainable Energy (2008), 12: 1-38.

[6] Bancha Kongtragool, Somchai Wongwises, A review of solar-powered Stirling engine and low temperature differential Stirling engine. Renewable and Sustainable Energy (2003), 7: 31-154.

[7] Schmidt G. Classical analysis of Stirling engine operation. A report published in German Engineering Union (Original German), vol. XV; 1871, p.1-12.

[8] Bancha Kongtragool, Somchai Wongwises, Investigation on power output of the gamma-configuration low temperature differential Stirling engines, (2005), 30: 465-476.

[9] Urieli U, Berchowitz DM. Stirling cycle machine analysis. Bristol Hilger Ltd: 1984.

[10] Finkelstein T, Thermodynamic analysis of Stirling engines, Spacecraft Rockets (1967), 4(9): 1184-1189.

[11] Stig Kilgard et al., Preliminary results from simulation of temperature oscillations in Stirling engine regenerator matrices, Energy, (2006), 31: 1371- 1383.

[12] Ihsan Batmaz, Suleiman Ustun, Design and manufacturing of a V-type Stirling engine with double heaters, Applied Energy (2008), 85: 1041-1049.

[13] Bancha Kongtragool, Somchai Wongwises, Thermodynamic analysis of a Stirling engine including dead volumes of hot space, cold space, and regenerator, Renewable Energy (2006), 31: 345-359.

[14] H. Karabulut et al., Nodal analysis of a Stirling engine with concentric piston and displacer, Renewable Energy (2006), 31: (2188-2197.

[15] Nezaket Parlak et al., Thermodynamic analysis of a gamma type Stirling engine in non-ideal adiabatic conditions, Reneable Energy (2009), 34: 266-273.

[16] H. Karbulut et al., Thermodynamic analysis of a βtype Stirling engine with a displacer driving mechanism by means of a lever, Renewable Energy (2009), 34: 202-208.

[17] Petrescu S, Costea M. Application of the direct method to irreversible Stirling cycle with finite speed. Int. J Energy Conver, Conserv. Environ. (2002), 26: 586-609

[18] Kongtragool B, Wongwises S. Thermodynamic analysis of a Stirling engine including dead volumes of hot space, cold space, and regenerator. Renewable Energy (2006), 31: 345-359.

[19] Finkelstein T. Insights into the thermodynamic analysis of Stirling cycle machines, AIAA-94-3951-CP (1994): 1829-1834.

[20] Costea M, Fedit M. The effect of the overall heat transfers coefficient variation on the optimal distribution of the heat transfer surface conductance of area in Stirling engine. J Energy Conversion Manag. (1998), 39 (16-18): 1753-1761.

[21] Isshiki S et al., Studies of flow resistance and heat transfer of regenerator wire meshes of Stirling engines in oscillatory flow. JSME Int. J Fluid Therm. Eng, Series B (1997), 40 (2): 281-289.

[22] Berrin Erbay L, Yavuz H. Analysis of the Stirling heat engine at maximum power conditions. Energy (1997), 22 (7): 645s-650

[23] Walker G. Stirling engines, Oxford Clarendon press; 1980

JJMIE
Jordan Journal of Mechanical and Industrial Engineering

Volume 4, Number 5, November 2010
ISSN 1995-6665
Pages 629 - 640

Investigation of Optimum Fuel Injection Timing of Direct Injection CI Engine Operated on Preheated Karanj-Diesel Blend

Kamal Kishore Khatri [a,*], Dilip Sharma [a], S. L. Soni [a], Satish Kumar [a], Deepak Tanwar [b]

[a]*Department of Mechanical Engineering, M.N.I.T., Jaipur 302017, India*

[b]*Department of Civil Engineering, M.N.I.T., Jaipur 302017, India*

Abstract

The conventional petroleum fuels are depleting rapidly and the prices are going up day by day. Moreover, these petroleum fuels are responsible for green house emissions and other forms of pollution in the environment. Among various options available, the fuels derived from vegetable oils have emerged as promising alternate fuels for IC engines. The use of unmodified or straight vegetable oils in diesel engine creates operational problems due to their high viscosity and poor volatility. In the present work, an experimental setup has been designed to reduce the viscosity of the fuel by blending Karanj oil with Petro-Diesel and preheating the Karanj-Diesel blend. Experiments are also conducted to determine the optimal injection pump timing for the selected blend, with respect to the engine performance parameters. Experiments are performed using Petro-Diesel and preheated Karanj-Diesel blend (in ratio 40:60 by volume) on constant speed direct injection C.I. engine. The effect of injection timing on the preheated Karanj-Diesel blend is investigated and the results are analyzed. On the basis of results obtained, the optimal injection timing is determined for Karanj-Diesel blend, which is found to be 19º BTDC.

Keywords: Brake specific fuel consumption; Brake thermal efficiency; Emissions; Biodiesel; Transesterification; Diesel engine.

Nomenclature

BIS	Bureau of Indian standards
BSFC	Brake specific fuel consumption
BTDC	Before top dead center
BTE	Brake thermal efficiency
C.I.	Compression ignition
CO	Carbon monoxide
HC	Unburned hydrocarbons
HSU	Hartridge smoke unit
K40	Preheated blend of 40% Karanj and 60% Petro-diesel by volume
KO	Karanj oil
NOx	Oxides of nitrogen
SVO	Straight vegetable oil

* Corresponding author. kamalkhatri@rediffmail.com

1. Introduction

Depleting oil reserves, increasing oil prices, lack of availability of the mineral oil and the problem of environmental pollutions have prompted research worldwide into alternate fuels for internal combustion engines. Vegetable oil based fuels have been proved as potential alternative greener energy substitute for fossil fuels. The vegetable oils are renewable in nature and have comparable properties with Petro-Diesel. These are biodegradable, non-toxic, and have potential to reduce the harmful emissions [1,2,3,4]. However, use of unmodified or straight vegetable oil (SVO) directly in the engine creates several operational and durability problems such as severe engine deposits, injector coking, piston ring sticking, gum formation and lubricating oil thickening. These problems relate to the high viscosity, poor volatility and cold flow characteristics of the vegetable oils due to large molecular weight and bulky molecular structure [5,6]. Researchers have suggested different techniques for reducing the viscosity of the vegetable oils, which are dilution/blending, heating/pyrolysis, micro-emulsification and transesterification [1,7,8]. The transesterification process has been proved as the most effective method and widely utilized. However, this method adds extra cost due to the chemical processing. Hence utilization of blended or heated vegetable oil as an alternate fuel is an attractive option in rural and remote areas of developing countries [5].

The vegetable oils can be blended in small proportion with the Petro-Diesel successfully [8,9,10]. But if greater blend ratio of the oil is to be used, then preheating of vegetable oil or its blend with petro-diesel is the viable solution of the problem. Several researchers have reported that the vegetable oils in small blending ratios with Petro-Diesel can be used safely and advantageously in the Diesel engine with the exception of the slight concern for the little increase of smoke level. The most of the emission like CO, CO_2, HC, NO_x and smoke are reduced when the vegetable oils are preheated compared to the unheated row vegetable oil although the level of emissions is slightly higher compared to the Petro-diesel [5,6,10,11].

Considering these facts, a set of engine experiments were conducted using preheated blend of Karanj oil with Petro-Diesel on a engine which is widely used for agriculture, irrigation and decentralized electricity generation. Further experimentations were carried out to determine the optimal injection timing for the given Karanj-Diesel blend.

Fuel modification method adopted in the present study or any other, can reduce the viscosity but other problems due to the differences in the properties like cetane number still exist. Hence, property changes associated with the differences in chemical structure between vegetable oil and petroleum-based diesel fuel may ask for change in the engine operating parameters such as injection timing, injection pressure etc. These operating parameters changes can cause different performance and exhaust emission than the optimized settings chosen by the engine manufacturer. Hence it is necessary to determine the changed optimum values of these parameters. In the present study, the attention is focused on finding the optimal injection pump timing for the Karanj-Diesel blend with respect to the performance parameters.

It is established that injection timing influences all engine characteristics significantly. The reason is that injection timing influences the mixing quality of the air fuel mixture and hence the whole combustion process. Several researchers have indicated that there is an advance in the fuel injection timing when the vegetable oil based fuel is used in place of Petro-Diesel in diesel engines. This is because of higher bulk modulus of vegetable oils than the mineral diesel. Due to higher bulk modulus and therefore higher sound velocity, the pressure waves from the fuel pump to the fuel injector travel faster and thus advances the fuel injection timing [12-14]. In addition to the advance injection timing, the vegetable oils have been noted to exhibit longer ignition delay periods especially at low load operating conditions. Longer delays between injection and ignition lead to unacceptable rates of pressure rise with the result of diesel knock, because too much fuel is ready to take part in premixed combustion. Hence the retardation of the injection timing will decrease the maximum pressure in the cylinder and leads to a lower peak rate of heat transfer and hence to lower combustion noise. The retarded injection leads to lower temperature, the NO_x emissions may also reduced. On the other hand the retarded injection timing may lead to increase in smoke emissions, but the trends vary significantly with the types and designs of the engines. HC emissions are already low for a direct injection diesel engine and vary only modestly with injection timing [13,14,15]. In the present research work, the effect of retarding the injection timing is investigated to find out the optimal injection timing of preheated Karanj- Diesel blend.

1.1. Selection of oil for study: Karanj oil

As per the information available about the inedible oils in the literature, Mahua, Neem, Karanj and Jatropha are the front runners in India in terms of the production and availability. Mahua is most abundantly available oil but the calorific value of Mahua is very low (30349 KJ/kg) [8]. Jatropha has also emerged as a major oil source but it is carcinogenic in nature. Neem oil can be a very good substitute but it should be spared for its well established use and practices in herbal and medical field. So by analyzing and comparing the properties of these oils, Karanj is chosen as SVO for the research.

The botanical name of Karanj tree is Pongamia Pinnata. It is chiefly found along the banks of streams and rivers or near the seacoast. It resists drought well, is moderately frost hardy and is highly tolerant of salinity. The tree starts bearing at the age of 4 - 7 years. The pods come to harvest at different periods of time in different parts of the country, but the harvest season extends in general from November - December to May - June. The yield of the seed is said to range from 9-90 kg per tree, indicating a yield potential of 900 to 9000 kg seed/ha (assuming 100 trees/ha). 25% of this yield might be safely considered as oil because the yield of oil from seeds is around 24 to 27.5%. The total yield in India is estimated to be about 135000 tons. But only 8000 tons of oil is presently being utilized which is only 6% of the total estimated produce. Thus there is an ample scope for utilizing the energy source (Karanj oil) as fuel [8,16,17]. Important physico-chemical properties of Karanj oil and Petro-Diesel have been shown in table 1.

2. Experimental Set-Up and Procedures

A naturally aspirated direct injection diesel engine is more sensitive to fuel quality. The main problem of using Karanj oil in unmodified form in diesel engine is its high viscosity. Therefore, it is necessary to reduce the fuel viscosity before injecting it in the engine. High viscosity of Karanj oil can be reduced by heating the oil using waste heat of exhaust gases from the engine and also blending the Karanj oil with diesel. Viscosity of Karanj oil and diesel was measured at different temperatures to find the effect of temperature on viscosity. A typical engine system widely used in the agricultural sector has been selected for present experimental investigations. A single cylinder, four stroke, constant speed, water cooled, direct injection diesel engine was procured for the experiments. The technical specifications of the engines are given in Table 2.

Power-star make electric dynamometer was used to measure torque or brake power. It consisted of an alternator to which electric bulbs were connected to apply load. The schematic layout of the experimental setup for the present investigation is shown in Fig.1.

Table 1 Comparison of physical and chemical properties of Karanj oil and diesel

S. No.	Parameters	Karanj oil	Diesel
1	Saponification Value	185 - 195	-
2	Iodine value	80 - 90	38.30
3	Acid Value (Max.)	20	0.06
4	Moisture (% max.)	0.25	24.66
5	Color in 1/4 inch cell (Y+5R)	40	102.5
6	Refractive Index (40 °C)	1.473 - 1.479	1.472
7	Specific Gravity (30 °C)	0.90	0.82
8	Cloud Point (°C)	-1	-11
9	Pour Point (°C)	-2 to -5	-12
10	Calorific Value (MJ/kg)	37	44
11	Viscosity (St at 30^0 C)	74.14	8.54
12	Cetane number	51.0	47.8
13	Flash Point (°C)	230	66
14	Carbon residue (%)	0.71	0.1
15	Ash content (%)	0.04	0.01
16	Sulphur content (%)	-	0.05

Table 2 Specifications of the Engine

S.No.	Component	Unit	Description
1.	Name of the engine	-	Kirloskar Oil Engine Model AV1
2.	Type of engine	-	Vertical, four stroke cycle, single acting, totally enclosed, high speed, C.I. engine
3.	No. of cylinders	-	1
4.	Direction of rotation		Counter clockwise (When looking at flywheel)
5.	IS Rating at 1500 rpm	kW(bhp)	3.7 (5.0)
6.	Bore	mm	80
7.	Stroke	mm	110
8.	Cubic Capacity	liters	0.553
9.	Compression Ratio	-	16.5 : 1
10.	No. of Injection Pumps and Type	-	1 number, Single cylinder, flange mounted without camshaft
11.	Governor type	-	Mechanical centrifugal type
12.	Class of governing	-	B1
13.	Injection timing	Degree crank angle	23º BTDC
14.	Fuel injection pressure	bar	200

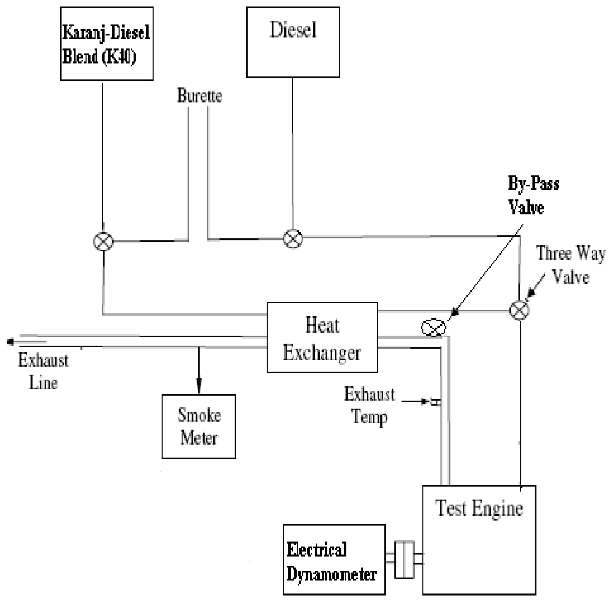

Fig.1 Schematic Diagram of Experimental Setup.

The main components of the experimental setup are two fuel tanks (Diesel and Karanj-Diesel blend), heat exchanger, exhaust gas line, and performance and emissions measurement equipment. The engine is started with diesel and once the engine warms up, it is switched over to Karanj-Diesel blend (K40). After concluding the tests with K40, the engine is again switched back to diesel before stopping the engine until the Karanj-Diesel blend (K40) is purged from the fuel line, injection pump and injector in order to prevent deposits and cold starting problems. A heat exchanger was designed to preheat the blend using waste heat of the exhaust gases. The temperature of the blend was maintained within the required range by providing a by-pass valve in exhaust gas line before the heat exchanger. A thermocouple was provided in the exhaust line to measure the temperature of the exhaust gases. Exhaust smoke was measured with the help of 'Envirotech APM 700 Smoke meter'.

3. Results and discussion

After finalizing Karanj oil as an alternate fuel, attempts were made to reduce its viscosity by preheating it, using the exhaust gases coming out from the engine. It was found that temperature obtained in the heat exchanger was not adequate to bring down the viscosity of pure Karanj oil equivalent to diesel. It is also known that the pure vegetable oils create more problems in engines than blended oils. So it was then decided to use Karanj oil as blending fuel in Diesel to obtain Karanj-Diesel blend. In the present study, viscosity was reduced by both preheating and blending. Before carrying out detailed experimentation, finalization of the optimum Karanj-Diesel blend was done. It was observed experimentally that the blend could be preheated up to 55-60 ºC at no load with heat exchanger developed. From the Fig. 2, it is observed that at this temperature range substitution of Diesel by Karanj oil to the extent of 40% makes a blend having viscosity equal to that of pure Diesel at room temperature. (BIS limits of viscosity: For Grade A diesel - 2.0 to 7.5 cSt at 38 °C, For Grade B diesel - 2.5 to 15.7 cSt at 38 °C) Thus the results in this research work pertain to preheated Karanj-Diesel blend having 40% Karanj oil and 60% Diesel oil (K40). Engine performance and smoke emissions at constant speed and variable load are covered in experimental investigations. Experiments were conducted for optimizing the fuel injection timing for K40. The fuel injection pressure was maintained at optimum injection pressure of 200 bar and tests were carried out at different injection timings starting from 23^0 BTDC to 15^0 BTDC, retarding the timing by the interval of 2^0 crank angle. The fuel injection timing was retarded through controlling the start of injection pump delivery, by inserting shims of different thickness between the fuel injection pump body and engine body. To perform all the experiments, the engine was run for sufficient time duration. During this period, the engine performed normally, with no undesirable combustion phenomena. The engine components were found to be in normal condition after the tests. The noise level during the operation was also within the limit.

3.1. Optimization of Performance parameters

Optimum fuel injection timing is that fuel injection timing, at which engine delivers maximum thermal efficiency, minimum BSFC. Engine was run at different fuel injection timings (23^0, 21^0, 19^0, 17^0, and 15^0 BTDC). BSFC, thermal efficiency, and smoke density were measured at different fuel injection timings for preheated Karanj-Diesel blend (K40). Injection pressure was maintained at optimum value of 200 bar for each injection timing. The base line data at standard injection timing of 23^0 BTDC for Diesel were also generated.

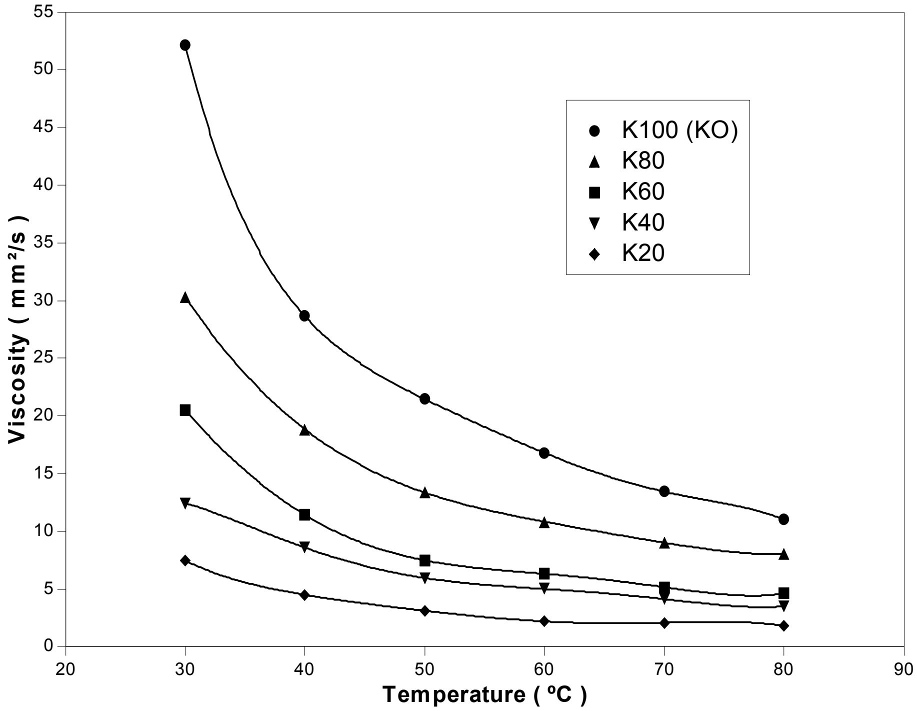

Fig.2 Effect of temperature on viscosity of KO and its blends with Diesel

3.1.1. Effect of injection timing on brake specific fuel consumption

Injection timing is a very important parameter that significantly influences all engine characteristics. This is mainly due to the fact that injection timing influences the mixing quality of the air–fuel mixture and, consequently, the combustion process, including harmful emission. Brake specific fuel consumption is a comparative parameter that shows how efficiently an engine is converting fuel into work. Brake Specific Fuel Consumption (BSFC) has been plotted against load for standard injection pressure at constant speed of 1500 rpm for different injection timing from 23º to 15º BTDC. Fig. 3 shows some typical curves for variation of BSFC with load. As seen from plots BSFC decreases with increase in of power output and then starts increasing after a point for the given injection pressures under study. The point at which it becomes minimum, is referred to as the "best economical load" point, which occurs at around 80-85% load for Karanj-Diesel blend. When we retard the injection timing, at first the BSFC decreases and then it increases. Lowest BSFC is observed at an injection timing 19 º BTDC. The value of lowest BSFC is 0.2691 Kg/KWh. Slight increase in the specific fuel consumption was observed at retarded injection timing from 19º to 15º BTDC.

3.1.2. Effect of injection timing on brake thermal efficiency

Brake Thermal Efficiency (BTE) is an important parameter, as it provides a measure of net power developed by the engine, which is readily available for use at the engine output shaft. In this Brake thermal efficiency curves are plotted at different injection timing at standard injection pressure. Typical variation of Brake Thermal Efficiency (BTE at standard conditions) with load at standard injection pressures of 200 bar is shown in Fig. 4. It has been observed from these plots that the brake thermal efficiency slightly increases with retarding the injection timing from 23º to 19º BTDC after that decrease in BTE are observed from 19º to 15º BTDC. From these plots it was also observed that maximum value of BTE lay between 80-85 % of full load for the given injection pressure under study. The maximum value of thermal efficiency was observed as 28.89 % at injection timing 19 º BTDC.

3.1.3. Effect of injection timing on Smoke Emission

Smoke is produced during acceleration, overloading or even during full load operation of the engine. Under these conditions more fuel is burned and the prevailing temperatures inside the combustion chamber become very high. Because of this high temperature there is thermal cracking of molecules rather than normal oxidation. This thermal cracking is in the form of soot/carbon. This soot is a graphite structure, jet black in colour and is called smoke. Smoke density is measured experimentally for different injection timing. The variation of smoke density with load is shown in Fig. 5, which shows minimum smoke during idling which increases with load. It is observed from these plots that the smoke density decreases with retarding the injection timing from 23º to 19º BTDC. However, it increases with further retarding the timing from 19º to 15º BTDC. From these plots it was observed that the minimum value of smoke density was observed at injection timing 19 º BTDC for complete range of load.

Based on these results obtained for BSFC, BTE and smoke density, 19 º BTDC was found the optimum injection timing for the K40.

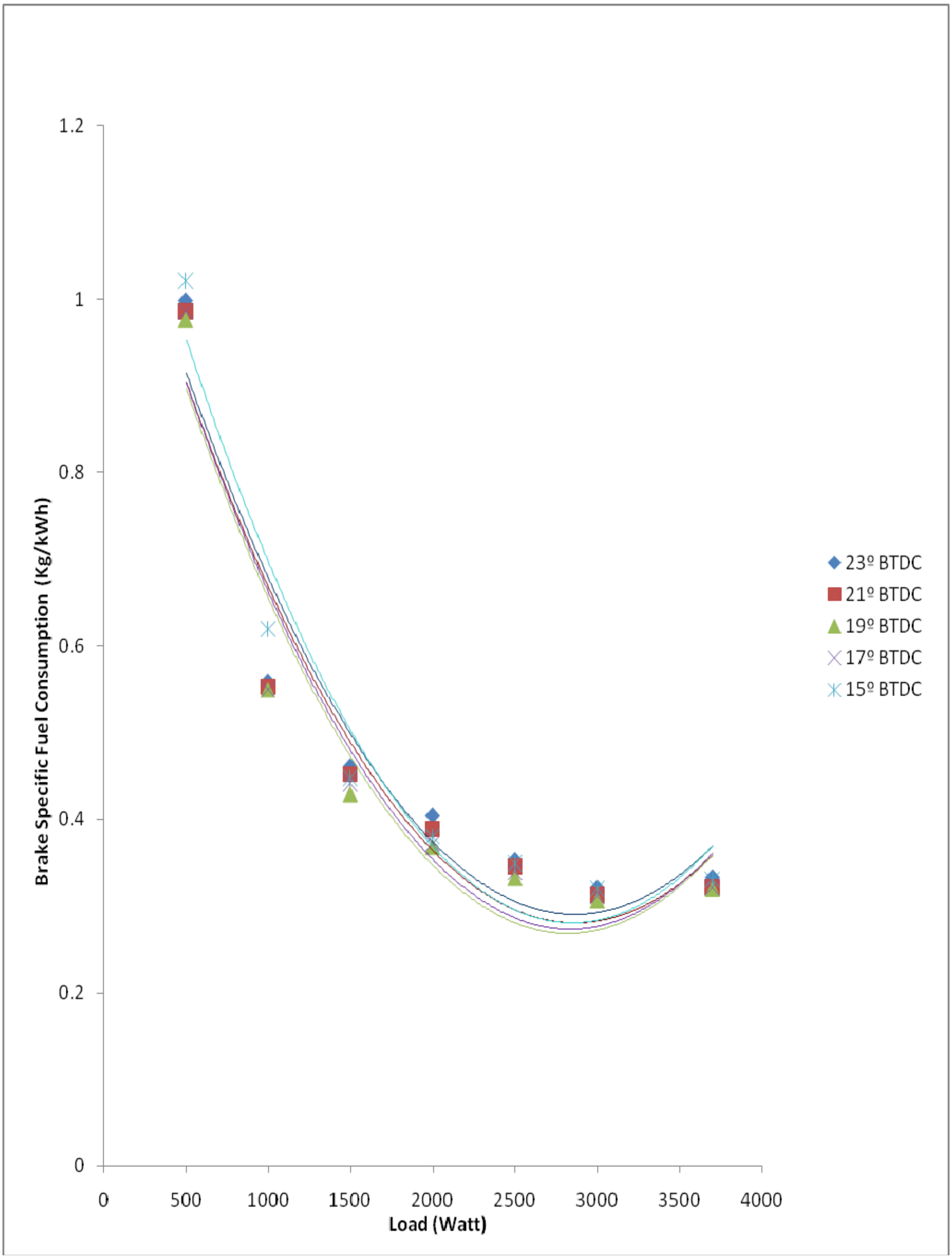

Fig.3 Variation of BSFC as a function of load for K40 at different injection timings

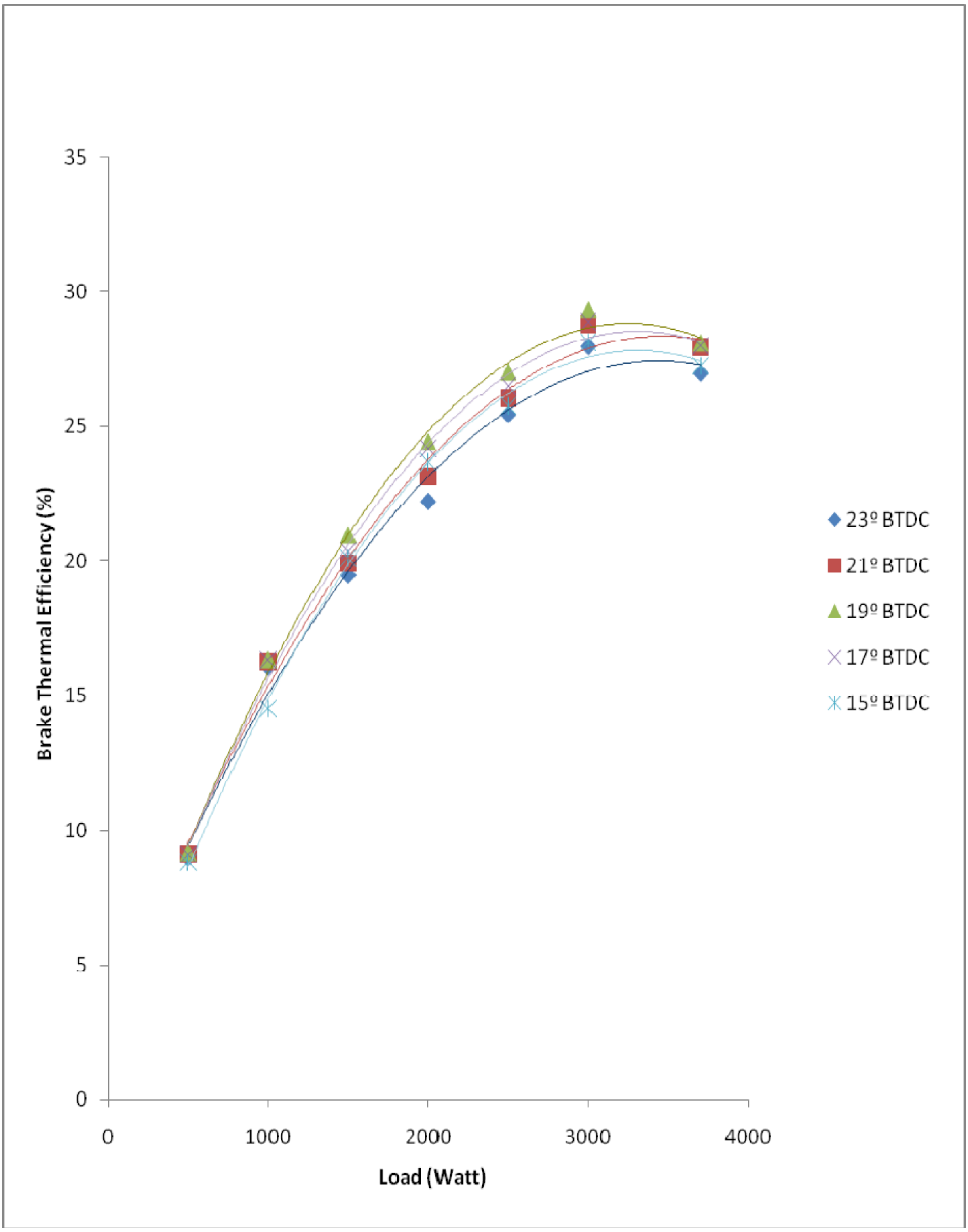

Fig.4 Variation of BTE as a function of load for K40 at different injection timings

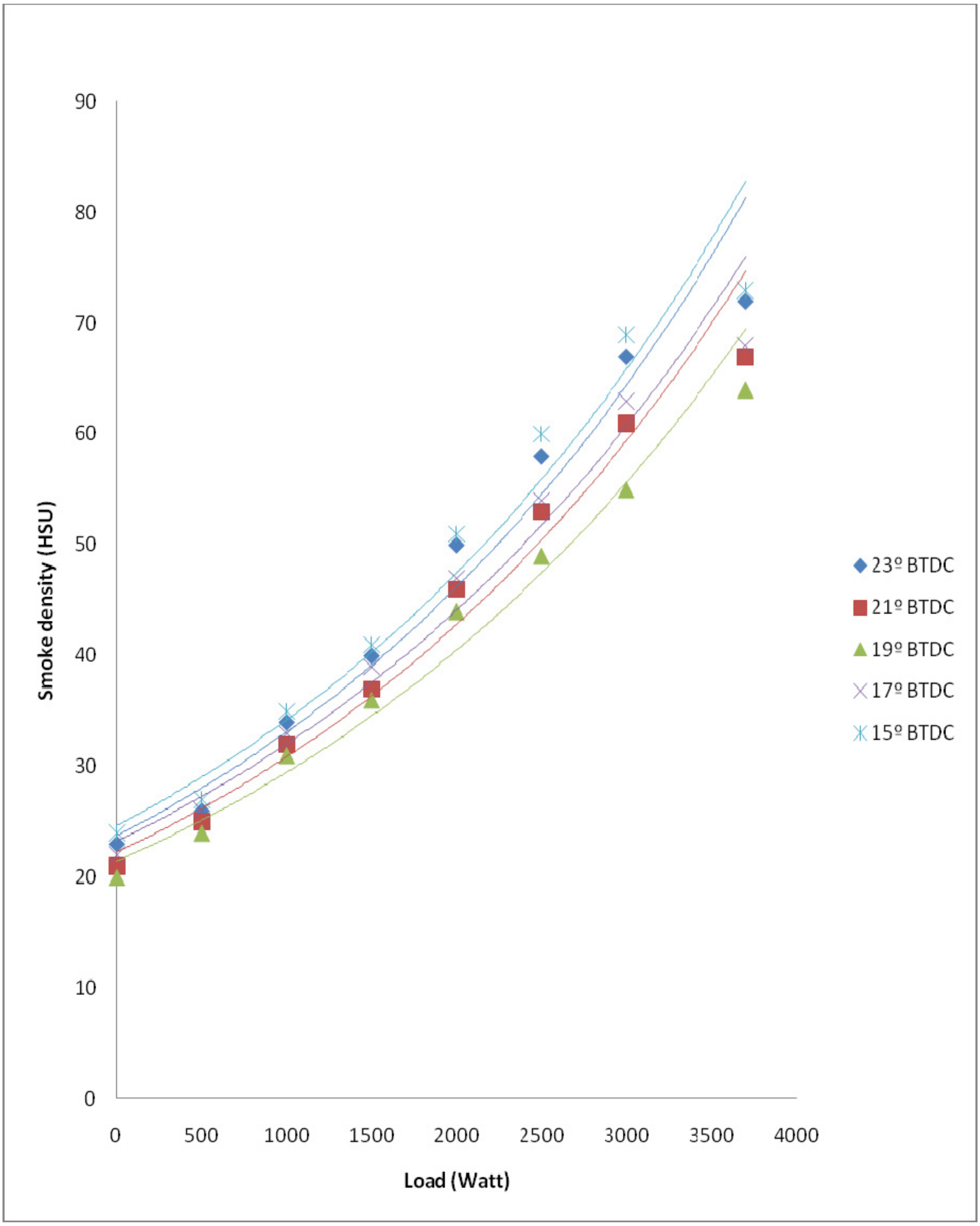

Fig.5 Variation of Smoke density as a function of load for K40 at different injection timings

3.2. Comparison of performance and smoke emission for different fuels

Variation of BSFC, BTE and smoke density as a function of load for Diesel, preheated K40 at standard injection timing and preheated K40 at optimum injection timing of 19º BTDC are shown in Fig.6, Fig.7 and Fig.8 respectively. It was observed that BSFC was lowest at all loads for pure Diesel (at standard timing of 23º BTDC) as shown in Fig.6. The minimum value of BSFC for pure Diesel was 0.2398 Kg/kWh. Highest value of BSFC was observed when running the engine with K40 at standard timing. The value of minimum BSFC for K40 at standard timing was 0.2901Kg/kWh. Lower calorific value of K40 leads to increased volumetric fuel consumption in order to maintain similar energy input to the engine. The value of

BSFC for K40 at optimum timing was lower as compared to the K40 at standard timing but higher than the value for Diesel. The value of minimum BSFC for K40 at optimum timing is 0.2691 Kg/KWh. This improvement may be due to the better mixing quality of air-fuel mixture because of retardation of injection timing. Despite the K40 at optimum timing, having higher brake specific fuel consumption than the Diesel, the brake thermal efficiency is practically the same as compared to the Diesel because of higher calorific value of Diesel. However the BTE for the K40 at optimum timing (28.89 %) is greater than the K40 at standard timing (27.52%) due to better mixing and hence better combustion efficiency. (Fig.7) Smoke density for Karanj-Diesel blend was greater than that of diesel. This is possibly a result of poor spray atomization and non –uniform mixture formation with Karanj oil. Smoke density increases with the increase in load in all the cases of fuels. The smoke density for the K40 at the optimum timing is lower than the smoke density for K40 at standard timing but it is greater than the Diesel. (Fig.8)

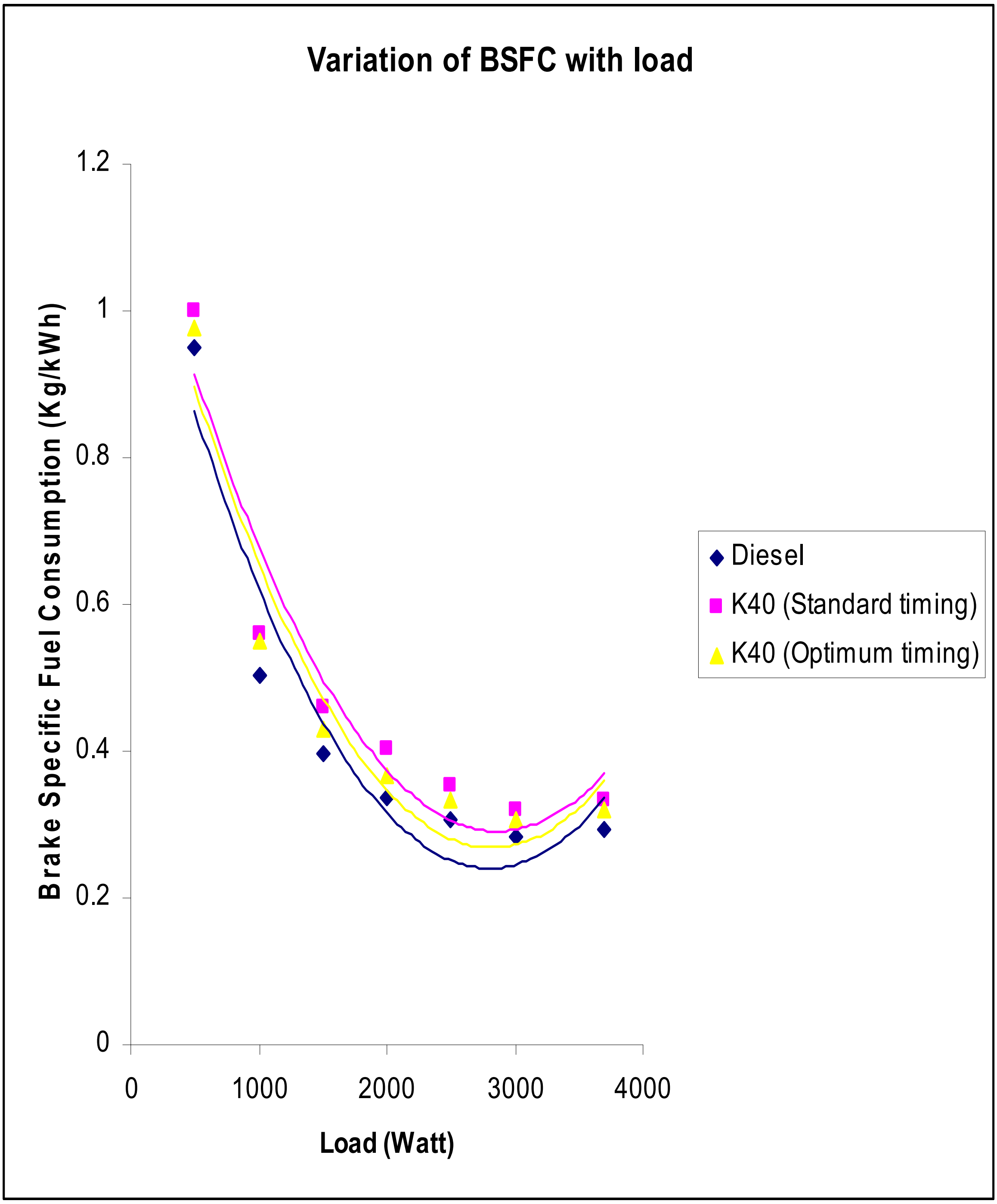

Fig. 6 Comparison of BSFC as a function of load for different fuels

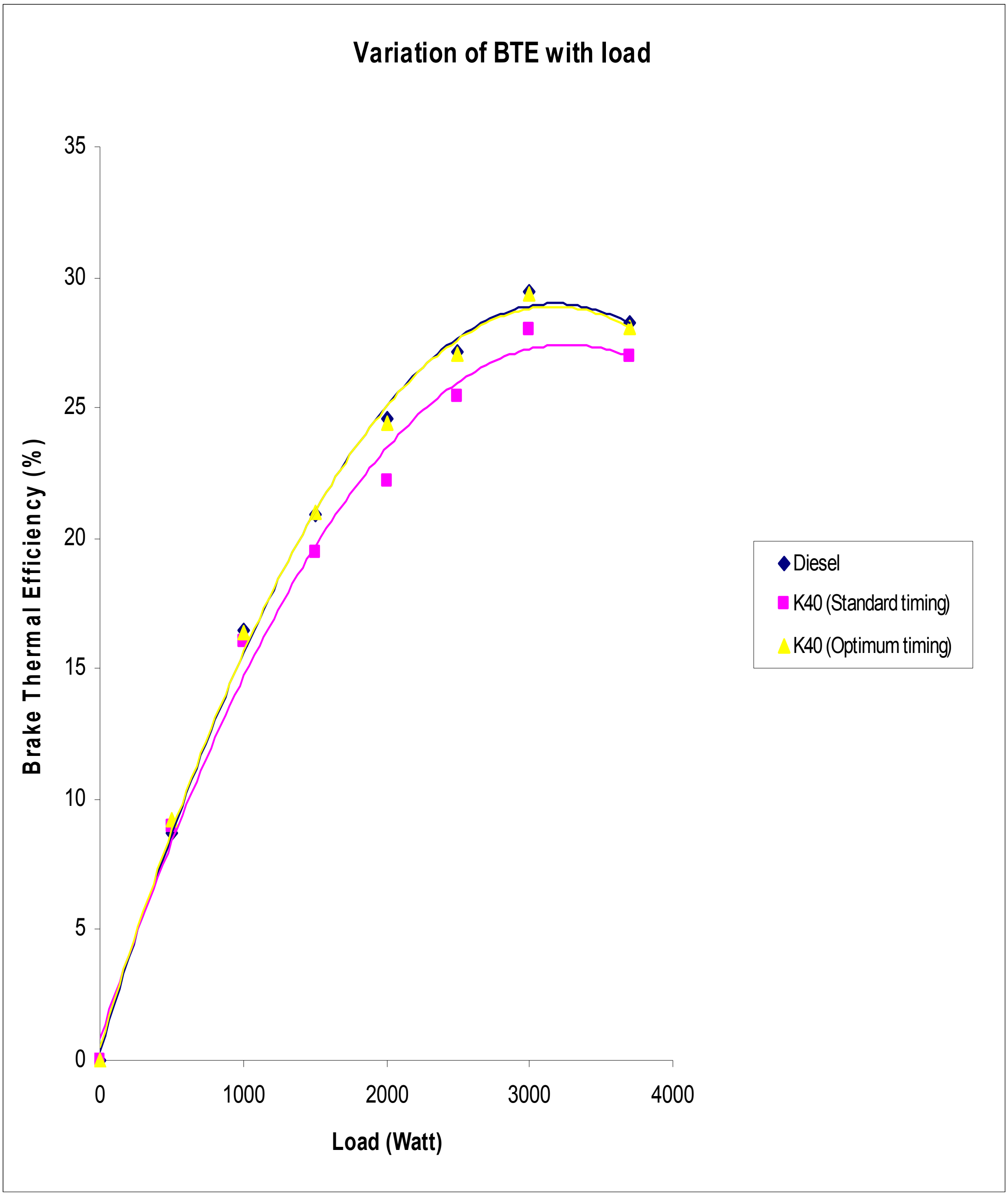

Fig. 7 Comparison of BTE as a function of load for different fuels

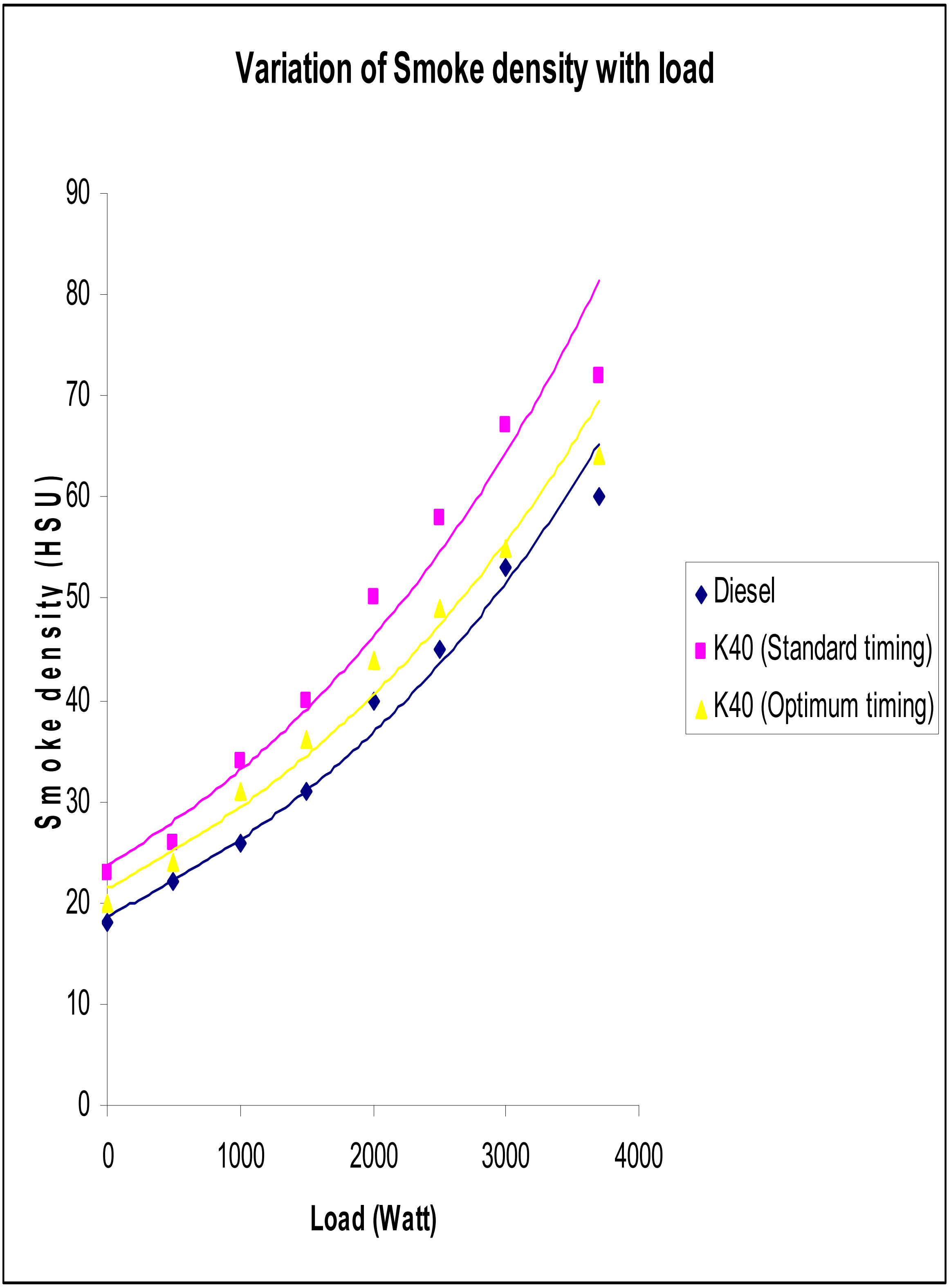

Fig.8 Comparison of Smoke density as a function of load for different fuels.

4. Conclusions

On the basis of the observations and the results of the experimental investigations on a single cylinder, four strokes, constant RPM, stationary, water cooled, compression ignition engine, run on Karanj-Diesel blend and Diesel oil at different injection timings, the following conclusions may be drawn from the present study.

The properties of Karanj -Diesel blend used for the study, are comparable with those of pure Diesel. The viscosity of Karanj oil is reduced by first preheating the Karanj oil and then by blending the Karanj oil with diesel. A suitable experimental setup developed, is able to reduce the viscosity of Karanj oil close to that of conventional diesel in order to make it suitable for use in a C.I. engine. Heating of the Karanj- Diesel blend is done through a heat exchanger, by utilizing the waste heat of the exhaust gases coming out from the engine. By the help of the heat exchanger developed, the temperature of the Karanj-Diesel blend can be raised to 55-60 ºC at no load. It is found that substitution of Diesel oil by Karanj oil to the extent of 40% is best possible in the temperature range of 55-60 ºC as the viscosity of blend becomes equal to that of pure Diesel. A successful operation of a compression ignition engine, fuelled with Karanj-Diesel blend over a wide range of load and injection timing without causing any undesirable combustion phenomena is observed. There is significant effect of injection timing on engine performance. For the above Karanj-Diesel blend (K40) injection timing of 19º BTDC is found to be the optimum injection timing, as highest brake thermal efficiency, lowest brake specific fuel consumption and lowest smoke density are observed over the entire load range at this injection timing. Similar values of brake thermal efficiency and higher values of brake specific fuel consumption in case of Karanj-Diesel blend can be attributed to low calorific value of Karanj oil as compared to that of Diesel oil. Slightly more smoke emissions are observed with Karanj-Diesel blend compared to the Diesel over the entire load range mainly due to poor atomization of Karanj oil. However the smoke level for K40 at optimum timing is less than the smoke level of K40 at standard timing.

Therefore, it may be concluded that preheating and blending of the vegetable oils with diesel, together can reduce the problems of straight vegetable oils drastically making it useful substitute for diesel fuel. The preheated Karanj-Diesel blend with optimized fuel injection timing can be used in CI engines more efficiently than the blend at standard injection timing.

References

[1] A.S. Ramadhas, S. Jayaraj and C. Muraleedharan, "Use of vegetable oils as I.C. engine fuels – A review" Renewable Energy Vol.29, 2004, 727-742

[2] H. Raheman, A.G. Phadatare , "Diesel engine emissions and performance from blends of karanja methyl ester and diesel" Biomass and Bioenergy Vol.27, 2004, 393-397

[3] H. B. Mathur, L. M. Das, "Utilization of non-edible wild oils as diesel engine fuels" Proceedings Bio-Energy Society Second Convention and Symposium, 1985, 198-202

[4] N. Hemmerlein, V. Korte, H. Richter and G. Schoroder, ''Performance, Exhaust Emissions and Durability of Modern Diesel Engines Running on Rapeseed Oil'' SAE Technical Paper Series No. 910848, SAE, Warrendale PA, 1991

[5] Avinash Kumar Agarwal, Deepak Agarwal, "Performance and emission characteristics of Jatropha oil (preheated and blends) in a direct injection compression ignition engine" Applied Thermal Engineering Vol.27, 2007, 2314–2323

[6] Godiganur Sharanappa, S. Rana Prathap Reddy and Ch. Suryanarayana Murthy, "Study on the performance and exhaust emissions of a diesel engine using preheated Mahua oil and its blends as fuel" International Conference on IC Engines and Combustion (ICONICE-2007), Jawaharlal Nehru Technological University Kukatpally, Hyderabad, 2007, 1-7

[7] Fangrui Ma, Milford A. Hanna, "Biodiesel production: a review" Bioresource Technology Vol.70, 1999, 1-15

[8] C. P. Sigar, "Comparative investigation on combustion and performance of a dual fuel engine using LPG and Biodiesel (Karanja Oil)" A Ph.D thesis, MNIT, Jaipur India, 2006

[9] Dilip Sharma, "Studies on alternate fuel substitution in engine operated end utility system" A Ph.D thesis, MNIT, Jaipur India, 2004

[10] S. Bari, T.H. Lim, "Effects of preheating of crude palm oil on injection system performance and emission of a diesel engine" Renewable Energy Vol.27, 2002, 339–351

[11] O.M.I. Nwafor, "Emission characteristics of diesel engine running on vegetable oil with elevated fuel inlet temperature" Biomass and Bioenergy Vol.27, 2004, 507 – 511

[12] M.E. Tat and J.H. Van Gerpen, "Report on Measurement of Biodiesel Speed of Sound and Its Impact on Injection Timing" National Renewable Energy Laboratory, Iowa State University Ames, Iowa. Available at www.osti.gov/dublincore/ecd/servlets/purl/15003584OZV07K/native/15003584.pdf Last accessed on Sept.11, 2008

[13] Breda Kegl, "Numerical analysis of injection characteristics using biodiesel fuel" Fuel Vol.85, 2006, 2377–2387

[14] Breda Kegl, "Experimental Investigation of Optimal Timing of the Diesel Engine Injection Pump Using Biodiesel Fuel" Energy & Fuels, Vol.20, 2006, 1460-1470

[15] Adnan Parlak, Halit Yasar, "The effects of injection timing on NOx emissions of a low heat rejection indirect diesel injection engine" Applied Thermal Engineering Vol.25, 2005, 3042–3052

[16] A report on "Pongamia Pinnata (L.) Pierre", Center for new crops and plants products, Purdue university, available at http://www.hort.purdue.edu/newcrop/duke_energy/Pongamia_pinnata.html Last accessed on Sept.15, 2008

[17] S.P. Wani, T.K. Sreedevi, "Pongamia's Journey from Forest to Micro enterprise for Improving Livelihoods" Available at www.icrisat.org/Biopower/Wani_Sreedevi_Pongamiajourney.pdf Last accessed on Feb. 4, 2008

JJMIE

Volume 4, Number 5, November 2010
ISSN 1995-6665
Pages 641 - 652

Jordan Journal of Mechanical and Industrial Engineering

Hydrodynamic Performance Evaluation of an Ellipsoidal Nose for a High Speed under Water Vehicle

K. N. S.Suman [a], D. Nageswara Rao [a], H. N. Das [b], G.Bhanu Kiran [c,*]

[a] Department of Mechanical Engineering, Andhra University, Visakhapatnam-530 003, India

[b] Hydrodynamics Research Wing, Naval Science and Technological Lab, Visakhapatnam - 530 027, India

[c] Department of Mechanical Engineering,GITAM University,Visakhapatnam-530 045 India

Abstract

The present work attempts to evaluate the functionality of an ellipsoidal head designed and fabricated for improved hydrodynamic performance of a high speed under water vehicle, which is predominantly used in defense applications. The importance of proper geometric shape for head portion of an under water vehicle is studied by the performance evaluation of different profiles through computational analysis. It is identified that the hydrodynamic performance of the vehicle can be improved with head having ellipsoidal profile. The designed vehicle having ellipsoidal heads of different major to minor axes ratio is fabricated and tested experimentally to validate the computational results.

Keywords: Under Water Vehicle; Drag; Cavitation; Hydrodynamic Performance; Design.

1. Introduction

High speed under water vehicles like torpedoes, submersibles, submarines are increasingly being proposed for diverse defence and commercial applications. These under water vehicles intended to design for better hydrodynamic and structural performance require cavitation susceptibility, minimum hydrodynamic resistance (drag) and structural weight for increasing payload carrying capacity, speed and operating range. The design of a vehicle with the above mentioned goal is always been of considerable interest to the designers of marine hydrodynamic structures.

Research in the area of design of under water vehicles has been carried by many researchers, in which Lumley [1] considered that the techniques to improve the hydrodynamic performance i.e. minimization of drag, regulating the dynamic pressure distribution etc., of a vehicle broadly can be classified as conventional and non-conventional. According to him the techniques involving stabilization of the boundary layer are referred as conventional techniques. Prandtl [2] used two methods of boundary layer control, which are suction and movement of the surface in the direction of flow. Schlichting[3] reported that

appropriate hull shape is a known means for extending the laminar boundary layer flow to a greater length. Several authors found that transition from laminar to turbulent flow can also be delayed by the use of suitable hull shaping. Methods for laminar and turbulent boundary layer flows with suction applied to prevent separation are discussed by Wuest [4]. The purpose of removing the fluid from boundary layer through suction is to stabilize the laminar layer and prevent it from becoming turbulent. Mecormick [5] was able to do some experimental investigation on these suction slots based on the findings of Loftin and Burrows [6]. Change of viscosity of the fluid can be considered as a non-conventional technique which is attempted by Toms[7]. Hoyt and Fabula [8], Thruston and Jones [9] performed experiments to predict the polymer concentration for maximum effectiveness in changing the viscosity of the fluid. M.Zahid Bashir, S.Bilal & M.A.Khan [11] numerically and experimentally determined the cavitation inception number for three axisymmetric head forms, at zero degree angle of incidence and compared with CFD results. John Lindsley Freudenthal [12] performed water tunnel experiment for the prediction of drag over a prototype model of axisymmetric submarine hull, compared the experimental results with CFD results. He also evaluated the formula for drag coefficient that uses only mean velocity measurements of axisymmetric body using assumptions of a self-similar wake and power law behavior of the wake scales. Paster, D. Raytheon Co., Portsmouth [13] explained how a reasonable hydrodynamic design can result in low drag and noise with minimum compromise in volume, which inturn results for reduced development and production costs. They suggested methods for estimating the drag as a function of speed, shape and size. Lt Cdr A Saiju and Cmde N Banerjee [14] performed wind tunnel

* Corresponding author. e-mail:bk_1381@yahoo.co.in

experiment for nose cone optimization of an underwater vehicle. They compared the results of wind tunnel over cavitation tunnel experimental results. C. J. Lu, Y. S. He, X. Chen, Y. Chen [15] focused on systematic study of Steady and unsteady flows of natural and ventilated cavitation through experimental observation. Some significant problems concerning ventilated cavitating flows, such as the critical status, hysteresis, surface wave, wall effect and ventilation manner, were investigated.

Review of the work reported so far reveals that several direct and indirect techniques were proposed separately by many researchers for improving the hydrodynamic performance of the vehicle. But many of these techniques demand for excessive experimentation which involves high cost and are mainly dependent on the unreliable fluid conditions prevailing during the motion of the vehicle in sea water. Of all the methods reported so far for better vehicle performance, hull shaping with a proper profile costs minimum and thus attracting the researchers to investigate on these lines. The parameters of the hull profile such as height, thickness and radius have a considerable effect on the performance of the vehicle with regard to its hydrodynamic characteristics.

The objective of the present paper is to design a better hull shape which is one of the popular techniques available to the designers for serving the dual purpose aim of drag reduction and pressure regulation for the proposed vehicle. An investigation based on numerical and experimental results is illustrated with reference to a specific model of an under water vehicle. Numerical analysis using the concept of Computational Fluid Dynamics (CFD) was firstly done to compute the hydrodynamic parameters such as pressure distribution, drag of the vehicle. The numerical predictions are compared with experimental investigations performed in wind tunnel.

2. Problem Description

The profile of an under water vehicle considered is shown in Fig.1. The hull body of the vehicle has three portions namely (a) nose cone or head (b) cylindrical middle compartment and (c) tail. Out of these three portions head is an important portion from pressure point of view, which may lead to cavitation. Cavitation susceptibility of the hull, apart from the drag is a challenging criterion for the designers.

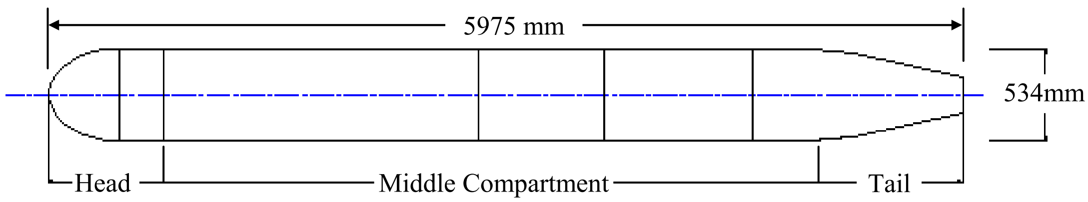

Figure 1: Profile of the under water vehicle

Head cavitation of these vehicles especially detrimental for effective functioning of its own sonar performance. Since cavitation inception is expected to occur at the location of minimum negative pressure, information about the unsteady pressure distribution over the torpedo head while underway is of vital importance to the designer. The location and magnitude of the minimum pressure on the body are determined for finding out the appropriate locations of the sensors such that their performance is least effected by the onset of cavitation. Apart from this, head portion of the vehicle should have high payload carrying capacity. Hence the design of a proper head profile which can serve as a nose cone of the under water vehicle satisfying all the above mentioned factors is important.

3. The Design Approach

The total length of the vehicle considered is of 5975 mm length and the middle compartment is of 534 mm diameter as shown in Fig.1. Four different axi-symmetric Head profiles (Fig.2) are considered for analyzing the drag and dynamic pressure distribution over the body.

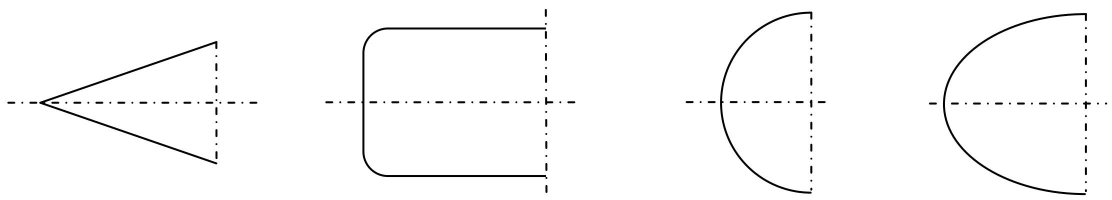

(a) Conical Profile (b) Stubbed Nose Profile (c) Spherical Profile (d) Elliptical Profile

Figure 2: Head profiles considered for analysis

All the above Head profiles are selected based on their aerodynamic characteristics available in the literature [10]. As it is decided not to alter the dimensions of the cylindrical middle compartment, head profiles dimensions are selected in such a way that they can be properly attached to the cylindrical middle compartment which is having a constant diameter.

Table 1: Dimensions of the Head profiles

Sl. No.	*Profile*	*Dimensions*
1	Cone	Height: 420 mm Radius: 267 mm
2	Stubbed nose profile	Length: 420 mm Radius: 267 mm Edge Radius: 5 mm
3	Sphere	Radius: 267 mm
4	Ellipse	Major Axis: 420 mm Minor Axis: 267 mm

4. Computational Analysis

The vehicle has an axisymmetric geometry and the bare hull is only taken for the analysis. The present exercise is intended to compute the drag and dynamic pressure distribution over the body in the flow field. The flow is assumed to be steady, incompressible and turbulent in nature. The computations presented in this work use, FLUENT 6.1.18 solver for solving the turbulent flow field over an arbitrary geometry and GAMBIT, the preprocessor of fluent as grid generator.

1.1. Grid Generation

The vehicle is modeled as a 2D axisymmetric body. The flow field boundaries are presented in fig. 3. The gridlines are geometrically stretched close to the body to obtain lesser spacing near the surface of the body than in the far field. A flow domain measuring 36 m × 4 m is considered to accommodate the 5.975 m long body and the grid generated in the entire flow field appears as in fig.4. The grid generated is of H type in nature and quite fine which contains 32,300 cells.

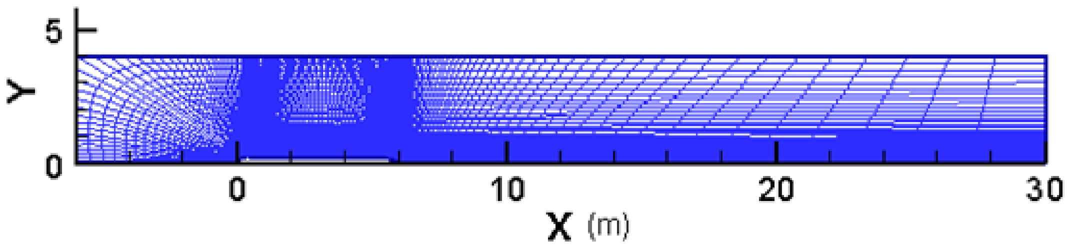

Figure 3: Boundary of the flow domain

4.2 Flow Solver

Fluent 6.1.18 uses a finite volume method for discretization of the flow domain. The Reynolds Time Averaged Navier-Stokes (RANS) equations are framed for each control volume in the discretized form. Pure upwind scheme is used for the momentum flux discretization.

STANDARD scheme is used for pressure and a SIMPLE (Strongly Implicit Pressure Link Equations) procedure is used for calculation of pressure field from the continuity equation.

4.2.1 Turbulence modeling

The eddy viscosity based k – ε (standard) model is used in the present work where the additional turbulent stresses arising out of the turbulent fluctuations are assumed to be replaced by viscous type stresses analogous to their laminar counterpart. As a result of this eddy viscosity hypothesis, the viscosity μ in all the transport equations is replaced by ($\mu_l + \mu_t$) where μ_l is the laminar viscosity and μ_t is the turbulent or eddy viscosity. Unlike μ_l in laminar flows however, the turbulent or eddy viscosity μ_t is not a fluid property but a function of the local state of turbulence defined by the turbulence kinetic energy, k and its dissipation rate ε as follows:

$$\mu_t = \rho C_\mu k^2 / \varepsilon$$

The field distribution of k and ε are evaluated solving the relevant transport equations.

4.2.2 Boundary conditions

The following boundary conditions are used for solving the flow field generated over the body: (i) Inlet velocity, (ii) Outlet pressure, (iii) Symmetry axis and (iv) Rigid walls. At inlet planes the known boundary values are prescribed in terms of velocity, turbulent kinetic energy - **k** and turbulent dissipation energy - **ε**. At the outlet gauge pressure is set to zero so that it remains at operating pressure. The axis of revolution is set as symmetry axes. At the wall all the two velocity components are set to zero.

For turbulent flow, the field values of k and ε are prescribed at the inflow boundaries. But the turbulence scalar equations are usually source dominant and the results therefore are more or less insensitive to the inlet field values prescribed. However, if the eddy viscosity level at the inlet is too low, numerical problems may arise. Assuming that the equations are valid only for fully turbulent flow, the inlet values of turbulent kinetic energy (k) is chosen as $10^{-4} * U^2$ and values of ε are so chosen that the inlet eddy viscosity is of the order of five times the laminar viscosity.

5. Computational Results and Discussions

Computations are performed for the flow velocity between 5 to 6 m/s satisfying the turbulent flow conditions. Control volumes are generated over the entire full-length model of the torpedo. But the pressure distribution is taken only on the head portion and extending to some part of middle portion, without giving importance to the later part of the body. The pressure distribution curves obtained for all the four different hull geometries are shown in figs. 5a-5d. The values of minimum negative pressure co-efficient (Cp) obtained from pressure distribution graphs and drag coefficient (CD) for all the hull geometries are presented in the Tables 2 and 3 respectively.

Table 2: Values of minimum pressure co-efficient for different profiles

Profile	Minimum Pressure Co-efficient (Cp)
Cone	-1.72
Stubbed nose profile	-0.98
Sphere	-0.721
Ellipse	-0.443

Table 3: Comparison of drag for different profiles

Profile	Form Drag	Skin Friction Drag	Overall Drag
Cone	0.13901508	0.0867318	0.22574688
Stubbed nose profile	0.12013323	0.089248875	0.2093821
Sphere	0.068183163	0.10391882	0.17210198
Ellipse	0.05470272	0.10500373	0.15970645

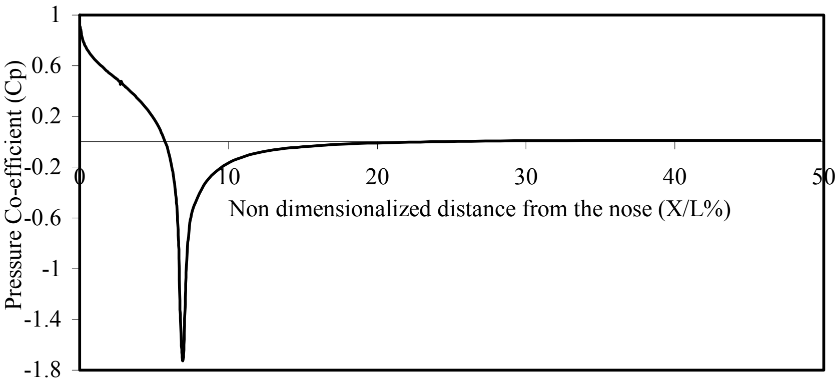

(a) conical profile

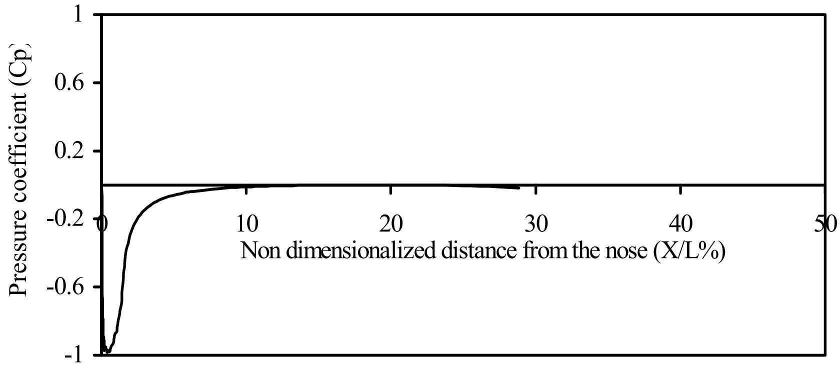

(b) stubbed nose profile

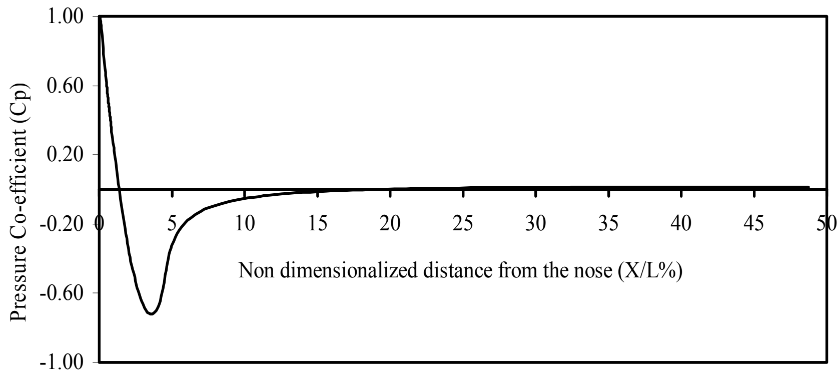

(c) spherical profile

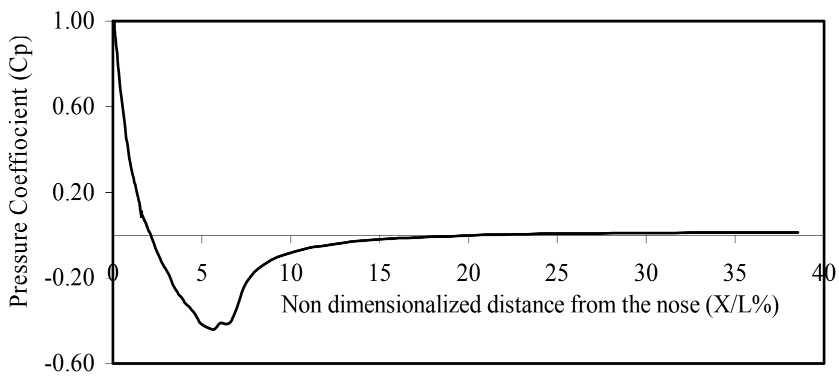

(d) elliptical profile

Figure. 5: Computational pressure distribution over the vehicle for different head profiles

From the preliminary computational analysis exercised over the hull profile having different head geometries it may be concluded that ellipsoidal head profile is suitable for imparting better hydrodynamic performance to the vehicle. It is further resolved to evaluate the suitable dimensions of the ellipsoidal profile for enhancing the performance of the vehicle in terms of hydrodynamic aspects. The minor axis length is kept constant since it is considered not to alter the radius of the cylindrical middle compartment. By varying only the major axis length of the ellipsoidal head, various profiles are generated. These ellipsoidal profiles having different major to minor axis ratios were solved again for evaluating their hydrodynamic performance and extracting suitable dimensions.

6. Experimental Investigations

The hydrodynamic characteristics are evaluated computationally for the ellipsoidal heads of different ratios of major to minor axes. These results are validated through experimentation carried out in a low speed wind tunnel on the fabricated ellipsoidal heads. The tunnel is of open circuit type where the air is drawn from the atmosphere and passes through the test section before it is discharged at reduced velocity back into atmosphere. The test section free stream Mach number is kept well below 0.3 and the facility can be extended to predict and validate the fluid dynamic characteristics of a body exposed to a flow in one medium to the flow in different medium. The various compartments in the wind tunnel and their specifications are presented in table 4.

Table 4: Wind tunnel compartments and specifications

Sl.No.	*Compartment*	*Dimensions*
1	Test Section	2 × 2 × 4.0 m
2	Plenum Chamber	4.3 × 4.3 × 4.0 m
3	Contraction	Section varying from 4.3 m × 4.3 m to 2 m × 2 m, 4.0 m long
4	Diffuser	Section varying from 2 m × 2 m to 3.048 m diameter of circle, 7.8 m long
5	DC motor	125 KW at 750 rpm
6	Fan	Sweep diameter 3.04 m, 12 blades made of CFRP
7	Maximum wind speed at test section	60 m/sec

A 125KW DC variable speed motor drives the 12 blades CFRP tunnel fan for achieving the desired wind speed in the tunnel test section. Pitot tube positioned in the plenum chamber 275mm above the base at the centerline of the tunnel measures the total pressure head. The free stream pressure at different locations in the tunnel is obtained by a system of Pitot tubes arranged at these locations flushed with the surface of the tunnel.

7. Pressure Tapping and Instrumentation on The Fabricated Models

Three ellipsoidal heads having different major to minor axis ratios are fabricated with Fiber Reinforced Plastic (FRP) upto a thickness of 6-8mm and prepared for experimentation. These heads are attached separately to a smooth cylindrical body resembling the middle portion of the vehicle modeled during computational analysis. Thus the fabricated full scale model without tail portion resulted in a blockage of approximately 4% which is considered to be acceptable. The model gave Reynolds number large enough to ensure that the it is essentially operated in the fully turbulent regime.

7.1 Pressure Tapping

Pressure taps of 1.4 mm diameter are drilled along vertical centerline on the surface of the model fabricated. Of, these 6 pressure taps are symmetrically distributed at bottom half of the model to verify yaw and pitch. 1.9 mm SS tubes of 1 mm inner diameter are inserted in to the pressure taps on the model from inside so as to make it flushed with the outer surface of the model (Fig.6).

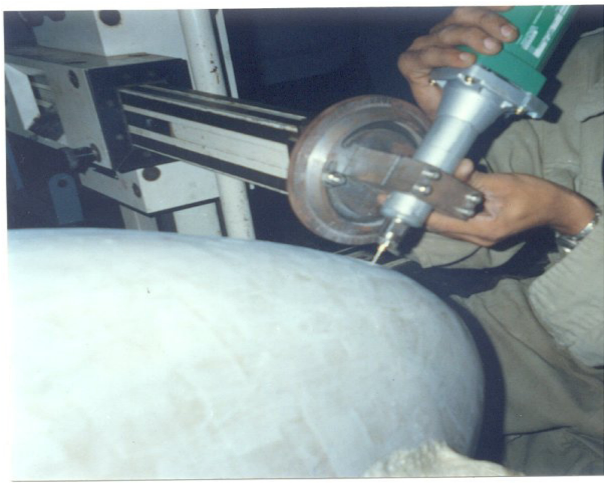

Figure 6: Drilling of pressure holes on the model

7.2 Instrumentation

Two scanivalves (low pressure transducers) having 48 selectable ports are mounted inside the model. These scanivalve ports are connected to the SS tubes press fitted to the pressure tapping on the body by means of 1.4 mm urethane tubes. Each scanivalve's signal output, control input and port address output connections are brought down to the instrumentation room and connected to the signal conditioner, solenoid controller and decoder respectively. The signal conditioner out put voltages are acquired by a Data Acquisition System (DAS) (Figs.7 and 8).

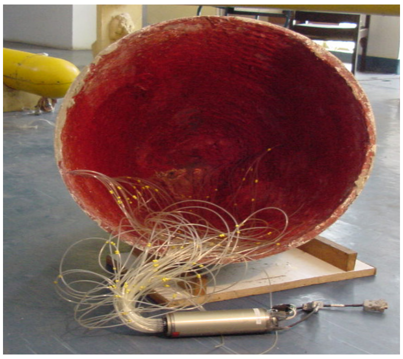

Figure 7: Pressure tapping and scanivalve arrangement

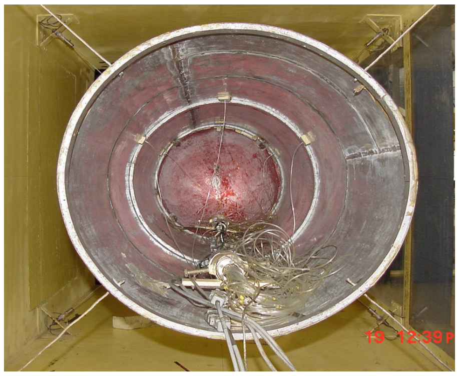

Figure 8: Pressure tapping instrumentation over the entire model

8. Mounting of The Model and Test Method

The model consisting of fabricated ellipsoidal head and cylindrical body is mounted along the centre line of the test section by suspending it from eight 3 mm wire ropes at 2 locations along the length. The model is accurately aligned along the centerline of the tunnel using spirit level and measuring distance from sidewalls precisely (Fig.9). Fan drive system is operated at different RPMs to achieve variable wind speeds in order to subject the model to a fluid flow having different Reynolds numbers. Pressure distribution at various Reynolds numbers are obtained from the scanivalves and are recorded on-line. The recorded data of pressures are plotted in terms of pressure co-efficient (C_p) vs the distance from the nose portion.

9. Discussion of Results

Investigations are carried out on the basic head profiles such as conical, stubbed nose, spherical and ellipsoidal profiles to arrive at the better profile for the under water vehicle of standard dimensions. It is concluded that ellipsoidal profile is the better among all the profiles for providing good hydrodynamic characteristics to the vehicle. It is further considered to alter the major to minor axes ratio of the ellipse and analyze the hydrodynamic performance of the vehicle to investigate the suitable dimensions of the ellipse.

Front View

Rear View

Figure 9: Ellipsoidal Model of 2.3:1 major to minor axes ratio mounted in the test section

9.1 Analysis of Computational Results for Minimum Pressure Value and Cavitation Susceptibility of the Vehicle

Cavitation is normally expected to occur at the location of minimum pressure occurrence. The value of the minimum pressure gives the measure of velocity and depth at which the vehicle should be operated without any cavitation. The location of the minimum pressure occurrence also gives the measure of placement of sensors in the head, so that their performance is least effected by the onset of cavitation. The information about the magnitude and location of the minimum pressure co-efficient for different heads of the vehicle are presented in Table 5. The operating velocity range or cavitation speed of the vehicle is calculated from the tabulated results as:

$$Cp = \frac{P - P_{ref}}{0.5\rho V^2}$$ at different depths of operation.

Where Cp = Pressure Co-efficient , P = Actual pressure acting at location of interest, P_{ref} = atmospheric pressure + ρgh ρ = density of fluid, kg/m^3

g = acceleration due to gravity, m/sec^2 , h = Vehicle operating depth, m

V = velocity of the vehicle, m/sec

Table 5: Comparison of minimum pressure co-efficient for different Ellipsoidal Heads

Axes ratio of Ellipsoidal Heads	*Value of Minimum Pressure Co-efficient*	*Location of occurrence (X/L%)*
1.6:1	-0.443	5.6
1.95:1	-0.309	6.68
2.32:1	-0.246	7.59
2.7:1	-0.198	8.52
3:1	-0.163	9.32
4:1	-0.106	12.11
5:1	-0.0719	14.37

From these results, it is observed that the pressure co-efficient is getting decreased with the increase in dimensions of the head profile. It is also observed that the location of the negative pressure co-efficient is tending to shift away from the nose portion as the axes ration increases (major axis).

Table 6: Cavitation inception speed for various ellipsoidal heads at different depths of operation

Head (axes ratio)	*Cavitation inception speed in m/sec at the operation depth of*			
	10 m	12 m	30 m	40 m
1.6:1	29.69	36.39	42.04	47.01
1.95:1	35.55	43.58	50.34	56.30
2.32:1	39.84	48.85	56.43	63.11
2.7:1	44.41	54.46	62.90	70.35
3:1	48.95	60.01	69.32	77.52
4:1	60.70	74.62	86.20	96.40
5:1	73.70	90.40	104.42	116.77

It may be observed from the table 6 that with the increase of the major axis, the operating velocity range of the vehicle increases at all depths. The operating velocity of the vehicle can be selected as per the nose shape or vice-versa to avoid cavitation.

9.2 Analysis of Drag

A graphical depiction of variation of overall drag, form drag and viscous drag for the vehicles with different ellipsoidal heads is in fig.10. It can be observed from the results that due to increase in length of the ellipsoidal head there is decrement in overall drag of the vehicle which composes of form drag and viscous drag. The viscous drag remains constant, as this is due to the body portion of the vehicle, which is parallel to the flow. In the present case the cylindrical portion of the body is parallel to the flow and its dimensions are kept constant. Hence the viscous drag remains constant.

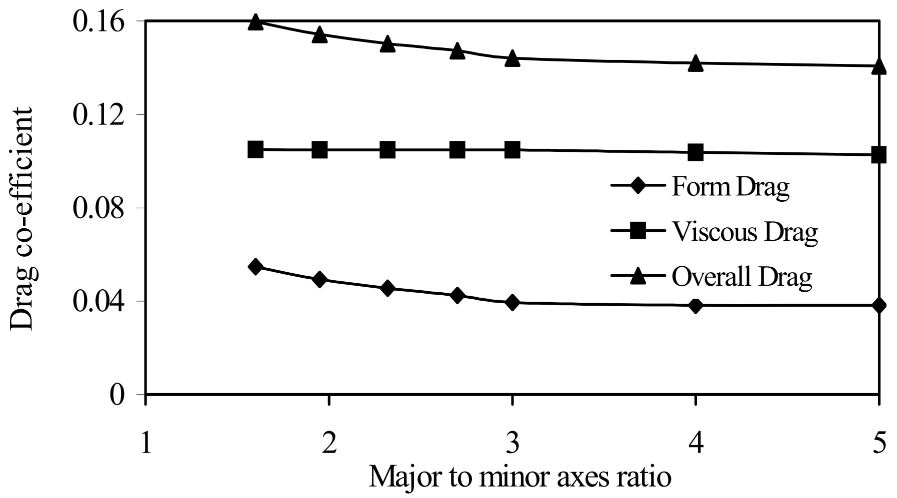

Figure10: Variation of drag co-efficient for different axes ratios of ellipsoidal profiles

The form drag obtained for different profiles is decreasing as the ratio of major to minor axes of the profile increases. The increase in momentum transfer within the boundary layer due to the increase in the axes ratio of the profile is one of the reasons for decrease in pressure drag.

The notable feature which can be observed from the above results is that the variation of form drag of the vehicle has become almost constant beyond the axes ration value of 3. The stabilization of the boundary layer beyond an axes ratio of 3 may be one possible reason for the negligible change in form drag. It is also observed from the results of pressure distribution and cavitation analysis that the vehicle consisting of ellipsoidal head with major to minor axis ratio of 3 is less susceptible to cavitation in the operating range. Hence it can be concluded that ellipsoidal head with major to minor axis ratio of 3 is sufficient for providing good hydrodynamic characteristics to the present under water vehicle.

9.3 Validation

The validity of the numerical analysis carried on different ellipsoidal heads practically tested on the fabricated noses using palm fibre reinforced plastic. Apart from the elliptical profile with an axes ratio of 3 arrived through numerical analysis another two ellipsoidal noses having major to minor axes ratio as 1.6, 2.32 are fabricated to verify the validity of the numerical results.

The experiments are carried on models developed in a wind tunnel at different wind speeds ranging from 14 m/sec to 60 m/sec. Error analysis for the experimental results is performed to estimate degree of uncertainty associated with the experimental results. Degree of Uncertainty associated with experimentally found pressure coefficient along the length of the vehicle for different ellipsoidal heads is given in Fig 11.

The pressure distribution plots practically obtained for all the bodies having different ellipsoidal heads are compared with corresponding computational results (Figs.12-14) and Table 7. The results obtained have shown a small deviation between fabricated and computed values. It may be observed that the trend of the pressure distribution plotted from experimental values is in close agreement with that of computational values. In the computational analysis the pressure values can be evaluated at many (infinite) locations of the hull and hence a large data can be generated and this enables the plot of the pressure distribution to follow a smooth trend. The experimental set up has limitations in providing pressure tappings over the surface which leads to less data compared to computational analysis and hence deviations in the results are observed. During the computational analysis the hull surface is assumed to be perfectly smooth. In the present model, the surface is made up of hand lay-up technique using coarse fibre which does not yield smooth surface. This also might be one of the reasons for small deviations to occur on the pressure distribution profiles.

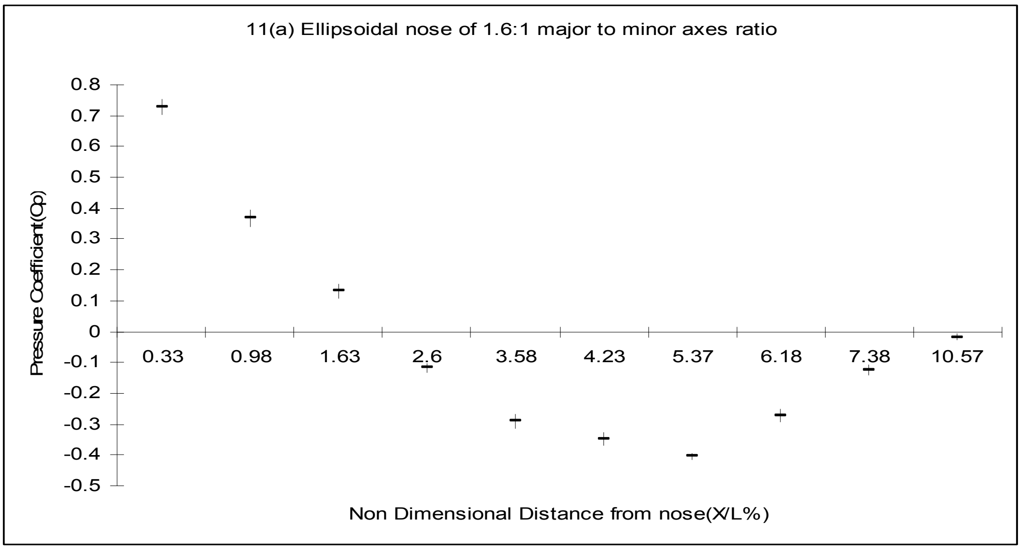

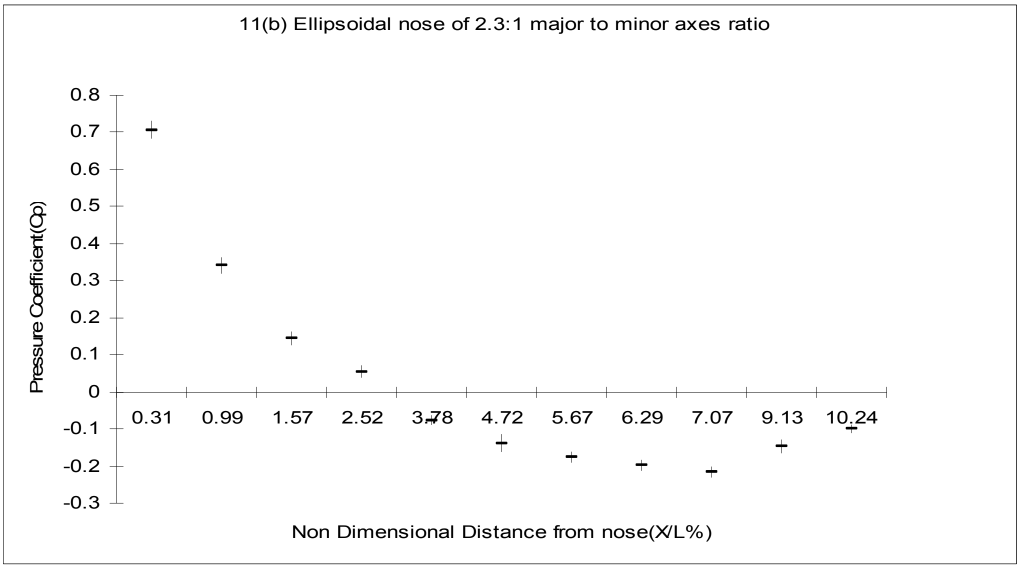

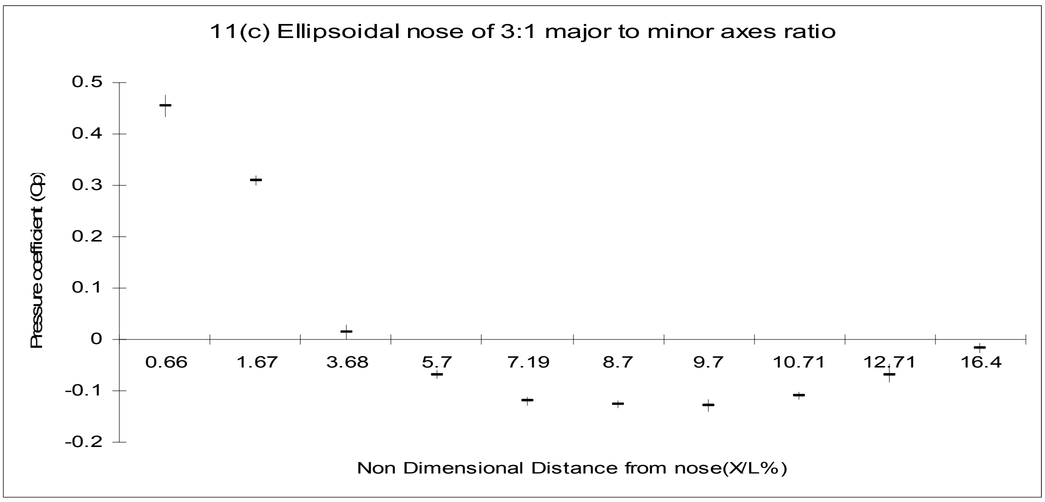

Figure 11: Degree of Uncertainty associated with pressure coefficient along the length of the vehicle for different ellipsoidal heads

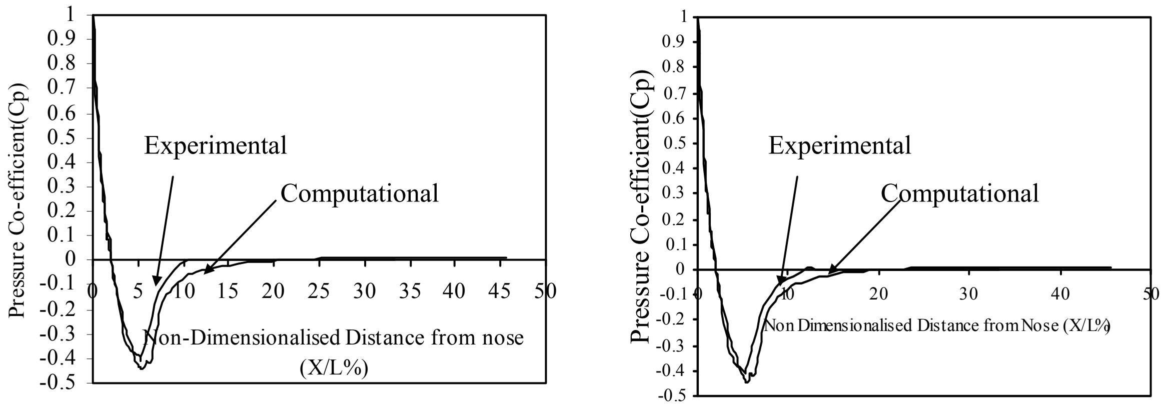

(a) Wind speed 25.17 m/s (Reynolds Number 3.36E06)

(b) Wind speed 35.68 m/s (Reynolds Number 4.76E06)

Figure 11: Comparison of pressure distribution obtained over ellipsoidal nose of 1.6:1 major to minor axes ratio for different wind speeds

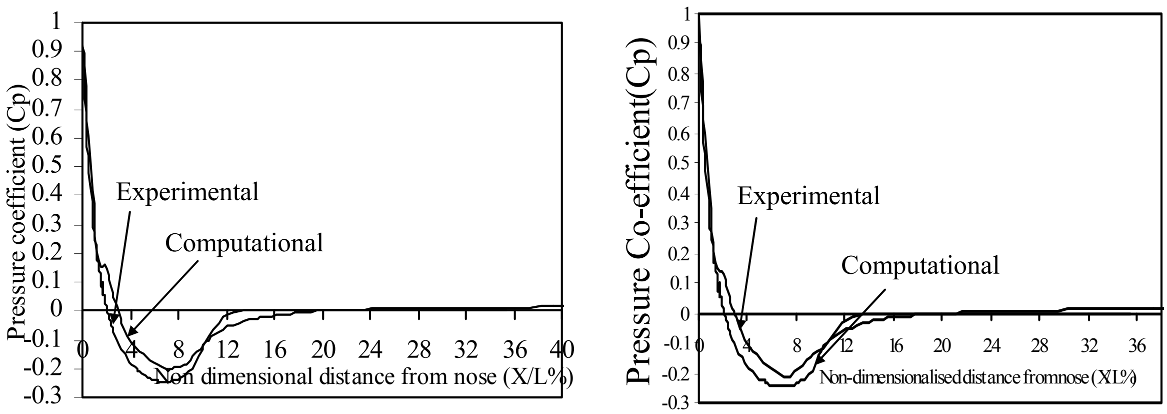

(a) Wind speed 26.8 m/s (Reynolds Number 4.26E06)

(b) Wind speed 35.68 m/s (Reynolds Number 4.76E06)

Figure 12: Comparison of pressure distribution obtained over ellipsoidal nose of 2.3:1 major to minor axes ratio for different wind speeds

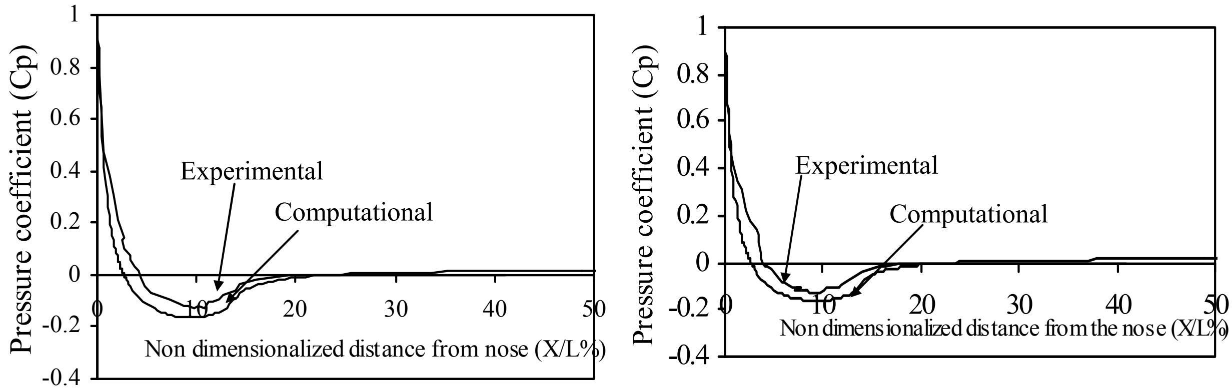

(a) Wind speed 26.8 m/s (Reynolds Number 4.26E06)

(b) Wind speed 23.6 m/s (Reynolds Number 3.76E06)

Figure 13: Comparison of pressure distribution obtained over ellipsoidal nose of 3:1 major to minor axes ratio for different wind speeds

Table 7: Comparison of the magnitude and location of minimum pressure co-efficient from experimental and computation analysis

Profile (major to minor axis ratio)	*Min. pressure co-efficient*	***Location of the pressure co-efficient (% of body length)***
1.6:1		
Computational	-0.443	5.637
Experimental	-0.404 ± 0.011	5.365
2.32:1		
Computational	-0.246	7.590
Experimental	-0.215 ± 0.014	7.086
3:1		
Computational	–0.1633	9.32
Experimental	–0.1278 ±0.121	9.70

10. Conclusions

The importance of ellipsoidal head for improving the hydrodynamic performance of a high speed under water vehicle having cylindrical mid-section and tapered after body has been identified through computational and experimental analysis. Among the several axi-symmetric head profiles tested

through computational analysis for their hydrodynamic performance, ellipsoidal head resulted to be better nose profile for improving the cavitation susceptibility and minimizing the overall drag of the vehicle. The obtained computational results have been validated by the experimental investigations carried on the full scale model of the vehicle through wind tunnel tests. The results obtained are in close agreement with only minor deviations.

References

[1] Lumley. J.L "Reduction of skin friction drag", Proceedings of 5th Symposium, Naval Hydrodynamics, Norway,1964

[2] Prandtl, "Boundary layer theory, Fluid Motion at Low Viscosity", Verhandlungen International Math. Congress, Heidelberg, 1904

[3] Schlichting, H. Boundary Layer Theory, Mc-Graw Hill Publications,1960

[4] Wuest, W. Theory of boundary layer suction to prevent separation. In: Lachmann G.V. Boundary layer and flow control, Pergaman Press, 196, 196.

[5] McCormick, B.W. "An experimental study of the drag reduction by suction through circumferential slots on a buoyant propelled axisymmetric body", Proceedings. of 5th Symposium Naval Hydrodynamics, Norway, 1964.

[6] Loftin, J.K. & Burrows, D.L. "Investigations relating to the extension of laminar flow by means of boundary layer suction through slot", NACA report , 1961.

[7] Toms, B.A.. "Some observations on the flow of linear polymer solution through straight tubes at average Reynolds number"', Proceedings of the International Rheological congress, Scheveningen, Holland, vol II, 1948.

[8] Hoyt, I.W. and Fabula, A.G. Effect of additives on fluid friction, In: Freiner (Ed.).Under Water Missile Propulsion, Compass Publication, 1968, 171- 183.

[9] Thruston, S & Jones, R.D. 'Experimental model studies of non-newtonian soluble coatings for drag reduction', In: L.Friener (Ed.). Underwater Missile Propulsion, Compass Publication, 1968, 191-203.

[10] Hoerner, S.F. Fluid Dynamic Drag, Authors Self Publication, New Jersy, 1965.

[11] M.Zahid Basher, S.Bilal & M.A.Khan, "Calculation of flow over Under water bodies with hull and sail", 2nd IBCAST,Burban,Pakistan, 1999.

[12] John Lindsley Freudenthal, "Experimental studies on the dragof an Axisymmetric hull", thesis in aerospace engineering, Mississippi, December 2002.

[13] Paster, D. Raytheon Co., Portsmouth "Importance of Hydrodynamic Considerations for Underwater Vehicle Design" IEEE oceans volume 18, 2003, 1413-1422.

[14] Lt Cdr A Saiju and Cmde N Banerjee, "Cavitation Investigation and nose cone optimization of an under water vehicle using wind tunnel", journal of ship technology, volume 1, 2005, 68-75.

[15] C. J. Lu, Y. S. He, X. Chen, Y. Chen "Numerical and Experimental Research on Cavitating Flows" Proceedings of the Fifth International Conference on Fluid Mechanics, Aug.15-19, 2007, Shanghai, China.

JJMIE

Volume 4, Number 5, November 2010
ISSN 1995-6665
Pages 653 - 664

Jordan Journal of Mechanical and Industrial Engineering

Design Optimization of Complex Structures Using Metamodels

M. RAMU [a], * , V. PRABHU RAJA[a] , P. R. THYLA [a], M. GUNASEELAN [b]

[a] Faculty, Mechanical Engineering Department, PSG College of tech., Coimbatore-641004, India

[b] Research Scholar, Mechanical Engineering Department, PSG College of tech., Coimbatore-641004, India

Abstract

Current engineering analyses rely on running expensive and complex computer codes. Statistical techniques are widely used in engineering design to construct approximate models of these costly analysis codes. These models referred as metamodels, are then used in place of the actual analysis codes to reduce the computational burden of engineering analyses. The intent of this study is to provide a comprehensive discussion of the fundamental issues that arise in design optimization using metamodels, highlighting concepts, methods, techniques, as well as practical implications. The paper addresses the selection of design of experiments, metamodel selection, sensitivity analysis and optimization.

Keywords: Metamodel, Experimental design, Central Composite Design, Optimization.

1. Introduction

Traditional engineering design optimization which is the process of identifying the right combination of product parameters is often done manually, time consuming and involves a step by step approach. Approximation methods are widely used to reduce the computational burden of engineering analyses. The use of long running computer simulations in design leads to a fundamental problem when trying to compare and contrast various competing options. It is also not possible to analyze all of the combinations of variables that one would wish. This problem is particularly acute when using optimization schemes. Metamodels, also referred as surrogate models, are a cheaper alternative to costly analysis tools and can significantly reduce the computational time involved. Modern optimization techniques like Genetic Algorithms (GA) have been found to be very robust and general for solving engineering design problems. Evolutionary algorithms such as GA have been used with metamodels (surrogate models) to reduce the cost of exact function evaluations. In this paper, a methodology of developing metamodel and applying it to the optimization problem is explained. As a case study, the roof slab of a Prototype Fast Breeder Reactor was taken and design optimization was carried out. In this approach, experimental design, metamodels, evolutionary algorithm, and finite element analysis tool are brought together to provide an integrated optimization system.

Metamodeling involves (a) choosing an experimental design for generating data, (b) choosing a model to represent the data, and (c) fitting the model to the observed data. There are several options for each of these steps, which will be discussed below. Forrester et. al [1] discussed the recent advances in surrogate based design for global optimization. Simpson et.al [2] has done a survey on the application of metamodels on design. The paper also gives the following recommendations: (i) If many factors(more than 50) must be modeled in a deterministic application, neural networks may be the best choice (ii) If the underlying function to be modeled is deterministic and highly nonlinear in a moderate number of factors (less than 50, say), then kriging may be the best choice despite the added complexity, (ii) In deterministic applications with a few fairly well behaved factors, another option for exploration is using the standard Response surface methodology approach. In Simpson, et al. [3], kriging methods are compared against polynomial regression models for the multidisciplinary design optimization of an aero spike nozzle. Alam et al [4] investigated the effects of experimental design on the development of artificial neural networks as simulation metamodels. This paper shows that a modified-Latin Hypercube design, supplemented by domain knowledge, could be an effective and robust method for the development of neural network simulation metamodels. Queipo et.al. [5] discussed the fundamental issues that arise in the SBAO of computationally

* Corresponding author. rmr_psg@yahoo.co.in

expensive models such as those found in aerospace systems. The paper mainly focused on the design of experiments based on Latin Hypercube Sampling (LHS) & Orthogonal Arrays (OA) and Surrogate modeling techniques based on polynomial regression model, kriging and radial basis function. Ruichen et.al [6] compares four popular metamodeling techniques— Polynomial Regression, Multivariate Adaptive Regression Splines, Radial Basis Functions, and Kriging— based on multiple performance criteria using fourteen test problems representing different classes of problems. Giunta, et al. [7] also compare kriging models and polynomial regression models for two 5 and 10 variable test problems. In Varadarajan, et al. [8], Artificial Neural Network (ANN) methods are compared with polynomial regression models for the engine design problem in modeling the nonlinear thermodynamic behavior. In Yang, et al., (9), four approximation methods— enhanced Multivariate Adaptive Regression Splines (MARS), Stepwise Regression, ANN, and the Moving Least Square— are compared for the construction of safety related functions in automotive crash analysis, for a relative small sampling size. Similarly many researchers have compared the various experimental designs and/or metamodeling techniques. Only limited researchers are explained about the application of metamodel in the optimization process. This paper explains the methodology of performing experimental design, creating metamodel and applying it to the optimization.

1.1. Design of Experiments Techniques

Design of Experiments includes the design of all information-gathering exercises where variation is present, usually under the full control of the experimenter. Often the experimenter is interested in the effect of some process or intervention on some objects. Design of experiments is a discipline that has very broad application. In the following part, we will introduce the most frequently used DOE techniques.

1.1.1. Full-factorial Design

A full-factorial design is one in which all combinations of all factors at all levels are evaluated. It is an old engineering practice to systematically evaluate a grid of points, requiring $n_1*n_2*n_3*...n_i$ (i is the number of factors, n is the number of levels for factor i) design point evaluations. This practice provides extensive information for accurate estimation of factor and interaction effects. However, it is often deemed cost-prohibitive due to the number of analyses required.

1.1.2. Orthogonal Arrays

The use of orthogonal arrays can avoid a costly full-factorial experiment in which all combinations of all factors at different levels are studied. A fractional factorial experiment is a certain fractional subset (1/2, 1/4, 1/8, etc.) of the full factorial set of experiments, carefully selected to maintain orthogonality (independence) among the various factors and certain interactions. While the use of orthogonal arrays for fractional factorial design suffers from reduced resolution in the analysis of results (i.e., factor effects are aliased with interaction effects as more factors are added to a given array), the significant reduction in the required number of experiments can often justify this loss in resolution as long as some of the interaction effects are assumed negligible. In fractional factorial designs, the number of columns in the design matrix is less than the number necessary to represent every factor and all interactions of those factors. Instead, columns are "shared" by these quantities, an occurrence known as confounding. Confounding results in the dilemma of not being able to realize which quantity in a given column produced the effect on the outputs attributed to that column. In such a case, the designer must make an assumption as to which quantities can be considered insignificant (typically the highest-order interactions) so that a single contributing quantity can be identified.

1.1.3. Latin Hypercube Design

Another class of experimental design which efficiently samples large design spaces is Latin Hypercube sampling. With this technique, the design space for each factor is uniformly divided (the same number of divisions (n) for all factors). These levels are then randomly combined to specify n points defining the design matrix (each level of a factor is studied only once). An advantage of using Latin Hypercubes over Orthogonal Arrays is that more points and more combinations can be studied for each factor. The Latin Hypercube technique allows the designer total freedom in selecting the number of designs to run (as long as it is greater than the number factors). While, the configurations are more restrictive using the Orthogonal Arrays. A drawback to the Latin Hypercubes is that, in general, they are not reproducible since they are generated with random combinations. In addition, as the number of points decreases, the chances of missing some regions of the design space increases.

1.1.4. Central Composite Design

Central Composite Design (CCD) is a statistically based technique in which a 2-level full-factorial experiment is augmented with a center point and two additional points for each factor (star points). Thus, five levels are defined for each factor, and to study n factors using Central Composite Design requires $2n + 2n + 1$ design point evaluations. The corner points are for the assessment of linear and 2-way interaction terms. Center points are used to detect curvature and sometime replicated in experimental DOE to estimate pure error. Star points are for the assessment of quadratic terms. Although Central Composite Design requires a significant number of design point evaluations, it is a popular technique for compiling data for Response Surface Modeling due to the expanse of design space covered, and higher order information obtained.

1.1.5. Box-Behnken Design

Box and Behnken developed a family of efficient three-level designs for fitting second-order response surfaces. It exists only for 3-7 factors. Number of runs is very close to CCD for the same number of factors. The Box-Behnken design doesn't have any corners and it is suitable for the situation when corners are not feasible (physical designs).

1.2. Approximating Methods

Approximation concepts were introduced in structural design optimization in the late 1970s to do the following:

- Reduce the number of independent design variables through design variable linking and reduced basis vectors concepts.
- Perform constraint deletion through truncation and regionalization schemes.
- Reduce the number of computer intensive, detailed analyses (or simulation code evaluations) through the use of mathematical approximations of the design optimization objective and constraint functions.

These approximations models can be used to reduce simulation codes or analyses that are computation intensive. They can also help to eliminate the computational noise for simulation codes in the case the outputs rapidly oscillate with gradual changes in the values of input parameters. Computational noise has a strong adverse effect on optimization by creating numerous local optima. Approximation models (Response Surface Models in particular) naturally smooth out the response functions, and, in many cases, help to converge to a global optimum faster. The usage of approximation is not restricted to optimization. It also provides an efficient means of post-optimization or sensitivity analysis. Their value is very high for computationally expensive engineering methods, such as Monte Carlo Simulation, Reliability-Based Optimization, or Probabilistic Design Optimization.

1.2.1. Response Surface Method

Response surface method is a collection of statistical and mathematical techniques useful for developing, improving, and optimizing processes. In some systems based on the underlying engineering, chemical, or physical principles, the nature of the relationship between y and x's might be know exactly. Then a model of the form $y=g(x_1,x_2,...,x_k)+e$ can be written. This type of relationship is often called a mechanistic model. However, the more common situation would be that the underlying mechanism is not fully understood, and the experimenter must approximate the unknown function g with an appropriate empirical $y = f(x_1, x_2,....., x_3) + e$. Usually the function f is a first-order or second-order polynomial. This empirical model is called a response surface model. The model then can be used in optimization studies with a very small computational expense, since evaluation only involves calculating the value of a polynomial for a given set of design variables. Accuracy of the model is highly dependent on the amount of information collected for its construction (number of exact analyses), shape of the exact response function being approximated (like the order of polynomial), and volume of the design space in which the model is constructed (the range covered by the RSM). In a sufficiently small volume of the design space, any smooth function can be approximated by a quadratic polynomial with good accuracy. For highly non-linear functions, polynomials of 3rd or 4th order can be used. If the model is used outside of the design space where it was constructed, its accuracy is impaired, and refining of the model is required. The response surface model relies on the fact that the set of designs on which it is based is well chosen. Randomly chosen designs may cause an inaccurate surface to be constructed or even prevent the ability to construct a surface at all. Because simulations are often time-consuming or the experiments are expensive, the overall efficiency of the design process relies heavily on the appropriate selection of a design set on which to base the approximations. CCD design, Box-Behnken design and D-optimal design are the widely used DOE methods to generate the design set for constructing a response surface model.

1.2.2. Kriging Meta Models

Kriging (named after the South-African mining engineer Krige) is an interpolation method that predicts unknown values. More precisely, a Kriging prediction is a weighted linear combination of all output values already observed. These weights depend on the distances between the new and the observed inputs. The closer the inputs, the bigger the weights are. Kriging models are extremely flexible due to the wide range of correlation functions which can be chosen for building the approximation model. Furthermore, depending on the choice of the correlation function, the model either can provide an exact interpolation of the data, or an inexact interpolation. The most popular DOE for Kriging is Latin Hypercube Design (LHS). LHS offers flexible design sizes n (number of scenarios simulated) for any value of k (number of simulation inputs). Geometrically, many classic designs consist of corners of k-dimensional cubes, so these designs imply simulation of extreme scenarios. LHS, however, has better space filling properties.

1.2.3. Neural Networks

Artificial Neural Networks (ANN) has been studied for many years in the hope of mimicking the human brain's ability to solve problems that are ambiguous and require a large amount of processing. Human brains accomplish this data processing by utilizing massive parallelism, with millions of neurons working together to solve complicated problems. Similarly, ANN models consists of many computational elements, called "neurons" to correspond to their biological counter-parts, operating in parallel and connected by links with variable weights. These weights are adapted during the training process, most commonly through the back-propagation algorithm, by presenting the neural network with examples of input-output pairs exhibiting the relationship the network is attempting to learn. The most common applications of ANN involve approximation and classification. Approximation models attempt to estimate input-output transformation functions, while classification involves using the known inputs to determine class membership. There is no much literature about the optimal experimental design for neural networks or even verification of the effectiveness of the traditional regression model based optimal design methods on the neural net.

2. Methodology

During the optimization process, the model of the component to be optimized will be called for analysis several times, each time with different geometric parameters. So the model has to be in parametric form, which enables it to change the parameter whenever required. So a parametric model of the component has to be modeled using CAD tool which is compatible with the analysis (CAE) tool. Sensitivity analysis of the component was performed to find the effect of the objective function and the state variables (stress/deformation) on the variation of geometric parameters. The parameters which influence more on the state variables are alone considered for the optimization study. In order to reduce the computation cost and to have a better sampling search in the design space, design of experiments was performed using Central Composite Design (CCD). For the sampling points, the computer experiment was conducted using ANSYS package and the results are fed to Minitab software to create the metamodel. This metamodel was used in Genetic Algorithm (GA) coding for optimization.

3. CASE STUDY

The foremost step in the metamodel based optimization is the development of metamodel. Development of metamodel requires lot of experiments to be carried out to the train the model. Experiments may not be feasible in case of complex problems like our case study and in such situations, simulation will be useful. This method of using computer simulation for developing metamodel is termed as design of computer experiments and is explained in detail in the following chapters.

3.1. Parametric Modeling and finite element analysis

As explained earlier, metamodel development requires lot of simulations, for which parametric model of the structure being optimized is required. The structure considered for the metamodel based optimization is a roof slab of a nuclear reactor. The roof slab acts as a support for various components of the reactor and is shown in Figure 1. The main objective of the optimization is to minimize the total weight of the roof slab. As the model will be explored during analysis for various combinations of parameters, a parametric model of the roof slab was developed. The variables taken for parametric modeling are various plate thicknesses and height of the roof slab.

The parametric model was created using the finite element software ANSYS. The necessary loading conditions (weight of various components on the roof slab) and boundary conditions are applied on the structure and a methodology of analyzing the structure for static loading condition was established.

3.2. Sensitivity analysis

The next step in metamodel based optimization is to predict the decision variables for the roof slab through an investigation of the sensitivity of the objective function on small increments of these variables. The design variables considered for the sensitivity analysis are Height (H1), Top and Bottom plate thickness (T_1), Inner shell thickness (T_3), Outer shell thickness (T_4), Stiffener thickness (T_5) and Intermediate Heat Exchanger (IHX), Primary Sodium Pump (PSP) shell thickness (R_1). Sensitivity analysis is carried out using ANSYS sweep optimization module and the analysis reveals that deformation is sensitive to the variations in the parameters H_1, and T_1, stress is sensitive to the variations in the parameters T_1, T_3, T_4, T_5 and R_1, and cost of the roof slab is sensitive to the variations in the parameters T_1 and T_4. So each parameter is contributing to in different aspects and hence all the parameters are taken as design variables for the optimization process. Figure 2 to 5 shows the sensitivity of the objective function (cost) and the state variables (stress and deformation) to the variation of the design variables.

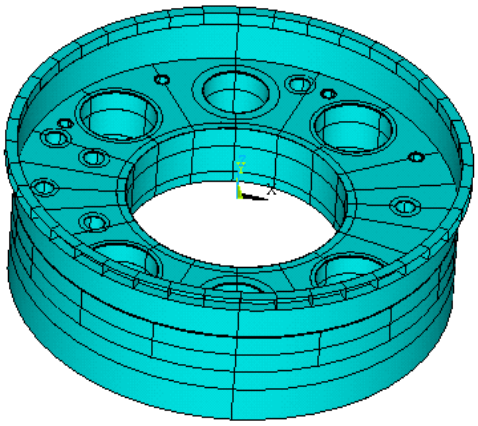

Figure 1. Parametric model of the roof slab

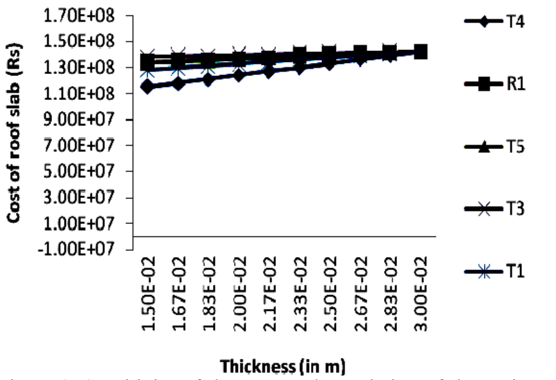

Figure 2. Sensitivity of the cost to the variation of the various thicknesses

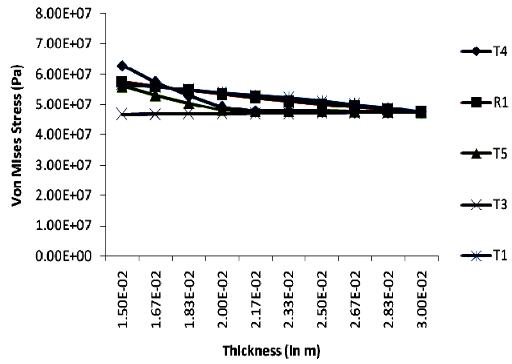

Figure 3. Sensitivity of the maximum stress developed in the roof slab to the variation of the various thicknesses

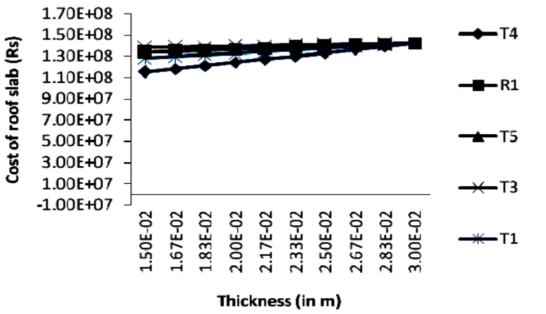

Figure 4. Sensitivity of the maximum deformation on the roof slab to the variation of the various thicknesses

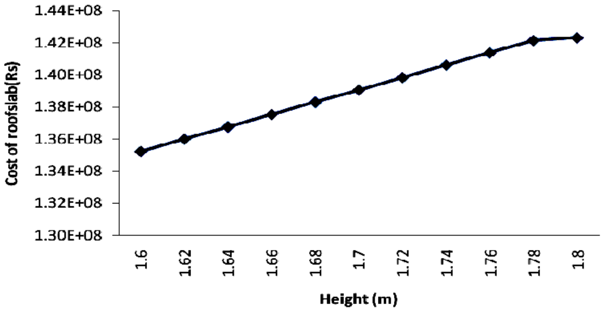

Figure 5. Sensitivity of the cost of the roof slab to the variation of the roof slab height

3.3. Experimental Design

An important issue to metamodeling is to achieve good accuracy of metamodels with a reasonable number of sample points. Experimental design is the sampling plan in design space. The type of experimental design adopted in this work was Central Composite Design (CCD), since many researchers have used this technique for the design of computer experiments [10, 11, 12]. Minitab software has been used to perform the experimental design. The factor H_1 has four levels and factors T_1, T_3, T_4, T_5 and R_1 have two levels each as given in Table 1. Table 2 shows the sample design points based on CCD.

Table 1. Various parameters considered for the optimization of roof slab

Factors	Levels			
	1	2	3	4
H_1(m)	1.8	1.6	-	-
T_1(m)	1.50	2.00	2.25	3.00
T_3(m)	1.50	2.00	2.25	3.00
T_4(m)	1.50	2.00	2.25	3.00
T_5(m)	1.50	2.00	2.25	3.00
R_1(m)	1.50	2.00	2.25	3.00

Table 2. Experimental design sample points based on CCD

H1 m	**T1** x 10^{-2} m	**T3** x 10^{-2} m	**T4** x 10^{-2} m	**T5** x 10^{-2} m	**R1** x 10^{-2} m
1.7	2.25	2.25	2.25	2.25	2.25
1.41	2.25	2.25	2.25	2.25	2.25
1.7	2.25	2.25	2.25	2.25	2.25
1.98	2.25	2.25	2.25	2.25	2.25
1.7	0.13	2.25	2.25	2.25	2.25
1.7	2.25	2.25	2.25	2.25	2.25
1.7	4.37	2.25	2.25	2.25	2.25
1.7	2.25	1.29	2.25	2.25	2.25
1.7	2.25	2.25	2.25	2.25	2.25
1.7	2.25	4.37	2.25	2.25	2.25
1.7	2.25	2.25	0.129	2.25	2.25
1.7	2.25	2.25	2.25	2.25	2.25
1.7	2.25	2.25	4.37	2.25	2.25
1.7	2.25	2.25	2.25	1.29	2.25
1.7	2.25	2.25	2.25	2.25	2.25
1.7	2.25	2.25	2.25	4.37	2.25
1.7	2.25	2.25	2.25	2.25	0.129
1.7	2.25	2.25	2.25	2.25	2.25
1.7	2.25	2.25	2.25	2.25	4.37
1.6	1.50	1.50	1.50	1.50	1.50
1.8	1.50	1.50	1.50	1.50	1.50
1.6	3.00	1.50	1.50	1.50	1.50
1.8	3.00	1.50	1.50	1.50	1.50
1.6	1.50	3.00	1.50	1.50	1.50
1.7	2.25	2.25	2.25	2.25	2.25
1.8	1.50	3.00	1.50	1.50	1.50
1.6	3.00	3.00	1.50	1.50	1.50
1.8	3.00	3.00	1.50	1.50	1.50
1.6	1.50	1.50	3.00	1.50	1.50
1.8	1.50	1.50	3.00	1.50	1.50
1.6	3.00	1.50	3.00	1.50	1.50
1.7	2.25	2.25	2.25	2.25	2.25
1.8	3.00	1.50	3.00	1.50	1.50
1.6	1.50	3.00	3.00	1.50	1.50
1.8	1.50	3.00	3.00	1.50	1.50
1.6	3.00	3.00	3.00	1.50	1.50
1.8	3.00	3.00	3.00	1.50	1.50
1.6	1.50	1.50	1.50	3.00	1.50
1.8	1.50	1.50	1.50	3.00	1.50
1.7	2.25	2.25	2.25	2.25	2.25
1.6	3.00	1.50	1.50	3.00	1.50
1.8	3.00	1.50	1.50	3.00	1.50
1.6	1.50	3.00	1.50	3.00	1.50
1.8	1.50	3.00	1.50	3.00	1.50
1.6	3.00	3.00	1.50	3.00	1.50
1.8	3.00	3.00	1.50	3.00	1.50
1.6	1.50	1.50	3.00	3.00	1.50

1.8	1.50	1.50	3.00	3.00	1.50
1.6	3.00	1.50	3.00	3.00	1.50
1.7	2.25	2.25	2.25	2.25	2.25
1.8	3.00	1.50	3.00	3.00	1.50
1.6	1.50	3.00	3.00	3.00	1.50
1.8	1.50	3.00	3.00	3.00	1.50
1.6	3.00	3.00	3.00	3.00	1.50
1.8	3.00	3.00	3.00	3.00	1.50
1.6	1.50	1.50	1.50	1.50	3.00
1.8	1.50	1.50	1.50	1.50	3.00
1.6	3.00	1.50	1.50	1.50	3.00
1.7	2.25	2.25	2.25	2.25	2.25
1.8	3.00	1.50	1.50	1.50	3.00
1.6	1.50	3.00	1.50	1.50	3.00
1.8	1.50	3.00	1.50	1.50	3.00
1.6	3.00	3.00	1.50	1.50	3.00
1.8	3.00	3.00	1.50	1.50	3.00
1.6	1.50	1.50	3.00	1.50	3.00
1.8	1.50	1.50	3.00	1.50	3.00
1.6	3.00	1.50	3.00	1.50	3.00
1.8	3.00	1.50	3.00	1.50	3.00
1.6	1.50	3.00	3.00	1.50	3.00
1.7	2.25	2.25	2.25	2.25	2.25
1.8	1.50	3.00	3.00	1.50	3.00
1.6	3.00	3.00	3.00	1.50	3.00
1.8	3.00	3.00	3.00	1.50	3.00
1.6	1.50	1.50	1.50	3.00	3.00
1.8	1.50	1.50	1.50	3.00	3.00
1.6	3.00	1.50	1.50	3.00	3.00
1.8	3.00	1.50	1.50	3.00	3.00
1.7	2.25	2.25	2.25	2.25	2.25
1.6	1.50	3.00	1.50	3.00	3.00
1.8	1.50	3.00	1.50	3.00	3.00
1.6	3.00	3.00	1.50	3.00	3.00
1.8	3.00	3.00	1.50	3.00	3.00
1.6	1.50	1.50	3.00	3.00	3.00
1.7	2.25	2.25	2.25	2.25	2.25
1.8	1.50	1.50	3.00	3.00	3.00
1.6	3.00	1.50	3.00	3.00	3.00
1.8	3.00	1.50	3.00	3.00	3.00
1.6	1.50	3.00	3.00	3.00	3.00
1.8	1.50	3.00	3.00	3.00	3.00
1.6	3.00	3.00	3.00	3.00	3.00

3.4. Metamodeling

Metamodeling, often referred as Response Surface Methodology (RSM), involves (a) choosing an experimental design for generating data, (b) choosing a model to represent the data, and (c) fitting the model to the observed data. Detailed description of the RSM is given in Simpson et. al. [2]. Based on the experimental design, the computer experiments were conducted for the various combinations of factors at different levels using the CCD experimental design. The metamodeling technique used in this study is polynomial regression and has been applied by a number of researchers [2, 9, 10, 11, 13] in designing complex engineering systems. The most widely used response surface approximating functions are low-order polynomials. For significant curvature, a second order polynomial which includes all two-factor interactions can be used. A second order polynomial model can be expressed as:

$$\hat{y} = \beta_0+\beta_1x_1+\beta_2x_2+\dots+\beta_kx_k+\beta_{12}x_1\,x_2+\dots+\beta_{k-1,}kx_{k-1}\,x_k+\beta_{11}x_1^2+\beta_{22}x_2^2+\dots+\beta_{kk}x_k^2 \quad (1)$$

The parameters of the polynomial in Equations (1) are usually determined by least squares regression analysis by fitting the response surface approximations to existing data. For the roof slab optimization problem, three metamodels are created to approximate the cost of roof slab, stress developed and deflection using CCD computer experimentation. In order to validate the metamodel some random experiments ware conducted and compared with the finite element simulation of the actual model. The regression coefficients for the three metamodel developed was given in Table 3. Table 4 shows the fitness of the metamodels. Validated regression models of the three responses generated are shown below.Table 3. Regression coefficients for the metamodels.

Table 3. Regression coefficients for the metamodel

Regression coefficients	COST	DMAX	SMAX
β_0	-6.66E+07	3.26E-02	6.97E+08
β_1	1.03E+08	-1.71E-02	-2.77E+08
β_2	1.22E+09	-5.67E-01	-1.12E+10
β_3	4.04E+07	-1.92E-02	-7.01E+06
β_4	6.40E+08	-1.36E-01	-3.80E+09
β_5	-1.95E+08	-8.67E-02	-6.76E+09
β_6	-4.60E+07	-1.12E-01	-8.42E+08
β_7	6.19E+07	1.47E-01	-4.05E+08
β_8	1.99E+08	-5.09E-02	-5.10E+07
β_9	2.16E+08	8.08E-02	1.08E+09
β_{10}	3.83E+08	6.83E-02	2.32E+09
β_{11}	3.08E+08	8.16E-02	5.57E+08
β_{12}	-2.34E+09	1.74E+00	7.65E+09
β_{13}	1.03E+08	-2.62E-01	-8.73E+10
β_{14}	-8.97E+08	-7.51E-01	-4.46E+09
β_{15}	6.58E+08	-5.29E-01	-1.01E+09
β_{16}	8.25E+08	9.55E-01	-1.10E+10
β_{17}	-1.62E+09	8.99E-01	-1.06E+10
β_{18}	6.03E+08	9.10E-01	4.04E+09
β_{19}	3.81E+08	-7.57E-01	-6.12E+09
β_{20}	-1.40E+09	-6.79E-01	-6.79E+09
β_{21}	1.38E+09	-8.01E-01	-6.96E+09
β_{22}	-2.98E+07	1.82E-03	4.35E+07
β_{23}	-4.39E+09	5.18E+00	2.64E+11
β_{24}	-1.95E+09	-3.22E-01	3.29E+09
β_{25}	2.26E+10	-2.00E-01	3.65E+10
β_{26}	2.50E+09	-1.11E-01	3.88E+10
β_{27}	2.50E+09	-2.11E-01	3.74E+09

Table 4. Fitness of metamodels

Response parameter	R-Squared value (%)	R-Squared (Adjusted) value (%)
Cost	78.44	77.76
Stress	82.48	74.86
Deformation	82.2	74.45

3.5. Optimization

The objective of this optimization is to minimize the weight of the roof slab. The method of probabilistic search based on evolutionary algorithms was chosen for the present optimization problem. The real-coded genetic algorithm (RCGA) is developed for obtaining the optimal dimensions of the roof slab of PFBR. The code template developed by Deb [14] was used for this purpose. Certain modifications in the algorithm of this program were necessary to apply it for the present study. RCGA is developed for six input variables and two constraints. The RCGA parameters chosen are; crossover probability=0.8, mutation probability=0.2, number of generation=100, and the population size=60. Various thicknesses of the roof slab and the height of the roof slab are considered as the design variables for optimization. The state variables in the optimization are maximum stress and maximum deformation. In this study the maximum stress is the material yield strength and maximum deflection is the permissible axial movement of the control plug. The range of various design variables with respect to the design requirement is:

- H_1 – [1600-1800] mm
- T_1 – [15 - 30] mm
- T_3 – [15 - 30] mm
- T_4 – [15 - 30] mm
- T_5 – [15 - 30] mm
- R_1 – [15 - 30]mm

The limits for the state variables are 128MPa and 4mm for maximum stress and deflection respectively. Optimization of the roof slab was carried out by this approach and the total volume of the roof slab is reduced by 14.6 % and the cost of roof slab is reduced by 41.4%. Table 5 shows the design and state variables after optimization. The optimized roof slab is also checked for its design adequacy under static and dynamic conditions in Finite Element package ANSYS.

Table 5. Results of optimization process

	Optimization Method	H1 (m)	T1 (m)	T3 (m)	T4 (m)	T5 (m)	R1 (m)	COST (in Cores)	Stress (MPa)	Deformation (m)
Optimized roof slab	GA	1.7	0.020	0.020	0.015	0.015	0.015	8.37	92.4	0.0037
Existing roof slab	-	1.8	0.03	0.03	0.03	0.03	0.03	14.3	82.7	0.0024

4. Conclusion

Traditional solution methods for optimizing complex real life engineering problems can be very expensive and often results in sub-optimal solutions. In this paper, an approach to develop metamodel for complex real time problem is presented. As a case study, a roof slab for which design optimization has to be carried out is considered. A metamodel based optimization approach is presented to address expensive computational cost of large FE runs using meta-models. With the proposed strategy of performing computer experiments, creating metamodel and the application of evolutionary algorithms, this optimization methodology can easily be adopted to more complex structural problems.

References

[1] A.I.J. Forrester, A.J. Keane, “Recent advances in surrogate-based optimization”, Progress in Aerospace Sciences, Vol. 45, 2009, 50–79.

[2] T.W. Simpson, J. D. Peplinski, P. N. Koch, “Metamodels for Computer based Engineering Design,” Engineering with Computers, Vol.17, 2001, 129-150.

[3] Simpson. T.W., Mauery. T. M, Korte. J.J., and Mistree. F, "Comparison of Response Surface and Kriging Models for Multidisciplinary Design Optimization," *7th AIAA/USAF/NASA/ISSMO Symposium on Multidisciplinary Analysis & Optimization,* St. Louis, MO, 1998.

[4] F.M. Alam, K.R. McNaught, T.J. Ringrose, “A comparison of experimental designs in the development of a neural network simulation metamodel”, Simulation Modeling Practice and Theory, Vol. 12, 2004, 559–578

[5] N.V. Queipo, R.T. Haftka, W. Shyy, T.Goel, R.Vaidhyanathan, P.K.Tucker, “Surrogate-based analysis and optimization”, Progress in Aerospace Sciences , Vol. 41, 2005, 1–28

[6] Ruichen. J, Wei. C, Simpson. T.W, “Comparative studies of metamodeling techniques under multiple modeling criteria”, 8th AIAA/USAF/NASA/ISSMO Multidisciplinary Analysis & Optimization Symposium, Long Beach, CA, 2000.

[7] Giunta, A, Watson L.T and Koehler. J, "A Comparison of Approximation Modeling Techniques: Polynomial Versus

Interpolating Models," 7th *AIAA/USAF/NASA/ISSMO Symposium on Multidisciplinary Analysis & Optimization,* St. Louis, 1998.

[8] S. Varadarajan, W. Chen, and C. Pelka, "The Robust Concept Exploration Method with Enhanced Model Approximation Capabilities", *Engineering Optimization, Vol. 32, No. 3,* 2000, 309-334.

[9] Yang. R.J, Gu. L, Liaw. L, Gearhart. C, Tho. C.H, Liu. X, and Wang. B.P, "Approximations for Safety Optimization of Large Systems", ASME Design Automation Conference, Baltimore, MD, 2000.

[10] W. Chen, J.K. Allen, D.N. Mavris, and F. Mistree, "A Concept Exploration Method for Determining Robust Top-Level Specifications," *Engineering Optimization,* Vol. 26, 1996, 137-158.

[11] Unal. R., Lepsch. R.A., Engelund. W and Stanley. D.O., "Approximation Model Building and Multidisciplinary Design Optimization Using Response Surface Methods," 6th *AIAA/USAF/NASA/ISSMO Symposium on Multidisciplinary Analysis and Optimization,* Bellevue, WA, 1996.

[12] S. Varadarajan, W. Chen, and C. Pelka, "The Robust Concept Exploration Method with Enhanced Model Approximation Capabilities", *Engineering Optimization, Vol. 32, No. 3,* 2000, 309-334.

[13] Venter.G, Haftka. R. T. and Starnes. J.H, Jr., "Construction of Response Surfaces for Design Optimization Applications," *6th AIAA/USAF/NASA/ISSMO Symposium on Multidisciplinary Analysis and Optimization* Bellevue, WA, 1996.

[14] Deb. K, Multi-Objective Optimization Using Evolutionary Algorithms, Wiley, 2001.

المملكة الأردنية الهاشمية

الجامعة الهاشمية

المجلة الأردنية للهندسة الميكانيكية والصناعية

JJMIE

مجلة علمية عالمية محكمة

http://jjmie.hu.edu.jo/

ISSN 1995-6665

المجلة الأردنية للهندسة الميكانيكية والصناعية
مجلة علمية عالمية محكمة

المجلة الأردنية للهندسة الميكانيكية والصناعية: مجلة علمية عالمية محكمة تصدر عن عمادة البحث العلمي والدراسات العليا في الجامعة الهاشمية بالتعاون مع صندوق دعم البحث العلمي في الأردن.

ترسل البحوث إلى العنوان التالي :

ترسل البحوث إلى العنوان التالي:

رئيس تحرير المجلة الأردنية للهندسة الميكانيكية والصناعية
عمادة البحث العلمي والدراسات العليا
الجامعة الهاشمية
الزرقاء - الأردن

هاتف : 3903333 5 00962 فرعي 4147
Email: jjmie@hu.edu.jo
Website: www.jjmie.hu.edu.jo